

Proceedings of the 12th UK Conference on Boundary Integral  
Methods UKBIM12

Edited by Dr Carlos Fresneda-Portillo

8th – 9th July 2019  
Oxford Brookes University

# Proceedings of the 12th UK Conference on Boundary Integral Methods - UKBIM12

Published by OXFORD BROOKES University,  
Oxford Brookes University,  
Copyright ©2019 The Authors  
ISBN 978-1-9997412-9-7

eISBN 978-1-9165043-8-7

# Preface

Boundary integral methods have become established for solving a wide variety of problems in science and engineering. UK based researchers have been active and made substantial contributions in the theory and development of boundary integral formulations, as well as their analysis, discretisation and numerical solution.

The UKBIM conference series aims to provide a forum where recent developments in boundary integral methods can be discussed in an informal atmosphere. The first UK conference on boundary integral methods (UKBIM) was held at the University of Leeds in 1997. Subsequent UKBIM conferences have taken place in Brunel (1999), Brighton (2001), Salford (2003), Liverpool (2005), Durham (2007), Nottingham (2009), Leeds (2011), Aberdeen (2013), Brighton (2015) and Nottingham-Trent (2017). The success of these events has made the conference a regular event for researchers based in the UK, and elsewhere, who are working on all aspects of boundary integral methods. This book contains the abstracts and papers presented at the Twelfth UK Conference on Boundary Integral Methods (UKBIM 12), held at Oxford Brookes University in July 2019.

The work presented at the conference, and published in this volume, demonstrates the wide range of work that is being carried out in the UK, as well as from further afield. I am grateful to the members of the scientific committee for their advice and support during the past year, and to all the authors and reviewers for their hard work in producing the high quality peer-reviewed papers for this book.

## Scientific Committee

- Dr David Chappell
- Prof. Ke Chen
- Dr Carlos Fresneda Portillo
- Dr Paul Harris
- Prof. Daniel Lesnic
- Dr Oleksandr Menshykov
- Prof. Sergey Mikhailov
- Prof. Jon Trevelyan
- Prof. Luiz Wrobel
- Nottingham Trent University
- University of Liverpool
- Oxford Brookes University
- University of Brighton
- Durham University
- Brunel University London

## Organising Committee

- Dr Carlos Fresneda Portillo
- Dr Layal Hakim
- Ms Lucia Sagredo
- Oxford Brookes University
- University of Exeter
- Oxford Brookes University

## Acknowledgements

This conference acknowledges the generous financial support provided from the Scheme 1 from the London Mathematical Society and the Conference Organisation Grant Scheme from the Institute of Mathematics and its Applications.

Furthermore, I would like to thank the organising committee: Lucia Sagredo and Layal Hakim for their support provided for organising this conference, as well as, Jose Espinosa for his support compiling the conference programme. As well, I would like to thank D. Lesnic, P. Harris, O. Menshykov and D. Chappell for the support provided.

I would also like to thank Prof. Chrisina Jayne for her efforts in obtaining a room for the conference in the main building of Oxford Brookes University.

Last but not least, I would like to thank my colleagues Dr Armando Coco, Dr James Maunder and Dr Kayvan Nejabati Zenouz for their support with this event.

Dr Carlos Fresneda Portillo, Chair of UKBIM12, July 2019.

# Contents

<b>1. Singular enrichment functions for Helmholtz scattering by polygonal objects</b> <i>B.D. Gilvey, G. Hattori, J. Trevelyan</i> . . . . .	1
<b>2 Towards a hybrid convolution quadrature method for the wave equation</b> <i>J. Rowbottom and D.J. Chappell</i> . . . . .	9
<b>3 Discontinuous isogeometric boundary element (IGABEM) formulations</b> <i>Y. Sun, C.H. Lu, G. Hattori, J. Trevelyan</i> . . . . .	15
<b>4 Numerical treatment of highly oscillatory PUBEM integrals</b> <i>B.D. Gilvey, J. Trevelyan</i> . . . . .	24
<b>5 The leading order equivalence of Oseen's and Imai's representations</b> <i>H.A. Adamu and E. A. Chadwick</i> . . . . .	32
<b>6 Enriched boundary element formulation for water coning</b> <i>J.A. Márquez Ruiz, B. Chenm, J. Trevelyan, P.A. Gourgiotis, E.L. Alburquerque</i> . . . . .	41
<b>7 Resolving Stokes flow around geometries with sharp corners</b> <i>L. Bystricky, S. Palsson and A.K. Tornberg</i> . . . . .	49
<b>8 BEM for Low Reynolds Number Flow Past in an Unbounded Domain</b> <i>B.C. Dang and E. A. Chadwick</i> . . . . .	61
<b>9 A boundary element formulation for PDEs containing fractional derivatives</b> <i>J.A.M. Carrer, J. Trevelyan, M. Seaid and S. Solheid</i> . . . . .	72
<b>10 Fast Boundary Element Methods for the Vlasov-Poisson System</b> <i>T. Keßler, S. Rjasanow and S. Weißer</i> . . . . .	82
<b>11 Asymptotic solutions of convolution integral equations</b> <i>D. Ponomarev</i> . . . . .	92
<b>12 A boundary-domain integral equation for the Neumann problem</b> <i>S.E. Mikhailov, T.G. Ayele and Z.W. Woldemicheal</i> . . . . .	102
<b>13 BEM for stress concentration and fracture analysis</b> <i>M.N. Perelmuter</i> . . . . .	113
<b>14 A boundary element formulation for stress concentration problems</b> <i>P.A. Gourgiotis, G. Hattori and J. Trevelyan</i> . . . . .	122
<b>15 A Single-Layer Approach for Biharmonic Data Completion</b> <i>R. Chapko and B.T. Johansson</i> . . . . .	133

<b>16 Gradient Recovery for the BEM-based FEM and VEM</b>	
<i>D. Seibel and S. Weißer</i> . . . . .	141
<b>17 A Boundary Integral Method For Modeling Cell Motion Due To Chemotaxis</b>	
<i>P.J. Harris</i> . . . . .	151
<b>Abstract only submissions</b>	
<i>Plenary Talk I: Highly accurate integral equation methods for laden drops</i>	
<i>A.K. Tornberg</i> . . . . .	160
<i>Plenary Talk II: Does the Galerking method converge for Laplace problems in Lipschitz domains?</i>	
<i>E. Spence</i> . . . . .	161
<i>A direction preserving discretisation for transporting densities</i>	
<i>D. Chappell, M. Richter and G. Tanner</i> . . . . .	162
<i>A DRBEM Formulation for Two-Dimensional Coupled Viscous Non-Linear Burger's Equations</i>	
<i>Salam Adel Ahmed, Luiz C. Wrobel and Jurij Iljaz</i> . . . . .	163
<i>A Green's integral representation for the two-dimensional steady Navier-Stokes equation</i>	
<i>E.A. Chadwick</i> . . . . .	164
<i>On Boundary-Domain Integral Equations for Stokes PDE System in <math>L_p</math>-based spaces for Variable-Viscosity Compressible Fluid on Lipschitz Domain</i>	
<i>S.E. Mikhailov</i> . . . . .	165
<i>Active control of nonstationary vibrations of plates under dynamic transverse loading</i>	
<i>Dr Oleksandr Menshykov</i> . . . . .	166
<i>Generalized Fourier Series Method for Elastic Plates</i>	
<i>C. Constanda and D. Doty</i> . . . . .	167

# Chapter 1

## Singular enrichment functions for Helmholtz scattering by polygonal objects

B.D. Gilvey<sup>1</sup>, J. Trevelyan, G. Hattori<sup>2</sup>

<sup>1</sup> Department of Engineering  
Durham University  
South Road  
DH1 3LE, Durham, UK.

<sup>2</sup> Department of Engineering  
University of Cambridge  
Trumpington Street  
CB2 1PZ, Cambridge, UK.

---

**Abstract.** *When considering Helmholtz scattering, convergence of both FEM and BEM is slower for polygonal objects (than smooth objects). This is due to the known singular behaviour at corner locations. Attempts to ameliorate this using enrichment functions have been made in an FEM setting [1]. The current work extends these ideas to conventional BEM and to PUBEM (Partition of Unity Boundary Element Method) [2]. The choice of enrichment functions  $\psi_l$  is informed by the asymptotic potential behaviour around a corner. The result is an enhanced function space including traditional Lagrangian shape functions, a series of plane waves and the new  $\psi_l$  functions. Configurations containing square scattering objects are studied, with Neumann boundary conditions. A substantial improvement is shown, with a significant reduction in the number of degrees of freedom required.*

---

### 1.1 Introduction

For Helmholtz problems in infinite domains in particular, it is well known that BEM provides a strong advantage over volumetric methods such as FEM. This is in part due to the reduction in dimensionality of the problem, but also due to the automatic satisfaction of the Sommerfeld radiation condition. Even with this advantage included, when the wavelength  $\lambda$  becomes small, relative to the domain of interest, the computational expense may become prohibitively large. There are numerous approaches to accelerate the solution of the resulting systems of equations,

such as fast multipole expansions [3], low-rank matrix approximations [4] and use of optimised linear algebra routines [5]. This paper will focus on an alternative option, which is to enrich the approximation space in order to reduce the number of degrees of freedom required, specifically with singular enrichment functions for corner locations.

Before presenting the proposed enrichment functions, a brief overview of enriched methods is provided here. Methods in which known local solutions of the underlying PDE are included as a basis are generally referred to as Trefftz methods. A successful choice of enrichment is a plane wave basis, which draws upon the Partition of Unity Method [6]. Some examples include the Partition of Unity Finite Element Method (PUFEM) [7, 8], the Discontinuous Enrichment Method [9], the Variational Theory of Complex Rays (VTCR)[10], the Ultraweak Variational Formulation (UWVF) [11] and the Plane Wave Discontinuous Galerkin Method (PWDG) [12]. Partition of Unity Boundary Element Method (PUBEM) was developed by Perrey-Debain et al.[13, 2, 14], extending the PUFEM ideas to a BEM setting. The result was a reduction in the number of degrees of freedom required per wavelength  $\tau$  from 8-10 to approximately 2.5. Another wave based method is that of Chandler-Wilde [15], later adapted to become the Numerical Asymptotic approach [16].

The substantial improvement offered by PUBEM is lessened when considering polygonal scattering objects, because the sharp corners introduce singularities which provide an additional challenge. To remedy this, it is possible to include additional, singular enrichment functions at corner locations. This has been utilised in the Ultra Weak Variation Formulation (UVWF)[1], combined with the Method of Fundamental Solutions (MFS) in [17], and is extended to a BEM and PUBEM setting, in the current work.

## 1.2 Preliminaries

In this section, a brief description of the problem under investigation is provided, along with the resulting BIE. We define a polygonal object  $\Omega_s \subset \mathbb{R}^2$  with the boundary  $\Gamma$ . The acoustic wave propagation occurs in the exterior domain  $\Omega_f = \mathbb{R}^2 \setminus \Omega_s$ . Considering the problem to be time-harmonic, we arrive at the Helmholtz equation

$$\nabla^2 u(\mathbf{x}) + k^2 u(\mathbf{x}) = 0, \quad \mathbf{x} \in \Omega_f,$$

where the wavenumber  $k = 2\pi/\lambda$ . The unknown potential is  $u \in \mathbb{C}$  and  $\nabla^2$  is the Laplacian operator. Impinging the object with an incident wave  $u^{inc}$  and imposing a sound-hard Neumann boundary condition  $\nabla u(\mathbf{x}) \cdot \mathbf{n} = 0$ ,  $\mathbf{x} \in \Gamma$ , results in the following BIE

$$c(p)u(p) + \int_{\Gamma} \frac{\partial G(p, q)}{\partial \mathbf{n}} u(q) d\Gamma_q = u^{inc}(p), \quad p \in \Gamma. \quad (1.1)$$

The points  $p = (x_p, y_p)$  and  $q = (x_q, y_q)$  are the source and field points respectively, and the vector  $\mathbf{n}$  is the unit normal vector outward pointing from  $\Omega_f$ .

## 1.3 Modified basis functions

We present in this section the proposed, enriched formulations. The enriched BEM formulation will be referred to as ‘XBEM’ and the enriched PUBEM will be referred to as ‘PUXBEM’. In XBEM, the unknown potential  $u$  over element  $e$  is expressed as

$$u = \sum_{j=1}^J N_j(\xi) u_j^e + \sum_{l=1}^L \psi_l(\xi) \bar{u}_l^e.$$

Where  $N_j$  is the traditional Lagrangian shape function for node  $j$ , and  $\psi_l$  represents the  $l_{th}$  proposed singular enrichment function. This results in the following XBEM discretisation of (1.1)

$$c(p)u(p) + \sum_{e=1}^E \sum_{j=1}^J \int_{-1}^1 \frac{\partial G(p, q)}{\partial \mathbf{n}} N_j(\xi) J^e d\xi u_j^e + \sum_{e=1}^E \sum_{l=1}^L \int_{-1}^1 \frac{\partial G(p, q)}{\partial \mathbf{n}} \psi_l(\xi) J^e d\xi \bar{u}_l^e = u^{inc}(p)$$

This introduces  $L$  new coefficients, into the solution vector, associated with the  $\bar{u}_l^e$  unknowns. In PUXBEM the unknown potential  $u$  over element  $e$  is expressed as

$$u = \sum_{j=1}^J \sum_{m=1}^M N_j(\xi) A_{jm}^e e^{ik \mathbf{d}_{jm} \cdot \mathbf{q}} + \sum_{l=1}^L \psi_l(\xi) B_l^e.$$

In which the potential is expressed as a linear combination of equispaced plane waves, having unknown amplitudes  $A_{jm}$  and direction vectors  $\mathbf{d}_{jm}$ , in addition to the singular enrichment functions  $\psi_l$ . The corresponding discretised PUXBEM BIE becomes

$$c(p)u(p) + \sum_{e=1}^E \sum_{j=1}^J \sum_{m=1}^M P_{jm}^e A_{jm}^e + \sum_{e=1}^E \sum_{l=1}^L Q_l^e B_l^e = u^{inc}(p),$$

where

$$P_{jm}^e = \int_{-1}^1 \frac{\partial G(p, q)}{\partial \mathbf{n}} N_j(\xi) e^{ik \mathbf{d}_{jm} \cdot \mathbf{q}} J^e d\xi,$$

$$Q_l^e = \int_{-1}^1 \frac{\partial G(p, q)}{\partial \mathbf{n}} \psi_l(\xi) J^e d\xi.$$

Two choices of  $\psi_l$  are proposed, both of which are informed by the known asymptotic behaviour around a corner, which for the sound-hard case is

$$u(r_b, \theta_b) \approx \sum_{n=1}^N J_{n\alpha}(kr_b) \cos n\alpha\theta_b, \quad 0 < \frac{\pi}{\alpha} < 2\pi. \quad (1.2)$$

The associated exterior angle for a corner is  $\pi/\alpha$ ,  $r_b$  is the Euclidean distance from the corner and angle  $\theta_b$  is measured from one of the planar surfaces at the corner as shown in Fig. 1.1. A plot of the family of Bessel functions from (1.2), taking  $N = 6$  and  $\alpha = \frac{2}{3}$  is shown in Fig. 1.2. It is clear that as  $r_b$  approaches zero, only the  $n = 1$  term has an infinite gradient, which one would expect to appropriately model a singularity. For this reason, differing from Luostari et al. [1] and Barnett & Betcke [17], the first enrichment function that we employ is simply the  $n = 1$  term in the series. The second option considered is  $r_b^\alpha$ , because as  $r_b$  becomes small, the asymptotic behaviour is the same, but it requires slightly less computational expense than using a Bessel function. Thus, we investigate the use of two candidate forms,  $\psi_{1,l}$  and  $\psi_{2,l}$ , of the enrichment function, being

$$\psi_{1,l} = r_b^\alpha \cos l\alpha\theta_b$$

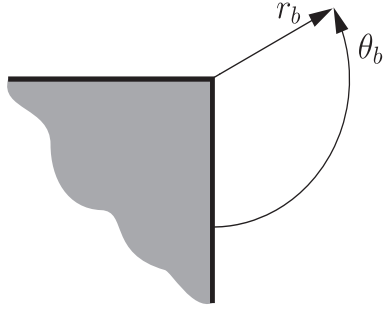


Figure 1.1: Polar coordinate system local to a corner.

$$\psi_{2,l} = J_{l\alpha}(kr_b) \cos l\alpha\theta_b.$$

We include a separate degree of freedom for each edge meeting at a corner, adding eight degrees of freedom to a square scattering object, for example. For clarification;

$$\bar{u}_L^e \neq \bar{u}_1^{e+1}$$

$$B_L^e \neq B_1^{e+1}$$

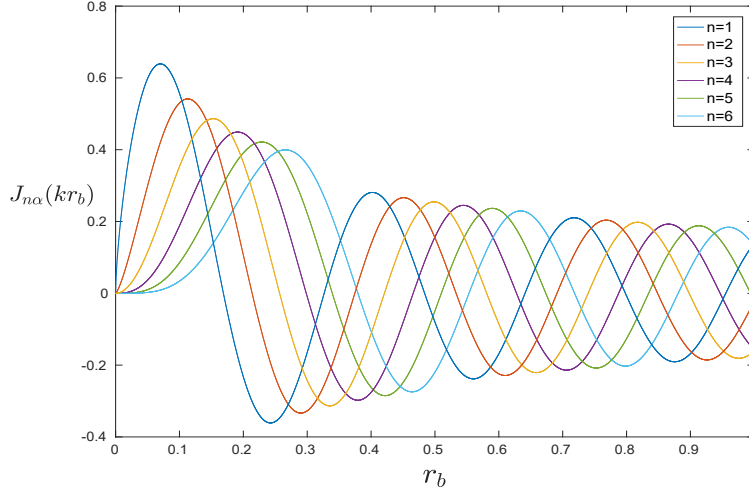


Figure 1.2: Bessel functions with  $n = 1-6$ ,  $\alpha = \frac{2}{3}$  and  $k = 20$ .

## 1.4 Numerical example

A unit square being impinged by a plane wave  $u^{inc}$  propagating in direction  $\phi_{inc} = \pi/4$ , is considered as a test case. This is illustrated in Fig. 1.3, for  $k = 50$ . Firstly, we set  $k = 20$ , and evaluate potential over a ring of points at  $r_{ip} = \sqrt{0.5^2 + 0.5^2} + \gamma$ , shown in Fig. 1.4. We vary the number of degrees of freedom and plot corresponding the relative error for the case  $\gamma = 1$  in Fig. 1.5. The relative error is defined as follows,

$$\epsilon = \frac{\|u - u_{ref}\|_{L_2}}{\|u_{ref}\|_{L_2}},$$

where  $u^{ref}$  is a reference solution. It is clear that there is a significant improvement over BEM, by using XBEM or PUXBEM. Furthermore, both of the proposed enrichment functions  $\psi_1$  and  $\psi_2$  offer similar improvement.

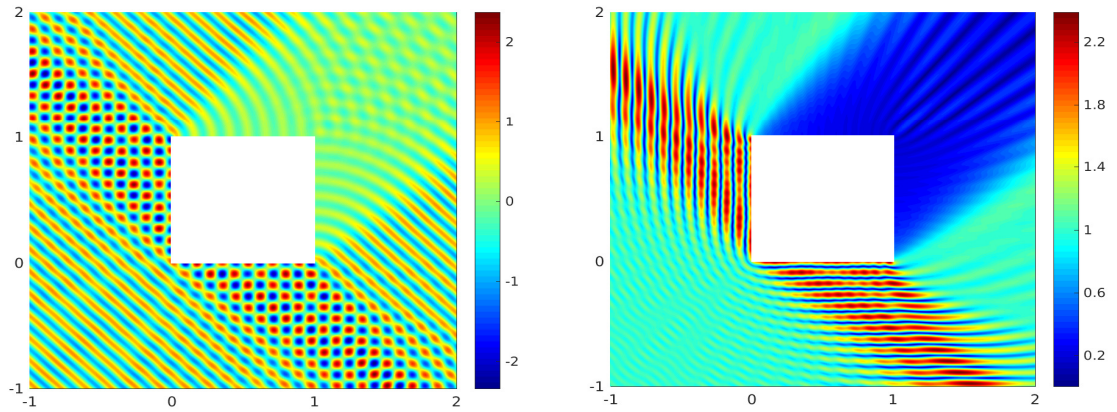


Figure 1.3: (left) Real part of the total potential, (right) absolute value of total potential. Unit square scatterer for the case  $k = 50$ .

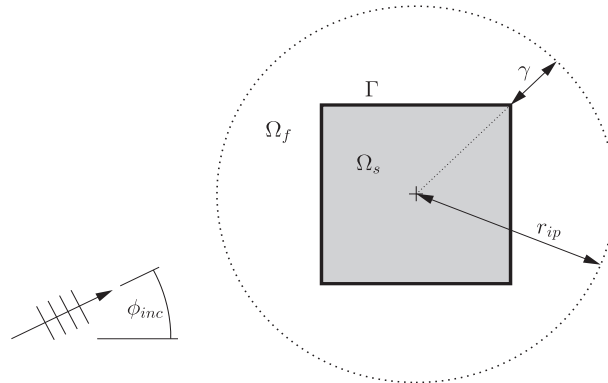


Figure 1.4: Internal point locations for a square scatterer.

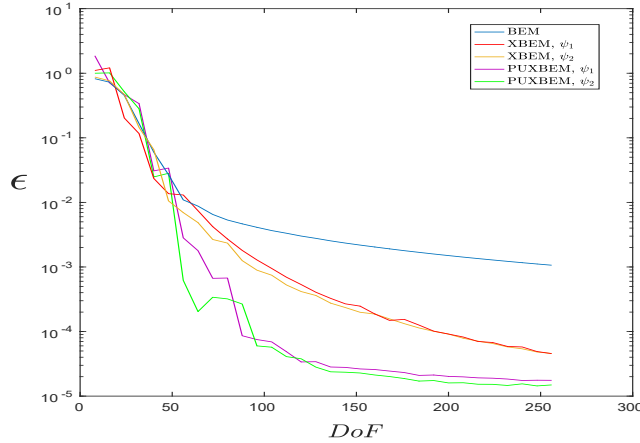


Figure 1.5: Relative error vs. DoF.

To add a deeper insight we fix the number of degrees of freedom to be 128 and vary  $k$ , plotting the resulting relative error in Fig. 1.6. Again, a notable improvement is seen, for both XBEM and PUXBEM. It is also apparent that as  $k$  increases, XBEM approaches the BEM result, whereas the error using PUXBEM remains consistently around two orders of magnitude lower. An explanation for this is that, at a lower frequency the singularity dominates the solution, thus BEM and PUXBEM perform similarly. As frequency increases, the singularity becomes less important, and as a result XBEM and BEM are similarly equipped, whereas PUXBEM has the additional plane wave basis to capture the higher frequency variation.

## 1.5 Conclusions and further work

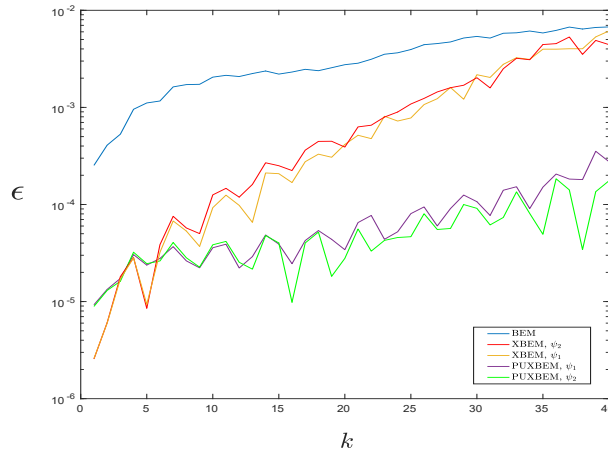


Figure 1.6: Relative error vs.  $k$  using 128 DoF.

In this paper, we introduced two candidate enrichment functions, with the intention of better representing the singularity that is present when considering polygonal scattering objects. The results indicate a clear benefit of this enrichment, particularly for lower  $k$ . When including a plane wave basis a reduction in error of approximately two orders of magnitude can be expected.

Also of note is that the largest improvement was offered by the Bessel-based  $\psi_2$  functions, but the improvement over the simpler  $\psi_1$  functions is minimal. As the  $\psi_1$  functions are faster to compute, the choice between the two could be informed by run-time or accuracy requirements. Further work could include higher frequency, and multiple scattering objects within the same domain.

## References

- [1] Luostari, T., Huttunen, T. and Monk, P.: The ultra weak variational formulation using Bessel basis functions. *Communications in Computational Physics*. **11**, 2012, 400-414.
- [2] Perrey-Debain, E., Trevelyan, J. and Bettess, P.: Wave boundary elements:a theoretical overview presenting applications in scattering of short waves. *Eng. Anal Bound. Elem.* **28**, (2004), 131-141.
- [3] Coifman, R., Rokhlin, V. and Wandzura, S.: The fast multipole method for the wave equation: A pedestrian prescription. *IEEE Antennas and Propagation Magazine*. **35**, (1993), 7-12.
- [4] Bebendorf, M.: Approximation of boundary element matrices. *Numerische Mathematik*. **86**, (2000), 565-589.
- [5] van't Wout, E., Gélat, P., Betcke, T. and Arridge, S.: A fast boundary element method for the scattering analysis of high-intensity focused ultrasound. *The Journal of the Acoustical Society of America*. **138**, (2015), 2726-2737.
- [6] Babuška, I. and Melenk, J. M.: The Partition of Unity Method. *International Journal for Numerical Methods in Engineering*. **40**, (1997), 727-758.
- [7] Laghrouche, O., Bettess, P. and Astley, R. J.: Modelling of short wave diffraction problems using approximating systems of plane waves. *International Journal for Numerical Methods in Engineering*. **54**, (2002), 1501-1533.
- [8] Laghrouche, O., Bettess, P., Perrey-Debain, E. and Trevelyan, J.: Wave interpolation finite elements for Helmholtz problems with jumps in the wave speed. *Computer Methods in Applied Mechanics and Engineering*. **194**, (2005), 367-381.
- [9] Farhat, C., Harari, I. and Franca, L. P.: The discontinuous enrichment method. *Computer Methods in Applied Mechanics and Engineering*. **190**, (2001), 6455-6479.
- [10] Ladevèze, P., Arnaud, L., Rouch, P. and Blanzé, C.: The variational theory of complex rays for the calculation of medium-frequency vibrations. *Engineering Computations*, **18**, (2001), 193-214.
- [11] Cessenat, O. and Despres, B.: Application of an ultra weak variational formulation of elliptic PDEs to the two-dimensional Helmholtz problem. *SIAM Journal on Numerical Analysis*, **35**, (1998), 255-299.
- [12] Hiptmair, R., Moiola, A. and Perugia, I.: Plane wave discontinuous Galerkin methods for the 2D Helmholtz equation: analysis of the p-version. *SIAM Journal on Numerical Analysis*, **49**, (2011), 264-284.
- [13] Perrey-Debain, E., Trevelyan, J. and Bettess, P.: New special wave boundary elements for short wave problems. *Communications in Numerical Methods in Engineering*. **18**, (2002), 259-268.
- [14] Perrey-Debain, E., Laghrouche, O., Bettess, P. and Trevelyan, J.: Plane-wave basis finite elements and boundary elements for three-dimensional wave scattering. *Philosophical Transactions of the Royal Society of London A: Mathematical, Physical and Engineering Sciences*. **362**, (2004), 561-577.

- [15] Chandler-Wilde, S.N. and Langdon, S.: A Galerkin boundary element method for high frequency scattering by convex polygons. *SIAM Journal on Numerical Analysis*. **45**, (2007), 610-640.
- [16] Groth, S.P., Hewett, D.P. and Langdon, S.: Hybrid numerical–asymptotic approximation for high-frequency scattering by penetrable convex polygons. *IMA Journal of Applied Mathematics*. **80**, (2015), 324-353.
- [17] Barnett, A.H. and Betcke, T.: An exponentially convergent nonpolynomial finite element method for time-harmonic scattering from polygons. *SIAM Journal on Scientific Computing*. **32**, (2010), 1417-1441.

## Chapter 2

# Towards a hybrid Convolution Quadrature method for the wave equation

**J. Rowbottom, D. Chappell**

Department of Physics and Mathematics,  
Nottingham Trent University  
Clifton Campus  
NG11 8NS, Clifton, Nottingham, UK.

---

**Abstract.** *An overview of the Convolution Quadrature method for solving the wave equation will be presented. We then discuss the computational issues arising when wave problems containing broadband frequency content are of interest. A hybrid model is proposed to address these issues, where the lower frequency content will be modelled via the Convolution Quadrature Boundary Element Method (CQBEM). The CQBEM provides an explicit connection to the frequency content of the wave modelled via the Z-transform, making it the ideal candidate for a hybrid scheme. The higher frequency content will be modelled using a statistical, or energetic, approach such as Statistical Energy Analysis or ray tracing. As a first step towards the formulation of the hybrid model, we discuss how to approximate a solution to the Helmholtz equation in terms of the phase and amplitude obtained from a frequency independent phase-space density.*

---

## 2.1 Introduction

Numerical wave equation solvers share the limitation that high frequency content in the time domain signal requires a discretised model containing many degrees of freedom. The computational cost depends on the choice of method and the number of spatial dimensions to be modelled [1]. A hybrid model is proposed to address these issues at high frequencies, where the lower frequency content will be modelled via the CQBEM and the higher frequency content will be modelled using a statistical approach.

The Boundary Element Method (BEM) has become a popular approach for wave analysis with many researchers using the BEM for a variety of problems [2, 3]. However, it is known that the application of a time-domain BEM may lead to instabilities in the time-stepping methods.

This disadvantage causes issues for solving engineering problems using a time-domain BEM [4, 5]. The BEM is advantageous as it discretises over the boundary only, whereas other numerical methods, such as the finite element method discretise over the whole domain.

The CQ approach was developed by Lubich in the late eighties [6, 7, 8] and provides a simple way to obtain a stable time stepping scheme using the Laplace transform of the kernel function. Since then, significant progress has been made in CQ methods for time-dependent wave simulation methods including high-order Runge Kutta implementations for a variety of wave equations [9, 10]. The CQ method possesses favourable stability properties due to an implicit regularization in time [11]. For the discretisation of boundary integral equations, its main advantage is that it avoids having to evaluate the convolution kernel in the time domain and one instead solves a simplified system of frequency domain boundary integral equations in the spatial region [11].

Examples of work on the CQBEM for solving a range of problems can be found in [12] as well as for a Neumann boundary value problem, such as the one considered here, in [13]. For high frequencies in the CQBEM we require a larger number of boundary elements to model the rapidly oscillating waves. The proposed hybrid method will be more computationally efficient as the computational solution time will be independent of frequency. At higher frequencies, wave problems in industry also exhibit a greater sensitivity to small uncertainties in the models, meaning that a hybrid method with less sensitivity to these uncertainties is of more interest to engineers or manufacturers.

In this paper, we will derive a system of equations to approximate a solution to the wave equation with a Neumann boundary condition via the direct-CQBEM. We then discuss the development of a hybrid method, which requires us to find a relationship between the solutions calculated via the CQBEM and a phase-space density function in order to couple the CQBEM with a high-frequency energy approach such as ray tracing [14].

## 2.2 Integral formulation of the wave equation

Let  $\Omega \subset \mathbb{R}^2$  be a domain with boundary  $\Gamma = \partial\Omega$ . We define the following Neumann boundary value problem for the homogeneous wave equation as follows

$$\partial_t^2 u = c^2 \Delta u \quad \text{in } \Omega \times (0, T), \quad (2.1a)$$

with initial conditions

$$u(\cdot, 0) = \partial_t u(\cdot, 0) = 0, \quad \text{in } \Omega \quad (2.1b)$$

and boundary condition

$$\frac{\partial u}{\partial \hat{\mathbf{n}}_{\mathbf{y}}} = h \quad \text{on } \Gamma \times (0, T) \quad (2.1c)$$

for some  $T > 0$ , where  $h$  is a given function of time and space,  $c > 0$  is the wave speed and  $\hat{\mathbf{n}}_{\mathbf{y}}$  is the unit outward normal to the boundary at  $\mathbf{y} \in \Gamma$ .

The solution to the boundary value problem above will be calculated via a direct boundary integral formulation as then the solution can be expressed in terms of physical quantities. The direct method involves applying Green's identities to derive a boundary integral representation of the wave equation in space and time. The solution along a locally differentiable part of the boundary is given as:

$$\int_0^t \int_{\Gamma} \left( \frac{\partial G}{\partial \hat{\mathbf{n}}_{\mathbf{y}}}(\mathbf{x} - \mathbf{y}, t - \tau) u(\mathbf{y}, \tau) - G(\mathbf{x} - \mathbf{y}, t - \tau) \frac{\partial u}{\partial \hat{\mathbf{n}}_{\mathbf{y}}}(\mathbf{y}, \tau) \right) d\Gamma_{\mathbf{y}} d\tau = \frac{1}{2} u(\mathbf{x}, t). \quad (2.2)$$

Here  $G(\mathbf{x}, t)$  is the free-space Greens function for the wave equation in two dimensions given by

$$G(\mathbf{x}, t) = \frac{H(t - \|\mathbf{x}\|)}{2\pi\sqrt{t^2 - \|\mathbf{x}\|^2}}, \quad (2.3)$$

where  $H$  is the Heaviside step-function. For simplicity, we can rewrite the boundary integral equation (2.2) in terms of boundary integral operators. We apply the Neumann boundary condition (2.1c) and write equation (2.2) as

$$\left(-\frac{1}{2}I + K\right)u = Vh, \quad (2.4)$$

where  $I$  is the identity operator and  $V$  and  $K$  are respectively the single and double layer potential boundary integral operators, which are given by

$$\begin{aligned} (Vh)(\mathbf{x}, t) &:= \int_0^t \int_{\Gamma} G(\mathbf{x} - \mathbf{y}, t - \tau)h(\mathbf{y}, \tau)d\Gamma_{\mathbf{y}}d\tau, \\ (Ku)(\mathbf{x}, t) &:= \int_0^t \int_{\Gamma} \frac{\partial G}{\partial \hat{\mathbf{n}}_{\mathbf{y}}}(\mathbf{x} - \mathbf{y}, t - \tau)u(\mathbf{y}, \tau)d\Gamma_{\mathbf{y}}d\tau. \end{aligned} \quad (2.5)$$

### 2.3 Time discretisation via Convolution Quadrature

For the time discretisation of (2.4) we employ the CQ method that was proposed by Lubich [6, 7]. We do not recall the theoretical framework here but summarise the application of the method, which is also discussed in [9]. We note that the boundary integral operator  $K$  in (2.4) takes the form of a time convolution and make use of the notation

$$\left(\tilde{K}(\partial_t)u\right)(\mathbf{x}, t) = (Ku)(\mathbf{x}, t), \quad (2.6)$$

to emphasise the time convolution. Note that  $\left(\tilde{K}(\partial_t)u\right)$  is standard notation for  $(K * u)$  in the CQ literature [8, 15, 16]. Here  $\tilde{K}(s)$  is the Laplace transform of  $K$ , where  $s$  is the transformed parameter - see (2.9). To discretise the time convolution we split the time interval  $[0, T]$  into  $N$  steps of equal length  $\Delta t = T/N$  and compute an approximate solution at the discrete time steps  $t_n = n\Delta t$ . The continuous convolution operator  $\tilde{K}(\partial_t)$  at the discrete times  $t_n$  is replaced by the discrete convolution operator

$$\left(\tilde{K}(\partial_t^{\Delta t})u^{\Delta t}\right)(\cdot, t_n) = \sum_{j=0}^n w_{n-j}^{\Delta t}(\tilde{K})u_j, \quad \text{for } n = 0, \dots, N-1, \quad (2.7)$$

where  $u_j = u^{\Delta t}(\cdot, t_j)$ . The convolution weights are defined by their z-transform

$$\tilde{K}\left(\frac{\gamma(z)}{c\Delta t}\right) = \sum_{n=0}^{\infty} w_n^{\Delta t}(\tilde{K})z^n, \quad |z| < 1. \quad (2.8)$$

The function  $\gamma(z) = \frac{1}{2}(z^2 - 4z + 3)$  is the quotient of the generating polynomials of the second order backward difference formula [9]. Here  $\tilde{K}(s)$  is the double layer potential for the Helmholtz equation with wavenumber  $k = is$  given by

$$\left(\tilde{K}(s)\tilde{u}\right)(\mathbf{x}) = \int_{\Gamma} \frac{\partial G_k}{\partial \hat{\mathbf{n}}_{\mathbf{y}}}(\mathbf{x} - \mathbf{y})\tilde{u}(\mathbf{y}, s)d\Gamma_{\mathbf{y}}, \quad (2.9)$$

where  $G_k(\mathbf{x}-\mathbf{y}) = -\frac{i}{4}H_0^{(1)}(k\|\mathbf{x}-\mathbf{y}\|)$  and  $\tilde{u}$  denotes the Laplace transform of  $u$ . The convolution weights can be calculated via an approximation of Cauchy's integral formula using the trapezoidal rule. The approximate convolution weights are then given by a scaled inverse discrete Fourier transform

$$w_j^{\Delta t}(\tilde{K}) = \frac{1}{2\pi i} \oint_C \tilde{K} \left( \frac{\gamma(z)}{c\Delta t} \right) z^{-(j+1)} dz \approx \frac{\lambda^{-j}}{N} \sum_{l=0}^{N-1} \tilde{K}(s_l) e^{2\pi i l j / N}, \quad (2.10)$$

where  $C$  can be chosen as a circular contour centered at the origin of radius  $\lambda < 1$ . The complex wavenumbers  $k_l$  are given by  $k_l = i s_l = \frac{i\gamma(z_l)}{c\Delta t}$ , where  $z_l = \lambda e^{-2\pi i l / N}$  for  $l = 0, 1, \dots, N-1$ . By extending the sum in (2.7) to  $j = N-1$  and substituting the approximate weights (2.10) into a time discretised version of (2.4), we obtain a new system of equations for  $u^{\Delta t, \lambda}(\mathbf{x}, t_n) = u_n(\mathbf{x})$ :

$$-\frac{1}{2}u_n + \sum_{j=0}^{N-1} w_{n-j}^{\Delta t, \lambda}(\tilde{K}) u_j^\lambda = V_n, \quad (2.11)$$

where  $V_n$  is a time-discrete approximation of  $(Vh)(\cdot, t_n)$ . Substituting the definition of  $w^{\Delta t, \lambda}$  into (2.11), then multiplying by  $\lambda^n$  and applying a discrete Fourier transform with respect to  $n$  gives

$$-\frac{1}{2}\tilde{u}_l(\mathbf{x}) + \left( \tilde{K}(s_l)\tilde{u}_l \right) (\mathbf{x}) = \tilde{V}_l(\mathbf{x}), \quad \mathbf{x} \in \Gamma, \quad (2.12)$$

where

$$\tilde{V}_l(\mathbf{x}) = \sum_{n=0}^{N-1} \lambda^n V_n(\mathbf{x}) e^{-2\pi i l n / N}. \quad (2.13)$$

We have thereby reduced the problem of numerically solving the wave equation to a system of Helmholtz equations with complex wave numbers  $k_l$ , for  $l = 0, 1, \dots, N-1$ .

## 2.4 Spatial discretisation: Boundary element method

For the spatial discretisation we employ a piecewise constant collocation boundary element method. For the space-time discrete solution at time  $t_n$  we assume our transformed solution  $\tilde{u}_l$  can be replaced with

$$\tilde{u}_l = \sum_{m=1}^M \tilde{u}_{l,m} b_m, \quad (2.14)$$

where  $b_m$  for  $m = 1, 2, \dots, M$ , are piecewise constant basis functions. We substitute (2.14) into our integral equations (2.12) and solve for our transformed solution coefficients  $\tilde{u}_{l,m}$ . We write this system of equations explicitly as

$$-\frac{1}{2} \sum_{m=1}^M \tilde{u}_{l,m} b_m(\mathbf{x}_i) + \sum_{m=1}^M \tilde{u}_{l,m} \left( \int_{\Gamma} \frac{\partial G_{k_l}}{\partial \hat{\mathbf{n}}_{\mathbf{y}}}(\mathbf{x}_i - \mathbf{y}) b_m(\mathbf{y}) d\Gamma_{\mathbf{y}} \right) = \tilde{V}_l(\mathbf{x}_i), \quad (2.15)$$

for  $l = 0, 1, \dots, N-1$  and where  $\mathbf{x}_i$ ,  $i = 1, 2, \dots, M$  are the collocation points, which are located in the centre of the corresponding boundary element. The function  $\tilde{V}_l(\mathbf{x})$  is calculated using the z-transform of  $V_n(\mathbf{x})$  as follows

$$\tilde{V}_l(\mathbf{x}) = \sum_{n=0}^{N-1} \lambda^n e^{-2\pi i l n / N} V_n(\mathbf{x}) = \sum_{n=0}^{N-1} \lambda^n e^{-2\pi i l n / N} \left( \int_0^{t_n} \int_{\Gamma} G(\mathbf{x} - \mathbf{y}, t - \tau) h(\mathbf{y}, \tau) d\Gamma_{\mathbf{y}} d\tau \right). \quad (2.16)$$

The solution coefficients for (2.1a) can then be approximated via a trapezoidal rule for the inverse z-transform as

$$u_{l,m} = \frac{\lambda^{-l}}{N} \sum_{j=0}^{N-1} \tilde{u}_{j,m} e^{2\pi i l j / N}, \quad (2.17)$$

and then the solution is given by

$$u_l = \sum_{m=1}^M u_{l,m} b_m. \quad (2.18)$$

## 2.5 Development of the hybrid method

We aim to develop a hybrid method that is capable of efficiently modelling waves with broadband frequency content. At high frequencies, the Helmholtz solution  $\tilde{u}$  may be well approximated in terms of the phase  $\phi$  and amplitude  $A$ , which can be provided via a high frequency energy method such as ray tracing [14]. We therefore require a direct link between the Helmholtz equation and a phase-space density function obtained from the ray tracing method. In particular, one can express the phase-space density  $\rho$  on  $\Gamma$  in the form

$$\rho(q, p) = \sum_{m=1}^M A_m^2(q) \delta\left(p - \frac{d\phi_m}{dq}\right), \quad (2.19)$$

where  $q$  is the arc-length boundary parameter,  $p$  is the tangential slowness and the sum corresponds to a superposition of plane waves. The corresponding solution to the Helmholtz equation is then given by

$$u(q) = \sum_{m=1}^M A_m(q) e^{i\omega\phi_m(q)}, \quad (2.20)$$

where  $\omega = ck$  is the angular frequency.

## 2.6 Conclusions

In this paper we have discussed the issues that arise when dealing with wave problems containing broadband frequency content and therefore an efficient method is of importance to deal with these issues. We proposed the development of a hybrid method in which the low frequency content will be modelled via a CQBEM and the high frequency content will be modelled via an energy approach, such as ray tracing. We then derived a CQBEM to numerically solve a boundary value problem for the wave equation with Neumann boundary conditions. The result was a system of Helmholtz problems with complex wavenumbers. We then discussed the relationship between the solution of the Helmholtz problems and a phase-space density function obtained from a frequency independent ray tracing method. At high frequencies the solutions for the Helmholtz problems may be well approximated in terms of their phase and amplitude, which can be extracted from a suitably defined phase-space density function.

## References

- [1] F. Fahy, Statistical energy analysis: a critical overview, *Phil. Trans. R. Soc. Lond. A* **346** (1994), pp. 431–447.
- [2] E. Perrey-Debain, J. Trevelyan, P. Bettess, Wave boundary elements: a theoretical overview presenting applications in scattering of short waves, *Eng. Anal. Bound. Elem.* **28** (2004), pp. 131–141
- [3] K. R. Pyatunin, N. V. Arkharova, and A. E. Remizov, Noise simulation of aircraft engine fans by the boundary element method, *Acoust. Phys.* **62** (2016), pp. 495–504.
- [4] S. Marburg and B. Nolte, Computational acoustics of noise propagation in fluids: finite and boundary element methods, *Springer, Verlag* (2008).
- [5] J. A. Hargreaves, Time domain boundary element method for room acoustics, *Ph.D. dissertation, University of Salford* (2007).
- [6] C. Lubich, Convolution quadrature and discretized operational calculus I, *Numer. Math.* **52** (1988), pp. 129–145.
- [7] C. Lubich, Convolution quadrature and discretized operational calculus II, *Numer. Math.* **52** (1988), pp. 413–481.
- [8] C. Lubich, On the multistep time discretization of linear initial-boundary value problems and their boundary integral equations, *Numer. Math.* **67** (1994), pp. 365–389.
- [9] L. Banjai and S. Sauter, Rapid solution of the wave equation on unbounded domains, *SIAM J. Num. Anal.* **47** (2008), pp. 229–247.
- [10] L. Banjai, M. Lopez-Fernandez and A. Schadle, Fast and oblivious algorithms for dissipative and 2D wave equations, *SIAM J. Num. Anal.* **55** (2017), pp. 621–639.
- [11] A. Reider, Convolution quadrature and boundary element methods in wave propagation: a time domain point of view, *PhD thesis, Vienna University of Technology* (2017).
- [12] W. Hackbusch, W. Kress and S.Sauter, Sparse convolution quadrature for the time domain boundary integral formulations of the wave equation, *IMA J. Numer. Anal.* **29** (2008), pp. 158–179.
- [13] D.J. Chappell, Convolution quadrature Galerkin boundary element method for the wave equation with reduced quadrature weight computation, *IMA J. Numer. Anal.* **31**(2) (2011), pp. 640–666.
- [14] O. Runborg, Mathematical models and numerical methods for high frequency waves, *Commun. Comput. Phys.* **2**(5) (2007), pp. 827–878.
- [15] D.J. Chappell, A convolution quadrature Galerkin boundary element method for the exterior Neumann problem of the wave equation, *Math. Methods Appl. Sci.* **32**(12) (2009), pp. 1585–1608.
- [16] T. Saitoh, S. Hirose, T. Fukui, Convolution quadrature boundary element method and acceleration by fast multipole method in 2-D viscoelastic wave propagation, *Theor. Appl. Mech.* **57** (2009), pp. 385–393.

## Chapter 3

# Discontinuous isogeometric boundary element method (IGABEM) in automotive acoustic fields

Y. Sun<sup>1,2,3</sup>, C.H. Lu<sup>1,2,3</sup>, J.Trevelyan<sup>4</sup>, G. Hattori<sup>5</sup>

<sup>1</sup> School of Automotive Engineering  
Wuhan University of Technology  
Luoshi Road  
430070, Wuhan, Hubei Province, China.

<sup>2</sup> Hubei Key Laboratory of Advanced Technology for Automotive Components  
Wuhan University of Technology  
Luoshi Road  
430070, Wuhan, Hubei Province, China.

<sup>3</sup> Hubei Collaborative Innovation Center for Automotive Components Technology  
Wuhan University of Technology  
Luoshi Road  
430070, Wuhan, Hubei Province, China.

<sup>4</sup> Department of Engineering  
Durham University  
DH1 3LE, Durham, UK.

<sup>5</sup> Department of Engineering  
University of Cambridge  
CB2 1PZ, Cambridge, UK.

---

**Abstract.** *The isogeometric boundary element method (IGABEM) has been successfully applied to acoustic problems with smooth boundary conditions since it was first put forward. However, in most real-world engineering design and analysis acoustic problems, geometric corners and discontinuities in boundary conditions can not be represented accurately by a continuous description. We propose a fully discontinuous IGABEM scheme to accommodate these discontinuities. In the fully discontinuous IGABEM formulation, both the primary variable and its derivative are expressed with a discontinuous form. In this paper, we study a simple car passenger compartment model characterised by panels with piecewise continuous impedance boundaries to compare the continuous and discontinuous formulations. The potential of discontinuous IGABEM will be underlined and new insights for further developments for acoustics in vehicle engineering will be obtained from the research.*

---

## 3.1 Introduction

The noise, vibration and harshness (NVH) performance is one of the most important indicators of the quality for an automotive manufacturer. Acoustic engineers in industry devote themselves to seek efficient methods to predicate the interior noise of the vehicle. The boundary element method is one of the most popular numerical methods in investigating the sound radiation in the automotive engineering, since it involves the problem discretisation and solution on the boundary of the domain and reduces the complexity of the mesh generation and the size of the problem. However, the process of producing an analysis-ready Computer Aided Engineering (CAE) model from NURBS-based Computer Aided Design (CAD) data is time consuming, especially for industrially relevant problems where mesh generation and refinement can take up to 80% of the entire analysis time.

Isogeometric analysis (IGA) was first put forward by Hughes et al. [1] and received a lot of attention from the industry since then. The idea of IGA employs the typical splines in computer-aid design (CAD), such as non-rational B-splines (NURBS), to capture the problem geometry as well as the solutions. NURBS are the standard geometry representations in CAD and have been widely used in IGA. The use of NURBS as an approximation space in FEM and BEM has been shown to improve convergence properties over the use of classical Lagrange polynomials. The isogeometric boundary element method (IGABEM) combines the IGA with the BEM. The introduction of NURBS enables the IGABEM to capture the model without changing the geometry, which makes it to have an obvious advantage in the computer-aid engineering (CAE). The IGABEM has been successfully applied in various areas, such as, potential problems [2], elasticity problems [3], electromagnetic solutions [4] and so on. Especially in the area of acoustic applications, Simpson et al. [5] employed IGABEM based on T-splines to solve both interior and exterior acoustic problems. Peake et al. proposed an extended isogeometric boundary element method (XIBEM) for two-dimensional Helmholtz problems [2] and then extended it to three dimensional acoustic problems [6].

In acoustic problems of relevance to the automobile industry, the boundary conditions are mostly discontinuous, the sound absorption properties of lining materials and windows being markedly different. The IGABEM formulations generally need to accommodate this discontinuity. Herein, we come up with a fully discontinuous IGABEM formulation, in which both the primary variable (potential) and its derivative are discontinuous. A suitable method for choosing the collocation points is proposed as well. Continuous and discontinuous formulations are compared. A simple car passenger compartment model characterised by panels with piecewise continuous impedance boundaries is presented to illustrate the potential of the proposed method for integrated engineering design and analysis.

## 3.2 Isogeometric Boundary Element Method Discretisation

### 3.2.1 B-splines and NURBS

In this section, we present a brief introduction to B-splines and NURBS. The interested reader can find a more detailed description in [7]. B-splines are piecewise polynomials defined by knot vector, which is constructed by a sequence of non-decreasing real numbers:

$$\Xi = \{\xi_1, \xi_2, \dots, \xi_{n+p+1}\}, \quad \xi_i \in \mathbb{R}, \quad (3.1)$$

where  $i = 1, 2, \dots, n+p+1$ ,  $n$  is the number of the basis functions,  $p$  is the curve degree,  $\xi_i$  denotes the  $i$ -th knot in the parameter space representing the parametric coordinates of the curve. Using the Cox-de Boor recurrence formula, the B-spline basis functions are defined recursively as:

$$p = 0 : N_{i,0}(\xi) = \begin{cases} 1 & \xi_i \leq \xi < \xi_{i+1} \\ 0 & \text{otherwise} \end{cases} \quad (3.2)$$

$$p > 0 : N_{i,p}(\xi) = \frac{\xi - \xi_i}{\xi_{i+p} - \xi_i} N_{i,p-1}(\xi) + \frac{\xi_{i+p+1} - \xi}{\xi_{i+p+1} - \xi_{i+1}} N_{i+1,p-1}(\xi). \quad (3.3)$$

A B-spline surface  $S^b(\xi, \eta)$  is a tensor product surface of two B-splines. Given a net of control points  $\mathbf{A}_{i,j}$  ( $i = 1, 2, \dots, n; j = 1, 2, \dots, m$ ), polynomial degrees  $p$  and  $q$ , two knot vectors  $\Xi = [\xi_1, \xi_2, \dots, \xi_{n+p+1}]$  and  $\Theta = [\eta_1, \eta_2, \dots, \eta_{m+q+1}]$ , a B-spline surface is defined as

$$S^b(\xi, \eta) = \sum_{i=1}^n \sum_{j=1}^m N_{i,p}(\xi) M_{j,q}(\eta) \mathbf{A}_{i,j}, \quad (3.4)$$

where  $N_{i,p}(\xi)$  and  $M_{j,q}(\eta)$  represent univariate B-spline basis functions of degree  $p$  and  $q$ , associated with knot vectors  $\Xi$  and  $\Theta$ , respectively. It should be noted that the concepts of control points and basis functions are similar to nodal coordinates and shape functions in BEM, respectively, but a key difference is that control points may lie off the physical boundary.

NURBS are developed from B-splines but the introduction of weights increases the flexibility and enables the exact representation of geometric entities like circular arcs and spheres. By defining a positive weight  $w_i$  to each basic function, the NURBS basis functions  $R_{i,p}(\xi)$  can be expressed as

$$R_{i,p}(\xi) = \frac{N_{i,p}(\xi) w_i}{\sum_{j=1}^n N_{j,p}(\xi) w_j}. \quad (3.5)$$

If all the weights are equal to 1, the NURBS will degenerate into B-splines. Analogous to a B-spline surface, the definition of a NURBS surface  $S(\xi, \eta)$  is defined by

$$S(\xi, \eta) = \sum_{i=1}^n \sum_{j=1}^m R_{i,j,p,q}(\xi, \eta) \mathbf{A}_{i,j} \quad (3.6)$$

with

$$R_{i,j,p,q}(\xi, \eta) = \frac{N_{i,p}(\xi) M_{j,q}(\eta) w_{i,j}}{\sum_{\hat{i}=1}^n \sum_{\hat{j}=1}^m N_{\hat{i},p}(\xi) M_{\hat{j},q}(\eta) w_{\hat{i},\hat{j}}}. \quad (3.7)$$

### 3.2.2 Boundary integral equations (BIE)

Given a domain  $\Omega \in \mathbb{R}^3$  enclosed by boundary  $\Gamma$ , the Time-harmonic acoustic problem is governed by the well-known Helmholtz equation:

$$\nabla^2 \phi(\mathbf{x}) + k^2 \phi(\mathbf{x}) = 0, \quad \mathbf{x} \in \Omega, \quad (3.8)$$

where  $\nabla^2$  is the Laplacian operator,  $\phi(\mathbf{x}) \in \mathbb{C}$  is the acoustic potential at the point  $\mathbf{x}$ ,  $\lambda$  is the wavelength, and  $k = 2\pi/\lambda$  is the wave number. The harmonic time dependence of the sound pressure is assumed as  $e^{-i\omega t}$ .

Eq. (3.8) is then the governing equation of a sound wave propagation problem subject to boundary conditions that may take the following forms:

- Dirichlet condition: the acoustic potential is known over the boundary:

$$\phi(\mathbf{x}) = \bar{\phi}(\mathbf{x}), \quad \mathbf{x} \in \Gamma. \quad (3.9)$$

- Neumann condition: the derivative of the acoustic potential is known over the boundary:

$$\frac{\partial \phi(\mathbf{x})}{\partial n} = \bar{q}, \quad \mathbf{x} \in \Gamma. \quad (3.10)$$

- Robin condition: the derivative of the potential is presented as a linear function of the potential:

$$\alpha \frac{\partial \phi(\mathbf{x})}{\partial n} = \beta \phi(\mathbf{x}) + \gamma, \quad \mathbf{x} \in \Gamma. \quad (3.11)$$

Particularly, in the context of an acoustic problem with absorbing boundaries it is often desirable to express the Robin condition in the form

$$\frac{\partial \phi(x)}{\partial n} = -i\rho_0\omega \frac{\phi(x)}{Z}, \quad (3.12)$$

where  $\rho_0$  is the material density,  $\omega$  is the frequency and  $Z$  is the boundary impedance, given by the acoustic pressure divided by the velocity of the fluid relative to that of the structure [8]. We note the frequency dependence of the impedance properties.

Using standard techniques, Eq. (3.8) can be reformulated as a boundary integral equation (BIE):

$$C(\mathbf{s}) + \int_{\Gamma} \frac{\partial G(\mathbf{s}, \mathbf{x})}{\partial n} \phi(\mathbf{x}) d\Gamma(\mathbf{x}) = \int_{\Gamma} G(\mathbf{s}, \mathbf{x}) \frac{\partial \phi(\mathbf{x})}{\partial n} d\Gamma(\mathbf{x}), \quad (3.13)$$

where  $\mathbf{s} \in \Gamma$  represents the source point,  $n$  is the unit outward pointing normal,  $C(\mathbf{s})$  is a jump-term depending on the geometry at the source point. If the source point lies on a smooth surface, the jump term  $C(\mathbf{s})=1/2$ .  $\phi(\mathbf{x})$  and  $\frac{\partial \phi(\mathbf{x})}{\partial n}$  are the acoustic potential and its derivative, respectively.

For 3D problems,  $G(\mathbf{s}, \mathbf{x})$  is the Green's function given by:

$$G(\mathbf{s}, \mathbf{x}) = \frac{e^{ikr}}{4\pi r}, \quad (3.14)$$

$\partial G(\mathbf{s}, \mathbf{x})/\partial n$  is the corresponding derivative expressed as:

$$\frac{\partial G(\mathbf{s}, \mathbf{x})}{\partial n} = \frac{e^{ikr}}{4\pi r^2} (ikr - 1) \frac{\partial r}{\partial n}, \quad (3.15)$$

where

$$r = |\mathbf{x} - \mathbf{s}|. \quad (3.16)$$

The integrals in Eq. (3.13) contain a weak singularity and any of the standard techniques in the BEM literature may be used to evaluate them [9].

### 3.2.3 IGABEM implementation

In IGABEM, NURBS basis functions are employed to represent the solution variables (acoustic potential and the normal derivative) as well as the geometry. The boundary is divided into  $E$  non-overlapping isogeometric patches  $\Gamma_e$ . A local coordinate system  $\mathbf{F}_e = (u, v)$  is defined on each patch  $\Gamma_e$  as follows:

$$\Gamma_e = \mathbf{F}_e(u, v), \quad u, v \in [0, 1]. \quad (3.17)$$

It should be noted that the integration is calculated knot span by knot span, e.g.  $[\bar{\xi}_i, \bar{\xi}_{i+1}] \times [\bar{\eta}_j, \bar{\eta}_{j+1}]$ , while in the integration using Gauss-Legendre quadrature, the parametric system  $Y = (\bar{\xi}, \bar{\eta})$  is defined in  $[-1, 1] \times [-1, 1]$ . Therefore, an additional transformation is needed to map from the local coordinates to the parametric space.

The Jacobian of transformation from the physical domain to a parametric domain can be expressed as:

$$J_Y = \left| \frac{\partial \mathbf{x}}{\partial \mathbf{F}} \frac{\partial \mathbf{F}}{\partial \mathbf{Y}} \right|, \quad (3.18)$$

where  $\frac{\partial \mathbf{x}}{\partial \mathbf{F}}$  is the Jacobian mapping from the global to local coordinates on each patch, and  $\frac{\partial \mathbf{F}}{\partial \mathbf{Y}}$  is the Jacobian mapping from local coordinates to the parametric space.

With the NURBS expansion, the acoustic potential and the normal derivative can be easily discretised as:

$$\phi(\mathbf{x}) = \sum_{i=1}^n \sum_{j=1}^m R_{i,j,p,q}(u(\mathbf{x}), v(\mathbf{x})) \tilde{\phi}_{j,p}, \quad (3.19)$$

$$\frac{\partial \phi(\mathbf{x})}{\partial n} = \sum_{i=1}^n \sum_{j=1}^m R_{i,j,p,q}(u(\mathbf{x}), v(\mathbf{x})) \tilde{q}_{j,p}, \quad (3.20)$$

where  $n$  and  $m$  are the number of control points,  $p$  and  $q$  are the curve degree in  $u$  and  $v$  direction, respectively.  $\tilde{\phi}_{j,p}$  and  $\tilde{q}_{j,p}$  are the coefficients for potentials and derivatives associated with control points. It should be noted that  $\tilde{\phi}_{j,p}$  and  $\tilde{q}_{j,p}$  are no longer the nodal potentials and derivatives since the control points may not lie on the geometry. The final isogeometric boundary integral equation can be written by substituting Eq. (3.19) and Eq. (3.20) into Eq. (3.13):

$$C(\mathbf{s}) + \sum_{e=1}^E \sum_{i=1}^n \sum_{j=1}^m P_{eij}(\mathbf{s}) \phi_{eij} = \sum_{e=1}^E \sum_{i=1}^n \sum_{j=1}^m Q_{eij}(\mathbf{s}) \frac{\partial \phi_{eij}}{\partial n} \quad (3.21)$$

with

$$P_{eij} = \int_{-1}^1 \int_{-1}^1 \frac{\partial G(\bar{\xi}, \bar{\eta})}{\partial n} R_{eij}(\bar{\xi}, \bar{\eta}) J_{Y_{eij}}(\bar{\xi}, \bar{\eta}) d\bar{\xi} d\bar{\eta} \quad (3.22)$$

$$Q_{eij} = \int_{-1}^1 \int_{-1}^1 G(\bar{\xi}, \bar{\eta}) R_{eij}(\bar{\xi}, \bar{\eta}) J_{Y_{eij}}(\bar{\xi}, \bar{\eta}) d\bar{\xi} d\bar{\eta}, \quad (3.23)$$

where  $R_{eij}$  are the corresponding NURBS basis functions, and  $J_{Y_{eij}}$  is the Jacobian from the mapping in Eq. (3.18). Here two indices  $i, j$  are used to refer to the control points and associated basis functions in an element, as a NURBS surface is obtained by taking a bidirectional net of control points, requiring two knot vectors such as (3.6).

In general, the control points are no longer able to be taken as the collocation points in IGABEM, since they may not lie on the geometry boundary (except in flat patches). Alternatively,

the Greville abscissae [10] may be used to define the position of collocation points in the parameter space.

Taking an arbitrary point  $\mathbf{s}$  in the domain to lie at each node in turn, the collocation form of the BIE yields a set of equations relating all potential and velocity coefficients as follows:

$$\mathbf{H}\mathbf{u} = \mathbf{G}\mathbf{q}, \quad (3.24)$$

where  $\mathbf{u}$ ,  $\mathbf{q}$  are vectors containing nodal values of  $\phi$ ,  $\frac{\partial\phi}{\partial n}$ . The fully populated matrix  $\mathbf{H}$  contains all integrals of the left-hand side terms of Eq. (3.21), and matrix  $\mathbf{G}$  is assembled by integrals of the right-hand side terms of Eq. (3.21).  $\phi$  and  $\partial\phi/\partial n$  are vectors containing acoustic potential and normal derivative coefficients, respectively.

By reordering all the unknowns and related coefficients to the left-hand side and all the knowns and related coefficients to the right-hand side, we obtain a linear system:

$$\mathbf{A}\mathbf{x} = \mathbf{b}, \quad (3.25)$$

where  $\mathbf{A}$  is an unsymmetrical and fully populated square matrix, the vector  $\mathbf{x}$  contains all unknown potential and derivative coefficients while the vector  $\mathbf{b}$  is calculated from all known coefficient and their associated terms. Eq. (3.25) is a linear system which can be solved directly.

### 3.3 Discontinuous Isogeometric Boundary Element Method

#### 3.3.1 Discontinuous isogeometric boundary patch

The use of discontinuous element can be traced back to the early conventional BEM literature. With the nodal and collocation points inside rather than on the element edges, the discontinuous elements have greater flexibility in building the boundary element mesh. They can be used to precisely represent the geometric or physical discontinuities in the problem, for example, the discontinuity of boundary conditions between the window and lining material of a vehicle passenger compartment. Also, parallel implementations can be accomplished since every term in the influence matrices  $H$  and  $G$  has only a single contribution from a single integral over an element. Discontinuous elements are also very flexible for local mesh refinement and adaptive techniques. In discontinuous IGABEM, more collocation points should be introduced to reach the number of unknowns in order to get a square final solution system (Eq. (3.25)). In a discontinuous model, there are multiple control points in the same location, each belonging to a different patch. This invokes the idea of double nodes in early BEM literature. In order to ensure a suitable number of collocation points, the simplest scheme is to locate them internally in each patch as shown in Fig.3.1. Although it usually increases the number of degrees of freedom, it has been found quite efficient in improving the accuracy and saving on model-building time.

#### 3.3.2 Collocation

In discontinuous elements, some control points will be coincident, but collocation at coincident points will result in a rank-deficient system of equations. A suitable collocation scheme is thus needed to determine the collocation points. In this work, we compared three following collocation strategies based on a cylinder example with mixed boundary conditions:

1. *Uniform collocation*: where the collocation points are uniformly distributed in the parameter domain.

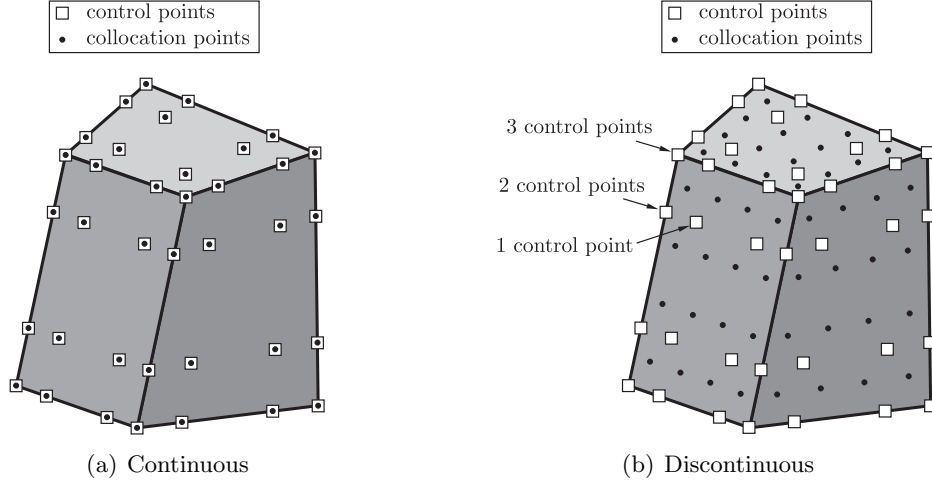


Figure 3.1: Isogeometric patches in 3D.

2. *Legendre polynomials*: where the collocation points are generated by mapping a number of Gaussian quadrature points in the parameter domain.
3. *Modified-Greville abscissae*: where the parameters correspond to collocation points defined by a Modified-Greville abscissae definition studied in [11], moving the first and the last collocation points away from the edges of the patches. Initially, the collocation points are generated as the Greville abscissae along each direction in the parameter space as

$$\xi'_i = \frac{1}{p}(\xi_{i+1} + \xi_{i+2} + \dots + \xi_{i+p}) \quad i = 1, 2, \dots, N, \quad (3.26)$$

where  $p$  is the degree of the NURBS, and  $N$  is the number of control points in the  $\xi$  direction.

Then, a coefficient  $\beta$  is brought in to move the first and the last collocation points of Eq. (3.26) inside the patch as

$$\xi'_1 = \xi'_1 + \beta(\xi'_2 - \xi'_1) \quad (3.27)$$

$$\xi'_n = \xi'_n + \beta(\xi'_n - \xi'_{n-1}), \quad (3.28)$$

where the coefficient  $\beta = 0.5$  has been proved to be the optimal value [11]. In this case, the knot vectors in both parametric directions are  $\Upsilon = \{0, 0, 0, 1, 1, 1\}$ ,  $p = 2$  and  $N = 3$ .

An example using the geometry of a quarter cylinder is analysed using the three collocation schemes to decide which strategy to use in this work. The cylinder geometry is shown in Figure 3.2(a). The rear surface of the cylinder lies in  $z = 0$  while the forward facing surface lies in  $z = 3$  of the Cartesian space, with dimensions in metres. We consider a spherical wave of wavelength  $\lambda = 5 \text{ m}$ , emanating from a point source located at  $[0, 0, 6]$ , passing through the domain.

The Neumann condition with

$$\bar{q} = 3(ikr - 1)e^{ikr}/2\pi r^3 \quad (3.29)$$

is applied on the patch lying in  $z = 0$ , and a Neumann condition with

$$\bar{q} = 3(1 - ikr)e^{ikr}/4\pi r^3 \quad (3.30)$$

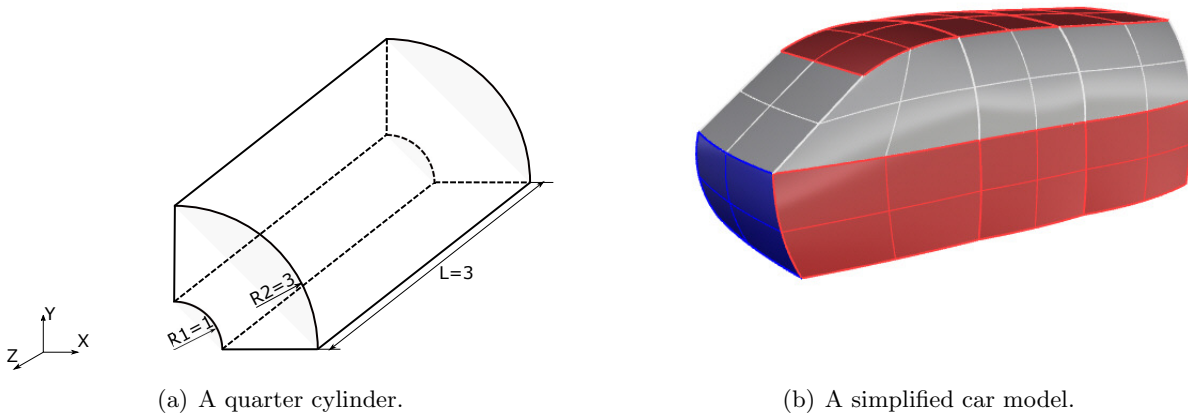


Figure 3.2: Two models.

is applied on the patch lying in  $z = 3$ , where  $r$  is the distance from the source points. In addition, the Dirichlet boundary condition  $\bar{\phi} = e^{ikr}/4\pi r$  is applied on all remaining patches.

We define an error metric  $\epsilon$  evaluated as

$$\epsilon = \frac{\|\phi - \phi_{ref}\|_{L_2(\Gamma)}}{\|\phi_{ref}\|_{L_2(\Gamma)}}, \quad (3.31)$$

where  $\phi_{ref}$  is the reference solution obtained from the converged result of a conventional BEM analysis using quadratic shape functions.

Figure 3.3(a) shows the calculation result of this problem, from which we can see that in the case of quadratic uniform knot vectors, the uniform collocation method gives rise to faster convergence and higher accuracy compared to the other two collocation strategies. Herein we proceed to the remaining analyses using uniformly distributed collocation points.

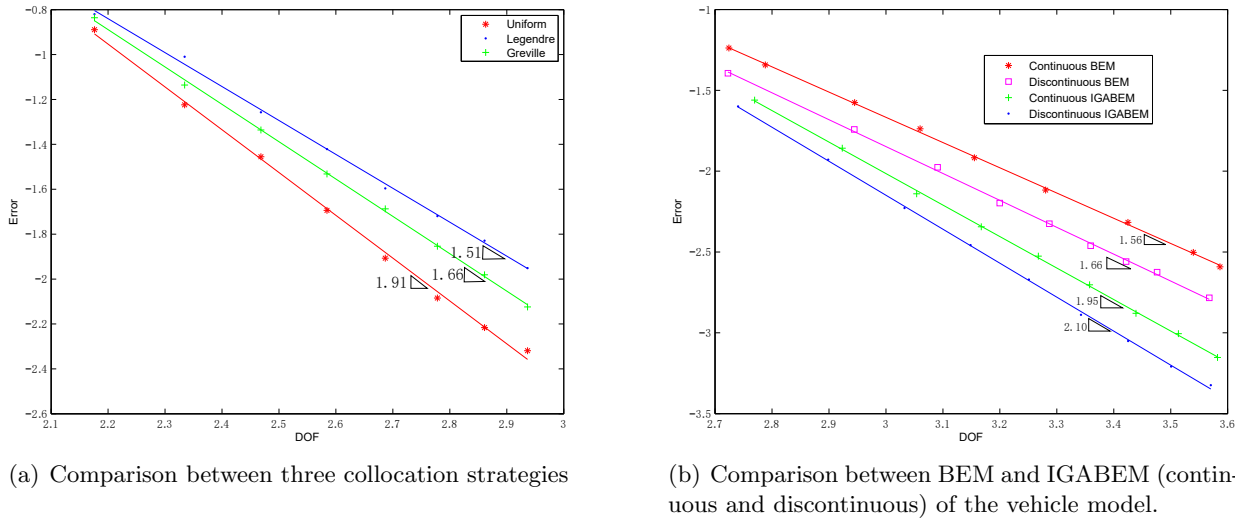


Figure 3.3: Calculation results of two models.

## 3.4 Computational Example: Vehicle Passenger Compartment

### 3.4.1 Model description and error measures

In this section, a simplified interior acoustic problem of a car passenger compartment characterised by 22 piecewise continuous impedance patches (shown in Fig. 3.2(b)) is studied. The sub-wavelength details of the compartment are omitted since they do not have significant influence on the solution.

The interior sound field can be simulated in the a closed space subject to three different boundary conditions:

(1) If a boundary surface is oscillating, e.g. the vehicle dashboard, the boundary condition can be expressed in a Neumann condition form:

$$\frac{\partial\phi(\mathbf{x})}{\partial n} = -i\rho_0\omega v, \quad (3.32)$$

where  $\rho_0 = 1.29 \text{ kg/m}^3$  is the air density,  $\omega = 2\pi C/\lambda$  is the circular frequency of the acoustic source,  $C = 340.29 \text{ m/s}$  is the sound speed,  $\lambda = 5 \text{ m}$  is the wave length and  $v$  is the amplitude of the normal component of the velocity on the surface. In this study we take  $v$  to be  $1.452 \text{ mm/s}$  following the work of Zhu [12].

(2) If the boundary surface has the property of total reflection, e.g. the window glass, the boundary condition on the surface can be expressed as a homogeneous Neumann condition form:

$$\frac{\partial\phi(\mathbf{x})}{\partial n} = 0. \quad (3.33)$$

(3) For absorbing boundaries, e.g. the interior lining material for the automobile, the boundary condition can be expressed as a Robin condition form:

$$\frac{\partial\phi(\mathbf{x})}{\partial n} = -i\rho_0\omega \frac{\phi(\mathbf{x})}{Z}, \quad (3.34)$$

taking  $\rho_0 = 1.29 \text{ kg/m}^3$  as the air density, frequency  $\omega = 712 \text{ rad/s}$  and wavelength  $\lambda = 3 \text{ m}$ . We follow the approach of Marburg [8] to determine the acoustic impedance; here, an average admittance  $Y_z$  was obtained experimentally as

$$Y_z = \frac{f}{2800}, \quad (3.35)$$

where  $f$  denotes the frequency in Hz. The impedance,  $Z$ , is the reciprocal of  $Y_z$ . In the current work we are considering the acoustics of a vehicle compartment at a frequency of 113 Hz.

The first Neumann boundary condition is applied on the blue panels as they represent the vehicle dashboard. The second Neumann boundary condition is applied on the grey panels as they represent the windows of the vehicle. A Robin condition is applied on the remaining panels which represent the vehicle inner lining materials.

In this example, the converged result of a conventional BEM analysis using quadratic shape functions is taken as the reference solution. Figure 3.3(b) presents the result comparison between the three different BEM schemes, from which we can conclude that discontinuous IGABEM outperforms the conventional BEM and continuous IGABEM in this approximation to a real vehicle problem and shows that the discontinuous IGABEM scheme is a promising method for simulating passenger compartment acoustics in the automotive sector.

## 3.5 Conclusion

In this work, a fully discontinuous IGABEM with a suitable collocation scheme is proposed. The discontinuous boundary patch has the ability to more efficiently approximate acoustic fields that exhibit large derivatives in the presence of discontinuous boundary conditions. A simplified vehicle model subjected to realistic boundary conditions commonly found in automotive acoustic applications has also been presented. It is observed that the discontinuous IGABEM provides a more accurate solution and shows better converge properties than the continuous form. This research will give hints for the development of discontinuous IGABEM in the acoustic field of the automotive engineering. More work on the numerical error of the discontinuous IGABEM in terms of frequency will be studied in the future.

## References

- [1] Hughes, T.J.R., Cottrell, J. and Bazilevs, Y.: Isogeometric analysis: CAD, finite elements, NURBS, exact geometry and mesh refinement. *Computer Methods in Applied Mechanics and Engineering* **194** (2005) 4135-4195.
- [2] Peake, M., Trevelyan, J. and Coates, G.: Extended isogeometric boundary element method (XIBEM) for two-dimensional Helmholtz problems. *Computer Methods in Applied Mechanics and Engineering* **259** (2013) 93-102.
- [3] Bai, Y., Dong, C. and Liu, Z.: Effective elastic properties and stress states of doubly periodic array of inclusions with complex shapes by isogeometric boundary element method. *Composite Structures* **128** (2015) 54-69.
- [4] Simpson, R., Liu, Z., Vazquez, R., and Evans, J.: An isogeometric boundary element method for electromagnetic scattering with compatible b-spline discretizations. *Journal of Computational Physics* **362** (2018) 264-289.
- [5] Simpson, R., Scott, M., Taus, M., Thomas, D. and Lian, H.: Acoustic isogeometric boundary element analysis. *Computer Methods in Applied Mechanics and Engineering* **269** (2014) 265-290.
- [6] Peake, M., Trevelyan, J. and Coates, G.: Extended isogeometric boundary element method (XIBEM) for three-dimensional medium-wave acoustic scattering problems. *Computer Methods in Applied Mechanics and Engineering* **284** (2015) 762-780.
- [7] Piegl, L. and Tiller, W.: The NURBS Book. (1997).
- [8] Marburg, S. and Hardtke, H.J.: A study on the acoustic boundary admittance. Determination, results and consequences. *Engineering Analysis with Boundary Elements* **23** (1999) 737-744.
- [9] Telles, J.C.F.: A self-adaptive coordinate transformation for efficient numerical evaluation of general boundary element integrals. *International Journal for Numerical Methods in Engineering* **4** (1987) 959-973.
- [10] Greville, T.: Numerical procedures for interpolation by spline functions. *Journal of the Society for Industrial and Applied Mathematics Series B Numerical Analysis* **24** (1964) 118-173.
- [11] Wang, Y.J., Benson, D.J.: Multi-patch nonsingular isogeometric boundary element analysis in 3D. *Computer Methods in Applied Mechanics and Engineering* **293** (2015) 71-91.
- [12] Zhu, J.: On the Simulation of the Interior Noise of a Light Bus, Ph.D. thesis, Jiangsu University (2005).

## Chapter 4

# Numerical treatment of highly oscillatory PUBEM integrals

B.D. Gilvey<sup>1</sup>, J. Trevelyan<sup>1</sup>

<sup>1</sup> Department of Engineering  
Durham University  
South Road  
DH1 3LE, Durham, UK.

---

**Abstract.** *For Helmholtz problems in the mid to high frequency range it is beneficial to include oscillatory basis functions, as in PUBEM (Partition of Unity Boundary Element Method) [1]. When employing PUBEM the number of degrees of freedom required to obtain ‘engineering accuracy’ is approximately a quarter of conventional BEM requirements. A fast and robust method of evaluating the highly oscillatory integrals that arise would unlock to full benefit of this substantial reduction in system size. A number of asymptotic methods such as repeated integration by parts, numerical steepest descent and the Filon method may be applied. Success of these methods varies, due to interaction between the plane wave basis and the fundamental solution, causing stationary points. For this reason the current work focuses on the method of stationary phase, combined with the trigonometric shape functions of [2].*

---

### 4.1 Introduction

BEM is often favoured over volumetric methods, for Helmholtz problems in infinite domains, as there is no requirement to truncate and apply artificial boundary conditions. Depending on the size of the domain of interest, this can result in a significant reduction in computational expense. An issue that both volumetric and BEM simulations share is dealing with problems in which the wavelength  $\lambda$  becomes small, relative to the domain of interest. When low order polynomial basis functions are employed, approximately 8-10 degrees of freedom are required per wavelength (a parameter we denote  $\tau$ ). Multiplying the polynomial basis with a series of plane waves is known as the Partition of Unity Boundary Element Method (PU-BEM)[1, 3, 4]. This plane wave basis offers a substantial improvement, reducing  $\tau$  to approximately 2.5. PU-BEM elements are typically larger than standard BEM elements, and it is common to increase the number of degrees of freedom by including extra plane waves at each node, rather than reducing

the element size. This may result in highly oscillatory integrals, which can provide a challenge for traditional quadrature techniques. For this reason, integration dominates the run time for PUBEM.

A number of alternative integration techniques exist, which are aimed at evaluating highly oscillatory integrals. A popular option being the numerical steepest descent (NSD) [5], which involves deforming the path of integration into the complex plane, where the behaviour is no longer oscillatory. NSD can be applied to PU-BEM integrals but it is not always straightforward to find the path of steepest descent, and the number of Gauss points required can slow the evaluation. Another approach is that of the asymptotic method, via repeated integration by parts [6], which is simple to implement and accurate for integrating over flat straight line elements, but struggles with smooth objects when there are a greater number of stationary points. A more recent method, which the authors have found to perform well with flat straight line elements, even in the presence of stationary points is the Filon method [7, 8, 9]. The approach proposed in the current work is the method of stationary phase (MSP) [10], in which we consider the overall value of each integral to be dominated by a window around stationary point locations. This assumes that in areas without stationary points, the integrals will largely cancel each other out, contributing negligible value.

## 4.2 Preliminaries

The focus of this paper is evaluating integrals over arc elements, thus a numerical example of scattering by a circle will be presented. Before defining the integrals, the boundary conditions and BIE are provided in this section. Consider a smooth object  $\Omega_s \subset \mathbb{R}^2$  with the boundary  $\Gamma$ . The acoustic wave propagation occurs in the exterior domain  $\Omega_f = \mathbb{R}^2 \setminus \Omega_s$ . Stipulating that the wave propagation is time-harmonic, produces the Helmholtz equation

$$\nabla^2 u(\mathbf{x}) + k^2 u(\mathbf{x}) = 0, \quad \mathbf{x} \in \Omega_f,$$

where the wavenumber  $k = 2\pi/\lambda$ . The unknown potential is  $u \in \mathbb{C}$  and  $\nabla^2$  is the Laplacian operator. Impinging the object with an incident wave  $u^{inc}$  and imposing a sound-hard Neumann boundary condition  $\nabla u(\mathbf{x}) \cdot \mathbf{n} = 0$ ,  $\mathbf{x} \in \Gamma$ , results in the following BIE

$$c(p)u(p) + \int_{\Gamma} \frac{\partial G(p, q)}{\partial \mathbf{n}} u(q) d\Gamma_q = u^{inc}(p), \quad p \in \Gamma.$$

The points  $p = (x_p, y_p)$  and  $q = (x_q, y_q)$  are the source and field points respectively, and the vector  $\mathbf{n}$  is the unit normal vector outward pointing from  $\Omega_f$ . As the examples provided in this paper will remain in two-dimensional space, the Green's function  $G(p, q)$  is

$$G(p, q) = \frac{i}{4} H_0^{(1)}(kr),$$

where  $H_0^{(1)}$  is the Hankel function of the first kind and of order zero,  $r$  is the Euclidean distance between  $p$  and  $q$ . In PU-BEM the basis is enriched with plane waves, such that the unknown potential is written as a linear combination of plane waves propagating in different directions, i.e.

$$u = \sum_{j=1}^J \sum_{m=1}^M N_j(\xi) A_{jm} e^{ik \mathbf{d}_{jm} \cdot \mathbf{q}},$$

$$\mathbf{d}_{jm} = (\cos \phi_{jm}, \sin \phi_{jm}), \quad \phi_{jm} = \frac{2\pi(m-1)}{M},$$

where  $A_{jm}$  are the unknown plane wave amplitudes,  $\mathbf{d}_{jm}$  are the direction vectors of the plane waves,  $i = \sqrt{-1}$  and  $M$  is the number of plane waves considered per node.  $N_j$  are shape functions for which we have selected the trigonometric functions of [2], shown in Fig. 4.1, for improved continuity at ends of elements.

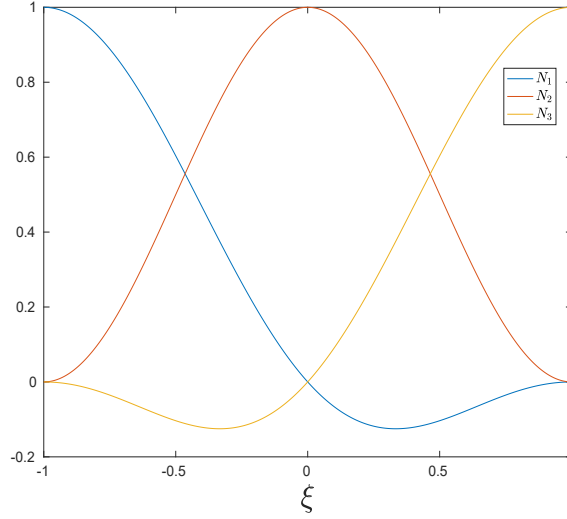


Figure 4.1: Trigonometric shape functions.

### 4.3 PU-BEM integral

For a circular arc element, we define the integral

$$I_1 = \frac{-ik}{4} \int_{-1}^1 H_1^{(1)}(kr) N_j(\xi) e^{ikd_m \cdot q(\xi)} \frac{\partial r}{\partial n(q)} J(\xi) d\xi. \quad (4.1)$$

The source point  $p$  and field point  $q$  are defined as follows

$$p = (R_1 \cos \psi, R_1 \sin \psi),$$

$$q = (R \cos \theta, R \sin \theta).$$

In the field of asymptotic integration, it is common to see integrals presented in the general form

$$I = \int_a^b f(x) e^{ikg(x)} dx.$$

In order to recast  $I_1$  from (4.1) in this form we replace the Hankel function with its asymptotic approximation for large argument

$$H_\nu^{(1)}(kr(\theta)) \approx \left( \frac{2}{\pi kr} \right)^{\frac{1}{2}} e^{i(kr - \frac{1}{2}\nu\pi - \frac{1}{4}\pi)} \sum_{s=0}^{\infty} i^s \frac{a_s(\nu)}{(kr)^s},$$

which produces the following

$$I = \frac{-iJ}{4} \left( \frac{2}{\pi} \right)^{\frac{1}{2}} e^{-\frac{3}{4}\pi i} \sum_{s=0}^{\infty} \frac{i^s a_s(1)}{k^{s-\frac{1}{2}}} \int_a^b f_2(\theta, s) e^{ikg(\theta)} d\theta,$$

where

$$f_2(\theta, s) = \frac{N_j(\theta)(R_1 \cos(\psi - \theta) - R)}{(r(\theta))^{s+\frac{3}{2}}}, \quad (4.2)$$

and

$$g(\theta) = \sqrt{(R \cos(\theta) - R_1 \cos(\psi))^2 + (R \sin(\theta) - R_1 \sin(\psi))^2} + d_x R \cos \theta + d_y R \sin \theta.$$

The formula for MSP is

$$I \approx f(x_0) \sqrt{\frac{2\pi}{k|g''(x_0)|}} e^{ikg(x_0)} e^{\pm \frac{i\pi}{4}},$$

in which  $x_0$  represents a stationary point. This can be used to reformulate (4.2), to produce

$$I = \gamma \sum_{s=0}^S \frac{i^s a_s(1)}{k^{s-\frac{1}{2}}} f(\theta_0, s) \sqrt{\frac{2\pi}{k|g''(\theta_0)|}} e^{ikg(\theta_0)} e^{\pm \frac{i\pi}{4}},$$

where

$$\gamma = \frac{-iJ}{4} \left( \frac{2}{\pi} \right)^{\frac{1}{2}} e^{-\frac{3}{4}\pi i}.$$

Generally we only require  $S = 1$ , which reduces the evaluation of (4.1) to the summation of only two terms, independent of  $k$ . Comparatively, when using a traditional quadrature scheme such as Gauss Legendre, we subdivide the interval of integration into lengths of  $\frac{\lambda}{4}$  to apply Gauss points, which is  $k$  dependent.

## 4.4 Numerical results

In this section, we observe the impact that approximating integrals has on the accuracy of the final solution. To do this we consider a unit circle, being impinged by an incident wave  $u^{inc}$ , shown in Fig. 4.2. A coarse mesh is used, containing four elements,  $M$  is selected such that  $\tau \approx 3.5$ . We first obtain our matrix of converged integrals, then inject an artificial error into each term, before solving for the unknown amplitudes. The resulting error  $\epsilon$  over the boundary  $\Gamma$  is compared, which we define

$$\epsilon = \frac{\|u - u_{ref}\|_{L_2}}{\|u_{ref}\|_{L_2}},$$

where  $u^{ref}$  is a reference solution. The errors that are injected into the terms are randomly generated values, within a certain range. We present results for  $\pm 0.5\%$ ,  $\pm 1\%$  and  $\pm 2\%$ , in Fig. 4.3. When stipulating the required accuracy of the final solution, a common threshold adhered

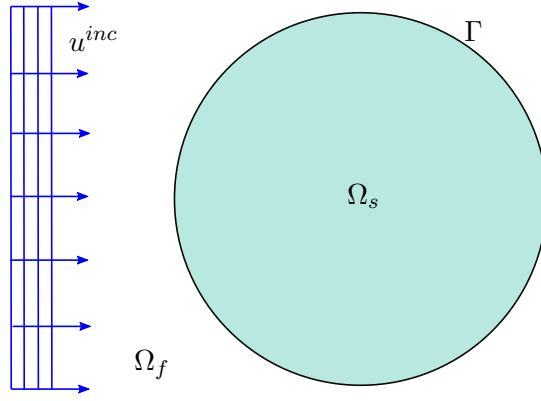


Figure 4.2: Circular scattering object, being impinged by the incident wave  $u^{inc}$ .

to by engineers is that of ‘engineering accuracy’, which is equal to 1%. With this in mind, Fig. 4.3 suggests that as long as the integration errors remain below 1% then the error in our final solution should be safely within 1%.

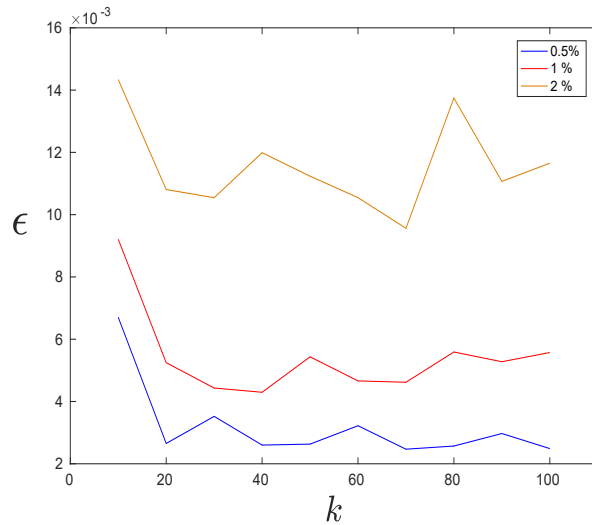


Figure 4.3:  $L_2$  error of potential over the boundary, after injecting 0.5%, 1% and 2% error into each integral.

#### 4.4.1 MSP results

We present here some preliminary results for a high frequency case. The wavelengths tested are  $\lambda = 0.0623, 0.02$  and  $0.01$ , which produces  $k = 100, 100\pi$  and  $200\pi$  respectively. For this problem, setting  $\tau = 3$  requires the total degrees of freedom to be 304,994 and 1884, for each respective system. If we wish to employ Gauss-Legendre, it is most effective to subdivide the interval of integration and apply Gauss points per subdivision. The timings, using MATLAB to integrate the resulting matrix are shown in Table 4.1. It is clear that increasing the frequency has a dramatic effect on run-time, as it takes 5.56 *hours* to perform the integration with

Gauss-Legendre alone for the  $k = 200\pi$  case. This highlights the power of MSP, and the challenge faced by traditional quadrature schemes. Although MSP is much faster, there are some locations in which the stationary phase approximation is less accurate, and the error exceeds the 1% threshold. In order to integrate the entire matrix effectively, we have employed MSP where possible and Gauss-Legendre in the challenging areas, the timings for this combination are shown in the fourth column of Table 4.1. These regions are clearly depicted for the  $k = 200\pi$  case in Fig. 4.4, which displays the integration errors of the corresponding 1884x1884 matrix terms. The small white regions are areas in which the relative error exceeds 1%, and the blue regions represent portions in which the error is acceptable. The largest errors occur in the leading diagonal, i.e. where the source point is within the interval of integration.

$k$	Gauss	MSP	MSP+Gauss
100	2.1 <i>m</i>	0.9 <i>s</i>	16 <i>s</i>
100 $\pi$	56 <i>m</i>	8.8 <i>s</i>	3.9 <i>m</i>
200 $\pi$	5.6 <i>h</i>	24 <i>s</i>	11 <i>m</i>

Table 4.1: Time taken to compute each matrix of integrals in hours(*h*), minutes(*m*) and seconds(*s*).

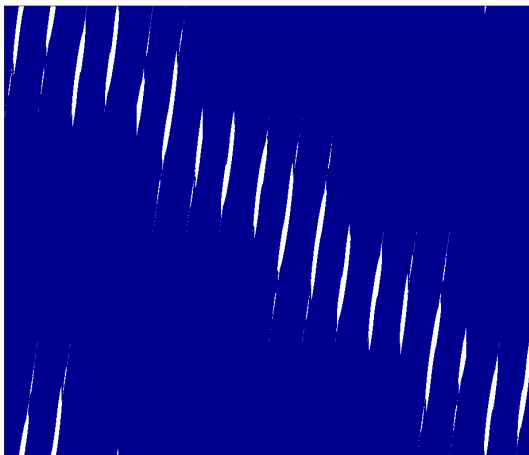


Figure 4.4: Acceptable regions (shown in blue), in which the relative error in the MSP integrals is less than 1%.

The stationary phase approximation assumes  $k$  is large, for this reason, as  $k$  decreases, the white regions become larger and Gauss-Legendre eventually becomes favourable. Numerical testing reveals that the largest errors are cases in which there are multiple stationary points, within close proximity to one another.

## 4.5 Conclusions and further work

A method of stationary phase approximation for PU-BEM integrals has been presented and implemented for a circular scattering object. It has been shown that for high frequency, MSP

provides significant acceleration of the integration, though care needs to be taken over integrals for some matrix terms around the leading diagonal, where two or more stationary points interfere. This suggests the possibility of a significant reduction in computational expense for solving high frequency acoustic problems, using PU-BEM. The results presented are preliminary and work is in progress to develop a targeted Gauss-Legendre scheme to integrate the unacceptable regions in which there are multiple stationary points. Secondly, alternate geometries and multiple scattering arrangements will be considered.

## References

- [1] Perrey-Debain, E., Trevelyan, J. and Bettess, P.: Wave boundary elements: a theoretical overview presenting applications in scattering of short waves. *Eng. Anal Bound. Elem.* **28**, (2004), 131-141.
- [2] M.J. Peake, J. Trevelyan and G. Coates: Novel basis functions for the partition of unity boundary element method for Helmholtz problems. *International Journal for Numerical Methods in Engineering.* **93**, (2013), 905-918.
- [3] Perrey-Debain, E., Trevelyan, J. and Bettess, P.: New special wave boundary elements for short wave problems. *Communications in Numerical Methods in Engineering.* **18**, (2002), 259-268.
- [4] Perrey-Debain, E., Laghrouche, O., Bettess, P. and Trevelyan, J.: Plane-wave basis finite elements and boundary elements for three-dimensional wave scattering. *Philosophical Transactions of the Royal Society of London. Series A: Mathematical, Physical and Engineering Sciences.* **362**, (2004), 561-577.
- [5] Honnor M.E. ,Trevelyan, J., and Huybrechs, D.: Numerical evaluation of 2D partition of unity boundary integrals for Helmholtz problems. *J. Comp. Appl. Math.* **234**, (2010), 1656-1662.
- [6] Iserles, A., and Nørsett, S.P.: Efficient quadrature of highly oscillatory integrals using derivatives. *Proc. R. Soc. Lond. Ser. A Math. Phys. Eng. Sci.* **461** (2005), 1383-1399.
- [7] Filon, L. N. G.: On a quadrature formula for trigonometric integrals. *Proc. Royal Soc. Edinburgh.* **49**, (1928), 38-47.
- [8] Iserles, A.: On the numerical quadrature of highly-oscillatory integrals I: Fourier transforms. *IMA. J. Num. Anal.* **24**, (2004), 1110-1123.
- [9] Iserles, A.: On the numerical quadrature of highly-oscillatory integrals II: Irregular oscillators. *IMA. J. Num. Anal.* **25**, (2004), 25-44.
- [10] Olver, F. W. J.: *Asymptotics and special functions.* Academic Press, Inc, New York, (1974).

## Chapter 5

# The leading order equivalence of Oseen's and Imai's representations in the far-field wake for steady two-dimensional flow

H.A. Adamu<sup>1,2</sup>, E.A.Chadwick<sup>1</sup>

<sup>1</sup> School of Computing Science and Engineering  
University of Salford  
The Crescent  
M5 4WT, Manchester, UK.

<sup>2</sup> Department of Mathematics  
Adamawa State University, Mubi  
P.M.B 25, Mubi-Adamawa State.  
Nigeria.

---

**Abstract.** Consider the far-field behind a body in a steady, two-dimensional uniform flow field. In the far-field the Oseen linearisation is valid, and in the far-field wake Imai's asymptotic expansion is applicable. The fundamental solution Green's function of the Oseen equation which represents a point force is called the Oseenlet. The drag and lift Oseenlets are given in [1], and from this representation we determine the corresponding Oseenlet vorticity and Oseenlet stream function. Imai [2] gives the velocity, vorticity and stream function in the far-field wake behind a body in terms of an asymptotic expansion. We shall show that the first terms in Imai's expansion are the same as the drag and lift Oseenlets when approximated in the wake. This demonstrates that Imai's and Oseen's treatments are the same to leading order, and from this we infer that the next order terms in Imai's expansion will correspond to the approximation of the next order terms in Oseen's linearisation. Future work will be to use Imai's result to infer the next order terms in the Oseen linearisation.

---

### 5.1 Introduction

The ultimate objective is to find an approximation to the point force in Navier-Stokes flow, which we call the NSlet. This is a useful solution for fluid problems for example, for modelling

oil flow exterior to a pipe. We may also find it can be used as a Green's function in the Green's integral representation in the same way as Eulerlets in Euler flow [7]. We start by investigating obtaining the NSlet from the terms in the Oseen linearisation and how these terms are linked to those in Imai's far-field approximation.

Oseen obtained the Oseenlet velocity in the early 1900's. The drag and lift Oseenlets are given in [1]. Moreover, in [1] Chadwick employed two methods, first the velocity was decomposed into potential and wake velocity and the second method used the Oseenlets. He further revealed that the Oseen velocity in the far field cannot be modelled using the Lamb -Goldstein method [10]-[11] rather by expanding each Oseenlets in a Taylor series. Thus, the velocity and pressure expansions in the far-field are obtained.

Moreover, Chadwick [4] also studied an experimental verification of an Oseen flow slender body theory by showing that the resulting lift equation had close agreement with experiment. It was further revealed that in the far-field region, the Navier–Stokes flow is expected to be approximated closely by Oseen flow. A comparison was made between the experiment, inviscid flow slender body theory, Chadwick's Oseen based flow theory and Jorgensen's extension [8] to viscous crossflow theory for slender bodies with elliptical cross-section. It was observed that the experiments follow a gradually increasing straight line variation which closely follows Oseen theory. On the other hand, Imai [2] gives the vorticity and stream function in the far-field wake behind a body in terms of an asymptotic expansion. In the present paper, from the drag and lift Oseenlet given in [1], we determine the corresponding Oseenlet vorticity and Oseenlet stream function. We also obtain the velocity, vorticity and stream function from Imai [2]. We then approximate both in the far-field and demonstrate that the Oseenlet velocity, vorticity and stream function are the same to leading order as Imai's first approximation.

Vorticity is defined as the curl of the velocity,  $\omega = \nabla \times u$  where  $\nabla$  is the differential operator and  $u$  is the velocity. It is the local rotation of the fluid. It is an important derived variable in fluid dynamics that plays both mathematical and physical roles in understanding fluid dynamics problems. However, for the 2-D flows, the vorticity vector has only one non-zero component (in the  $x_3$ -direction) where the Cartesian coordinates are given as  $(x_1, x_2, x_3)$ . In addition, stream function  $\psi$  also plays an important role in understanding fluid flow and therefore, it is important to understand its concept and derivation [6]. It is related to the velocity using the Cauchy-Riemann equations [5].

## 5.2 Governing equations

The Navier-Stokes equation for an incompressible fluid is given as:

$$\rho u_j^\dagger \frac{\partial u_i^\dagger}{\partial x_j} = -\frac{\partial p^\dagger}{\partial x_i} + \mu \frac{\partial^2 u_i^\dagger}{\partial x_j^2} \quad (5.1)$$

where  $u_i^\dagger$  is the fluid velocity,  $p^\dagger$  is pressure,  $\rho$  is the density of the fluid and  $\mu$  is the dynamic coefficient of viscosity. In the far-field, the velocity tends to a uniform stream

$$u_i^\dagger = U\delta_{i1} + u_i + u_i^I + \dots$$

where  $u_i^I$  is the second order linearisation,  $U$  is the uniform stream,  $\delta_{ij} = \begin{cases} 1 & i = j \\ 0 & \text{otherwise,} \end{cases}$

$U \gg O(u_i) \gg O(u_i^I) \gg \dots$  and ' $O$ ' means 'of the order'. Indices  $1 \leq i, j \leq 2$  where repeated index implies summation.

However, Oseen equation is obtained by linearising the Navier-Stokes equation. Thus, the far-field Oseen equation is given as

$$\rho U \frac{\partial u_i}{\partial x_1} = -\frac{\partial p}{\partial x_i} + \mu \frac{\partial^2 u_i}{\partial x_j \partial x_j} \quad (5.2)$$

giving the solution  $\omega = \Re \sum_{n=0}^{\infty} C_n e^{kx_1} K_n(kr) e^{ni\theta}$ , where  $\omega$  is the vorticity,  $K_n$  is the modified Bessel function of order  $n$ . From this, the far-field Imai's approximation to leading order in modified Bessel function expansion is  $\omega = \Re \left( \frac{c}{\zeta} e^{-\eta^2} \right) + \dots$ , where  $r$  is the 2-D radius defined by  $r = \sqrt{x_i x_i}$ ,  $\theta$  is the 2-D polar angle  $\theta = \cos^{-1}(\frac{x_1}{r})$ ,  $\zeta = \xi + i\eta$ ,  $\xi = (2kr)^{\frac{1}{2}} \cos \frac{1}{2}\theta$ ,  $k = \frac{\rho U}{2\mu}$ ,  $\eta = (2kr)^{\frac{1}{2}} \sin \frac{1}{2}\theta$ ,  $c$  is a complex constant,  $\Re$  represents real part and  $i$  is the imaginary part. The drag Oseenlet velocity as given by [1] is

$$u_i^{(1)} = \frac{1}{2\pi\rho U} \left[ \frac{\partial}{\partial x_i} \left( \ln r + e^{kx_1} K_0(kr) \right) - 2k e^{kx_1} K_0(kr) \delta_{i1} \right] \quad (5.3)$$

and the lift Oseenlet is

$$u_i^{(2)} = \frac{1}{2\pi\rho U} \varepsilon_{ij3} \frac{\partial}{\partial x_j} \left( \ln r + e^{kx_1} K_0(kr) \right) \quad (5.4)$$

where  $\varepsilon_{ijk}$  is called the Levi-Civita symbol. It is a tensor of rank three defined by

$$\varepsilon_{ijk} = \begin{cases} 0, & \text{if if any two labels are the same} \\ 1, & \text{if if i,j,k is an even permutation of 1,2,3} \\ -1, & \text{if if i,j,k is an odd permutation of 1,2,3.} \end{cases}$$

Meanwhile, Imai's approximation as given in [2] is

$$\psi = \frac{\Gamma}{2\pi} \log r - \frac{m}{2} \left( \operatorname{erf} \eta - \frac{\theta}{\pi} \right) \quad (5.5)$$

where  $m = \Gamma = \frac{1}{\rho}$  for unit force and  $k(r - x_1) = \eta^2 \approx k \frac{x_2^2}{2x_1}$  in the wake.

## 5.3 Vorticity Evaluation

### 5.3.1 The drag Oseenlet vorticity

From (5.3), it follows that

$$u_1^{(1)} = \frac{1}{2\pi\rho U} \left[ \frac{\partial}{\partial x_1} \left( \ln r + e^{kx_1} K_0(kr) \right) - 2k e^{kx_1} K_0(kr) \right] \quad (5.6)$$

and

$$u_2^{(1)} = \frac{1}{2\pi\rho U} \left[ \frac{\partial}{\partial x_2} \left( \ln r + e^{kx_1} K_0(kr) \right) \right] \quad (5.7)$$

Therefore, to derive the vorticity, we use the expression

$$\omega = \left[ \nabla \times u_i^{(1)} \right]_3 = \frac{\partial}{\partial x_1} u_2^{(1)} - \frac{\partial}{\partial x_2} u_1^{(1)} \quad (5.8)$$

Therefore,

$$\begin{aligned} \frac{\partial}{\partial x_2} u_1^{(1)} &= \frac{1}{2\pi\rho U} \frac{\partial}{\partial x_2} \left\{ \frac{\partial}{\partial x_1} (\ln r + e^{kx_1} K_0(kr)) - 2k e^{kx_1} K_0(kr) \right\} \\ \frac{\partial}{\partial x_1} u_2^{(1)} &= \frac{1}{2\pi\rho U} \frac{\partial}{\partial x_1} \left\{ \frac{\partial}{\partial x_2} (\ln r + e^{kx_1} K_0(kr)) \right\}. \end{aligned}$$

However, substituting these into (5.8) and simplifying gives

$$\omega = \frac{1}{\pi\rho U} \left\{ e^{kx_1} \frac{\partial}{\partial x_2} (K_0(kr)) \right\}. \quad (5.9)$$

Therefore, (5.9) is the expression for the Oseenlet vorticity.

### 5.3.2 Equivalence of Oseen's and Imai's vorticity in far-field

To demonstrate that the Oseenlet vorticity and Imai's vorticity are equivalent, we approximate (5.9) in the far-field and compare with Imai's vorticity where

$$e^{kx_1} \frac{\partial}{\partial x_2} (K_0(kr)) \approx -\frac{kx_2}{r} \sqrt{\frac{\pi}{2kr}} e^{-k(r-x_1)}.$$

Now substituting into (5.9) we have

$$\omega \approx -\frac{1}{\pi\rho U} \left\{ \frac{k^2 x_2}{r} \sqrt{\frac{\pi}{2kr}} e^{-k(r-x_1)} \right\}. \quad (5.10)$$

Therefore, (5.10) is the far-field Oseenlet vorticity, while Imai's vorticity as given in [2] given is

$$\omega = -\frac{2k^2}{\rho U \sqrt{\pi}} \frac{\eta}{\xi^2 + \eta^2} e^{-\eta^2}. \quad (5.11)$$

Therefore, putting  $k(r - x_1) = \eta^2 \approx k \frac{x_2^2}{2x_1}$ ,  $r = \frac{\eta^2 + \xi^2}{2k}$ ,  $\xi = (2kr)^{\frac{1}{2}} \cos \frac{1}{2}\theta$  and  $\eta = (2kr)^{\frac{1}{2}} \sin \frac{1}{2}\theta$  into (5.10), it is shown that Oseenlet vorticity is the same as Imai's approximation of vorticity.

## 5.4 Stream function Evaluation

### 5.4.1 Drag Oseenlet stream function

From the Cauchy-Riemann equations, the drag Oseenlet velocity (5.3) can be written in terms of the stream function such that

$$\psi = \int_{X_i}^{x_i} \varepsilon_{3ij} u_i^{(1)} dx_j'$$

where  $\psi$  is the stream function,  $x'_j$  is the variable of integration and  $u_i^{(1)}$  is the drag Oseenlet velocity. The constant  $X_i$  is chosen such that  $\psi(x_i) = 0$ . Integrating along  $x_1$  only gives  $\psi = -\int_{X_1}^{x_1} u_2' dx_1'$ , this implies that

$$\psi = -\frac{1}{2\pi\rho U} \int_{X_1}^{x_1} \frac{\partial}{\partial x_2} (\ln r' + e^{kx_1'} K_0(kr')) dx_1' \quad (5.12)$$

where  $r' = \sqrt{x_1'^2 + x_2^2}$ . However, (5.12) consist of the potential term and the wake term. i.e

$$\psi = -\frac{1}{2\pi\rho U} (\psi^{pot} + \psi^{wake})$$

where  $\psi^{pot} = \int_{X_1}^{x_1} \frac{\partial}{\partial x_2} (\ln r') dx_1'$  gives the velocity potential and  $\psi^{wake} = \int_{X_1}^{x_1} \frac{\partial}{\partial x_2} (e^{kx_1'} K_0(kr')) dx_1'$  give the wake velocity. To evaluate the potential term, we use complex analysis, letting  $z = x_1 + ix_2, z' = x_1' + ix_2$  and  $Z = X_1 + ix_2$ , see 5.1.

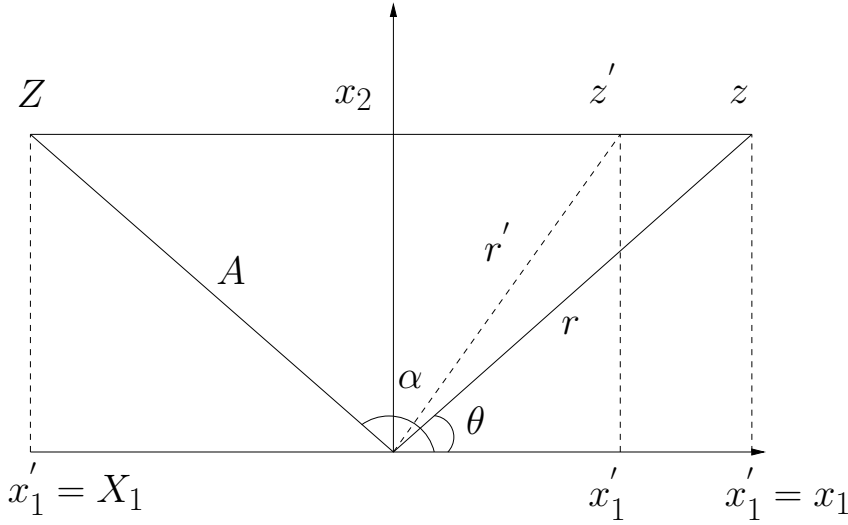


Figure 5.1: Points of integration

Consider  $\Psi = \frac{d}{dz} \ln z = \frac{1}{re^{i\theta}} = \frac{e^{-i\theta}}{r} = \frac{r \cos \theta - ir \sin \theta}{r^2}$ . Therefore, the negative of the imaginary part of  $\Psi$  gives  $-Im\{\frac{d}{dz} \ln z\} = \frac{x_2}{r^2} = \frac{\partial}{\partial x_2} \ln r$ . So,

$\psi^{pot} = -Im\{\int \frac{\partial}{\partial z'} \ln z' dz\} = -Im\{[\ln z']_Z^z\} = -Im\{\ln z - \ln Z\} = -Im\{\ln r + i\theta - \ln A - i\alpha\} = -\theta + \alpha$ . As  $\psi^{pot}$  is a potential, we can ignore the constant  $\alpha$ , and without loss of generality we can let

$$\psi^{pot} = -\theta. \quad (5.13)$$

The wake term from (5.12) can be determined from  $\psi^{wake} = -\frac{1}{2\pi\rho U} \int_{X_1}^{x_1} \frac{\partial}{\partial x_2} (e^{kx_1'} K_0(kr')) dx_1'$ , but  $\frac{\partial}{\partial x_2} K_0(kr) = -\frac{kx_2}{r} K_1(kr) \approx -\frac{kx_2}{r} \sqrt{\frac{\pi}{2kr}} e^{-kr}$  from Abramowitz and Stegun [9]. Therefore, the approximation to the wake term is obtained as

$$\psi^{wake} \approx -\frac{1}{2\pi\rho U} \int_{X_1}^{x_1} \left\{ \frac{kx_2}{r'} \sqrt{\frac{\pi}{2kr'}} e^{-k(r'-x_1')} \right\} dx_1'. \quad (5.14)$$

Finally, the expression for the Oseenlet stream function is obtained by adding (5.13) and (5.14)

$$\psi = \frac{1}{2\pi\rho U} \left\{ \theta - \int_{X_1}^{x_1} \left\{ \frac{kx_2}{r'} \sqrt{\frac{\pi}{2kr'}} e^{-k(r'-x_1')} \right\} dx_1' \right\}. \quad (5.15)$$

## 5.4.2 Equivalence of Oseen's and Imai's stream function in far-field

The Oseenlet stream function is given by (5.15) and that of Imai's stream function [2] is given as

$$\psi = \frac{1}{2\pi\rho U} \{\theta - \pi \operatorname{erf} \eta\} \quad (5.16)$$

To show that Imai's stream function and Oseenlet stream function are equivalent, recall that  $k(r - x_1) = \eta^2 \approx k \frac{x_2^2}{2x_1}$  and  $\operatorname{erf} \eta = \frac{2}{\sqrt{\pi}} \int_0^\eta e^{-\eta'^2} d\eta'$ , so let  $\psi_1 = \frac{1}{2\pi\rho U} \int_{X_1}^{x_1} \frac{kx_2}{r'} \sqrt{\frac{\pi}{2kr'}} e^{-k(r'-x_1')} dx_1'$ , where  $\psi = \frac{\theta}{2\pi\rho U} - \psi_1$ , implies that  $\psi_1 \approx \frac{1}{2\pi\rho U} \frac{2}{\sqrt{\pi}} \int_0^\eta \eta' e^{-\eta'^2} \frac{2}{\eta'} d\eta'$  thus,  $\psi_1 = \frac{1}{2\rho U} \operatorname{erf} \eta$ . Therefore,

$$\psi = \frac{1}{2\pi\rho U} \{\theta - \pi \operatorname{erf} \eta\}. \quad (5.17)$$

Thus, equation (5.17) is the Oseenlet stream function and it is shown that it is equivalent to the Imai's stream function given in (5.16).

## 5.5 Velocity

### 5.5.1 Drag Oseenlet velocity

Recall that the drag Oseenlet is given in (5.3) as

$$u_i^{(1)} = \frac{1}{2\pi\rho U} \left[ \frac{\partial}{\partial x_i} (\ln r + e^{kx_1} K_0(kr)) - 2k e^{kx_1} K_0(kr) \delta_{i1} \right] \text{ where}$$

$$u_1^{(1)} = \frac{1}{2\pi\rho U} \left[ \frac{\partial}{\partial x_1} (\ln r + e^{kx_1} K_0(kr)) - 2k e^{kx_1} K_0(kr) \right] \quad (5.18)$$

and

$$u_2^{(1)} = \frac{1}{2\pi\rho U} \left[ \frac{\partial}{\partial x_2} (\ln r + e^{kx_1} K_0(kr)) \right]. \quad (5.19)$$

Recall that Imai's first approximation to the stream function is  $\psi = \frac{1}{2\pi\rho U} \{\theta - \pi \operatorname{erf} \eta\}$  where  $m = \frac{1}{\rho U}$ . We can now obtain the velocity using the relation  $u_i = \varepsilon_{ij3} \frac{\partial \psi}{\partial x_j}$ . It follows that  $u_1 = \frac{\partial \psi}{\partial x_2}$  and  $u_2 = -\frac{\partial \psi}{\partial x_1}$ . Therefore, Imai's velocity can be represented as

$$u_i^{(1)} = \varepsilon_{ij3} \frac{\partial}{\partial x_j} \left\{ -\frac{1}{2\pi\rho U} \operatorname{erf} \eta + \frac{\theta}{\pi} \right\} \quad (5.20)$$

so

$$u_1^{(1)} = -\frac{1}{2\pi\rho U} \left( \pi \frac{\partial}{\partial x_2} \operatorname{erf} \eta - \frac{\partial \theta}{\partial x_2} \right) \quad (5.21)$$

and

$$u_2^{(1)} = \frac{1}{2\pi\rho U} \left( \pi \frac{\partial}{\partial x_1} \operatorname{erf} \eta - \frac{\partial \theta}{\partial x_1} \right) \quad (5.22)$$

### 5.5.2 Equivalence of Oseen's and Imai's velocity in the far-field

To show that the Oseen's velocity is equivalent to Imai's velocity, we first show that the first components  $u_1$  from equation (5.18) and (5.21) are equivalent. Similarly, the second components  $u_2$  from equation (5.19) and (5.22) are also equivalent. Now, the first terms give  $\frac{\partial(\ln r)}{\partial x_1} = \frac{x_1}{r^2}$  and  $\frac{\partial\theta}{\partial x_2} = \frac{x_1}{r^2}$ . These are shown to be the same. However, the next terms in the velocity components give,  $\frac{\partial}{\partial x_1} (e^{kx_1} K_0(kr)) - 2k e^{kx_1} K_0(kr) \approx \frac{\partial}{\partial x_1} (e^{kx_1} \frac{\sqrt{\pi}}{\sqrt{2kr}} e^{-kr}) - 2k e^{kx_1} \frac{\sqrt{\pi}}{\sqrt{2kr}} e^{-kr}$ . But  $\frac{\partial}{\partial x_1} (\frac{1}{\sqrt{r}}) = \frac{x_1}{2r^2\sqrt{r}} = O(\frac{1}{r\sqrt{r}})$  which is of lower order as  $r \rightarrow \infty$ . Therefore,  $\frac{\partial}{\partial x_1} (e^{kx_1} K_0(kr)) - 2k e^{kx_1} K_0(kr) = \{ \frac{kx_1}{r} \sqrt{\frac{\pi}{2kr}} e^{-k(r-x_1)} + k \sqrt{\frac{\pi}{2kr}} e^{-k(r-x_1)} - 2k \sqrt{\frac{\pi}{2kr}} e^{-k(r-x_1)} \}$ . Simplifying gives

$$\frac{\partial}{\partial x_1} (e^{kx_1} K_0(kr)) - 2k e^{kx_1} K_0(kr) \approx \frac{-k(r-x_1)}{r} \sqrt{\frac{\pi}{2kr}} e^{-k(r-x_1)}$$

Recall that  $k(r-x_1) = \eta^2 \approx k \frac{x_2^2}{2x_1}$  and  $r = \frac{\eta^2 + \xi^2}{2k}$ ,  $[\xi = (2kr)^{\frac{1}{2}} \cos \frac{1}{2}\theta, \eta = (2kr)^{\frac{1}{2}} \sin \frac{1}{2}\theta]$  where  $\xi^2 + \eta^2 = 2kr$ ,  $\sin^2 \frac{1}{2}\theta = O(1)$ . Thus,

$$\frac{\partial}{\partial x_1} (e^{kx_1} K_0(kr)) - 2k e^{kx_1} K_0(kr) \approx -2k \sqrt{\frac{\pi}{2kr}} e^{-k(r-x_1)}. \quad (5.23)$$

Therefore, substituting into (5.18) give

$$\begin{aligned} \frac{\partial}{\partial x_1} (e^{kx_1} K_0(kr) - 2k e^{kx_1} K_0(kr)) &\approx \frac{1}{2\pi\rho U} (-2k \sqrt{\frac{\pi}{2kr}} e^{-k(r-x_1)}) \\ &\approx -\frac{\sqrt{k}}{\rho U \sqrt{2\pi x_1}} e^{-\eta^2}. \end{aligned}$$

Therefore,

$$u_1^{(1)} \approx -\frac{\sqrt{k}}{\rho U \sqrt{2\pi x_1}} e^{-\eta^2}. \quad (5.24)$$

This is the second term in the Oseenlet velocity. However, evaluating the second term in Imai's velocity, we have  $\pi \frac{\partial}{\partial x_2} \text{erf} \eta$ , but  $\frac{\partial}{\partial \eta} (\text{erf} \eta) = \frac{2}{\sqrt{\pi}} e^{-\eta^2}$ . Therefore,  $\pi \frac{\partial}{\partial x_2} \text{erf} \eta = \pi \frac{\partial \eta}{\partial x_2} \frac{\partial}{\partial \eta} (\text{erf} \eta)$ , but  $\eta \approx \sqrt{\frac{k}{2x_1}} x_2$ , implies that  $\frac{d\eta}{dx_2} = \sqrt{\frac{k}{2x_1}}$ , therefore

$$u_1^{(1)} \approx -\frac{1}{2\rho U} \frac{\partial}{\partial x_2} \text{erf} \eta = -\frac{\sqrt{k}}{\rho U \sqrt{2\pi x_1}} e^{-\eta^2}. \quad (5.25)$$

Therefore, it is shown that the first components of Imai and Oseenlet velocity are equivalent.

Now, we can show that the second components are also equivalent. The second components of Oseenlet and Imai's velocity are given in (5.19) and (5.22) respectively. It can be seen that  $\frac{\partial(\ln r)}{\partial x_2} = \frac{x_2}{r^2}$ , similarly  $-\frac{\partial\theta}{\partial x_1} = \frac{x_2}{r^2}$ . Meanwhile, the second term in the Oseenlet velocity as given in (5.19) gives  $\frac{\partial}{\partial x_2} (e^{kx_1} K_0(kr)) \approx (e^{kx_1} \frac{\sqrt{\pi}}{\sqrt{2kr}} e^{-kr})$ , but  $\frac{\partial}{\partial x_2} (\frac{1}{\sqrt{r}}) = \frac{x_2}{2r^2\sqrt{r}} = O(\frac{1}{r\sqrt{r}})$  which is of

lower order as  $r \rightarrow \infty$  and  $\frac{\partial}{\partial x_2}(e^{-kr}) = -k \frac{x_2}{r} e^{-kr} = O(1)$ . Therefore,

$$\begin{aligned} \frac{\partial}{\partial x_2}(e^{kx_1} K_0(kr)) &\approx \frac{\partial}{\partial x_2}\left(e^{kx_1} \frac{\sqrt{\pi}}{\sqrt{2kr}} e^{-kr}\right) \\ &\approx \left[\left(e^{kx_1} \frac{\sqrt{\pi}}{\sqrt{2kr}} e^{-kr}\right) \frac{\partial}{\partial x_2} e^{-kr}\right] \left(1 + O\left(\frac{1}{r\sqrt{r}}\right)\right) \\ &\approx \left(e^{kx_1} \frac{\sqrt{\pi}}{\sqrt{2kr}} \left(\frac{-kx_2}{r} e^{-kr}\right)\right) \\ &\approx -\frac{\sqrt{\pi}}{x_1} \eta e^{-\eta^2}. \end{aligned}$$

Thus,

$$\frac{\partial}{\partial x_2}(e^{kx_1} K_0(kr)) \approx -\frac{\sqrt{\pi}}{x_1} \eta e^{-\eta^2}. \quad (5.26)$$

Therefore, (5.26) is the second term in the Oseenlet velocity. However, Imai's second term can be evaluated as  $\pi \frac{\partial}{\partial x_1} e r f \eta$ , but  $\frac{\partial}{\partial \eta}(e r f \eta) = \frac{2}{\sqrt{\pi}} e^{-\eta^2}$ . Therefore,  $\pi \frac{\partial}{\partial x_1} e r f \eta = \pi \frac{\partial \eta}{\partial x_1} \frac{\partial}{\partial \eta}(e r f \eta)$ , but  $\eta \approx \sqrt{\frac{k}{2x_1}} x_2$ , implies that  $\frac{d\eta}{dx_1} = -\frac{1}{2} \frac{\eta}{x_1}$ , therefore,

$$\pi \frac{\partial}{\partial x_1} e r f \eta = -\frac{\sqrt{\pi}}{x_1} \eta e^{-\eta^2}. \quad (5.27)$$

Therefore, it is shown that Oseenlet velocity and Imai's first approximation of velocity are equivalent.

## 5.6 Conclusion

We derived the Oseenlet vorticity and stream function, evaluated the far-field approximations and compared with Imai's first approximation of vorticity and stream function. We further obtained the far-field approximation of velocity from Imai's approximation of stream function and compared with the Oseenlet velocity. The results show that the derived Oseenlet vorticity, velocity and stream function are equivalent to the Imai's approximations to leading order. The future work will be to infer the corresponding second order term in the Oseen linearisation

	Oseenlet	Imai's approximation
Velocity	$u_i = \frac{1}{2\pi\rho U} \left[ \frac{\partial}{\partial x_i} (\ln r + e^{kx_1} K_0(kr)) - 2k e^{kx_1} K_0(kr) \delta_{i1} \right]$	$u_i = \varepsilon_{ij3} \frac{\partial}{\partial x_j} \left\{ -\frac{1}{2\pi\rho U} e r f \eta + \frac{\theta}{\pi} \right\}$
Stream function	$\psi = \frac{1}{2\pi\rho U} \left\{ \theta - \int_{X_1}^{x_1} \frac{\partial}{\partial x_2} e^{kx_1} K_0(kr) dx \right\}$	$\psi = \frac{1}{2\pi\rho U} \left\{ \theta - \pi e r f \eta \right\}$
Vorticity	$\omega = \frac{1}{\pi\rho U} \left\{ e^{kx_1} \frac{\partial}{\partial x_2} (K_0(kr)) \right\}$	$\omega = -\frac{2k^2}{\rho U \sqrt{\pi}} \frac{\eta}{\xi^2 + \eta^2} e^{-\eta^2}$

Table 5.1: Comparison between Oseenlet and Imai's first approximation

from Imai's second approximation to the Navier-Stokes equation. This is the second order term in the NSlet expansion, which has not yet been given in the literature to the best knowledge of the authors.

## References

- [1] Chadwick, E.: The far-field Oseen velocity expansion. *Proc. R. Soc. A.* **454**, (1998) 2059-2082.
- [2] Imai I.: On the asymptotic behaviour of viscous fluid flow at a great distance from a cylindrical body, with special reference to Filon's paradox. *Proceedings of the Royal Society of London A: Mathematical, Physical and Engineering Sciences.* **208**, (1951) 487-516.
- [3] Chadwick, E.: A slender body theory in Oseen flow obtained by expanding the Oseenlets in the Green's integral representation. *Fluid Dyn Res.* **41** (2009), 045-508.
- [4] Chadwick, E, H.M. Khan., M. A Moatamedi., M. Mappin and M. Penny.:Experimental verification of an Oseen flow slender body theory *Jour. of Fluid Mech.*, **645** (2010), 271-279.
- [5] Anderson, J.R. Governing equations of fluid dynamics. *Comp. Fluid Dyn.* **3** (2009), 15-51.
- [6] Morton B. The generation and decay of vorticity. *Geophysical and Astrophysical Fluid Dyn.*,**28** (2014), 277-308.
- [7] E. Chadwick, J. Christian and K. Chalasani.: Using eulerlets to model steady uniform flow past a circular cylinder. *European Journal of Computational Mechanics: Advances in Boundary Element Techniques.* **27**,(2018) 465-478.
- [8] Jorgensen, L. H.: Elliptic cones alone and with wings at supersonic speeds. *Tech. Rep. NACA.* **1376**,(1957).
- [9] Abramowitz, M. and Stegun, I.A.: Morton B. Handbook of mathematical functions. *New York: Donover* ,(1965).
- [10] Lamb, H.: Hydrodynamics. *Cambridge University Press.*,(1932).
- [11] Goldstein, S.: On the vortex theory of screw propellers. *Proceedings of the Royal Society of London A: Mathematical, Physical and Engineering Sciences.*,**123**(1929).

## Chapter 6

# Enriched BEM for water coning

J.A. Márquez Ruiz<sup>1</sup>, B. Chen<sup>2</sup>, J. Trevelyan<sup>1</sup>, P.A. Gourgiotis<sup>1</sup> & E.L.Albuquerque<sup>3</sup>

- <sup>1</sup> Department of Engineering  
Durham University  
South Road  
DH1 3LE, Durham, UK.
- <sup>2</sup> Department of Engineering Science  
University of Oxford  
Parks Road  
OX1 3PJ, Oxford, UK.
- <sup>3</sup> Department of Engineering Mechanics  
University of Brasília  
Campus Universitário Darcy Ribeiro  
70910-900 Brasília, DF, Brazil.

---

**Abstract.** *The efficiency and cost-effectiveness of oil and gas production are detrimentally affected by the phenomenon of water coning. Here, a pressure difference causes water to be drawn towards the pump and to mix with the products that are extracted, requiring an expensive separation and cleansing operation. Engineers can mitigate this effect, and stop it from occurring, by careful design of their pumping strategy to ensure water ingress does not take place.*

*The process may be modelled as one of potential flow in multiple layered regions which may be oil- and/or gas-rich or water-saturated. Between the layers lies a moving interface as driven by the evolving pressure distribution. Tracking the movement of the interface, one can ensure the water-filled region does not reach the pump opening. The boundary element modelling of the potential problem is here enriched using non-polynomial functions that are better able to capture the typical flux density distribution allowing accurate results to be obtained from coarse meshes. While the current work is 2D, the full benefit will be realised in 3D.*

---

## 6.1 Introduction

Water coning is a problem of interest to petroleum engineers working in oil and gas recovery. There is a wide literature on water coning since the early studies describing the phenomenon [1]. It is prevalent where there are aquifers in the vicinity of the oil/gas rich strata from which the

hydrocarbons are being pumped, and where there is a high permeability in the vertical direction. Since the water has the higher density of the fluids it generally lies below the oil/gas. As the pump operates, the local changes in pressure cause the water contained below the oil/gas region to be drawn upwards towards the pump. For a single vertical pump the water is drawn up in an axisymmetric pattern giving rise to a broadly conical geometry, giving the phenomenon its name. As time progresses, the extent of water penetration towards the pump is defined by the opposing forces of gravitation (pulling the water down) and suction from the pump (pulling the water up). The water coning becomes balanced when these forces are equilibrated. However, if the pumping rate is excessive, the water reaches the pump and becomes introduced into the oil products recovered. Expensive separation and remediation procedures to the oil/water mixture motivate research into a better understanding of the water coning mechanism. While some strategies in industry involve first finding the pumping rate that gives water intrusion and then reducing it, we attempt to identify the optimal rates by numerical modelling. There are similar problems with gas coning, where a critical flow rate can be identified from theoretical analysis, and active control strategies can yield pumping rates close to this optimum [2].

The problem may be modelled as moving interface problem, the interface separating the regions containing oil (above) and water (below). The situation is illustrated in Figure 6.1. Azim

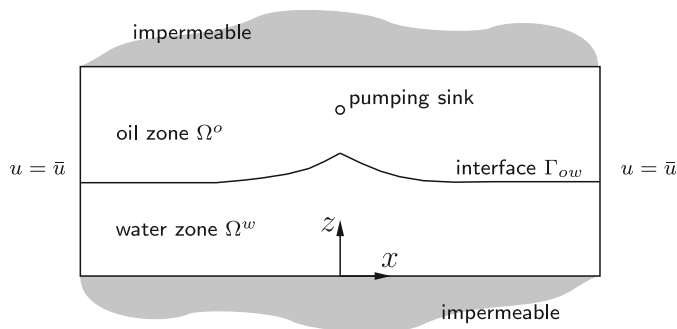


Figure 6.1: The water coning problem

[3] modelled the problem using tetrahedral finite elements, with the interface modelled using triangular planar elements. But the situation is more conveniently modelled using the Boundary Element Method (BEM). A pioneering study of implementing BEM to simulate water coning was conducted by Lucas et al. [4] who explored the geometrical evolution and stability relating to different pumping conditions with particular numbers or arrangements of sinks. Zhang et al. [5] analysed continuous and pulsed pumping strategies in aquifers, and found that including capillarity in the BEM model gave results that more closely approximated the phreatic surfaces observed experimentally. Gontijo et al. [6] used the BEM to simulate the case with only one pump sink in the oil zone in two dimensions (2D). In their research, the system was divided into two sub-regions with continuous linear elements implemented along the interface and the outer boundary. A refined mesh was used to capture the high pressure gradients that arise at certain stages during the process. While this is not problematic for a small 2D simulation, the consequences of a requirement for such a fine mesh for a full 3D analysis motivate us to seek a more efficient simulation technique.

One approach that can be used to improve convergence in finite element and/or BEM simulations is the use of enrichment. Here, the classical piecewise polynomial approximating functions are augmented by other (often non-polynomial) functions that have better convergence

properties for the PDE under consideration. These methods share a common ancestry in the Partition of Unity Method (PUM) [7]. The enrichment functions can be found by consideration of the local asymptotic behaviour of the solution (for example, the use of XFEM in linear elastic fracture mechanics, where the form of the displacement field in the vicinity of a crack tip is used to enrich fracture predictions on coarse meshes). Alternatively, sets of plane waves and/or Bessel functions could be used to enrich wave simulations, and this has been done in a wide variety of contexts, including FEM, BEM, isogeometric, Discontinuous Enrichment, Discontinuous Galerkin and Ultraweak Variational Methods. While the above examples use enrichment functions that emerge from the governing physics of the problem at hand, another alternative is an engineering approach in which we could use any enriching functions that we have reason to believe will offer improvement in capturing the solution. One example that is pertinent to the current paper is Mohamed [8], who successfully used a family of Gaussian functions to enrich transient finite element approximations in heat transfer based on engineering experience of their resemblance to temperature distributions found in the vicinity of heat sources. In all of the above examples, a common outcome is the availability of highly accurate results from coarse discretisations with significant reductions in the size of the linear system compared to that required using piecewise polynomial approximation spaces.

In the study of Gontijo [6], it may be noticed that the interface flux density resembles a Gaussian function, and we hypothesise that improved computational efficiency may be available by using a coarse BEM mesh on the interface, but using enrichment functions of a Gaussian (or similar) form to capture the behaviour. In this paper we develop a set of enrichment functions and propose an enriched BEM scheme for the water coning problem. It should be noted that we do not attempt to model oil recovery approaches such as the pumping of water into the reservoir to replace the oil extracted.

## 6.2 Governing equations

We consider a multizone problem in the  $x - z$  plane containing regions  $\Omega^w$ , labelled the water zone, lying underneath the oil zone  $\Omega^o$  as depicted in Figure 6.1. We denote the density,  $\rho^w, \rho^o$ , using superscripts  $o, w$  throughout to indicate the oil and water regions respectively. Consideration of the flow in porous media as governed by the Darcy equation, and assuming incompressibility, leads to us seeking the velocity potential  $u^i$ , defined as

$$u^i = \frac{p^i}{\rho^i g} + z, \quad i = o, w, \quad (6.1)$$

where  $p$  is the fluid pressure, as the solution to the Poisson equation

$$\nabla^2 u^i = S^i \quad (6.2)$$

where  $S^i$  denotes the effect of sources and sinks within the zone. For the water zone,  $S^w = 0$ . On the interface, the usual continuity conditions apply, i.e.  $p_1 = p_2$  and  $q_1 = -q_2$ , where  $q = -K \partial u / \partial n$ , with  $K$  being the conductivity and  $n$  the unit outward normal. We note that if the fluid densities are chosen to be different (6.1) suggests the existence of a potential jump at the interface.

The fluid velocity is given by the potential gradient  $q$  and this implicitly carries information about the movement of the interface. Gontijo [6] shows that, if we denote the height of the

interface as  $z = \eta(x, t)$  and consider a time step  $\Delta t$ , the development of the interface location between time step  $m$  and time step  $m + 1$  may be written

$$\eta_{m+1} = \eta_m - \frac{K}{\varphi} q_m \Delta t \sqrt{1 + \left( \frac{\partial \eta}{\partial x} \right)_m^2} \quad (6.3)$$

where  $\varphi$  denotes the porosity of the rock medium.

### 6.3 Boundary element formulation

We solve the Poisson equation using the BEM in 2D, and this is based on collocating a regularised boundary integral equation (BIE) over  $\Gamma \equiv \partial\Omega$ ,

$$\int_{\Gamma} q^*(\mathbf{x}, \mathbf{x}') (u(\mathbf{x}') - u(\mathbf{x})) d\Gamma(\mathbf{x}') = \int_{\Gamma} u^*(\mathbf{x}, \mathbf{x}') q(\mathbf{x}') d\Gamma(\mathbf{x}') + u^* Q \quad (6.4)$$

at a sufficient number of points  $\mathbf{x} \in \Gamma$  to yield a square system when  $\Gamma$  and the unknowns  $u, q$  are discretised. Here  $u^*, q^*$  are the fundamental solutions for the Laplace operator in 2D and are well known and  $Q$  describes the strength of a sink in the domain  $\Omega$ . The derivation of this equation is standard and not repeated here. The presence of two material domains requires a multizone approach and standard techniques are used.

A classical discretisation involves the expansion of  $u$  and  $q$  in low order polynomial shape functions,  $N_j$ , i.e.

$$u(\xi) = \sum_{j=1}^J N_j(\xi) u_j, \quad q(\xi) = \sum_{j=1}^J N_j(\xi) q_j, \quad \xi \in [-1, 1] \quad (6.5)$$

over each element containing  $J$  nodes and parameterised by local coordinate  $\xi$  in the usual way. Now we propose an enriched approximation space to be used over a selection of elements on the interface, and given by the augmented expansion

$$u(\xi) = \sum_{j=1}^J N_j(\xi) u_j + \sum_{m=1}^{M_u} \lambda_m^u \psi_m^u(x) \quad (6.6)$$

$$q(\xi) = \sum_{j=1}^J N_j(\xi) q_j + \sum_{m=1}^{M_q} \lambda_m^q \psi_m^q(x) \quad (6.7)$$

where  $\psi_m^u$  and  $\psi_m^q$  are sets of enrichment functions designed to efficiently capture the variation in  $u$  and  $q$  respectively. The coefficients  $\lambda_m^u, \lambda_m^q$  are the amplitudes of these functions and become part of the solution vector alongside the conventional unknowns  $u_j, q_j$ . Notice that, over the elements enriched in this way, the unknowns  $u_j, q_j$  can no longer be interpreted as nodal values of  $u, q$ . It should further be noticed that introducing the enrichment causes the number of degrees of freedom to be increased by  $M_u + M_q$ , so the same number of additional equations need to be developed in order to retain a square system. These may be simply found from the consideration of additional collocation points at non-nodal locations. In practice, it has been found effective to use a degree of oversampling so that more additional equations are used than this minimum, leading to an overdetermined system of equations that needs to be solved in a least squares sense.

## 6.4 Choice of enrichment functions

The selection of the form of  $\psi_m^u$  and  $\psi_m^q$  is informed by the results of a refined polynomial BEM model. It is found that the pumping has negligible effect on the potential outside the range  $|x| = 3$  m and on the flux outside range  $|x| = 6.25$  m. Hence, we seek our enrichment functions in the larger of these ranges.

The distribution of potential on the interface is found to be well approximated by a second order rational function and the flux density to be well approximated by Gaussian distributions. From this initial characterisation of the distributions we proceed to optimise the coefficients  $a_1, a_2, s_1, s_2$  in our candidate functions  $\beta^u, \beta^q$ , being

$$\beta^u(x, a_1, a_2) = \frac{x^2 + a_1}{x^2 + a_2} \quad (6.8)$$

$$\beta^q(x, s_1, s_2) = e^{-(x/s_1)^2} + e^{-(x/s_2)^2} \quad (6.9)$$

The values of the coefficients were tested against an error metric

$$E_u(a_1, a_2) = \sum_{t=1}^T \left\{ \int_{\Gamma_{ow}} [u(x) - \lambda_u^t \beta^u(x, a_1, a_2)]^2 d\Gamma \right\}^{1/2} \quad (6.10)$$

where the summation takes place over all time steps and  $\lambda_u^t$  is the coefficient providing a best fit (in the least squares sense) such that  $\lambda_u^t \beta^u \approx u(x)$  at the time step  $t$ . A similar metric  $E_q(s_1, s_2)$  was used to describe how well  $\beta^q(x, s_1, s_2)$  approximates  $q$  as a function of  $s_1, s_2$ . The response surface method yielded the optimum values  $a_1 = 17.54, a_2 = 24.31, s_1 = 0.64, s_2 = 2.11$ .

Finally, in order to ensure that the enrichment functions vanish at the end of the enriched region ( $x = \pm 6.25$  m), and thereby make this a continuous formulation, we subtract the values of  $\beta^u, \beta^q$  at  $x = \pm 6.25$  m to arrive at the enrichment functions  $\psi_m^u$  and  $\psi_m^q$  to use in (6.6) and (6.7):

$$\psi_m^u(x) = \beta^u(x, 17.54, 24.31) - \beta^u(6.25, 17.54, 24.31) \quad (6.11)$$

$$\psi_m^q(x) = \beta^q(x, 0.64, 2.11) - \beta^q(6.25, 0.64, 2.11) \quad (6.12)$$

## 6.5 Results

We consider the case shown in Figure 6.2 with properties of oil  $\rho^o = 1000\text{kg/m}^3, K^o=2\text{m/s}$ , and of water  $\rho^w = 1000\text{kg/m}^3, K^w=1\text{m/s}$ . Dirichlet conditions  $u = \bar{u} = 4$  are applied on the left and right sides, and homogeneous Neumann conditions at the top and bottom to model the impermeable layers above and below. In the figure, the sink located at (0,3) is shown as an asterisk and is activated for the first 20 time steps. The (originally horizontal) interface is modelled with only four elements, the central two of which are enriched (compared with the 50 interface elements required in the unenriched model [6]). Linear elements ( $J = 2$ ) are used throughout. The points depicted  $\times$  are explored as additional collocation points.

We compare the results from the enriched model (NDOF = 43) with both fine and coarse polynomial models, the refined model (NDOF = 85) taken from [6], and for comparison a coarse polynomial model (NDOF = 41) as in Figure 6.2. The comparison of the potential distribution along the interface  $\Gamma_{ow}$ , presented in Figure 6.3 shows that all models are capable of finding a good approximation to the potential field. This is no surprise since the distribution

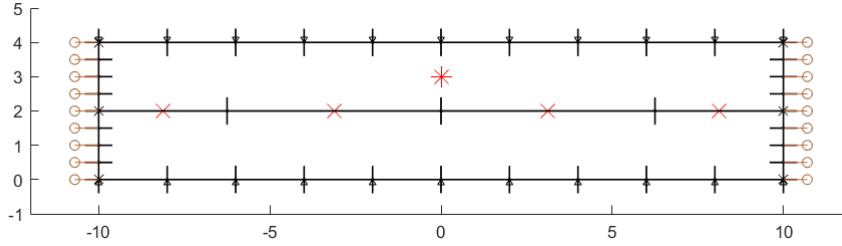


Figure 6.2: Model geometry and mesh

is approximately linear apart from some fine detail around  $x = 0$ . However, it is in modelling the flux density distribution that the enrichment is shown well. The comparison of flux density results along  $\Gamma_{ow}$  is shown in Figure 6.4, and this shows the enriched model (with 7 DOF along the interface) to provide results that correlate well with the refined polynomial model (with 51 DOF along the interface).

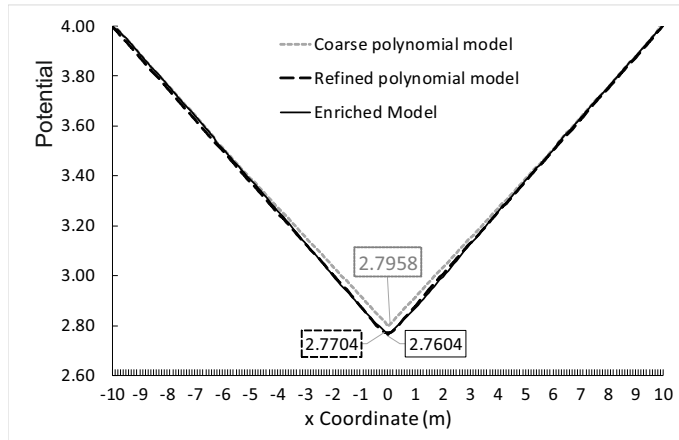


Figure 6.3: Interface potential distribution

As expected, the coarse linear elements are completely unable to capture this distribution without enrichment. The main result of interest in practical terms is the avoidance of water ingress to the pump, and the key information here is the height of the water cone. Since the movement of the interface is driven by the flux density  $q$ , as is evident in (6.3), an accurate prediction of flux densities is key. In Figure 6.5 we plot the evolution of the height of the cone over the duration of the simulation.

It can clearly be seen that the enrichment applied to the coarse model is able to provide an excellent prediction of the cone tip elevation.

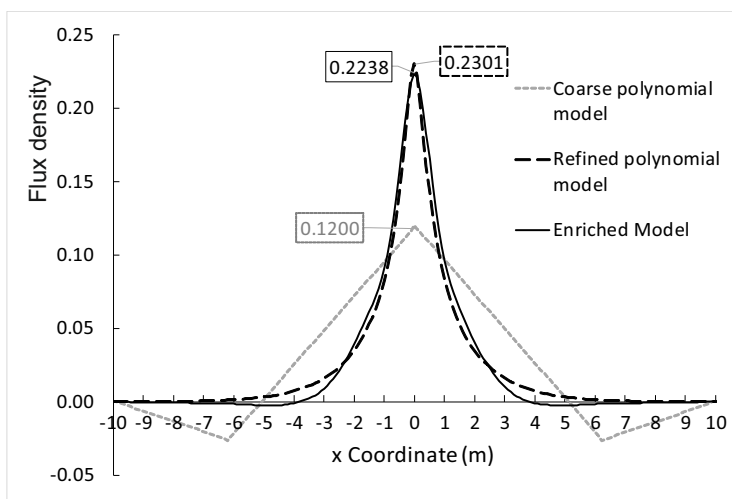


Figure 6.4: Interface flux density distribution

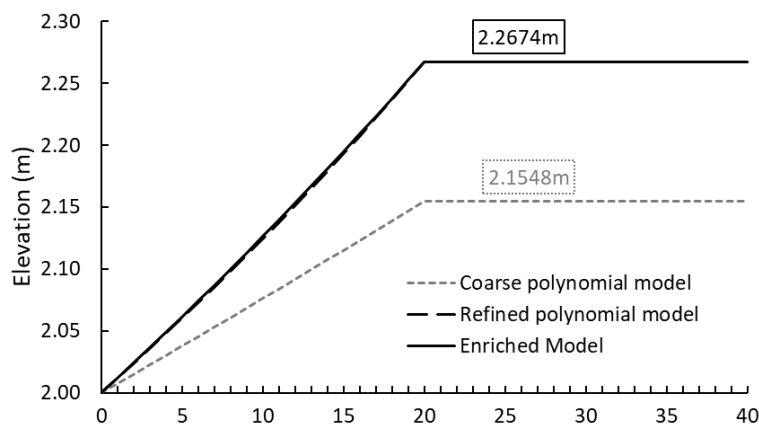


Figure 6.5: Evolution of cone tip height

## 6.6 Conclusions and further work

An enriched BEM scheme has been presented for the efficient simulation of water coning in reservoir modelling. Enrichment functions for the potential and flux density distributions on the oil/water interface were derived and optimised using a response surface methodology. These were inserted into a BEM scheme so the amplitudes of the enrichment functions became auxiliary unknowns to be solved for alongside the traditional terms in a solution vector. The results demonstrate that the enriched scheme is capable of delivering accurate results from a coarse discretisation.

These are preliminary results and several aspects remain to be investigated. Firstly, as is commonly reported in enriched methods, the system suffers from a high degree of ill-conditioning and this needs to be understood better. Numerical experiments suggest that the errors in predicting cone tip elevations can be significantly reduced by oversampling and solving an overdetermined system of equations. This merits further investigation, as does the possibility of treating the enrichment function for the flux density (6.9) as two separate functions, each being a single Gaussian curve, as in [8]. Once these aspects are better understood, the 3D

implementation can proceed to unlock the full potential of enrichment in this application of interest to the petrochemical community.

## References

- [1] Muskat, M. and Wycokoff, R.D.: An approximate theory of water-coning in oil production. *Transactions of the AIME*, (1935) 144-163.
- [2] Fortaleza, E.L.F., Limaverde Filho, J.O.A., Gontijo, G.S.V., Albuquerque, E.L., Simões, R.D.P., Soares, M.M., Miranda, M.E.R. and Abade, G.C.: Analytical, numerical and experimental study of gas coning on horizontal wells. *Journal of the Brazilian Society of Mechanical Sciences and Engineering*. **41**, (2019) 141.
- [3] Azim, R.A.: Evaluation of water coning phenomenon in naturally fractured oil reservoirs. *Journal of Petroleum Exploration and Production Technology*. **6**, (2016) 279-291.
- [4] Lucas, S.K., Blake, J.R. and Kucera, A.: A boundary-integral method applied to water coning in oil reservoirs. *The ANZIAM Journal*. **32**, (1991) 261-283.
- [5] Zhang, H., Baray, D.A. and Hocking, G.C.: Analysis of continuous and pulsed pumping of a phreatic aquifer. *Advances in Water Resources*. **22**, (1999) 623-632.
- [6] Gontijo, G.S.V, Albuquerque, E.L. and Fortaleza, E.L.F: Study on the Water Coning Phenomenon in Oil Wells Using the Boundary Element Method. *Proc. BETEQ Conference*, (2014) Florence.
- [7] Melenk, J.M. and Babuška, I.: The partition of unity finite element method: basic theory and applications. *Computer Methods in Applied Mechanics and Engineering*. **139**, (1996) 289-314.
- [8] Mohamed, M.S., Seaid, M., Trevelyan, J. and Laghrouche, O.: A partition of unity FEM for time-dependent diffusion problems using multiple enrichment functions. *International Journal for Numerical Methods in Engineering*. **93**, (2013) 245-265.

## Chapter 7

# An Accurate BIE Model of Drops Moving Near Corners

L. Bystricky, S. Pålsson, A. K. Tornberg

Department of Mathematics,  
KTH Royal Institute of Technology  
Lindstedtsvägen 25  
SE-100 44, Stockholm, Sweden.

---

**Abstract.** *Boundary integral equations (BIEs) have been shown to be an efficient method for simulating the movement of drops in a Stokesian fluid [10]. Recasting the governing incompressible Stokes equations as a BIE allows us to model the behaviour of a drop with a discretization of the drop interface only. BIEs have several other advantages including good conditioning and high accuracy [1]. Previous work has studied the behaviour of drops in confined geometries using a BIE approach [11, 18]. The current chapter extends this approach to the modelling of drops near corners. Traditionally, BIEs struggle to achieve high accuracy in the vicinity of corners due to weak singularities that occur at the corner. Recursively compressed inverse preconditioning (RCIP)[5, 7] is one approach to handle these singularities without introducing any additional unknowns beyond what is needed to sufficiently resolve the geometry. Combined with high-order adaptive time-steppers and the spectral-Ewald method for fast periodic summation [11], we are able to achieve an efficient, highly accurate model of drop movement near corners.*

---

### 7.1 Introduction

The movement of drops in a confined geometry is of interest in many microfluidic devices [17]. Resolving such problems numerically is very challenging, due, among other reasons, to the moving, deformable interfaces of the drops. Boundary integral methods have been used to model such problems [10, 11, 15]. Recasting the governing incompressible Stokes equations as a boundary integral equation (BIE) allows us to reduce the dimension of the problem by restricting any unknowns to the drop (or wall) interface. This results in a much smaller (but dense) linear system to solve. In the context of drop movement BIEs are particularly attractive, as the drop interface can be explicitly tracked as it evolves in time.

A BIE model of drop movement in wall-confined geometries has been presented for the three-dimensional [18] and periodic two-dimensional [11] cases. This chapter presents an extension

of [11] that allows for the modelling of drop movement near walls with sharp corners. Handling such problems is numerically difficult because of the singularities that occur near corners. Local refinement around the corners is a possibility, however this becomes prohibitively expensive as the resolution or number of corners increases.

Accurately resolving BIEs in the vicinity of corners is an active area of research. In [14] for example, the Stokes equations are solved to high precision using custom quadrature rules that are tailored to the asymptotic behaviour of the harmonic Green's function near the corner. This approach introduces a modest increase in memory requirements, but requires knowledge of how the solution behaves asymptotically near the corner. The approach that we will take, recursively compressed inverse preconditioning, requires only a small amount of precomputation for each corner, however it introduces a modest increase in memory requirements and is entirely kernel-independent, meaning that it does not require knowledge of the asymptotics of the solution near the corner. This allows us to treat all corners with a single operator.

## 7.2 Governing Equations

We will be considering  $N_d$  drops in a domain of  $d$  dimensions. Let  $\Omega_0$  denote the bulk fluid, and  $\Omega_k$ ,  $k = 1, \dots, N_d$ , denote the drops. The bulk fluid has viscosity  $\mu_0$ , while drop  $k$  has viscosity  $\mu_k$ . The viscosity contrast at the interface between the fluid inside drop  $k$  to the bulk fluid is the viscosity contrast at the interface  $\Gamma_k$ . In addition to the drops, there may be solid walls. We will denote  $\gamma$  to be the union of the boundaries of the drops and solid walls will be permitted to have sharp corners. Figure 7.1 provides a sketch of a computational domain.

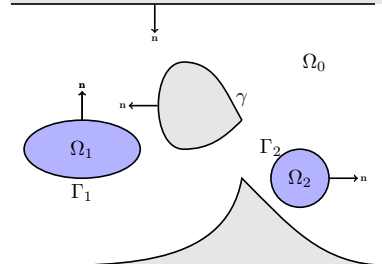


Figure 7.1: Sketch of a computational domain.  $\Omega_0$  is the bulk fluid with viscosity  $\mu_0$ , while  $\Omega_1$  and  $\Omega_2$  are drops containing fluid of possibly different viscosities  $\mu_1$  and  $\mu_2$ .

The bulk fluid, as well as the fluid inside each drop must satisfy the incompressible Stokes equations,

$$-\mu_k \Delta \mathbf{u}_k + \nabla p_k = 0, \quad \mathbf{x} \in \Omega_k, \quad k = 0, \dots, N_d, \quad (7.1a)$$

$$\nabla \cdot \mathbf{u}_k = 0, \quad \mathbf{x} \in \Omega_k, \quad k = 0, \dots, N_d, \quad (7.1b)$$

where  $(\mathbf{u}_k, p_k)$  is the fluid velocity and pressure inside  $\Omega_k$ . Equation (7.1a) is a statement of momentum conservation, and (7.1b) is the incompressibility constraint and is a statement of mass conservation.

### 7.2.1 Boundary Conditions

We will take no-slip boundary conditions on the solid walls, i.e

$$\mathbf{u}_0 = 0, \quad \mathbf{x} \in \gamma. \quad (7.2)$$

In addition, we will take the flow to be periodic over a square box of side length  $L$ , i.e.  $\mathbf{u}(\mathbf{x}) = \mathbf{u}(\mathbf{x} + \mathbf{p}L)$ , where  $\mathbf{p} \in \mathbb{Z}^2$ . We will assume an ambient flow  $\mathbf{u}^\infty(\mathbf{x})$  would exist in the absence of any solids or drops.

On the drops, we require the fluid velocity to be continuous as we pass from inside to outside the drop. The surface forces, however, are allowed to be discontinuous. In general the forces acting on  $\Gamma_k$  from inside the drop will not be equal to the force acting on  $\Gamma_k$  from outside the drop. The difference between the inside force and the outside force will be denoted  $\Delta \mathbf{f}_k$ . We will relate  $\Delta \mathbf{f}_k$  to the curvature of  $\Gamma_k$ ,  $\kappa$ , and the surface tension of the interface,  $\sigma_k$ , by

$$\Delta \mathbf{f}_k(\mathbf{x}) = \sigma_k(\mathbf{x})\kappa(\mathbf{x}) - \nabla_s \sigma_k(\mathbf{x}), \quad k = 1, \dots, N_d, \quad (7.3)$$

where  $\nabla_s$  denotes the gradient along the interface. A detailed derivation of this constitutive relation is given in [13]. For the remainder of this chapter, we will restrict our attention to the case where the viscosity of all the drops is equal to the viscosity of the bulk fluid ( $\lambda_k = 1$ ,  $k = 1, \dots, N_d$ ). In addition, we will assume that the surface tension  $\sigma$  is constant. The more general case of different viscosity ratios and non-uniform surface tension is treated in [10, 11, 15].

### 7.2.2 Boundary Integral Formulation

We begin by defining the two-dimensional Stokeslet,  $G_{ij}(\mathbf{x})$ , and stresslet,  $T_{ijk}(\mathbf{x})$ , as

$$G_{ij}(\mathbf{x}) = -\delta_{ij} \log(|\mathbf{x}|) + \frac{x_i x_j}{|\mathbf{x}|^2},$$

$$T_{ijk}(\mathbf{x}) = -4 \frac{x_i x_j x_k}{|\mathbf{x}|^4}.$$

Using the Stokeslet and the stresslet, we can define the periodic single- and double-layer potentials over a boundary  $\Lambda$ ,  $\mathbb{S}_\Lambda[\mathbf{g}](\mathbf{x})$  and  $\mathbb{D}_\Lambda[\mathbf{g}](\mathbf{x})$  respectively as

$$\mathbb{S}_\Lambda[\mathbf{g}](\mathbf{x}) = \frac{-1}{4\pi} \sum_{\mathbf{p} \in \mathbb{Z}^2} \int_\Lambda g_i(\mathbf{y}) G_{ij}(\mathbf{x} - (\mathbf{y} + L\mathbf{p})) \, ds(\mathbf{y}),$$

$$\mathbb{D}_\Lambda[\mathbf{g}](\mathbf{x}) = \frac{-1}{4\pi} \sum_{\mathbf{p} \in \mathbb{Z}^2} \int_\Lambda g_i(\mathbf{y}) T_{ijk}(\mathbf{x} - (\mathbf{y} + L\mathbf{p})) n_k(\mathbf{y}) \, ds(\mathbf{y}),$$

where  $\mathbf{n}(\mathbf{x})$  is the unit normal at  $\mathbf{x}$  pointing into  $\Omega_0$ .

Adopting the approach in [18], a BIE formulation for the velocity at any point  $\mathbf{x} \in \Omega_0$  is given by

$$\mathbf{u}(\mathbf{x}) = \sum_{k=1}^{N_d} \mathbb{S}_{\Gamma_k}[\Delta \mathbf{f}_k](\mathbf{x}) + \beta(\mathbf{x}) + \mathbf{u}^\infty(\mathbf{x}). \quad (7.4)$$

The  $\beta(\mathbf{x})$  term is the contribution from the solid walls. In [12] a double-layer potential over the solid boundaries is combined with a completion flow for each solid obstacle. Numerical

results in three-dimensions [18] suggests that a more numerically stable approach is to use the combined-layer formulation given in [4],

$$\beta[\mathbf{q}](\mathbf{x}) = 2\mathbb{D}_\gamma[\mathbf{q}](\mathbf{x}) + \eta\mathbb{S}_\gamma[\mathbf{q}](\mathbf{x}),$$

where  $\mathbf{q}$  is unknown and called the Hebecker density, and  $\eta \neq 0$  is an arbitrary constant.

To obtain a BIE system we take the limit as  $\mathbf{x} \rightarrow \mathbf{x}_0$ , where  $\mathbf{x}_0$  is a point either on  $\Gamma_k$ ,  $k = 1, \dots, N_d$ , or on  $\gamma$ . To do this, we make use of the jump relations of the single- and double-layer potential,

$$\lim_{\mathbf{x} \rightarrow \mathbf{x}_0 \in \Lambda} \mathbb{S}_\Lambda[\mathbf{g}](\mathbf{x}) = \mathbb{S}_\Lambda[\mathbf{g}](\mathbf{x}_0), \quad (7.5a)$$

$$\lim_{\mathbf{x} \rightarrow \mathbf{x}_0 \in \Lambda} \mathbb{D}_\Lambda[\mathbf{g}](\mathbf{x}) = \frac{1}{2}\mathbf{g}(\mathbf{x}_0) + \mathbb{D}_\Lambda[\mathbf{g}](\mathbf{x}_0). \quad (7.5b)$$

Applying (7.5) to (7.4) and matching to the boundary condition (7.2) yields the BIEs,

$$\mathbf{u}(\mathbf{x}_0) = \beta[\mathbf{q}](\mathbf{x}_0) + \sum_{k=1}^{N_d} \mathbb{S}_{\Gamma_k}[\Delta\mathbf{f}_k](\mathbf{x}_0) + \mathbf{u}^\infty(\mathbf{x}_0), \quad \mathbf{x}_0 \in \Gamma_k, \quad k = 1, \dots, N_d, \quad (7.6a)$$

$$\mathbf{q}(\mathbf{x}_0) + \beta[\mathbf{q}](\mathbf{x}_0) = \sum_{k=1}^{N_d} \mathbb{S}_{\Gamma_k}[\Delta\mathbf{f}_k](\mathbf{x}_0) + \mathbf{u}^\infty(\mathbf{x}_0), \quad \mathbf{x}_0 \in \gamma. \quad (7.6b)$$

Note that  $\mathbf{q}(\mathbf{x}_0)$  and  $\mathbf{u}(\mathbf{x}_0)$  are unknown, however  $\Delta\mathbf{f}_k(\mathbf{x}_0)$  is known from (7.3). The only equation that requires the solution of a linear system is thus (7.6b). Once we have found  $\mathbf{u}(\mathbf{x}_0)$ , for  $\mathbf{x}_0 \in \Gamma_k$ ,  $k = 1, \dots, N_d$ , we can update the position of the interface by evolving the ODE,

$$\frac{d\mathbf{x}_0}{dt} = \mathbf{u}(\mathbf{x}_0), \quad \mathbf{x}_0 \in \Gamma_k, \quad k = 1, \dots, N_d.$$

For details on how this ODE can be numerically evaluated see [9] or [11].

The equation (7.6b), can be written in the abstract form

$$(\mathcal{I} + \beta)\mathbf{q}(\mathbf{x}) = \mathbf{h}(\mathbf{x}), \quad \mathbf{x} \in \gamma, \quad (7.7)$$

where  $\mathcal{I}$  is the identity operator. If  $\gamma$  is  $C^1$  smooth, then  $\beta$  is a compact operator whose eigenvalues accumulate at zero, and (7.7) can be analyzed using Fredholm analysis. In particular, the Fredholm alternative applies and can be used to demonstrate existence and uniqueness of solutions [1].

If however,  $\gamma$  is only Lipschitz smooth, (i.e it is allowed to have corners, but not cusps) then  $\beta$  is no longer compact and Fredholm theory no longer applies. Furthermore, the double-layer operator in  $\beta$  involves the normal vector, which does not exist at corners, meaning that (7.7) does not hold pointwise. Boundary integral equations on Lipschitz domains have been well studied [1], and it can be shown that (7.7) does in fact have a unique solution [16]. At the corners the density function  $\mathbf{q}$  is singular, however it remains possible to evaluate  $\beta[\mathbf{q}](\mathbf{x})$ , for  $\mathbf{x} \in \Omega$ , or  $\mathbf{x} \in \gamma$  provided  $\mathbf{x}$  is not a corner point.

## 7.3 Discretization

It remains to actually compute the solution to (7.7). We will use the Nyström method [1]. If we write  $\beta[\mathbf{q}](\mathbf{x})$  as

$$\beta[\mathbf{q}](\mathbf{x}) = \int_{\gamma} K(\mathbf{x}, \mathbf{y}) \mathbf{q}(\mathbf{y}) \, ds(\mathbf{y}),$$

then we can approximate  $\beta[\mathbf{q}](\mathbf{x})$  as

$$\beta[\mathbf{q}](\mathbf{x}) \approx \sum_{j=1}^N K(\mathbf{x}, \mathbf{y}_j) \mathbf{q}(\mathbf{y}_j) w_j, \quad (7.8)$$

where  $\{\mathbf{y}_j\}_{j=1}^N \in \gamma$  and  $\{w_j\}_{j=1}^N$  are appropriately chosen quadrature nodes and weights respectively. The single-layer operators  $\mathbb{S}_{\Gamma_k}$ ,  $k = 1, \dots, N_d$ , can be similarly discretized. To create a linear system to solve, we will evaluate (7.8) at the target points  $\{\mathbf{y}_i\}_{i=1}^N$  in the reference cell. Then enforcing (7.6b) at the same points yields the linear system

$$\mathbf{q}(\mathbf{y}_i) + \sum_{j=1}^N K(\mathbf{y}_i, \mathbf{y}_j) \mathbf{q}(\mathbf{y}_j) w_j = \sum_{k=1}^N \tilde{\mathbb{S}}_{\Gamma_k} [\Delta \mathbf{f}_k](\mathbf{y}_i) + \mathbf{u}^{\infty}(\mathbf{y}_i), \quad i = 1, \dots, N, \quad (7.9)$$

where  $\tilde{\mathbb{S}}_k$  is the discretized single-layer operator over  $\Gamma_k$ . If  $\gamma$  is at least  $C^1$  smooth, then  $\beta$  is compact, and the matrix in this linear system inherits several properties from the operator  $(\mathcal{I} + \beta)$ . In particular, it is invertible and its eigenvalues accumulate at a point away from zero. From this it follows that the condition number is independent of mesh resolution. It also follows that to solve the linear system the iterative linear solver GMRES is a good choice because the number of GMRES iterations required to reach a given tolerance is also resolution independent [3]. We will use the spectral Ewald method [8] to sum the infinite periodic replicates in  $\mathcal{O}(N \log N)$  operations. Since the number of GMRES iterations needed is constant,  $\mathcal{O}(1)$ , the total number of operations needed to solve (7.9) (provided  $\gamma$  is  $C^1$  smooth) is  $\mathcal{O}(N \log N)$ .

The discretization (7.9) is not easy to evaluate numerically. In particular  $K(\mathbf{y}_i, \mathbf{y}_i)$  is singular, and  $\mathbb{S}_{\Gamma_k} [\Delta \mathbf{f}_k](\mathbf{y}_i)$  can be nearly singular if  $\mathbf{y}_i$  is close  $\Gamma_k$ , as occurs when a drop comes close to a solid wall. In two dimensions the singularity and near singularity can be handled using techniques from [6]. This is explained in detail and demonstrated in [10, 11].

### 7.3.1 RCIP

Near the corners, the Hebecker density function  $\mathbf{q}$  is singular and cannot be accurately integrated with standard Gauss-Legendre quadrature. Custom quadrature rules can be developed [14], however these rules require knowledge of the asymptotics of  $\beta$  near the corner, and to the authors' knowledge no such rules exist for the Stokeslet and stresslet. Additionally, these rules introduce a modest number of additional unknowns. Local refinement, where the panels closest to the corners are dyadically refined  $n_{\text{sub}}$  times (as seen in Figure 7.2), is not numerically stable, and the condition number as well as the number of required GMRES iterations grows as the number of unknowns increases. In practice, for many problems the numerical instability may be quite manageable, and there exist techniques to stabilize the local refinement [2] if necessary, however the increase of the number of unknowns is still undesirable.

An alternative approach, recursively compressed inverse preconditioning (RCIP) [7], can achieve the same accuracy as local refinement without introducing any additional unknowns,

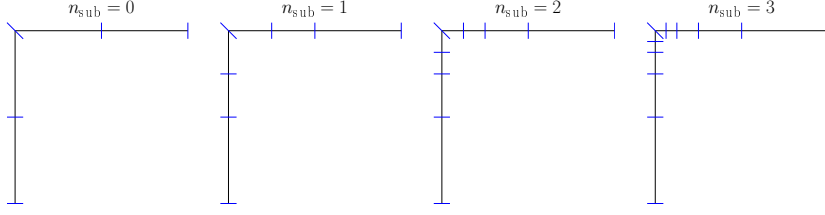


Figure 7.2: Local refinement around a corner. The panel closest to the corner is split dyadically  $n_{\text{sub}}$  times. Each split adds two new panels and  $2n_q$  unknowns. The integrals over each panel are approximated using a  $n_q$  Gauss-Legendre quadrature rule.

while keeping the condition number independent of  $N$ . RCIP relies on the discretization of a transformed density  $\tilde{\mathbf{q}}$  that is piecewise smooth. This transformed density is discretized on two separate meshes: a coarse mesh  $\gamma_{\text{coa}}$  that is sufficient to resolve the geometry and the right hand side, and a fine mesh  $\gamma_{\text{fin}}$  that is heavily refined around the corners. The smoothness of  $\tilde{\mathbf{q}}$  means that we can accurately integrate it using composite Gauss-Legendre quadrature and use accurate polynomial interpolation to restrict/prolong  $\mathbf{q}$  from one mesh to another.

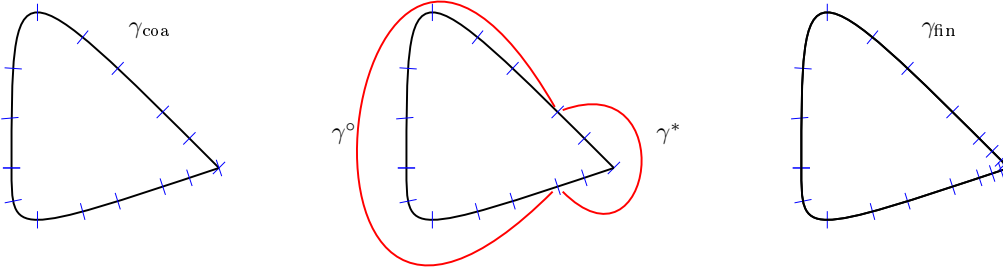


Figure 7.3: Panel based discretization of the geometry. The domain  $\gamma$  is first discretized with a coarse mesh,  $\gamma_{\text{coa}}$ . The two panels on either side of the corner are denoted  $\gamma^*$ , and the remaining panels are denoted  $\gamma^\circ$ . The panels in  $\gamma^*$  closest to the corner are dyadically refined  $n_{\text{sub}}$  times to obtain the fine mesh  $\gamma_{\text{fin}}$ .

To define the transformed density  $\tilde{\mathbf{q}}$ , we begin by writing  $\beta$  as  $\beta = \beta^* + \beta^\circ$ , where  $\beta^*$  contains the kernel interactions near the corners (i.e. both source and target points are in  $\gamma^*$ ), and  $\beta^\circ$  contains the remainder. Note that  $\beta^\circ$  is a compact operator. The transformed density  $\tilde{q}$  is then defined as

$$\tilde{\mathbf{q}}(\mathbf{x}) = (\mathcal{I} + \beta^*)\mathbf{q}(\mathbf{x}).$$

Rewriting (7.7) in terms of  $\tilde{\mathbf{q}}$  and using the split of  $\beta$  described above gives the transformed BIE,

$$(\mathcal{I} + \beta^\circ(\mathcal{I} + \beta^*)^{-1})\tilde{\mathbf{q}}(\mathbf{x}) = \mathbf{h}(\mathbf{x}), \quad \mathbf{x} \in \gamma. \quad (7.10)$$

We can see right away that  $\tilde{\mathbf{q}}$  is piecewise smooth. We know that  $\mathbf{h}(\mathbf{x})$  is smooth, as it does not depend on the geometry of  $\gamma$ . Since  $\beta^\circ$  does not include the corner interactions, it maps a function to one that is smooth around the corner. This leaves the remaining term  $\mathcal{I}\tilde{\mathbf{q}} = \tilde{\mathbf{q}}$ , which by contradiction must be smooth.

To turn (7.10) into a linear system, we apply a Nyström method on  $\gamma_{\text{coa}}$  to obtain  $\mathbf{B}_{\text{coa}}^\circ$ , the discretized  $\beta^\circ$ , and a separate Nyström method on  $\gamma_{\text{fin}}$  to obtain  $\mathbf{B}_{\text{fin}}^*$ , the discretized  $\beta^*$ . The discrete transformed BIE is then

$$(\mathbf{I}_{\text{coa}} + \mathbf{B}_{\text{coa}}^\circ \hat{\mathbf{R}}) \tilde{\mathbf{q}}(\mathbf{y}_i) = \mathbf{h}(\mathbf{y}_i), \quad i = 1, \dots, N, \quad (7.11)$$

where  $\{\mathbf{y}_i\}_{i=1}^N$  are the quadrature nodes on  $\gamma_{\text{coa}}$ . The matrix  $\hat{\mathbf{R}}$  is known as the compressed inverse of  $(\mathbf{I}_{\text{fin}} + \mathbf{B}_{\text{fin}}^*)$ , and is the prolongation of  $(\mathbf{I}_{\text{fin}} + \mathbf{B}_{\text{fin}}^*)^{-1}$  from  $\gamma_{\text{fin}}$  to  $\gamma_{\text{coa}}$ . The matrix  $\mathbf{B}_{\text{fin}}^*$  contains only the interactions between two points near the corner, and thus has the structure

$$\mathbf{B}_{\text{fin}}^* = \begin{pmatrix} \mathbf{0} & \mathbf{0} \\ \mathbf{0} & \mathbf{B}_{\text{fin}}^{**} \end{pmatrix}.$$

Since outside of  $\gamma^*$ ,  $\gamma_{\text{coa}}$  and  $\gamma_{\text{fin}}$  coincide, the matrix  $\hat{\mathbf{R}}$  can be written in block form as

$$\hat{\mathbf{R}} = \begin{pmatrix} \mathbf{I}_{\text{coa}}^\circ & \mathbf{0} \\ \mathbf{0} & \mathbf{R} \end{pmatrix},$$

where  $\mathbf{I}_{\text{coa}}^\circ$  is the identity on  $\gamma_{\text{coa}}^\circ$  and  $\mathbf{R}$  is the compressed inverse of  $(\mathbf{I}_{\text{fin}}^* + \mathbf{B}_{\text{fin}}^{**})$ .

Computing  $\hat{\mathbf{R}}$  could in principle be done by directly computing  $(\mathbf{I}_{\text{fin}} + \mathbf{B}_{\text{fin}}^*)^{-1}$  and then restricting it to  $\gamma_{\text{coa}}$  using high-order composite polynomial interpolation. In practice however, this is not feasible because  $\mathbf{B}_{\text{fin}}^* \in \mathbb{R}^{n \times n}$ , where  $n = n_q(n_{\text{pan}} + 2n_{\text{sub}})$ . Fortunately, a recursion relation exists that allows us to compute  $\hat{\mathbf{R}}$  as the final step in a sequence of four panel problems.

Let  $\gamma_i^*$ ,  $i = 1, \dots, n_{\text{sub}}$ , be subsets of  $\gamma^*$ , with  $\gamma_{i-1}^* \subset \gamma_i^*$  and  $\gamma_{n_{\text{sub}}}^* = \gamma^*$ . With a slight abuse of notation, on each  $\gamma_i^*$ , define a six panel “type-b” mesh,  $\gamma_{ib}^*$  and a four panel “type-c” mesh  $\gamma_{ic}^*$ . Both the type-b and type-c meshes are centered at the corner. These meshes are nested, in the sense that the four panels of  $\gamma_{(i-1)c}^*$  overlap with the inner four panels of  $\gamma_{ib}^*$ . See Figure 7.4.  $\gamma_{1b}^*$  corresponds to the six panels closest to the corner on  $\gamma_{\text{fin}}^*$ , and  $\gamma_{n_{\text{sub}}c}^*$  corresponds to the four panels on  $\gamma_{\text{coa}}$ .

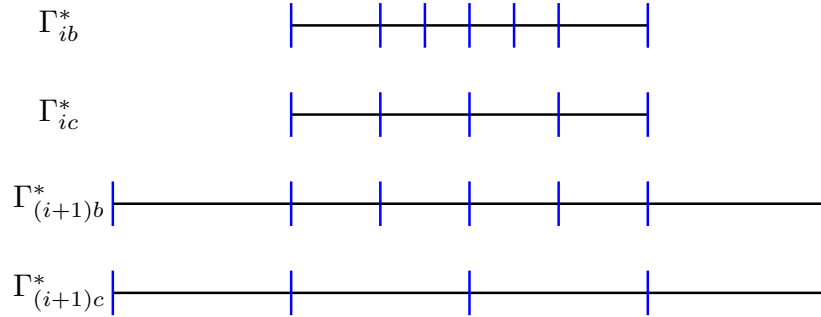


Figure 7.4: Sketch of type-b and type-c meshes in parameter space.

We will need the prolongation matrix  $\mathbf{P}_{bc}$ , which is the  $6n_q \times 4n_q$  matrix that interpolates values from points on  $\gamma_{ic}^*$  to points on  $\gamma_{ib}^*$ . We will also define  $\mathbf{P}_{W_{bc}}$  to be the  $6n_q \times 4n_q$  matrix

$$\mathbf{P}_{W_{bc}} = \mathbf{W}_b \mathbf{P}_{bc} \mathbf{W}_c^{-1},$$

where  $\mathbf{W}_b$  and  $\mathbf{W}_c$  are diagonal matrices containing the (unscaled) quadrature weights on a type-b mesh and a type-c mesh respectively. Both  $\mathbf{P}_{W_{bc}}$  and  $\mathbf{P}_{bc}$  are independent of the level  $i$ .  $\mathbf{P}_{bc}$  can be constructed using standard polynomial interpolation techniques.

Now let  $\mathbf{B}_{ib}$  be the discretization of  $\beta$  on  $\Gamma_{ib}^*$ . We will split  $\mathbf{B}$  as  $\mathbf{B}_{ib}^* + \mathbf{B}_{ib}^\circ$ , where  $\mathbf{B}_{ib}^*$  is the discretization where only the entries whose source and target indices are on the inner four panels are retained and  $\mathbf{B}_{ib}^\circ$  is the remainder. Likewise let  $\mathbf{I}_b^\circ$  be the identity matrix over the left and right outer panels, and zero on the inner four panels.

The recursion relation to compute  $\mathbf{R} = \mathbf{R}_{n_{\text{sub}}}$  is

$$\mathbf{R}_0 = \mathbf{P}_{W_{bc}}^T (\mathbf{I}_b + \mathbf{B}_{1b}) \mathbf{P}_{bc}, \quad (7.12a)$$

$$\mathbf{R}_i = \mathbf{P}_{W_{bc}}^T (\mathbb{F}\{\mathbf{R}_{i-1}^{-1}\} + \mathbf{I}_b^\circ + \mathbf{B}_{ib}^\circ) \mathbf{P}_{bc}, \quad i = 1, \dots, n_{\text{sub}}, \quad (7.12b)$$

where  $\mathbb{F}\{\cdot\}$  zero pads the operator to make it the same size as  $\mathbf{I}_b$ .

Since  $\mathbf{R}_{n_{\text{sub}}} = \mathbf{R}$ , once we run this recursion we have all the information needed for  $\hat{\mathbf{R}}$ . A derivation and more detailed explanations of all the terms in (7.12) is given in [5]. Once we have  $\hat{\mathbf{R}}$  we can solve (7.11) for  $\tilde{\mathbf{q}}$ .

Given  $\tilde{\mathbf{q}}$ , evaluating  $\beta[\mathbf{q}](\mathbf{x})$  can be done by applying the regular quadrature rule on  $\gamma_{\text{coa}}$ ,

$$\beta[\mathbf{q}](\mathbf{x}) = \sum_{i=1}^N \hat{\mathbf{R}} \tilde{\mathbf{q}}_i w_i,$$

defined on  $\gamma_{\text{coa}}$ . Note that  $\hat{\mathbf{R}}$  can be thought of as a way to correct the quadrature weights to account for the fact that  $\mathbf{q}$  is singular near the corner. This quadrature rule is as accurate as if we had the values of  $\mathbf{q}$  on  $\gamma_{\text{fin}}$ .

In addition to having the same accuracy as if we had the density on the fine grid, RCIP preserves one of the key advantages of BIEs. Unline with local refinement, the condition number of the linear system does not grow with  $n_{\text{sub}}$  when using RCIP. The condition number for local refinement and RCIP as a function of  $n_{\text{sub}}$  is shown in Figure 7.5. Recall that in addition to the condition number growing, the size of the linear system is also growing if we are using local refinement, while it remains the same size if we are using RCIP.

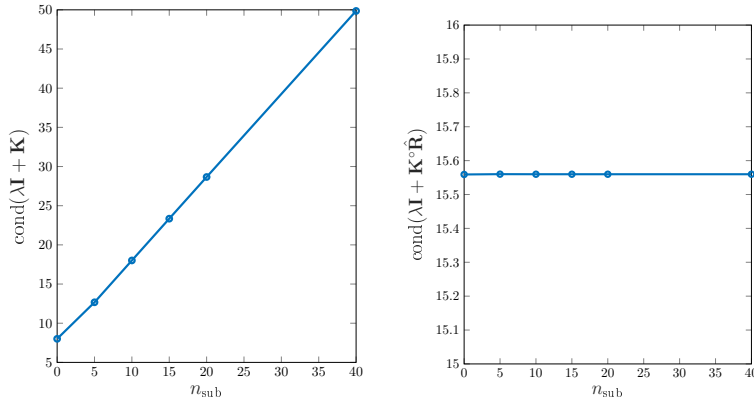


Figure 7.5: Condition number of the linear system as a function of  $n_{\text{sub}}$ . Left: local refinement. Right: RCIP.

## 7.4 Numerical Results

We will demonstrate the performance of this method using two metrics: i) a numerical convergence study, and ii) a demonstration of the conservation of drop area. The second test follows from the fact that as the fluid inside the drop is incompressible, its area must remain fixed. Thus in order for a simulation to be physically realistic, the drop areas should be conserved as we advance the simulation in time (to a level determined by the accuracy of the time stepper).

### 7.4.1 Convergence Study

Analytic results for drop simulations are difficult to come by. A conformal mapping based approach for two bubbles in an unbounded extensional flow is used to validate the model in [11]. Since we are looking at periodic geometries, such test cases are more difficult to construct. Another standard convergence study, the method of manufactured solutions, does not readily apply to boundary integral equations because by prescribing an exact solution, the right hand side becomes inhomogenous.

Instead we will perform a numerical self-convergence study, i.e. comparing the drop movements at various spatial resolutions, and demonstrating that they converge to a high resolution simulation. Figure 7.6 shows snapshots of a simulation of a drop moving past an obstacle with a corner. The drop is discretized such that an equal spacing between discretization points  $\Delta s$  is maintained even as the drop stretches, see [10, 11]. The solid is discretized with the same number of points as the drop at  $t = 0$ . The simulation is run multiple times for different values of  $\Delta s$ , and at the time horizon, the positions of the discretization points are interpolated to a grid with the same number of points as the reference solution. The  $\ell_\infty$  error of the discretization points at the time horizon is plotted on the left in Figure 7.7. We see that without RCIP, the  $\ell_\infty$  error decreases very slowly, but with  $n_{\text{sub}} = 60$  and RCIP, the  $\ell_\infty$  error decreases very quickly before leveling off around  $10^{-10}$ . The remaining error is dominated by time-stepping error.

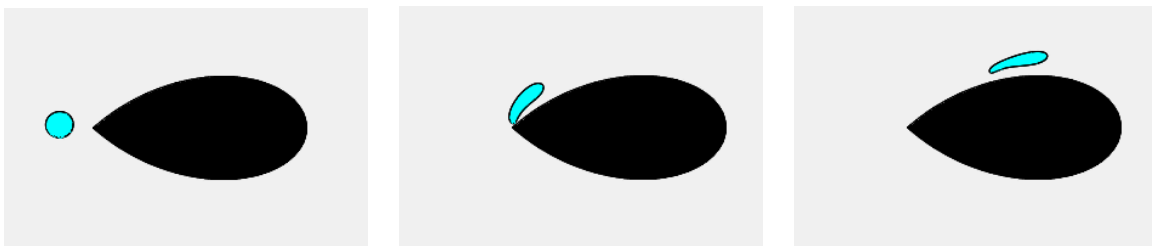


Figure 7.6: Snapshots of a simulation of a drop moving past an obstacle with a corner. This simulation is doubly periodic, but only part of the reference cell is shown.

### 7.4.2 Area Conservation

As mentioned above, the area of each drop should remain constant as the simulation advances in time. Since nothing in our method enforces this as an explicit constraint, due to numerical errors in both the spatial and the temporal discretization, the actual drop areas will vary slightly each time step. This is in practice not necessarily a bad thing, as it gives us an easy to compute way to determine one measure of accuracy for our simulation.

The right plot in Figure 7.7 shows the error in the drop area for the simulation in Figure 7.6 at the time horizon as a function of  $\Delta s$ . If RCIP is not used, the error in the area decreases

with  $\Delta s$ , however it remains much larger than if we use RCIP. With RCIP the error in the area stays below  $10^{-8}$  for all  $\Delta s$ . The spatial error in this case is dominated by the time-stepping error.

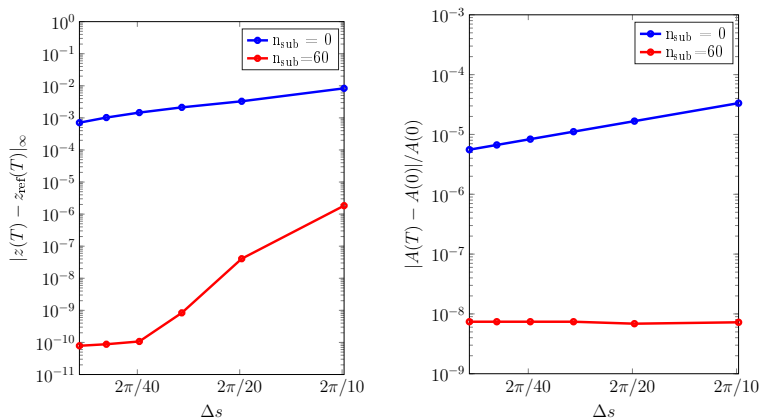


Figure 7.7: Left: convergence study comparing a simulation at various discretization levels to a reference solution computed on a very fine grid. Right: errors in the drop area as a function of  $\Delta s$ . Both tests are for the simulation shown in Figure 7.6

Figure 7.8 shows snapshots of a more complicated example involving multiple drops confined in a channel with a corner. The error in the total drop area at the time horizon is below  $10^{-8}$ .

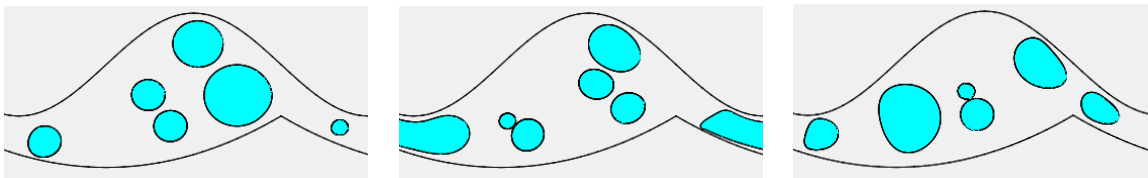


Figure 7.8: Snapshots of simulation of multiple drops in a confined channel. This simulation is periodic, but only the reference cell is shown. The error in the total drop area at the time horizon is below  $10^{-8}$ .

## 7.5 Conclusion

A BIE model to simulate drop movement around a sharp corner has been demonstrated. Previous BIE models of wall-confined drops were restricted to smooth walls because of the excessive refinement needed to accurately resolve walls with sharp corners. By using a technique known as RCIP, we are able to accurately simulate drop movement near sharp corners without introducing any additional unknowns. Combined with accurate quadrature, high order adaptive time stepping, and fast-summation techniques, this provides a highly accurate, computationally

competitive method capable of simulating very complicated flows.

## References

- [1] Atkinson, K.: *The Numerical Solution of Integral Equations of the Second Kind*. Cambridge University Press, Cambridge (1997).
- [2] Bremer, J.: On the Nyström discretization of integral equations on planar curves with corners, *App. & Comp. Harmonic Anal.* **32** (2012), 45-64.
- [3] Campbell, S. L., Ipsen, I. C. F., Kelley, C. T., Meyer, C. T., Xue. Z. Q., Convergence estimates for solution of integral equations with GMRES. *J. Integral Equ. & Appl.* **8** (1996), 19-34.
- [4] Hebeker, F.: Efficient boundary element methods for three-dimensional exterior viscous flow, *Num. Meth. PDEs.* **2** (1986), 273-297.
- [5] Helsing, J.: Solving integral equations on piecewise smooth boundaries using the RCIP method: a tutorial. (2018).
- [6] Helsing, J. and Ojala, R.: On the evaluation of layer potentials close to their sources, *J. Comput. Phys.* **227** (2008), 2899-2921.
- [7] Helsing, J. and Ojala, R.: Corner singularities for elliptic problems: Integral equations, graded meshes, quadrature, and compressed inverse preconditioning, *J. Comput. Phys.* **227** (2008), 8820-8840.
- [8] Lindbo, D. Tornberg, A. K., Spectrally accurate fast periodic summation for periodic Stokes potentials. *J. Comput. Phys.* **229** (2010), 8994-9010.
- [9] Pålsson, S., Sorgentone, C. and Tornberg A.K.: Adaptive time-stepping for surfactant laden drops, in *Proceedings of the 11th UK Conference on Boundary Integral Methods*, Nottingham Trent University Press, (2017), 161-171.
- [10] Pålsson, S., Siegel, M. and Tornberg A.K.: Simulation and validation of surfactant-laden drops in two-dimensional Stokes flow. *J. Comput. Phys.* **386** (2019), 218-247.
- [11] Pålsson, S., Ojala, R. and Tornberg, A.K.: An integral equation method to simulate surfactant-covered droplets deforming in wall-bounded Stokes-flow. In preparation (2019).
- [12] Power, H. and Miranda G.: Second Kind Integral Equation Formulation of Stokes Flow Past a Particle of Arbitrary Shape, *SIAM J. App. Math.* **47** (1987), 689-698.
- [13] Pozrikidis, C.: *Boundary Integral and Singularity Methods for Linearized Viscous Flow*. Cambridge University Press, Cambridge (1992).

- [14] Rachh, M. and Serkh, K.: On the solution of Stokes equation on regions with corners. (2017).
- [15] Sorgentone, C., Tornberg, A.K.: A highly accurate boundary integral equation method for surfactant-laden drops in 3D, *J. Compt. Phys.* **360** (2018), 167-191.
- [16] Verchota, G.: Layer potentials and boundary value problems for Laplace's equation in Lipschitz domains, *J. Func. Anal.* **59** (1983), 572-611.
- [17] Zhang, Z., Xu, J. and Drapaca, C.: Particle squeezing in narrow confinements. *Microfluidics and Nanofluidics* **22** (2018).
- [18] Zinchenko, A. and Davis, R.: A boundary-integral study of a drop squeezing through interparticle constrictions, *J. Fluid Mech.* **564** (2006), 227-266.

## Chapter 8

# BEM for Low Reynolds Number Flow Past a Steady Circular Cylinder in an Unbounded Domain

B.C. Dang<sup>1,2</sup>, E.A. Chadwick<sup>1</sup>

- <sup>1</sup> School of Computing, Science and Engineering  
University of Salford  
Greater Manchester  
M5 4WT, United Kingdom.
- <sup>2</sup> Department of Mathematics  
Faculty of Natural Sciences  
University of Jos  
PMB 2084, Jos Plateau State, Nigeria.

---

**Abstract.** Consider a two dimensional steady low Reynolds number flow past a circular cylinder. The theoretical treatment in Chadwick [1] is detailed and elaborated. A Boundary Integral representation that matches an outer Oseen flow and inner Stokes flow is given, and the matching error is shown to be smallest when the outer domain is as close as possible to the body. Also, it is shown that as the Green's function is approached, the oseenlet becomes the stokeslet to leading order and has the same order of magnitude error as the matching error. This means a novel Boundary Integral representation in terms of oseenlets is possible. To test this, we have developed a corresponding Boundary Element code that uses point collocation weighting functions, linear shape functions, two-point Gaussian quadrature with analytic removal of the Green's function singularity for the integrations. We compare against various methods for the benchmark problem of flow past a circular cylinder. The other methods are: representations using stokeslets (that suffer from Stokes' paradox giving an unbounded velocity); Lamb's [9] treatment; Yano and Kieda's Oseen flow treatment [17]; and the matched asymptotic formulation of Kaplun [7]. In particular we use the drag coefficient for the comparison. The advantage of this method over existing ones is demonstrated and discussed.

---

## 8.1 Introduction

The Boundary Element Method can be traced back to the 1960's [2], its numerical implementation was made robust with the advent of computers that aid solving sets of integral equations. Although not a requirement for an integral formulation of a partial differential equation, a Green's function within a Boundary Integral Method (BIM) [4] has advantages. For example, the formulation is expressed on the boundary and so has one dimension less than the domain. With the development of quadratures and stable discretisation, the evaluation of integrals becomes more accurate and efficient.

Studies of slow motion of viscous fluid flow past a body in an unbounded domain dates back to the work of Stokes in 1851 [14]. Because of the difficulty in satisfying boundary conditions both at the cylinder surface and the far-field, Stokes draws a conclusion that such a solution does not exist and this hypothesis was later termed Stokes' paradox. Several analytical studies began to emanate, seeking solution to the Stokes' paradox and this include the approximation given by Oseen [11] solved approximately by Lamb [8], [9], and Imai [6]. However, Oseen's approximation assumes linearisation to the free stream velocity which breaks down on the body boundary. To overcome this, the method of matched asymptotic expansions was presented by Proudman and Pearson [13] and Kaplun [7] and it combines linearisation to Stokes flow in the near-field matched to linearisation to Oseen flow in the far-field region. Experimental studies [16] with different qualitative and quantitative results have also been presented, in particular for the benchmark problem of steady flow past a circular cylinder.

Further to different numerical methods used, Yano and Kieda [17] applied a discrete singularity method to solve a two-dimensional flow by distributing oseenlets, sources, sinks and vortices in the interior of an obstacle with a least square criterion to satisfy the boundary condition. Their result was benchmarked against the analytic results of Lamb [9], Kaplun [7] and the experiment of Tritton [16] for the drag coefficient. It was revealed that when the Reynolds number is below one ( $Re < 1$ ), there is good agreement, but when the Reynolds number is in the range 1 to 4, the analytical results do not align very close with experiment except the numerical studies presented by Yano and Kieda [17]. The analytical results work well for body surfaces with simple geometries, but as soon as the geometry becomes complicated, numerical approaches provide better basis for analysis. To apply to more complicated geometries, Lee and Leal [10] considered a matched asymptotic expansion method that used Green's integral representations of the velocity. Chadwick [1] takes this approach and matched Stokes and Oseen flow within a boundary integral formulation. It was found that the error is least if the matching boundary is on the body itself. Here, it is noted that this approach does not break down on the body boundary because in the formulation the oseenlet approximates to the stokeslet.

In this paper, the above mentioned approach in Chadwick [1] is tested by developing a Boundary Element Method using point collocation weighting functions, linear shape functions, two-point Gaussian quadrature with analytic removal of the Green's function singularity for the integrations. The Green's integral representation of oseenlets are distributed over the boundary surface. The Boundary Element Method in this study compares favourably with Tritton experiment [16], analytical results of Lamb [9], Kaplun [7], Tomotika [15] and the numerical results of Yano and Kieda [17] for the drag coefficient. Hence, our method is simple, yet robust in solving steady two-dimensional flow past a circular cylinder in an unbounded domain.

## 8.2 Formulation of Governing Equations

The motion of any continuous fluid is governed by the Navier-Stokes equation, and for a creeping flow, a linearisation of the Navier-Stokes equation yields Stokes and Oseen equation which govern a viscous fluid. Hence, away from a body surface the Oseen equation governs the flow in an outer region, see figure 8.1a given by

$$\rho U \frac{\partial u_i}{\partial x_1} = -\frac{\partial p}{\partial x_i} + \mu \frac{\partial^2 u_i}{\partial x_j \partial x_j} + f_i \quad (8.1)$$

$$\frac{\partial u_i}{\partial x_i} = 0 \quad (8.2)$$

where (8.2) is the continuity equation,  $\rho$  is the density of the fluid,  $u_i$  is the velocity,  $p$  is the pressure,  $\mu$  is the viscosity,  $U$  is the uniform stream velocity and  $f_i$  is the applied force. Similarly, near the body Stokes equation governs the flow in an inner region, see figure 8.1b given by

$$0 = -\frac{\partial p}{\partial x_i} + \mu \frac{\partial^2 u_i}{\partial x_j \partial x_j} + f_i \quad (8.3)$$

$$\frac{\partial u_i}{\partial x_i} = 0 \quad (8.4)$$

The viscous forces in (8.3) are dominant over the inertial forces, and by dimensionless analysis, the dimensionless Reynolds number tends to zero near the body with length dimension  $l$  and  $Re = \frac{\rho U l}{\mu} \rightarrow 0$ . To apply the Green's integral, it is supposed that an external force is exerted by the body on the fluid such that the applied force is  $f_i$ .

The work of Chadwick [1] considers a matched near-field region using Stokes flow and the far-field using Oseen flow. The common boundary where the matching takes effect, has  $L$  as the length dimension of the matched region and it is seen that  $Re \frac{L}{l}$  is the error. So the error is reduced by choosing  $L = l$ , and Oseen flow assumed everywhere in the flow field, as shown in section 8.4.

## 8.3 Green's Function for Oseen and Stokes Equation

The oseenlet is the Green's function of the Oseen equation. In the limit as the Reynolds number tends to zero, the oseenlet approximates to the stokeslet which is the Green's function of the Stokes equation. The drag and lift oseenlet are

$$u_i^{(1)} = \frac{1}{2\pi\rho U} \left( \frac{\partial}{\partial x_i} \left( \ln r + e^{kx_1} K_0(kr) \right) - 2ke^{kx_1} K_0(kr) \delta_{i1} \right), \quad p^{(1)} = -\frac{1}{2\pi} \frac{\partial}{\partial x_1} (\ln r) \quad (8.5)$$

and

$$u_i^{(2)} = \frac{1}{2\pi\rho U} \varepsilon_{ij3} \frac{\partial}{\partial x_j} \left( \ln r + e^{kx_1} K_0(kr) \right), \quad p^{(2)} = -\frac{1}{2\pi} \frac{\partial}{\partial x_2} (\ln r) \quad (8.6)$$

where  $K_0$  is the modified Bessel function of order zero and  $k = \frac{\rho U}{2\mu}$ , also  $\varepsilon_{ijk} = 1$  for  $(i, j, k) = (1, 2, 3), (2, 3, 1), (3, 1, 2)$ ,  $\varepsilon_{ijk} = -1$  for  $(i, j, k) = (1, 3, 2), (2, 1, 3), (3, 2, 1)$ ,  $\varepsilon_{ijk} = 0$  otherwise and  $\delta_{ij}$  is Kronecker delta such that  $\delta_{ij} = 1$  for  $i = j$  and  $\delta_{ij} = 0$  for  $i \neq j$ .

To obtain the stokeslet from the oseenlet, consider  $kr \rightarrow 0$ ,  $e^{kx_1} = 1 + kx_1 + O(k^2r^2)$  and  $K_0(kr) = -\ln r + O(r^2 \ln r)$ . This will yield the drag and lift stokeslet respectively given as

$$u_i^{(1)} = \frac{1}{4\pi\mu} \left( \delta_{i1} \ln r - \frac{x_1 x_i}{r^2} \right) (1 + O(kr)), \quad p^{(1)} = -\frac{1}{2\pi} \frac{x_1}{r^2} \quad (8.7)$$

and

$$u_i^{(2)} = \frac{1}{4\pi\mu} \left( \delta_{i2} \ln r - \frac{x_2 x_i}{r^2} \right) (1 + O(kr)) + C_i, \quad p^{(2)} = -\frac{1}{2\pi} \frac{x_2}{r^2} \quad (8.8)$$

where  $C_i = \frac{\delta_{i2}}{4\pi\mu}$ . Thus, up to order  $kr$  and a constant, the two-dimensional stokeslet is given by

$$u_i^{(m)} = \frac{1}{4\pi\mu} \left( \delta_{im} \ln r - \frac{x_m x_i}{r^2} \right) (1 + O(kr)) + C_i^{(m)}, \quad p^{(m)} = -\frac{1}{2\pi} \frac{x_m}{r^2} \quad (8.9)$$

where  $C_i^{(m)} = \frac{\delta_{i2} \delta_{m2}}{4\pi\mu}$ .

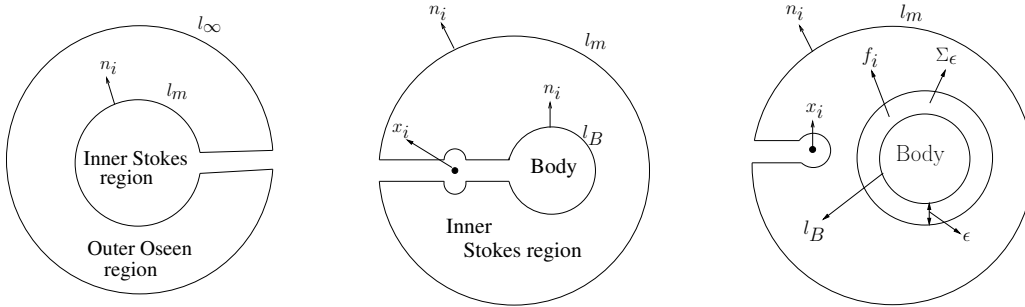
## 8.4 Green's Integral Formulation

### 8.4.1 Outer Region

Consider the space  $\Sigma$  enclosed by the boundary around and approaching the point  $x_i$ , the body boundary  $l_B$ , and the boundary on the far-field tending to an infinite distance away  $l_\infty$ , see figure 8.1. The Green's integral formulation for the Oseen flow [12] can be found by considering the integral,

$$\begin{aligned} & \int_{\Sigma} \left( -\rho U \frac{\partial u_i^{(m)}(z)}{\partial y_1} - \frac{\partial p^{(m)}(z)}{\partial y_i} - \mu \frac{\partial^2 u_i^{(m)}(z)}{\partial y_j \partial y_j} + f_i^{(m)}(z) \right) u_i(y) d\Sigma \\ & + \int_{\Sigma} \left( -\rho U \frac{\partial u_i(y)}{\partial y_1} - \frac{\partial p(y)}{\partial y_i} + \mu \frac{\partial^2 u_i(y)}{\partial y_j \partial y_j} - f_i(y) \right) u_i^{(m)}(z) d\Sigma = 0 \end{aligned} \quad (8.10)$$

where  $y_i$  is a vector position of the exterior domain integrated space  $\Sigma$ , and in this case an area integral, and  $z_i = x_i - y_i$ , so the differential equation for the Green's functions satisfies the conjugate Oseen equation since  $\frac{\partial}{\partial y_j} = -\frac{\partial}{\partial x_j}$  and  $f_i^{(m)}(z) = \delta(z) \delta_{im}$  where  $\delta(z)$  is the Dirac delta function.



(a) Green's integral representation for outer Oseen flow (b) Green's integral representation of inner Stokes flow (c) Spatial distribution of point sources

Figure 8.1: Green's integral representation of a body in a near-field and far-field region

In the outer region, there is no body force so  $f_i = 0$  and the point  $x_i$  is in the inner region, so there is no contribution  $f_i^{(m)}(z)$  around the point  $x_i$ . Rearranging (8.10) then gives

$$\begin{aligned}
0 &= \int_{\Sigma} -\rho U \frac{\partial}{\partial y_1} \left( u_i^{(m)}(z) u_i(y) \right) d\Sigma \\
&\quad - \int_{\Sigma} \frac{\partial}{\partial y_i} \left( p^{(m)}(z) u_i(y) + p(y) u^{(m)}(z) \right) d\Sigma \\
&\quad + \int_{\Sigma} - \left( \mu \frac{\partial}{\partial y_j} \left( \frac{\partial u_i^{(m)}(z)}{\partial y_j} u_i(y) \right) + \mu \frac{\partial}{\partial y_j} \left( \frac{\partial u_i(y)}{\partial y_j} u_i^{(m)}(z) \right) \right) d\Sigma .
\end{aligned} \tag{8.11}$$

From the continuity equation (8.2), it can be seen that  $\mu \frac{\partial u_i^{(m)}}{\partial y_j} \frac{\partial u_i}{\partial y_j}$  cancel out in (8.11) from applying the divergence theorem. This then gives the Oseen's integral representation as

$$\begin{aligned}
0 &= \int_{l_m} \left( \rho U u_i^{(m)}(z) u_i(y) n_1 + \left( p^{(m)}(z) u_i(y) + p(y) u_i^{(m)}(z) \right) n_i \right) dl \\
&\quad + \int_{l_m} \mu \left( \frac{\partial u_i^{(m)}(z)}{\partial y_j} u_i(y) - \frac{\partial u_i(y)}{\partial y_j} u_i^{(m)}(z) \right) n_j dl
\end{aligned} \tag{8.12}$$

where  $l_m$  is the matching boundary. From Fishwick and Chadwick [3] the far field integral bounding the exterior domain  $\Sigma$  in the Oseen representation is zero, where the boundary of the domain in two-dimension is a closed curve.

### 8.4.2 Inner Region

The same approach used in the preceding section can be applied to give the Green's integral representation for the inner Stokes flow over a different domain integral, see figure 8.1b. Again there is no body force, so  $f_i = 0$ , but there is a contribution around the point  $x_i$ . Evaluating the Green's function force term in (8.10) gives

$$- \int_{\Sigma} f_i^{(m)}(z) u_i(y) d\Sigma = - \int_{\Sigma} \delta(z) \delta_{im} u_i(y) d\Sigma = -u_m(x) .$$

Rearranging and simplifying then gives

$$\begin{aligned}
-u_m(x) &= \int_{\Sigma} -\rho U \frac{\partial}{\partial y_1} \left( u_i^{(m)}(z) u_i(y) \frac{\partial}{\partial y_i} \left( p^{(m)}(z) u_i(y) + p(y) u^{(m)}(z) \right) \right) d\Sigma \\
&\quad + \int_{\Sigma} -\mu \frac{\partial}{\partial y_j} \left( \left( \frac{\partial u_i^{(m)}(z)}{\partial y_j} u_i(y) \right) + \left( \frac{\partial u_i(y)}{\partial y_j} u_i^{(m)}(z) \right) \right) d\Sigma .
\end{aligned}$$

Finally, applying the divergence theorem to the space in figure 8.1b gives the boundary integral representation

$$\begin{aligned}
u_m^s(x) = & - \int_{l_B} \left( p^{(m)s}(z)u_i^s(y) + p^s(y)u_i^{(m)s}(z) \right) n_i dl \\
& - \int_{l_B} \mu \left( \frac{\partial u_i^{(m)s}(z)}{\partial y_j} u_i^s(y) - \frac{\partial u_i^s(y)}{\partial y_j} u_i^{(m)s}(z) \right) n_j dl \\
& + \int_{l_m} \left( p^{(m)s}(z)u_i^s(y) + p^s(y)u_i^{(m)s}(z) \right) n_i dl \\
& + \int_{l_m} \mu \left( \frac{\partial u_i^{(m)s}(z)}{\partial y_j} u_i^s(y) - \frac{\partial u_i^s(y)}{\partial y_j} u_i^{(m)s}(z) \right) n_j dl .
\end{aligned} \tag{8.13}$$

### 8.4.3 Matching Inner and Outer region

Here the inner and outer region are matched using equation (8.13) and (8.12), an error introduced as a result of the matching is giving next. In two-dimensions, the constant term  $C_i^{(m)}$  give the leading order approximation to the velocity oseenlet  $(1 + O(\frac{1}{\ln kr})) = \left(1 + O\left(\frac{1}{\ln Re \frac{L}{l}}\right)\right)$  on the matching boundary where  $r = O(L)$ . Hence, the matching integral in (8.13) is

$$\begin{aligned}
& \int_{l_m} \left( p^{(m)s}(z)u_i^s(y) + p^s(y)u_i^{(m)s}(z) \right) n_i dl + \int_{l_m} \mu \left( \frac{\partial u_i^{(m)s}(z)}{\partial y_j} u_i^s(y) - \frac{\partial u_i^s(y)}{\partial y_j} u_i^{(m)s}(z) \right) n_j dl \\
& \times \left( 1 + O\left(\frac{1}{\ln Re \frac{L}{l}}\right) \right) = - \int_{l_m} \left( \rho U u_i^{(m)}(z)u_i(y)n_1 + \left( p^{(m)}(z)u_i(y) + p(y)u_i^{(m)}(z) \right) n_i \right) dl \\
& + \int_{l_m} \mu \left( \frac{\partial u_i^{(m)}(z)}{\partial y_j} u_i(y) - \frac{\partial u_i(y)}{\partial y_j} u_i^{(m)}(z) \right) n_j dl = 0
\end{aligned} \tag{8.14}$$

So, to make the error as small as possible, we let  $L = l$  and consider Oseen flow everywhere in the flow field.

## 8.5 Green's Integral for the Boundary Element Method

Now consider the space  $\Sigma$  enclosed by the boundary around the body boundary  $l_B$ , and the boundary on the far-field an infinite distance away  $l_\infty$ . The body is represented by a distribution of forces  $f_i$  in the region  $\Sigma_\epsilon$  which is a distance  $\epsilon$  away from the body boundary  $l_B$ , see figure

8.1 and (8.12) then becomes (up to the error in the matching (8.14))

$$\begin{aligned}
\int_{\Sigma} \left( -f_i^{(m)}(z)u_i(y) + f_i(y)u_i^{(m)}(z) \right) d\Sigma &= \int_{\Sigma} -\rho U \frac{\partial}{\partial y_1} \left( u_i^{(m)}(z)u_i(y) \right) d\Sigma \\
&\quad - \int_{\Sigma} \frac{\partial}{\partial y_i} \left( p^{(m)}(z)u_i(y) + p(y)u^{(m)}(z) \right) d\Sigma \\
&\quad - \int_{\Sigma} \left( \mu \frac{\partial}{\partial y_j} \left( \frac{\partial u^{(m)}(z)}{\partial y_j} u_i(y) \right) + \mu \frac{\partial}{\partial y_j} \left( \frac{\partial u_i(y)}{\partial y_j} u_i^{(m)}(z) \right) \right) d\Sigma \quad (8.15) \\
&= \int_{l_{\infty}} \left( \rho U u_i^{(m)}(z)u_i(y)n_1 + \left( p^{(m)}(z)u_i(y) + p(y)u_i^{(m)}(z) \right) n_i \right) dl \\
&\quad - \int_{l_{\infty}} \mu \left( \frac{\partial u_i^{(m)}(z)}{\partial y_j} u_i(y) - \frac{\partial u_i(y)}{\partial y_j} u_i^{(m)}(z) \right) n_j dl = 0 \quad .
\end{aligned}$$

We let

$$\int_{\Sigma_{\epsilon}} f_i(y)u_i^{(m)}(z)d\Sigma = \int_{l_B} F_i(y)u_i^{(m)}(z)dl \quad (8.16)$$

on the body boundary so that as  $\epsilon \rightarrow 0$ , it gives the force on the body as

$$F_i(y) = \lim_{\epsilon \rightarrow 0} \int_0^{\epsilon} f_i(y)d\epsilon \quad . \quad (8.17)$$

Therefore,

$$\begin{aligned}
u_m &= \int_{\Sigma} \left( -f_i^{(m)}(z)u_i(y) + f_i(y)u_i^{(m)}(z) \right) d\Sigma \\
&= \int_{\Sigma_{\epsilon}} f_i(y)u_i^{(m)}(z)d\Sigma \quad (8.18)
\end{aligned}$$

Hence,

$$u_m(x) = \int_{l_B} F_i(y)u_m^{(i)}dl \quad (8.19)$$

because by symmetry,  $u_i^{(m)} = u_m^{(i)}$  from (8.5) and (8.6).

To proceed with the numerical method, (8.19) is discretised in the Boundary Element Method given next.

## 8.6 Numerical Method

In the preceding section, the oseenlet is derived and given in (8.19) for a two-dimensional flow satisfying the Oseen equation for the far-field region and it was also shown above that in the matched region the oseenlet becomes the stokeslet. We shall compute the drag experienced by a circular cylinder in a steady flow in an unbounded domain. To do this, (8.19) is discretised using the Boundary Element Method with a point collocation weighting function as seen in figure 8.2a, where  $x_{\alpha i}$  is the position  $x_i$  of node  $\alpha$ , the two nodal points are given by  $x_{\alpha i}$  and  $x_{\alpha i+1}$  while the midpoint between them is the collocation point. We have chosen the collocation point not to lie on the nodes so that the Green's function singularity in the integral is more easily removed, because the singularity lies wholly within the element integration rather than divided across two

elements. For ease of numerical formulation, the boundary is approximated by a linear rather than a curved variation, but as the number of nodes are increased the collocation points will move closer to the boundary and so this is not expected to be a problem.

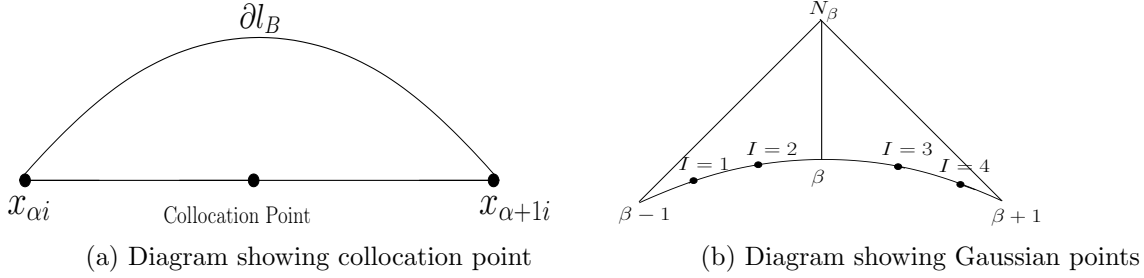


Figure 8.2: Figure showing the nodal points and Gaussian points used for collocation

In figure 8.2b, a two-point Gaussian quadrature is shown with Gaussian points  $I = 1, 2$  for the integral from node  $\beta - 1$  to  $\beta$ , and  $I = 3, 4$  for the integral from node  $\beta$  to  $\beta + 1$ ,  $N_\beta$  is the linear shape function at node  $\beta$  and  $gpw_I$  is the Gaussian point weight at point  $I$ . Hence (8.19) now becomes

$$\begin{aligned} u_i(x) &= \int_{l_B} N_\beta f_{\beta j} u_i^{(j)} dl \\ &= f_{\beta j} N_{\beta j} u_{ijI} gpw_I \end{aligned} \quad (8.20)$$

where there are implied summations over  $1 \leq \beta \leq n$  (for  $n$  nodes), over  $1 \leq I \leq 4$  (for Gaussian points associated with node  $\beta$ , see figure 8.2), and over  $1 \leq j \leq 2$  (for spatial dimension).

Also,  $u_{ijI}$  is the value of the oseenlet Green's function  $u_i^{(j)}$  positioned at the Gaussian point  $I$  of node  $\beta$ , and determined at the node  $\alpha$ . Hence, this collocation point method transforms the integral equation into a linear system of algebraic equations with a no slip boundary condition yielding

$$\mathbf{A}\mathbf{f} = \mathbf{Y} \quad (8.21)$$

where  $\mathbf{A}$  is a  $2n \times 2n$  matrix,  $\mathbf{f}$  is the force coefficient and  $\mathbf{Y}$  is an  $n$  dimensional vector given by applying the boundary condition.

### 8.6.1 Discussion of Results

The drag coefficient  $C_D$  from the Boundary Element Method presented in this study is compared against results of Lamb [9] (8.22), Tomotika [15] (8.23), Kaplun [7] (8.24), experimental results of Tritton [16] and Yano and Kieda [17] numerical results, all these for a Reynolds number  $Re$  ranging between 0 and 4, see figure 8.4. The approximation of the drag coefficients for the various listed results are

$$\text{Lamb: } C_D = \frac{4\pi}{ReT_1} \quad (8.22)$$

$$\text{Tomotika: } C_D = \frac{4\pi}{ReT_1} (1 - T_2) \quad (8.23)$$

$$\text{Kaplun: } C_D = \frac{4\pi}{ReT_1} (1 - 0.87T_1^{-2}) \quad (8.24)$$

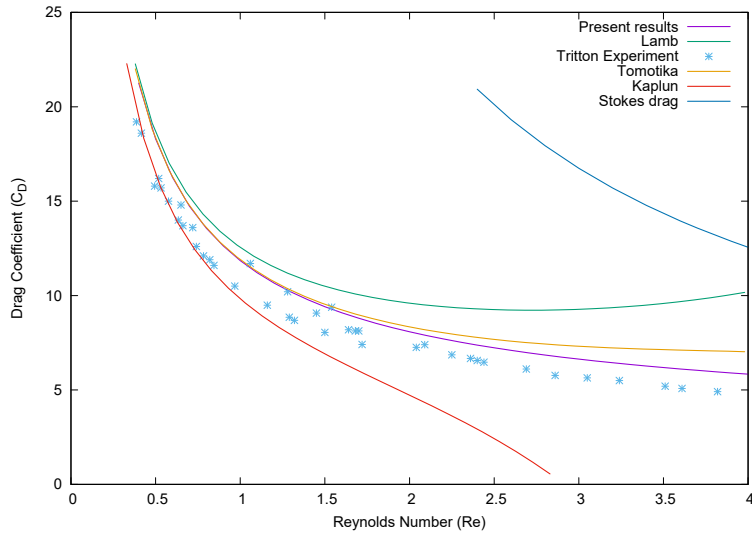


Figure 8.4: Drag coefficient  $C_D$  are plotted against the Reynolds number ( $0 < Re < 4$ )

where the Reynolds number  $Re$  is defined by  $Re = \frac{aU}{\nu}$ , with  $a$  as the cylinder radius, and  $\nu = \frac{\mu}{\rho}$  is the kinematic viscosity with  $\mu$  as the dynamic viscosity of the ambient fluid. The parameter  $T_1 = \left(\frac{1}{2} - \gamma - \log \frac{Re}{4}\right)^{-1}$ , with  $\gamma = 0.577216\dots$  is the Euler constant.

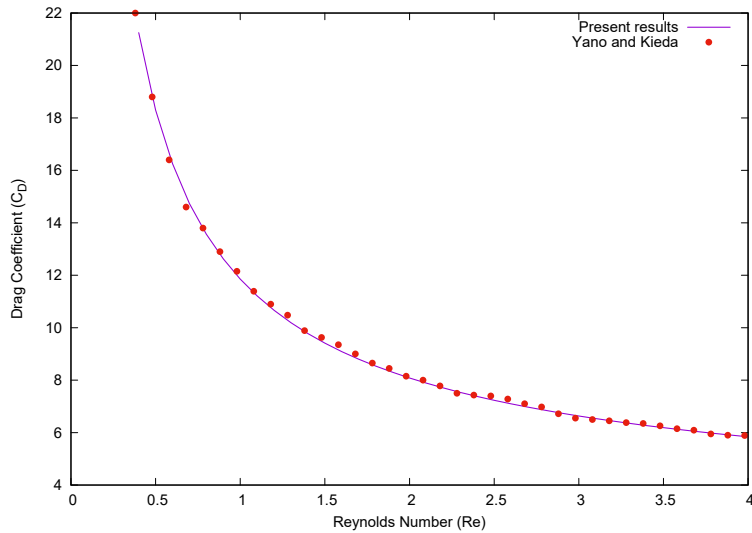


Figure 8.3: Comparing present result with Yano and Kieda [17]

This figure 8.3 shows that our results are aligned almost exactly with the discrete singularity numerical results of Yano and Kieda [17]. In figure 8.4, the drag coefficient is plotted against the Reynolds number, Stokes' drag coefficient is shown to vary significantly, Lamb's [9] and Kaplun's [7] vary increasingly as the Reynolds number is increased beyond 1, and our results together with Yano and Kieda [17] give the closest match to Tritton's experiment [16]. The Stokes drag shows clearly that the velocity diverges when considering a 2D flow past a circular cylinder in an unbounded domain as expected from Stokes paradox. Meanwhile in figure 8.3, present result

is compared with the discrete singularity numerical results of Yano and Kieda [17] and it shows good agreement.

## 8.7 Conclusion and Future Work

A Boundary Element Method for solving a two-dimensional steady flow past a circular cylinder has been presented. Our results agree against the other benchmark results and are an improvement at the higher Reynolds number range up to 4. So our representation gives a good description of the flow field even outside the low-Reynolds number region of  $Re < 1$ . In particular, it gives better results than the matched asymptotic method of Kaplun [7]. The present result is also able to deal with complicated geometries. For future work, we shall consider extending this to use an elliptical cross-sectional body and compare it with the the matched asymptotic expansion of Proudman and Pearson [13] and Lee and Leal [10]. Finally we will apply it to manoeuvring bodies such as swimming organism with applications to micro robotics.

## References

- [1] Chadwick, E.A.: The Far-field Green's Integral in Stokes Flow from the Boundary Integral Formulation. *CMES*. **96(3)**, (2013) 177-184.
- [2] Cheng, A.H-D. and Cheng, D.T.: Heritage and early history of the boundary element method. *Engineering Analysis with Boundary Elements* **29(3)** (2005), 268-302.
- [3] Fishwick, N. and Chadwick, E.: The evaluation of the far-field integral in the Green's function representation for steady Oseen flow. *Physics of Fluids* **18(11)** (2006), 113101.
- [4] Hao, W., Hu, B., Li, S., and Song, L.: Convergence of boundary integral method for a free boundary system. *Journal of Computational and Applied Mathematics* **334** (2018), 128-157.
- [5] Imai, I.: On the asymptotic behaviour of viscous fluid flow at a great distance from a cylindrical body, with special reference to Filon's paradox. *Proc. Roy. Soc. Lon. A.* **208(1095)** (1951), 487-516.
- [6] Imai, I.: A new method of solving Oseen's equation and it's application to the flow past an elliptic cylinder. *Proc. Roy. Soc. Lon. A.* **224** (1954), 141-160.
- [7] Kaplun S.: Low Reynolds number flow past a circular cylinder. *J. of math. and mech.* (1957), 595-603.
- [8] Lamb, H.: On the uniform motion of a sphere through a viscous fluid. *The London, Edinburgh, and Dublin Philosophical Magazine and Journal of Science* **21(121)** (1911) 112-121.
- [9] Lamb H.: Hydrodynamics. *Cambridge University Press* (1932).
- [10] Lee, S.H. and Leal, L.G.: Low-Reynolds-number flow past cylindrical bodies of arbitrary cross-sectional shape. *J. fluid mech.* **164** (1986), 401-427.
- [11] Oseen, C.W.: Uber die Stokes' sche Formel und Uber eine verwandte Aufgabe in der Hydrodynamik *Arkiv Mat. Astron. och Fysik*, **6(1)** (1910).
- [12] Oseen, C.W.: Neuere methoden und ergebnisse in der hydrodynamik. *Leipzig: Akademische Verlagsgesellschaft mb H.* (1927).
- [13] Proudman, I. and Pearson, J.R.A.: Expansions at small Reynolds numbers for the flow past a sphere and a circular cylinder. *J. fluid mech.* **2(3)** (1957), 237-262.

- [14] Stokes, G.G.: *On the effect of the internal friction of fluids on the motion of pendulums*. Pitt Press Cambridge (1851).
- [15] Tomotika, S. and Aoi, T.: An expansion formula for the drag on a circular cylinder moving through a viscous fluid at small Reynolds numbers. *The Quarterly Journal of Mechanics and Applied Mathematics* **4(4)** (1951), 401-406.
- [16] Tritton, D.J.: Experiments on the flow past a circular cylinder at low Reynolds numbers *J. fluid mech.* **6(4)** (1959), 547-567.
- [17] Yano, H. and Kieda, A.: An approximate method for solving two-dimensional low-Reynolds number flow past arbitrary cylindrical bodies *J. fluid mech.* **97(1)** (1980), 157-179.

## Chapter 9

# A boundary element formulation for PDEs containing fractional derivatives

J.A.M. Carrer<sup>1</sup>, J. Trevelyan<sup>2</sup>, M. Seaid<sup>2</sup> & B.S. Solheid<sup>1</sup>

<sup>1</sup> Programa de Pós-Graduação em Métodos Numéricos em Engenharia  
Universidade Federal do Paraná  
Caixa Postal 19011  
CEP 81531-990, Curitiba, Brazil.

<sup>2</sup> Department of Engineering  
Durham University  
South Road  
DH1 3LE, Durham, UK.

---

**Abstract.** *We address partial differential equations including fractional time derivatives, i.e. those containing derivative terms  $\partial^\alpha u / \partial t^\alpha$ , where  $\alpha$  is non-integer. These occur in a broad range of problems in physics, finance, hydrology, epidemiology and ecology. To avoid dealing directly with the fractional derivative, an inverse operation employing the Riemann-Liouville operator is used, thereby transferring the fractional time derivative to the second order spatial derivatives. A boundary integral equation may be derived by applying the weighted residual method to the PDE reformulated in this way. This gives us a formulation we call FD-BEM, where  $F$  indicates we are working with fractional calculus, and  $D$  indicates this is a domain form, since the boundary element equation includes a domain integral term containing the time derivative of the variable of interest.*

*We present the FD-BEM formulation and show that the results compare well against analytical solutions, and are also favourable when compared against a finite difference implementation for problems for which no analytical solution is available. We demonstrate the rapid changes in the solution variable associated with  $\alpha < 0.5$ . For these problems, very small time steps are required to capture the solution accurately at early times  $t$ . We propose simple approaches to ameliorate this difficulty.*

---

## 9.1 Introduction

The classic diffusion problem can be looked upon as a case of a more general problem, which is described by a fractional differential equation. The fractional calculus is as old as the standard calculus, e.g. [1, 2], but only recently the numerical solution of problems governed by differential equations of fractional orders has received a great deal of attention. Most of the formulations are based on the Finite Difference Method (FDM), e.g., among others [3, 4, 5, 6, 7]. Finite Element Method (FEM) formulations, e.g. [8, 9, 10, 11], and Boundary Element Method (BEM) formulations, e.g. [12, 13], can also be cited.

The anomalous diffusion problem is described by a partial differential equation that contains a fractional time derivative of order  $\alpha$ ,  $0 < \alpha < 1$ , instead of the usual first order time derivative. The fractional differential operators are non-local: this means that when solving such kind of problems, the determination of a future state of the system depends on the current and previous states, that is, depends on the history. The solution of the anomalous diffusion equation, for two-dimensional problems, by a BEM formulation is the purpose of the present work. The main characteristics of the formulation can be described as follows: i) to avoid dealing directly with the fractional time derivative, represented by the Caputo derivative, see [2], an inverse operation, carried out by employing the Riemann-Liouville operator, is initially accomplished, replacing the fractional time derivative by an ordinary derivative and transferring the fractional derivative to the second order spatial derivatives; ii) starting with a typical weighted residual equation, with the steady-state fundamental solution as the weighting function, the final result is an BEM containing a domain integral with the integrand constituted by the product of the fundamental solution with the first order time derivative of the basic variable of the problem: the resulting formulation is of the type D-BEM, D meaning domain. It will be referred to as FD-BEM, due to the nature of the problem. Note that the Riemann-Liouville operator appears under the domain and boundary integrals; therefore, due to the evaluation of the integral presented in the Riemann-Liouville operator, the solution of the problem for a specific value of time, say  $t_{n+1}$ , requires that all the previous values of the variables, up to the previous time  $t_n$ , must be taken into account, constituting which can be called the history contribution of the analysis.

Two examples are presented and discussed. In the first, the BEM results are compared with the analytical solution. In the second, with the results furnished by a Finite Difference Method (FDM) formulation.

## 9.2 The Anomalous Diffusion Problem

The governing equation for the anomalous diffusion problem is written as:

$$\frac{\partial^\alpha u}{\partial t^\alpha} = D \left( \frac{\partial^2 u}{\partial x^2} + \frac{\partial^2 u}{\partial y^2} \right), \quad 0 < \alpha < 1 \quad (9.1)$$

where  $D$  is the diffusion coefficient, assumed constant. For a domain  $\Omega$ , its boundary  $\Gamma$  can be represented as:  $\Gamma = \Gamma_u \cup \Gamma_q$ . The boundary conditions are then schematically defined as follows:

$$\text{Dirichlet boundary condition: } u(X, t) = \hat{u}(X, t), \quad X \in \Gamma_u \quad (9.2)$$

$$\text{Neumann boundary condition: } D \frac{du}{dn} = D \left( \frac{\partial u}{\partial x} n_x + \frac{\partial u}{\partial y} n_y \right) = q(X, t) = \hat{q}(X, t), \quad X \in \Gamma_q \quad (9.3)$$

In (9.3),  $n_x$  and  $n_y$  are the components of the unit outward vector to the boundary. The initial condition is defined as:

$$u(X, 0) = u_0(X) \quad (9.4)$$

In equations (9.2), (9.3) and (9.4),  $X = (x, y)$ . In equation (9.1), the fractional derivative of  $\alpha$ -order in the Caputo sense is given by:

$$\frac{\partial^\alpha u}{\partial t^\alpha} = D^\alpha(u(t)) = \frac{1}{\Gamma(1-\alpha)} \int_0^t \frac{1}{(t-\tau)^\alpha} \frac{\partial u(\tau)}{\partial \tau} d\tau \quad (9.5)$$

The fractional time derivative on the left-hand-side of equation (9.1) can be transformed into a derivative of order one, by means of the Riemann-Liouville fractional derivative, defined as:

$$RL^\alpha(u(t)) = \frac{1}{\Gamma(1-\alpha)} \frac{d}{dt} \int_0^t \frac{u(\tau)}{(t-\tau)^\alpha} d\tau \quad (9.6)$$

Note that, from the definitions given by (9.5) and (9.6), both Caputo and Riemann-Liouville are integro-differential operators in which the sequence integration-differentiation is inverted. When the initial conditions are null, both definitions coincide. The Riemann-Liouville operator has the following property:

$$RL^{1-\alpha} \left( \frac{\partial^\alpha u(t)}{\partial t^\alpha} \right) = \frac{\partial u}{\partial t} \quad (9.7)$$

Then, applying the operator  $RL^{1-\alpha}(\cdot)$  to both sides of equation (9.1), one has:

$$\frac{\partial u}{\partial t} = DRL^{1-\alpha} \left( \frac{\partial^2 u}{\partial x^2} + \frac{\partial^2 u}{\partial y^2} \right) = \frac{D}{\Gamma(\alpha)} \frac{d}{dt} \int_0^t \frac{1}{(t-\tau)^{1-\alpha}} \left( \frac{\partial^2 u(X, \tau)}{\partial x^2} + \frac{\partial^2 u(X, \tau)}{\partial y^2} \right) d\tau \quad (9.8)$$

Equation (9.8) is the equation to be solved by the Boundary Element Method.

### 9.3 The boundary element method

The Boundary Element Method formulation is presented succinctly in the sequence. The procedure is based on the weighting residuals approach, e.g. [14, 15], with the steady state fundamental solution playing the role of the weighting function. The resulting formulation presents a domain integral whose integrand contains the time derivative of the variable of interest. Formulations of this type are usually called D-BEM, D meaning domain in reference to the domain integral. In this work, due to the presence of the fractional derivative, the formulation will be named FD-BEM, F meaning fractional.

If the basic steps have already been done, the new aspects will be discussed. Recalling that:

$$RL^{1-\alpha}(u) = \frac{1}{\Gamma(\alpha)} \frac{d}{dt} \int_0^t \frac{u(x, \tau)}{(t-\tau)^{1-\alpha}} d\tau \quad (9.9)$$

and assuming that  $u$  is constant inside each time interval  $\Delta t$ , a generic term can be written as:

$$\frac{d}{dt} \int_{j\Delta t}^{(j+1)\Delta t} \frac{1}{(t-\tau)^{1-\alpha}} d\tau u_{j+1} \Big|_{t=(n+1)\Delta t} = \Delta t^{\alpha-1} \left[ \frac{1}{(n+1-j)^{1-\alpha}} - \frac{1}{(n-j)^{1-\alpha}} \right] u_{j+1} \quad (9.10)$$

Representing the term between brackets as:

$$B_{(n+1)(j+1)} = \left[ \frac{1}{(n+1-j)^{1-\alpha}} - \frac{1}{(n-j)^{1-\alpha}} \right] \quad (9.11)$$

one has, once the integral in equation (9.9) is evaluated:

$$RL^{1-\alpha}(u)|_{t=(n+1)\Delta t} = \frac{\Delta t^{\alpha-1}}{\Gamma(\alpha)} \left[ u_{n+1} + \sum_{j=0}^{n-1} B_{(n+1)(j+1)} u_{j+1} \right] \quad (9.12)$$

Based on equation (9.12), one can also write:

$$RL^{1-\alpha}(q)|_{t=(n+1)\Delta t} = \frac{\Delta t^{\alpha-1}}{\Gamma(\alpha)} \left[ q_{n+1} + \sum_{j=0}^{n-1} B_{(n+1)(j+1)} q_{j+1} \right] \quad (9.13)$$

Substituting equations (9.12) and (9.13) in the weighting residual equation, and following the usual BEM approach, the basic equation of the FD-BEM formulation can be written as:

$$\begin{aligned} u_{n+1}(\xi) &= \int_{\Gamma} q_{n+1} w d\Gamma - \int_{\Gamma} u_{n+1} Q d\Gamma - \frac{\Gamma(\alpha)}{\Delta t^{\alpha}} \int_{\Omega} (u_{n+1} - u_n) w d\Omega \\ &- \sum_{j=0}^{n-1} B_{(n+1)(j+1)} \left[ u_{n+1}(\xi) + \int_{\Gamma} u_{j+1} Q d\Gamma - \int_{\Gamma} q_{j+1} w d\Gamma \right] \end{aligned} \quad (9.14)$$

In equation (9.14), the index  $n+1$  refers to the time  $t_{n+1} = (n+1)\Delta t$ , where  $\Delta t$  is the time-step, and  $w = w(\xi, X)$  is the fundamental solution, defined as:

$$w = w(\xi, X) = -\frac{1}{2\pi D} \ln r \quad (9.15)$$

where  $\xi = (\xi_x, \xi_y)$  is the source point,  $X = (x, y)$  is the field point, and  $r$  is the distance between them. Besides:

$$q = D \left( \frac{\partial u}{\partial x} n_x + \frac{\partial u}{\partial y} n_y \right) = D \frac{du}{dn} \quad (9.16)$$

and

$$Q = D \left( \frac{\partial w}{\partial x} n_x + \frac{\partial w}{\partial y} n_y \right) = D \frac{dw}{dn} \quad (9.17)$$

After carrying out boundary and domain discretization, the resulting system can be written, in matrix form, as:

$$\begin{aligned} \begin{bmatrix} \mathbf{H}^{bb} & \mathbf{0} \\ \mathbf{H}^{db} & \mathbf{I} \end{bmatrix} \begin{Bmatrix} \mathbf{u}_{n+1}^b \\ \mathbf{u}_{n+1}^d \end{Bmatrix} &= \begin{bmatrix} \mathbf{G}^{bb} \\ \mathbf{G}^{db} \end{bmatrix} \{\mathbf{q}_{n+1}^b\} \\ &- \sum_{j=0}^{n-1} B_{(n+1)(j+1)} \left( \begin{bmatrix} \mathbf{H}^{bb} & \mathbf{0} \\ \mathbf{H}^{db} & \mathbf{I} \end{bmatrix} \begin{Bmatrix} \mathbf{u}_{n+1}^b \\ \mathbf{u}_{n+1}^d \end{Bmatrix} - \begin{bmatrix} \mathbf{G}^{bb} \\ \mathbf{G}^{db} \end{bmatrix} \{\mathbf{q}_{n+1}^b\} \right) \\ &+ \frac{\Gamma(\alpha)}{\Delta t^{\alpha}} \begin{bmatrix} \mathbf{M}^{bb} & \mathbf{M}^{bd} \\ \mathbf{M}^{db} & \mathbf{M}^{dd} \end{bmatrix} \begin{Bmatrix} \mathbf{u}_{n+1}^b - \mathbf{u}_n^b \\ \mathbf{u}_{n+1}^d - \mathbf{u}_n^d \end{Bmatrix} \end{aligned} \quad (9.18)$$

In equation (9.18), the superscripts  $b$  and  $d$  correspond to boundary and domain variables, whereas double superscripts are interpreted as follows: the first indicates the position of the source point and the second, the position of the field point. Besides,  $\mathbf{I}$  is the identity matrix. The null matrix shows that there is no dependence of the boundary values upon the domain values.

For anisotropic media, the corresponding differential equation reads:

$$\frac{\partial^\alpha u}{\partial t^\alpha} = D_x \frac{\partial^2 u}{\partial x^2} + D_y \frac{\partial^2 u}{\partial y^2} \quad (9.19)$$

The development of a D-BEM formulation for the solution of equations (9.19) follows the same steps presented above. Now, the fundamental solution is, e.g. [16, 17]:

$$w = w(\xi, X) = -\frac{1}{2\pi\sqrt{D_x D_y}} \ln \sqrt{(x - \xi_x)^2 + \frac{D_x}{D_y} (y - \xi_y)^2} \quad (9.20)$$

where  $D_x$  and  $D_y$  are the diffusion coefficients in the  $x$ - and  $y$ -directions respectively.

## 9.4 Examples

### 9.4.1 Domain under initial conditions

This first example is constituted of a rectangular domain defined on the region  $0 \leq x \leq \pi$  and  $0 \leq y \leq \pi/2$ . The boundary conditions are:

$$u(0, y, t) = u(\pi, y, t) = 0 \quad (9.21)$$

The initial condition is given by:

$$u_0(x, y) = \sin x \quad (9.22)$$

From the boundary conditions in (9.21) and the initial condition in (9.22), this is, in fact, a one-dimensional problem. To simulate this problem through a two-dimensional formulation, the following boundary conditions are adopted at  $y = 0$  and  $y = \pi/2$ :

$$q(x, 0, t) = q(x, \pi/2, t) = 0 \quad (9.23)$$

The analytical solution is given by, see [18]:

$$u_0(x) = E_\alpha(-t^\alpha) \sin x \quad (9.24)$$

In equation (9.24),  $E_\alpha(\cdot)$  is the Mittag-Leffler function, see [19], defined according to:

$$E_\alpha(z) = \sum_{k=0}^{\infty} \frac{z^k}{\Gamma(1 + \alpha k)} \quad (9.25)$$

where  $z \in \mathbb{C}$ ,  $\alpha$  is the fractional order of the derivative, and  $\Gamma(\cdot)$  is the gamma function. When  $\alpha = 1$ , one has:

$$E_1(z) = e^z \quad (9.26)$$

and equation (9.24) turns the well-known analytical solution of the diffusion problem, which means that the analytical solution for the diffusion equation can be looked upon as a particular case of the anomalous diffusion. The BEM mesh is depicted in Figure 9.1, and consists of 48 linear elements and 256 triangular linear cells. The analyses were carried out with  $D = 1.0$ , for  $\alpha = 1.0; 0.8; 0.5$ . The results for  $u(\pi/2, \pi/4, t), 0 \leq t \leq 2$  are depicted in Figure 9.2, whereas the results for  $u(x, \pi/4, 0.25), 0 \leq x \leq \pi$ , are depicted, in Figure 9.3. The time-step length shows a strong dependence on the parameter  $\alpha$ , with smaller values of  $\alpha$  requiring smaller  $\Delta t$  values. In this example, for  $\alpha = 1.0$  and  $\alpha = 0.8$ ,  $\Delta t_{BEM} = 0.005$ , whereas for  $\alpha = 0.5$ ,  $\Delta t_{BEM} = 0.0025$ . The results presented in Figures 9.2 and 9.3 showed good agreement with the analytical solution. Far from arriving to general conclusions, those results are very promising and encouraging.

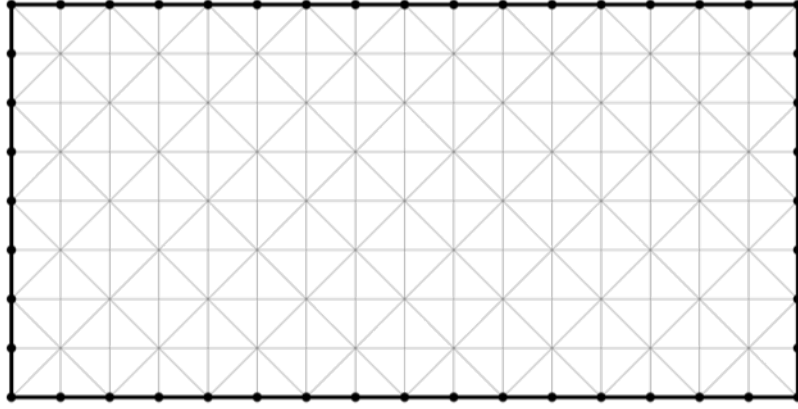


Figure 9.1: BEM mesh

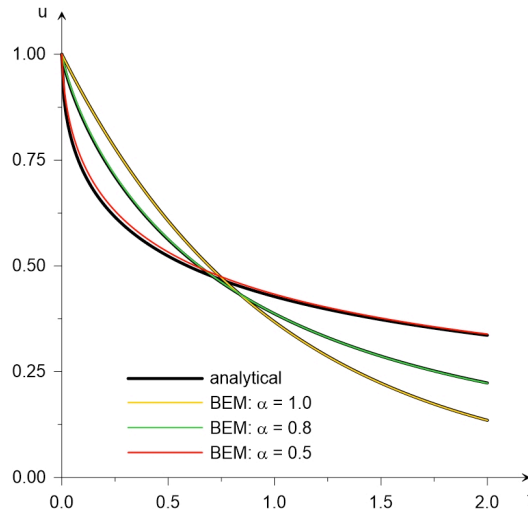


Figure 9.2: Domain under initial condition: results for  $u(\pi/2, \pi/4, t)$

#### 9.4.2 Square domain with linear initial conditions

This example presents the analysis of a square domain in the region  $0 \leq x, y \leq L$ . In a sub-domain  $\Omega_o$ , with  $9L/20 \leq x, y \leq 11L/20$ , the initial condition varies linearly from  $C_o$  in the centre of  $\Omega_o$  to zero in its borders. The boundary conditions are:

$$u(0, y, t) = u(L, y, t) = u(x, 0, t) = u(x, L, t) = 0 \quad (9.27)$$

The BEM mesh is constituted by 160 linear boundary elements and 3200 triangular linear cells, as shown in Figure 9.4.

In the analyses,  $L = 10$  and  $C_o = 10$ . Two cases were considered: in the first, it is assumed the medium to be isotropic and  $D = 1.0$  was adopted. The second case presents an anisotropic medium, for which  $D_x = 1.0$  and  $D_y = 0.1$ . The results at  $(L/2, L/2, t)$  for the first and the second cases are presented, respectively, in Figures 9.5 and 9.6.

Figures 9.7 and 9.8 present the comparison between BEM and FDM results at  $t = 1$  s for  $\alpha = 0.5$ . In the anisotropic case, the isolines are no longer circular and become more ellipsoidal,

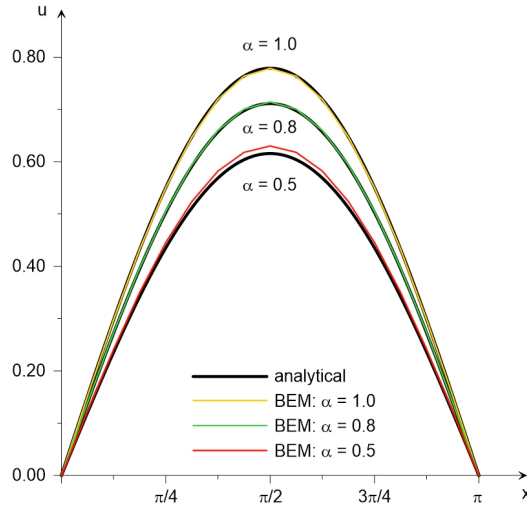


Figure 9.3: Domain under initial condition: results for  $u(x, \pi/4, 0.25)$

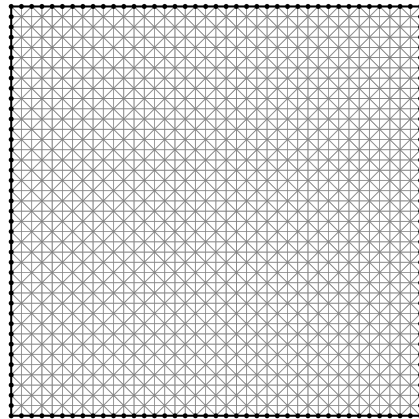


Figure 9.4: BEM mesh

with the main axis in the  $x$ -direction. This is an expected behaviour, well characterized by both formulations. For the two cases, the BEM analyses were carried out with  $\Delta t_{BEM} = 0.00625$  when  $\alpha = 0.5$  and with  $\Delta t_{BEM} = 0.0125$  when  $\alpha = 1.0$ . For the isotropic problem, FDM analyses were carried out with  $\Delta t_{FDM} = 0.0003125$  when  $\alpha = 0.5$  and with  $\Delta t_{FDM} = 0.003125$  when  $\alpha = 1.0$ . For the anisotropic problem, these values are  $\Delta t_{FDM} = 0.00125$  when  $\alpha = 0.5$  and  $\Delta t_{FDM} = 0.0025$  when  $\alpha = 1.0$ . The BEM analyses, once more, showed less dependency on the time-step length than the FDM ones.

## 9.5 Conclusions

The main novelty of this work is the D-BEM formulation developed for the solution of the anomalous diffusion equation. The formulation was developed using the Riemann-Liouville operator, with the integral that appears in this operator being computed under the assumption that the variable of interest and its normal derivative are constant in the time-steps in which the

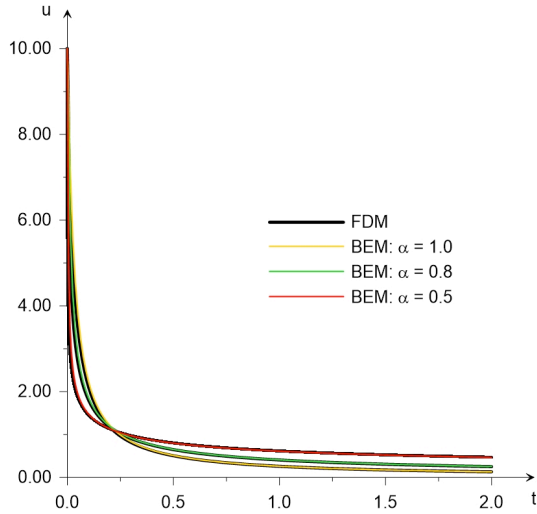


Figure 9.5: Square Domain: results at  $u(5.0, 5.0, t)$  for  $D_x = D_y = 1.0$

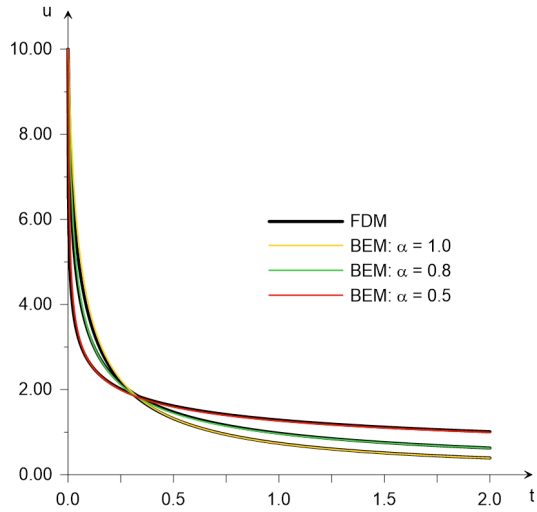


Figure 9.6: Square Domain: results at  $u(5.0, 5.0, t)$  for  $D_x = 1.0$  and  $D_y = 0.1$

domain of integration was divided. The formulation can provide reliable results for values of the fractional order derivative greater than or equal to 0.5. However, from the authors' experience, it seems that for values of  $\alpha$  smaller than 0.5, the search for accurate solutions becomes more and more difficult, as very small time-steps are required to perform the analysis, turning the solution very time-consuming. As a suggestion to overcome such a difficulty, the use of variable time steps seems to be very promising: beginning the analysis with very small values, greater values can be used as the time increases, turning in this way the formulation more efficient. It is one possibility that deserves attention. Another one is the use of more sophisticated interpolation functions. These comments, or suggestions, for future developments are included just because the formulation proposed here can be improved even more, although it can already be used as a reliable tool for the solution of the anomalous diffusion problems, as the examples included here demonstrated. The solution of the wave-diffusion equation can also be undertaken by a similar

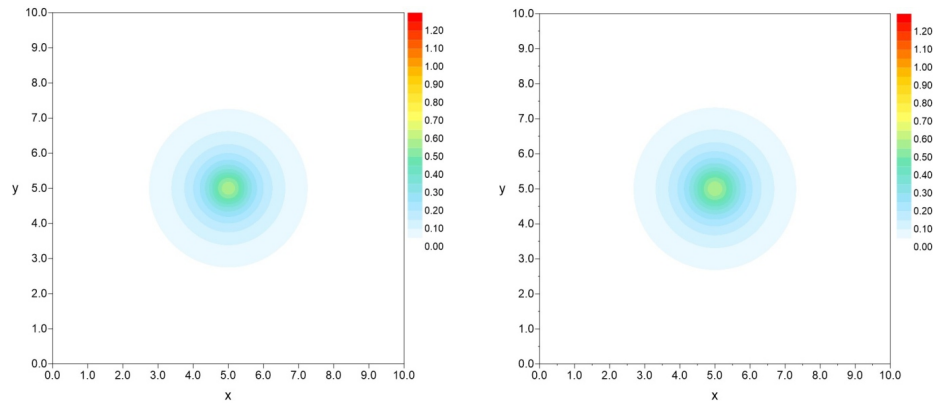


Figure 9.7: Square Domain: results at  $u(x, y, 1.0)$  for  $D_x = 1.0$  and  $D_y = 1.0$  and  $\alpha = 0.5$ . Left image: BEM, right image: FDM.

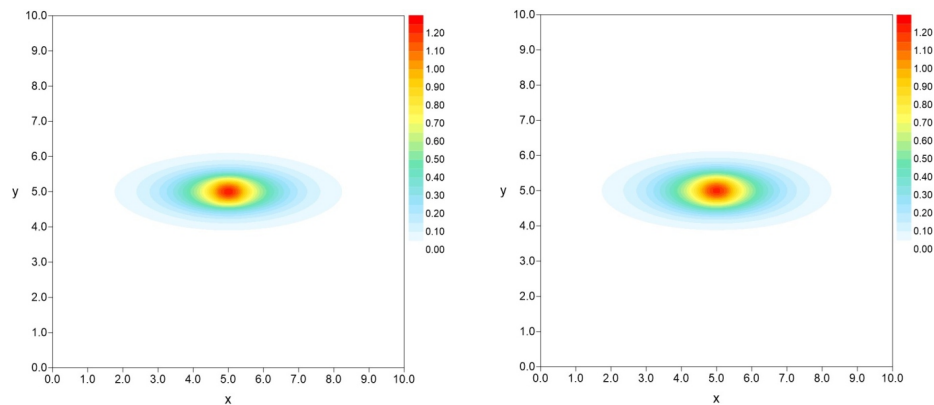


Figure 9.8: Square Domain: results at  $u(x, y, 1.0)$  for  $D_x = 1.0$  and  $D_y = 0.1$  and  $\alpha = 0.5$ . Left image: BEM, right image: FDM.

formulation.

## Acknowledgement

The first author would like to thank the support from the Brazilian Council for Scientific and Technological Development (CNPq), under the process number 201451/2018-2/PDE.

## References

- [1] Miller, K.S. and Ross, B: *An Introduction to the Fractional Calculus and Fractional Differential Equations*, (1993) Wiley-Interscience.
- [2] Ortigueira, M.D.: *Fractional Calculus for Scientist and Engineers*. (2011) Lectures Notes in Electrical Engineering, volume 84, 2011, Springer.

- [3] Meerschaert, M.M. and Tadjeran, C.: Finite Difference Approximations for Fractional Advection-Dispersion Flow Equations. *Journal of Computational and Applied Mathematics*. **172**, (2004) 65-77.
- [4] Yuste, S.B. and Acedo, L.: An Explicit Finite Difference Method and a New von Neumann-Type Stability Analysis for Fractional Diffusion Equations. *SIAM Journal on Numerical Analysis*. **42**, (2005) 1862-1874.
- [5] Tadjeran, C. and Meerschaert, M.M.: A Second-Order Accurate Numerical Method for the Two-Dimensional Fractional Diffusion Equation. *Journal of Computational Physics*. **220**, (2007) 813-823.
- [6] Murio D.A.: Implicit Finite Difference Approximation for Time Fractional Diffusion Equations. *Computers and Mathematics with Applications*, **56**, (2008) 1138-1145.
- [7] Sousa, E. and Li, C.: A Weighted Finite Difference Method for the Fractional Diffusion equation Based on the Riemann-Liouville Derivative. *Applied Numerical Mathematics*. **90**, (2015) 22-37.
- [8] Roop, J.P.: Computational Aspects of FEM Approximation of fractional Advection Dispersion Equations on Bounded Domains in  $\mathbb{R}^2$ . *Journal of Computational and Applied Mathematics*. **193**, (2006) 243-268.
- [9] Agrawal, O.P.: A General Finite Element Formulation for Fractional Variational Problems. *Journal of Mathematical Analysis and Applications*. **337**, (2008) 1-12.
- [10] Deng, W.H.: Finite Element Method for the Space and Time Fractional Fokker-Planck Equation. *SIAM Journal on Numerical Analysis*. **47**, (2008) 204-226.
- [11] Huang, Q., Huang, G. and Zhan, H.: A Finite Element Solution for the Fractional Advection-Dispersion Equation. *Advances in Water Resources*. **31**, (2008) 1578-1589.
- [12] Katsikadelis, J.T.: The BEM for Numerical Solution of Partial Fractional Differential Equations. *Computers and Mathematics with Applications*, **62**, (2011) 891-901.
- [13] Dehghan, M. and Safarpour, M.: The Dual Reciprocity Boundary Elements Method for the Linear and Nonlinear Two-Dimensional Time-Fractional Partial Differential Equations. *Mathematical Methods in the Applied Sciences*. **39**, (2016) 3979-3995.
- [14] Brebbia, C.A., Telles, J.C.F. and Wrobel, L.C.: *Boundary Element Techniques: Theory and Application in Engineering*, (1984) Springer Verlag.
- [15] Zienkiewicz, O.C. and Morgan, K: *Finite Elements & Approximation*, (1983) John Wiley & Sons, Inc., New York.
- [16] Berger, J.R. and Karageorghis, A.: The Method of Fundamental Solutions for Heat Conduction in Layered Materials. *International Journal for Numerical Methods in Engineering*. **45**, (1999) 1681-1694.
- [17] Carrer, J.A.M., Cunha, C.L.N. and Mansur, W.J.: The Boundary Element Method Applied to the Solution of Two-Dimensional Diffusion-Advection Problems for Non-Isotropic Materials. *Journal of the Brazilian Society of Mechanical Sciences and Engineering*, **39**, (2017) 4533-4545.
- [18] Ray, S.S.: Exact Solutions for Time-Fractional Diffusion-Wave Equations by Decomposition Method. *Physica Scripta*. **75**, (2007) 53-61.
- [19] Haubold, H.J., Mathai, A.M. and Saxena, R.K.: Mittag-Leffler Functions and Their Applications. *Journal of Applied Mathematics*. (2011) on line.

# Chapter 10

## Fast Boundary Element Methods for the Vlasov-Poisson System

T. Keßler, S. Rjasanow, S. Weißer

Department of Mathematics  
Saarland University  
Campus E1 1  
66123 Saarbrücken, Germany

---

**Abstract.** We present a grid-free method for the numerical treatment of the three-dimensional Vlasov-Poisson system for collisionless electron plasma. The particle density function defined on the six-dimensional phase space is discretised with a standard particle method. These particles interact through a non-local electric field whose potential solves the Poisson equation, where the right-hand side is given by the charge density of the particles. The solution of the Poisson equation is split into two parts: a particle-particle part and a solution of a Laplace problem. Solving the later with the Boundary Element Methods (BEM) leads to a (volume) grid-free method. This reduces the three-dimensional volume problem to a two-dimensional problem on the boundary. Consequently, the number of degrees of freedom of the BEM is typically much smaller than the number of particles.

The electric field is approximated by  $\mathcal{H}^2$ -matrices which are computed on the fly. The computational complexity for the evaluation of the electric field is linear in the number of particles and nearly linear in the number of degrees of freedom of the BEM. The numerical experiments confirm the theoretical complexity estimates. Furthermore, we show that we are able to simulate classical plasma phenomena, as well as plasmas in complex domains with mixed boundary conditions.

---

### 10.1 Introduction

Particle methods for the simulation of collisionless plasmas has been used since the 1950s, starting with the Particle In Cell Method (PIC). We refer the reader to the classical textbooks [3, 9] for an introduction to the basic concepts and the history of the PIC method. The review articles [6] and, more recently, [12] discuss advanced aspects of plasma simulations with particle methods. An obvious strategy for simulation of the particle system is a direct summation. The force acting on a particle is determined by a summation over all interaction partners. Since particles in a plasma interact via long-range Coulomb forces, an accurate computation of the

acceleration of a single particle requires a summation over all other particles in the plasma. This results in a quadratic computational complexity, which is prohibitively expensive with present computer hardware, even for medium-sized problems. Therefore, it is key to find approximations to the forces which significantly reduce the computational complexity but, at the same time, preserve their long-range character and produce consistent results.

Over the years several fast algorithms for the approximate evaluation of particles forces have been suggested, noticeable are the treecode of Barnes and Hut [2] and the closely related algorithm by Appel [1], and the Fast Multipole Method [7, 8].

In this paper, we present a unified hierarchical framework for the grid-free simulation of plasma in bounded domains with the help of modern  $\mathcal{H}^2$ -matrices. For a more in-depth discussion of the algorithm see [10]. Both the particle-particle and the particle-boundary interactions have linear complexity in the number of particles. We propose the usage of interpolation for the approximation in the far field. It is very easy to implement, as it only needs the value of a rather general kernel function at the interpolation points and furthermore, it is directly applicable to the approximation of vector-valued functions. The contribution of the boundary values to the electric field are computed via the Boundary Element Methods which only require a discretisation of the boundary of the domain. This reduces the three-dimensional problem posed on the whole domain to a system of integral equations on a two-dimensional manifold. Similar ideas have already been presented in [5]. The authors used a treecode-based approximation scheme with a boundary integral formulation to simulate plasmas in one- and two-dimensional domains. In contrast to their algorithm, we have both theoretical proofs and numerical evidence for linear complexity, both in the number of particles and the number of elements of the surface mesh. Additionally, we treat the particle and the boundary part evenly in terms of the approximation schemes we use.

## 10.2 Vlasov–Poisson system

We consider the Vlasov–Poisson system for the particle density function  $f$  of an electron plasma,

$$\begin{aligned} \frac{\partial f}{\partial t}(t, x, v) + (v, \nabla_x f(t, x, v)) - (E(t, x), \nabla_v f(t, x, v)) &= 0, \\ E(t, x) &= -\nabla_x \phi(t, x), \\ -\Delta_x \phi(t, x) &= \frac{1}{\beta} \rho_{\text{total}}(t, x) \end{aligned} \tag{10.1}$$

at position  $x$  in a domain  $\Omega \subset \mathbb{R}^3$  with velocities  $v \in \mathbb{R}^3$ , subject to boundary conditions which are given later. The charge density is computed by

$$\rho_{\text{total}}(t, x) = - \int_{\mathbb{R}^3} f(t, x, v) \, dv.$$

Here,

$$\beta = \left( \frac{\lambda_D}{L_0} \right)^2$$

is a non-dimensional quotient of the Debye length

$$\lambda_D = \sqrt{\frac{\varepsilon_0 k_B T_0}{n_0 q_0^2}}$$

and the characteristic length  $L_0$  and  $\varepsilon_0$  is the electric field constant,  $k_B$  is the Boltzmann constant and  $T_0, n_0, q_0$  denote the characteristic temperature, particle density and charge of the plasma, respectively.

Following the Direct Simulation Monte Carlo (DSMC) method, the particle density function is approximated by a weighted sum of products of point measures in phase space  $\Omega \times \mathbb{R}^3$ ,

$$\nu(t) = w \sum_{i=1}^{N_p} \delta_{x_i(t)} \otimes \delta_{v_i(t)},$$

defined by a system of  $N_p$  particles with corresponding positions  $(x_i)_{i=1}^{N_p}$ , velocities  $(v_i)_{i=1}^{N_p}$  and the numerical weight  $w$ . The charge density becomes

$$\rho_{\text{total}}(t) = -w \sum_{i=1}^{N_p} \delta_{x_i(t)}.$$

The weight is computed as

$$w = \frac{|\Omega|}{N_p},$$

where  $|\Omega|$  denotes the volume of  $\Omega$ .

The trajectories of the particles follow the differential equations

$$\begin{aligned} \dot{x}_i(t) &= v_i(t), \\ \dot{v}_i(t) &= -E(t, x_i(t)), \end{aligned} \tag{10.2}$$

for  $t > 0$  and  $i = 1, \dots, N_p$ . The main scope of this paper is an efficient computation of the electric field given by equation (10.1) for an arbitrary domain  $\Omega$ .

In the following, we assign an individual charge, mass and weight to each particle. The charge density is now written as

$$\rho_{\text{total}}(t) = \sum_{i=1}^{N_p} w_i q_i \delta_{x_i(t)}.$$

From now on, we focus on the grid-free computation of the electric field. For this, let us assume the Poisson problem

$$\begin{aligned} -\Delta \phi &= \frac{1}{\beta} \rho_{\text{total}} && \text{in } \Omega, \\ \phi &= g_D && \text{on } \Gamma = \partial\Omega, \end{aligned} \tag{10.3}$$

with given Dirichlet datum  $g_D$ . Keeping in mind that the fundamental solution of the Laplace equation is given by

$$U(x, y) = \frac{1}{4\pi} \frac{1}{|x - y|}, \quad x, y \in \mathbb{R}^3, x \neq y, \tag{10.4}$$

a particular solution  $\phi_p$  of the Poisson equation above for a fixed time  $t > 0$  is

$$\phi_p(t, x) = \frac{1}{4\pi\beta} \sum_{j=1}^{N_p} w_j \frac{q_j}{|x - x_j(t)|}, \tag{10.5}$$

defined on  $\mathbb{R}^3$ , except for the positions of the particles.

In order to find a solution of the BVP (10.3) with the help of  $\phi_p$ , we have to solve the auxiliary problem

$$\begin{aligned} -\Delta\phi_0 &= 0 & \text{in } \Omega, \\ \phi_0 &= g_D - \phi_p & \text{on } \Gamma = \partial\Omega. \end{aligned} \quad (10.6)$$

The solution of the original problem is now

$$\phi = \phi_0 + \phi_p, \quad (10.7)$$

and the electric field at the time  $t$  in the position of particle  $i$  is computed as

$$E(t, x_i(t)) = -\nabla\phi_0(t, x_i(t)) + \frac{1}{4\pi\beta} \sum_{\substack{j=1 \\ j \neq i}}^{N_p} w_j q_j \frac{x_i(t) - x_j(t)}{|x_i(t) - x_j(t)|^3}. \quad (10.8)$$

Whereas the evaluation of  $\phi_p$  is grid-free by its nature, the numerical treatment of equation (10.6) involves, as a rule, the discretisation of the domain. When discretising  $\Omega$  with a volume mesh, this approach turns into the usual PIC method, if one further regularises  $\rho_{\text{total}}$ . However, this approach is not feasible for complex or irregular geometries, because one loses the highly structured mesh exploited by the choice of Poisson solvers, for example based on the Fast Fourier Transform.

For these domains, we propose the usage of fast Boundary Element Methods in order to solve the BVP (10.6), combined with a hierarchical evaluation of  $\phi_p$  and its gradient for the Dirichlet datum and the representation formula, respectively.

### 10.3 Boundary Element Methods

Boundary Element Methods (BEM) are reviewed for the Poisson problem with Dirichlet boundary conditions on a bounded polyhedral domain  $\Omega \subset \mathbb{R}^3$  with boundary  $\Gamma = \partial\Omega$ . Given a volume source term  $g_V \in L_2(\Omega)$  and a Dirichlet datum  $g_D \in H^{1/2}(\Gamma)$ , the problem reads

$$\begin{aligned} -\Delta\phi &= g_V & \text{in } \Omega, \\ \phi &= g_D & \text{on } \Gamma. \end{aligned} \quad (10.9)$$

The boundary value problem is considered in the weak sense, such that the solution is sought in the Sobolev space  $H^1(\Omega)$ . We may follow the idea of the previous section and construct a particular solution  $\phi_p$  in order to homogenise the right hand side of the differential equation. An appropriate choice is the Newton potential

$$\phi_p(x) = (Ng_V)(x) = \int_{\Omega} U(x, y) g_V(y) dy \quad \text{for } x \in \mathbb{R}^3, \quad (10.10)$$

where  $U(x, y)$  is the fundamental solution given in (10.4). For  $g_V = \rho_{\text{total}}/\beta$  we recover (10.5). The problem (10.9) has a unique solution that admits for  $x \in \Omega$  the representation formula

$$\phi(x) = \int_{\Gamma} U(x, y) \gamma_1 \phi(y) ds_y - \int_{\Gamma} \gamma_{1,y} U(x, y) \gamma_0 \phi(y) ds_y + (Ng_V)(x) \quad (10.11)$$

where  $\gamma_0\phi$  denotes the Dirichlet and  $\gamma_1\phi$  the Neumann trace of the unknown solution  $\phi$ . For sufficiently smooth data and  $x \in \Gamma$  it holds

$$\gamma_0\phi(x) = \phi|_{\Gamma}(x) \quad \text{and} \quad \gamma_1\phi(x) = \lim_{\Omega \ni \tilde{x} \rightarrow x} n_{\Omega} \cdot \nabla\phi(\tilde{x}).$$

These trace operators can be extended to linear bounded operators with the following mapping properties:

$$\gamma_0 : H^1(\Omega) \rightarrow H^{1/2}(\Gamma) \quad \text{and} \quad \gamma_1 : H_{\Delta}^1(\Omega) \rightarrow H^{-1/2}(\Gamma).$$

Here,  $H^s(\Gamma)$ ,  $s \in \mathbb{R}$  denote the Sobolev–Slobodkii space on the boundary  $\Gamma$  and

$$H_{\Delta}^1(\Omega) = \{\phi \in H^1(\Omega) \mid \Delta\phi \in L_2(\Omega)\}.$$

We apply the Dirichlet trace operator to the representation formula (10.11) and obtain the integral equation

$$V\gamma_1\phi = \left(\frac{1}{2}I + K\right)\gamma_0\phi - N_0g_V. \quad (10.12)$$

This equation contains the standard boundary integral operators which are well studied, see, e.g., [11]. For  $x \in \Gamma$ , we have the single-layer potential operator

$$(V\zeta)(x) = \gamma_0 \int_{\Gamma} U(x, y)\zeta(y) \, ds_y \quad \text{for } \zeta \in H^{-1/2}(\Gamma),$$

the double-layer potential operator

$$(K\xi)(x) = \lim_{\varepsilon \rightarrow 0} \int_{y \in \Gamma: |y-x| \geq \varepsilon} \gamma_{1,y} U(x, y)\xi(y) \, ds_y \quad \text{for } \xi \in H^{1/2}(\Gamma),$$

and  $N_0g_V = \gamma_0 N g_V$ .

Obviously, if the traces  $\gamma_0\phi$  and  $\gamma_1\phi$  of the unknown solution  $\phi$  are known, the representation formula (10.11) can be used to evaluate  $\phi$  inside the domain  $\Omega$ . We aim to approximate the unknown Neumann trace on the whole boundary  $\Gamma$  with the help of a Galerkin BEM, following [11]. Therefore, let  $\Gamma$  be meshed by a quasi-uniform, conforming surface triangulation that is shape-regular in the sense of Ciarlet with  $N_{\Gamma}$  triangles and  $M_{\Gamma}$  nodes. We apply the conforming approximation spaces

$$S_h^0(\Gamma) = \text{span}\{\varphi_k^0\}_{k=1}^{N_{\Gamma}} \subset H^{-1/2}(\Gamma), \quad \text{and} \quad S_h^1(\Gamma) = \text{span}\{\varphi_i^1\}_{i=1}^{M_{\Gamma}} \subset H^{1/2}(\Gamma),$$

where  $\varphi_k^0$  denotes the piecewise constant function that is one on the triangle of index  $k$  and zero else, and  $\varphi_i^1$  denotes the usual hat function corresponding to the node with index  $i$ . The Galerkin discretisation of the integral equation reads

$$V_h \underline{t}_h = \left(\frac{1}{2}M_h + K_h\right) \underline{\phi}_h - \underline{N}_0, \quad (10.13)$$

where

$$\underline{N}_0[\ell] = (N_0g_V, \varphi_{\ell}^0)_{L_2(\Gamma)} \quad (10.14)$$

for  $\ell = 1, \dots, N_{\Gamma}$ . We can omit the Newton potential when utilising the proposed decomposition (10.7) with  $\phi_0$  as solution of (10.6). This ansatz yields for the approximation of the Neumann trace  $t_{0,h} \approx \gamma_1\phi_0$  the system of linear equations

$$V_h \underline{t}_{0,h} = \left(\frac{1}{2}M_h + K_h\right) \underline{\phi}_{0,h},$$

where  $\phi_{0,h} \approx \gamma_0\phi_0 = g_D - \gamma_0 u_p$ .

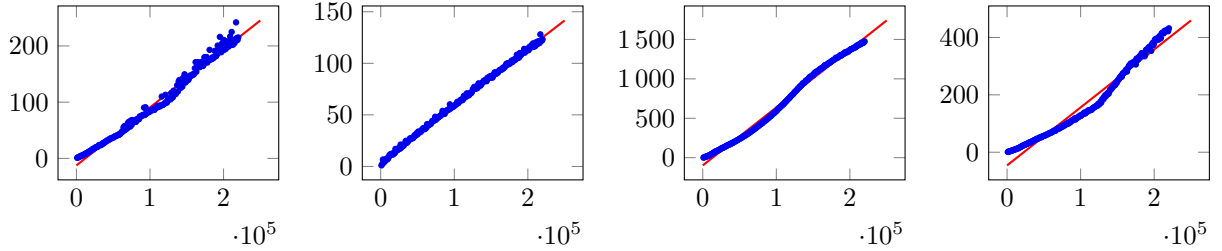


Figure 10.1: Timings relative to 1000 particles from left to right: building the cluster basis, evaluation of  $\underline{N}_0$ , the particle field and the gradient of the representation formula.

## 10.4 Numerical examples

In this section we present several numerical examples. We begin with benchmarking the evaluation of the electric field and conclude with physically motivated examples that demonstrate classical plasma phenomena.

### 10.4.1 Verification of linear complexity

We numerically validate the linear scaling of the computational time for the evaluation of the electric field at the positions of the particles. The computation is split into four parts:

1. Building the cluster basis in  $\mathcal{O}(N_p \log N_p)$ ,
2. computation of  $\underline{N}_0$  according to (10.14) in linear complexity,
3. computation of the particle-particle force, see (10.8) in linear complexity, and
4. evaluating the gradient of the representation formula (10.11) in linear complexity.

For our tests, we triangulate the surface of the unit ball in  $\mathbb{R}^3$  and uniformly distribute negatively charged particles inside the domain. Appropriate nondimensionalisation is irrelevant for this test, so we set all masses, charges and weights to unity. Homogeneous Dirichlet boundary conditions are chosen for the electric potential. We use  $d = 5$  interpolation nodes at each spatial direction for the  $\mathcal{H}^2$ -matrix approximation. The minimal cluster leaf size  $n_{\min}$  is  $2d^3$  and the admissibility constant  $\eta$  is 2.

Figure 10.1 shows the relative computational times for a fixed mesh with varying number of particles. Although formally being of complexity  $\mathcal{O}(N_p \log N_p)$ , we observe a linear scaling of the computation of the cluster basis. Furthermore, the absolute timings are in the order of 100 ms making this part of the algorithm negligible compared to rest of the algorithm which takes in the order of seconds. The evaluation of  $\underline{N}_0$  almost perfectly scales linearly with the number of particles. The evaluation of the gradient of the Newton potential and of the representation formula follow a linear trend.

### 10.4.2 Physically motivated examples

For most applications the plasma contains positively and negatively charged particles. Usually, the positive charge exists of ionised atoms and electrons form the negatively charged part. Since the atoms are much heavier than the electrons they are modelled as immobile. This gives rise

to a homogeneous positive background charge, such that the system is electrically neutral from the outside. The Poisson equation in (10.1) changes to

$$-\Delta_x \phi = \frac{1}{\beta} \left[ 1 - w \sum_{i=1}^{N_p} \delta_{x_i} \right]$$

with boundary conditions

$$\phi = g_D \quad \text{on } \Gamma$$

Note that the integral of the right-hand side over  $\Omega$  is zero, as  $w = |\Omega|/N_p$ . A particular solution for the homogeneous background charge is  $\phi_b(x) = -|x|^2/(6\beta)$ ,  $x \in \Omega$ . By subtracting traces of the particular solution  $\phi_b$ , we transform the boundary value problem to

$$\begin{aligned} -\Delta_x \phi_e &= \frac{1}{\beta} w \sum_{i=1}^{N_p} \delta_{x_i}, \quad \text{in } \Omega, \\ \phi_e &= g_D - g_b \quad \text{on } \Gamma. \end{aligned}$$

The electric field is now obtained by

$$E = -\nabla \phi_e - \nabla \phi_b.$$

As  $\phi_b$  is independent of the geometry and the distribution of the particles, its evaluation and the evaluation of its gradient are grid-free, as well as the computation of  $\phi_e$ .

## Plasma oscillations

As a first example with a homogeneous background charge, we examine plasma oscillations. The geometry is a cylinder along the  $z$ -axis with radius 1 and height 5, centered in 0. It is discretised with 2110 triangles. The characteristic quantities are  $L_0 = 0.1$  m,  $n_0 = 10^{12}$  m<sup>-3</sup> and  $k_B T_0 = 1$  eV. 5000 particles are distributed uniformly in a smaller cylinder of height 4 around the centre of the geometry. Their initial velocities are set to 0. The boundary is absorbing; at the bases we set homogeneous Dirichlet conditions and homogeneous Neumann conditions on the rest. To prevent the particles from being absorbed at the lateral surface of the cylinder, we add a constant magnetic field in the order of 10 mT along the  $z$ -axis. The acceleration due to the magnetic field is computed with the Boris scheme [3, 4] using a time step size of  $10^{-4}$ . In an infinite system, the plasma oscillates with the plasma frequency

$$\omega_p = \sqrt{\frac{n_0 e^2}{\varepsilon_0 m_e}},$$

which depends only on the electron density.

As we simulate the plasma in a bounded domain, we cannot expect the plasma to oscillate with the frequency  $\omega_p$ . Instead, we validate that the frequency for the bounded domain is still a function of the square root of  $n_0$ . In order to do so, we vary the electron density  $n$  from  $n_0$  to  $100n_0$ . Counting the number of particles in three parts of the cylinder,  $z \in [-2.5, 2]$ ,  $z \in [-0.25, 0.25]$  and  $z \in [2, 2.5]$  at each time step, we extract the dominating non-zero frequency after with the help of the Discrete Fourier Transform. The numbers of particles in the left, the middle and right part of the cylinder for  $n = 10n_0$  is shown in Figure 10.2. The distribution of

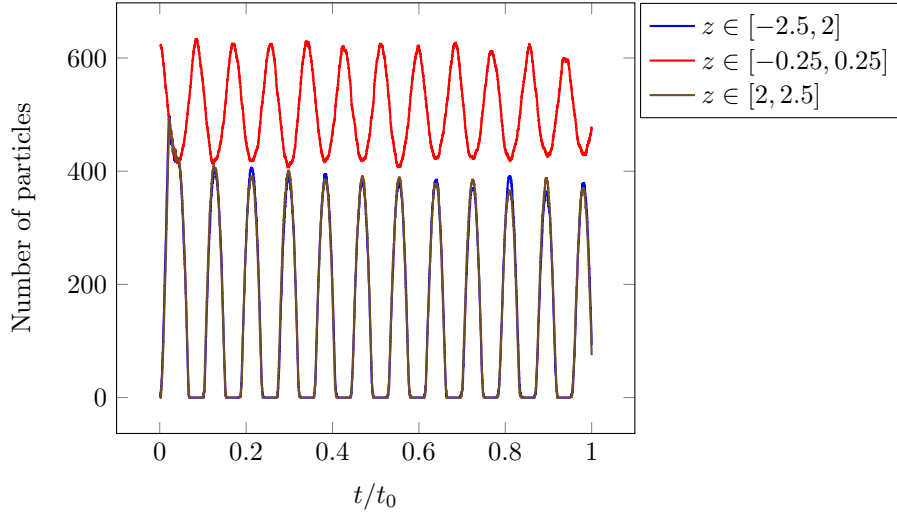


Figure 10.2: Number of particles in three parts of the cylinder over time for  $n = 10n_0$ .

the particles oscillates with dominating frequency of 12 in units of  $1/t_0$ , which corresponds to a angular frequency of  $\omega_c = 3.2 \cdot 10^8 \text{ s}^{-1}$  in physical units. This is in the order of the plasma frequency  $\omega_p = \sqrt{10n_0e^2/(\epsilon_0m_e)} \approx 1.8 \cdot 10^8 \text{ s}^{-1}$ . The spectra of the lines in Figure 10.2 only differ in magnitude, not in the positions of peaks. Therefore, we only show the spectrum of the second line of Figure 10.2 in Figure 10.3. Repeating this several densities between  $n_0$  and  $100n_0$  yields Figure 10.4, from which the dependency of the frequency on the square root of the density is clearly deduced.

### Plasma sheath

A classical nonlinear phenomenon in plasma physics is the formation of sheaths. For this example, we set  $L_0 = 0.1 \text{ m}$ ,  $n_0 = 10^{13} \text{ m}^{-3}$  and  $k_B T_0 = 1 \text{ eV}$ . We uniformly distribute 10 000 particles with velocity following a Maxwellian distribution with temperature 1 and bulk velocity 0 within the unit sphere, which is discretised with 1 280 triangles. The particles are absorbed at the boundary; for the electric potential, we impose homogeneous Dirichlet boundary conditions. The system is evolved with a time step size of  $10^{-3}$ . Figure 10.5 shows the number of particles within the unit sphere as a function of time. At the beginning, the fastest particles leave the sphere, giving rise to a positive charge at the boundary. With the growing potential barrier, the particles are excluded from a thin area near the boundary, the so called sheath, and are confined inside the sphere. Figure 10.6 includes the final radial distribution function of the particles inside the sphere and the analytical radial distribution function of a uniformly distributed random variate inside the unit sphere. While the final positions are still uniformly distributed up to a radius of approximately 0.6, the distribution strongly deviates from the uniform distribution especially close to radii of 1, where it suddenly drops to 0.

### 10.4.3 Summary

To summarise, the numerical examples show that we are capable to simulate important nonlinear plasma phenomena like plasma oscillations or the formation of sheaths. The results also match available theoretical predictions. Furthermore, the numerical study demonstrates the linear

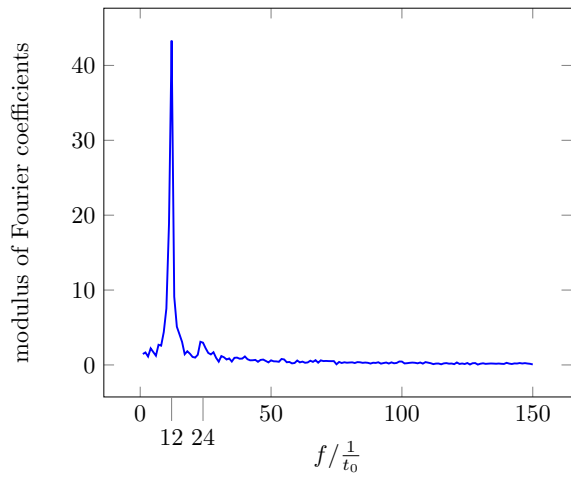


Figure 10.3: Fourier spectrum of the number of particles in the middle of the cylinder, the red line in Figure 10.2. The constant mode is excluded from the spectrum.

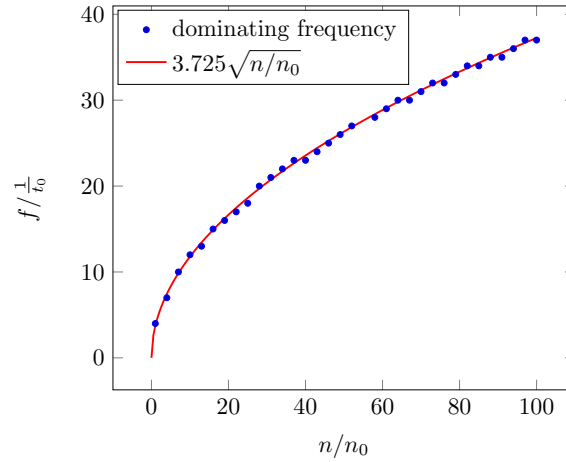


Figure 10.4: Frequency of the oscillation of the number of particles in the middle of the cylinder as a function of the electron density.

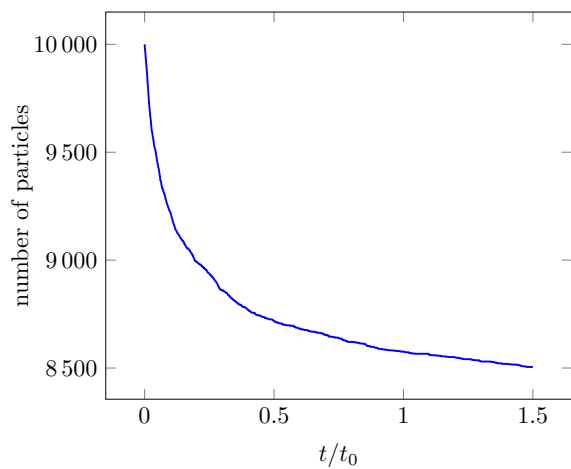


Figure 10.5: Number of particles inside the sphere over time.

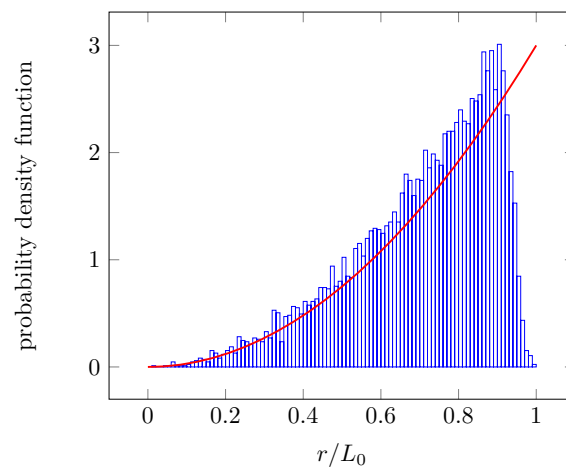


Figure 10.6: Radial histogram of the final particle distribution inside the sphere. The solid red line shows the probability density function of the uniform distribution.

complexity of our method and its applicability on three-dimensional domains with mixed boundary values.

## References

- [1] A. W. Appel. An efficient program for many-body simulation. *SIAM J. Sci. Statist. Comput.*, 6(1):85–103, 1985.
- [2] J. Barnes and P. Hut. A hierarchical  $o(n \log n)$  force-calculation algorithm. *Nature*, 324:446–449, 1986.
- [3] C.K. Birdsall and A.B. Langdon. *Plasma Physics via Computer Simulation*. Series in Plasma Physics. Taylor & Francis Group, New York, 2005.
- [4] J.P. Boris. The acceleration calculation from a scalar potential. Technical report, Plasma Physics Laboratory, Princeton University MATT-152, 1970.
- [5] A. J. Christlieb, R. Krasny, J. P. Verboncoeur, J. W. Emhoff, and I. D. Boyd. Grid-free plasma simulation techniques. *IEEE T Plasma Sci*, 34(2):149–165, 2006.
- [6] J. M. Dawson. Particle simulation of plasmas. *Rev. Mod. Phys.*, 55:403–447, 1983.
- [7] L. Greengard and V. Rokhlin. A fast algorithm for particle simulations. *J. Comput. Phys.*, 73(2):325–348, 1987.
- [8] L. Greengard and V. Rokhlin. The rapid evaluation of potential fields in three dimensions. In C. Anderson and C. Greengard, editors, *Vortex Methods*, volume 1360 of *Lecture Notes in Mathematics*, pages 121–141. Springer, 1988.
- [9] R.W. Hockney and J.W. Eastwood. *Computer Simulation Using Particles*. CRC Press, 1988.
- [10] T. Keßler, S. Rjasanow, and S. Weißer. Vlasov-Poisson system tackled by particle simulation utilising boundary element methods. *arXiv e-prints*, page arXiv:1811.03404, Nov 2018.
- [11] O. Steinbach. *Numerical approximation methods for elliptic boundary value problems: finite and boundary elements*. Springer, New York, 2007.
- [12] J. P. Verboncoeur. Particle simulation of plasmas: review and advances. *Plasma Physics and Controlled Fusion*, 47(5A):A231–A260, 2005.

## Chapter 11

# Asymptotic solutions of convolution integral equations with even positive definite kernels on small or large intervals

Dmitry Ponomarev<sup>1,2</sup>

<sup>1</sup> Institute of Analysis and Scientific Computing  
Technical University of Vienna (TU Wien)  
Wiedner Hauptstrasse 8-10  
1040 Vienna, Austria.

<sup>2</sup> St. Petersburg Department of Steklov Mathematical Institute RAS  
Fontanka 27  
191023 St. Petersburg, Russia.

---

**Abstract.** *One-dimensional convolution integral equations with real-valued regular symmetric kernels naturally arise in a number of inverse problems for elliptic PDEs when field values on an one-dimensional set are known whereas the source term is not. In certain geometrical configurations this can be rephrased as an issue of inversion of a compact self-adjoint integral operator, a problem that can be solved by constructing an approximation of the resolvent of this operator, given its approximate eigendecomposition. Motivated by this application and number of other contexts where convolution integral operators play a crucial role, we consider a generic eigenvalue problem for a self-adjoint convolution integral operator on an interval where the kernel is real-valued even  $C^1$ -smooth function which (in case of large interval) is absolutely integrable on the real line. We show how this spectral problem can be solved by two different asymptotic techniques that take advantage of the size of the interval. In case of small interval, this is done by approximation with an integral operator for which there exists a commuting differential operator thereby reducing the problem to a boundary-value problem for second-order ODE, and often giving the solution in terms of explicitly available special functions such as prolate spheroidal harmonics. In case of large interval, the solution hinges on solvability, by Riemann-Hilbert approach, of an approximate auxiliary integro-differential half-line equation of Wiener-Hopf type, and culminates in simple characteristic equations for eigenvalues, and, with such an approximation to eigenvalues, approximate eigenfunctions are given in an explicit form. We note that, unlike finite-rank approximation of a compact operator, the auxiliary problems arising in both small- and*

*large-interval cases admit infinitely many solutions (eigenfunctions) and hence structurally better represent the original integral operator.*

---

We are concerned with a convolution Fredholm equation of the second kind on a finite interval. That is, given constants  $a > 0$ ,  $\lambda \in \mathbb{C}$  and functions  $K(x)$ ,  $g(x)$ , the problem consists in finding functions  $f(x)$  which satisfy

$$\int_A K(x-t) f(t) dt = \lambda f(x) + g(x), \quad x \in A := (-a, a). \quad (11.1)$$

Equations of this type arise in many applications ranging from a variety of physical problems to the theory of signal processing [2, 7], stochastic processes [5], analytic function approximation [18] and construction of weighted orthogonal bases [21]. Among particular applications, to name a few, are the problems of geological prospecting [15], electrostatics and hydrodynamics problems with circular geometry [13, 14], neutron transport and radiative transfer in a slab [19, 30], study of thermodynamic limits Bose or Fermi quantum gases [28, 29] and antiferromagnetic Heisenberg chain [9].

In particular, we will be dealing with a homogeneous version of (11.1), a problem tantamount (under appropriate restriction on a class of kernel functions) to finding a spectral decomposition of a convolution integral operator defined by the kernel function  $K(x)$ . In other words, we are interested in finding the set of all pairs  $(\lambda, f) \in (\mathbb{R}, L^2(A))$  such that

$$\int_A K(x-t) f(t) dt = \lambda f(x), \quad x \in A. \quad (11.2)$$

We note that equation (11.2) is a more delicate version of (11.1) as it requires more sophisticated analysis. On the other hand, knowledge of complete set of solutions of (11.2) allows solving (11.1), but also, as it is often the case, the solution procedure of (11.2) can be modified (simplified) to deal directly with (11.1). The advantage of solving (11.2) over (11.1) is also that the spectral decomposition permits solving much more general operator problems such as the one arising in approximation theory with quadratic truncated convolution operator equation [18].

Equations (11.1)-(11.2) have been a subject of study for many years. We do not aim to review these works here, instead we just mention that while a closed form solution is not available except for very few special cases (such as polynomial or trigonometric kernel function), majority of efforts in this topic were focussed on study of bounds and asymptotical behavior of eigenvalues [4, 5, 31] whereas in direction of obtaining eigenfunctions usually one of two strategies is pursued.

One possibility is a reduction of the integral equation to an auxiliary problem which is also not explicitly solvable but can give some analytical insight or practical advantage (e.g. better convergence of an iterative numerical scheme, or construction of solutions for general right-hand sides  $g(x)$  in terms of the auxiliary problem solution) [19, 26].

In the alternative strategy, one hopes to solve the original equation asymptotically in the case when the interval  $A$  is large. For constructive asymptotic solution techniques, apart from a crude periodic approximation [8], the typical assumptions on the kernel function are real-valuedness, even parity, positive definiteness,  $L^1$ -regularity and, also, the kernel function was supposed explicitly or implicitly (by imposing conditions on derivative of its Fourier transform at the origin) to have rapid (in most cases even exponential) decay at infinity [12, 16, 17, 23]. This last assumption is too restrictive as it does not allow (except some exceptional cases of (11.1)

with particular values of  $\lambda$  [1, 13, 14, 28, 29]) one to treat even very simple (and yet important for applications listed above) kernels such as, for example,  $\frac{1}{1+x^2}$  and  $\frac{1}{(1+x^2)^{3/2}}$ . It is the main purpose of this work to present a new method that allows dealing with kernels of algebraic decay. For the sake of simplicity of technical arguments, we restrict ourselves to the case when Fourier transform of the kernel function decays monotonically on the real line with distance from the origin, an assumption which is also often used [4, 12].

We also complement our method with a strategy to deal with equation (11.2) on small intervals. This part is meant to demonstrate an essentially different approach compared to commonly used finite-rank approximation of the integral operator obtained by series expansion of the kernel function.

We note that these results are generalization and significant simplification of the previous author's work related to Love/Lieb-Liniger/Gaudin equation [3] where the spectral problem for the integral operator with a particular kernel function  $K(x) = \frac{1}{1+x^2}$  was treated.

## 11.1 Assumptions and some properties

Under assumption that  $K \in L^1(\mathbb{R}) \cap C^1(\mathbb{R})$  is an even real-valued function, the convolution integral operator in the left-hand side of (11.2), that we denote  $\mathfrak{K}$ , is compact on  $L^2(A)$  and self-adjoint. By the Spectral Theorem, spectrum of  $\mathfrak{K}$  is purely discrete with real eigenvalues  $(\lambda_n)_{n=1}^\infty$  converging to zero and corresponding eigenfunctions  $(f_n)_{n=1}^\infty$  forming a basis of the range of  $\mathfrak{K}$ . Moreover, assuming that  $\mathfrak{K}$  is positive definite (i.e.  $\int_A F(x) \int_A K(x-t) F(t) dt dx > 0$  for any  $F \in L^2(A)$ ) and that, for  $k \in \mathbb{R}$ , kernel's Fourier transform  $\hat{K}(k) = \int_{\mathbb{R}} e^{2\pi i k x} K(x) dx$  decays strictly monotonically with increase of  $|k|$ , we have, from Parseval's identity,  $0 < \lambda_n < \hat{K}(0)$ ,  $n \in \mathbb{N}_+$ . Positive definiteness can also be used to prove that eigenfunctions cannot vanish at the endpoints of the interval and the spectrum is simple (see [3, 7]). This, alongside with the parity of  $K$ , implies that each eigenfunction of  $\mathfrak{K}$  is either odd or even and can be chosen to be real-valued. In what follows, we will also repeatedly use an elementary fact that Fourier transform of real-valued functions preserves their parity.

## 11.2 Solution for large $A$

Let us introduce, for  $k \in \mathbb{R}$ ,  $\kappa \in \mathbb{R}_+$ ,

$$\mathcal{G}(k, \kappa) := \frac{\hat{K}(\kappa)(k^2 - \kappa^2)}{(\hat{K}(\kappa) - \hat{K}(k))(k^2 + 1)},$$

$$\mathcal{X}_+(k, \kappa) := \mathcal{G}^{1/2}(k, \kappa) \exp\left(\pm \frac{i}{2} \mathcal{H}[\log \mathcal{G}(\cdot, \kappa)](k)\right),$$

where  $\mathcal{H}[F](k) := \frac{1}{\pi} \text{p.v.} \int_{\mathbb{R}} \frac{F(\tau)}{k-\tau} d\tau$  is the Hilbert transform of  $F$ .

With help of these quantities, the main result can be formulated as follows.

**Theorem 1** Denote as  $(\kappa_n^{(e)})_{n=1}^\infty$ ,  $(\kappa_n^{(o)})_{n=1}^\infty$  all positive solutions of two sets of transcendental equations

$$2\pi\kappa a - \arctan \frac{1}{\kappa} - \frac{1}{2} \mathcal{H}[\log \mathcal{G}(\cdot, \kappa)](\kappa) = \pi m, \quad m \in \mathbb{Z},$$

$$2\pi\kappa a - \arctan \frac{1}{\kappa} - \frac{1}{2} \mathcal{H}[\log \mathcal{G}(\cdot, \kappa)](\kappa) = \pi \left( m + \frac{1}{2} \right), \quad m \in \mathbb{Z},$$

respectively, assuming that these sets are sorted in ascending order, i.e.  $\kappa_{n-1}^{(e)} < \kappa_n^{(e)}$ ,  $\kappa_{n-1}^{(o)} < \kappa_n^{(o)}$ ,  $n \in \mathbb{N}_+$ . Eigenvalues corresponding to even and odd eigenfunctions then are given by

$$\lambda_n^{(e)} = \hat{K}(\kappa_n^{(e)}) + \delta_{n,a}^{(e)}, \quad \lambda_n^{(o)} = \hat{K}(\kappa_n^{(o)}) + \delta_{n,a}^{(o)},$$

for some constants  $\delta_{n,a}^{(e)}, \delta_{n,a}^{(o)} \in \mathbb{R}$  such that  $\delta_{n,a}^{(o)}, \delta_{n,a}^{(e)} \rightarrow 0$  as  $a \rightarrow +\infty$ , for any fixed  $n \in \mathbb{N}_+$ . Corresponding sets of even and odd eigenfunctions are, respectively, furnished by

$$\begin{aligned} f_n^{(e)}(x) &= \frac{2(-1)^{n-1}}{\left[-2\kappa_n^{(e)} (\log \hat{K})'(\kappa_n^{(e)})\right]^{1/2}} \cos(2\pi\kappa_n^{(e)}x) \\ &+ \frac{i}{\pi} \int_{\mathbb{R}} \frac{e^{-2\pi ika}}{(k+i) \mathcal{X}_+(k, \kappa_n^{(e)})} \left[ \frac{\hat{K}(k)}{\hat{K}(k) - \hat{K}(\kappa_n^{(e)})} \right. \\ &\left. - \frac{2\kappa_n^{(e)}}{\left(k^2 - (\kappa_n^{(e)})^2\right) (\log \hat{K})'(\kappa_n^{(e)})} \right] \cos(2\pi kx) dk + \mathcal{E}_{n,a}^{(e)}(x), \end{aligned}$$

$$\begin{aligned} f_n^{(o)}(x) &= \frac{2(-1)^{n-1}}{\left[-2\kappa_n^{(o)} (\log \hat{K})'(\kappa_n^{(o)})\right]^{1/2}} \sin(2\pi\kappa_n^{(o)}x) \\ &- \frac{1}{\pi} \int_{\mathbb{R}} \frac{e^{-2\pi ika}}{(k+i) \mathcal{X}_+(k, \kappa_n^{(o)})} \left[ \frac{\hat{K}(k)}{\hat{K}(k) - \hat{K}(\kappa_n^{(o)})} \right. \\ &\left. - \frac{2\kappa_n^{(o)}}{\left(k^2 - (\kappa_n^{(o)})^2\right) (\log \hat{K})'(\kappa_n^{(o)})} \right] \sin(2\pi kx) dk + \mathcal{E}_{n,a}^{(o)}(x), \end{aligned}$$

with some  $\|\mathcal{E}_{n,a}^{(e)}\|_{L^\infty(A)}, \|\mathcal{E}_{n,a}^{(o)}\|_{L^\infty(A)} \rightarrow 0$  as  $a \rightarrow +\infty$ , for any fixed  $n \in \mathbb{N}_+$ .

**Proof:** We give merely a sketch of the proof outlining main steps and skipping approximation error estimates.

Continuity and strict monotonic decay of  $\hat{K}(k)$ , along with the bounds  $0 < \lambda < \hat{K}(0)$ , imply that there exists unique  $k_0 > 0$  such that  $\hat{K}(\pm k_0) = \lambda$ .

Let us define, for  $x \in \mathbb{R} \setminus A$ ,  $f(x) = \frac{1}{\lambda} \int_A K(x-t) f(t) dt$ .

It turns out that we can express solution of the original problem in terms of its own extension by continuity to the exterior of the interval  $A$  and, in particular, the half-line  $x > a$ . That is, we have

$$f(x) = \int_{\mathbb{R} \setminus A} R(x-t) f(t) dt = \int_a^\infty (R(x-t) \pm R(x+t)) f(t) dt, \quad x \in A, \quad (11.3)$$

where plus and minus signs correspond to the cases of even and odd eigenfuntions, respectively, and

$$R(x) := \int_{\mathbb{R}} e^{-2\pi i k x} \left( \frac{\hat{K}(k)}{\hat{K}(k) - \lambda} - \frac{2\lambda}{\hat{K}'(k_0)} \frac{k_0}{k^2 - k_0^2} \right) dk + \frac{2\pi i \lambda}{\hat{K}'(k_0)} \exp(-2\pi i k_0 |x|), \quad x \in \mathbb{R}.$$

Therefore the problem is reduced to finding this continuous extension that we denote  $\phi(x) := f(x+a)$ ,  $x > 0$ .

One can show that  $\phi(x)$  satisfies the following approximate integro-differential equation

$$\phi''(x) + 4\pi^2 k_0^2 \phi(x) = \int_0^\infty \left( \frac{d^2}{dx^2} + 4\pi^2 k_0^2 \right) T_0(x-t) \phi(t) dt - \frac{8\pi^2 k_0 \lambda}{\hat{K}'(k_0)} \phi(x), \quad x > 0. \quad (11.4)$$

The standard Wiener-Hopf approach can be extended to treat equation (11.4). In particular, Fourier transform of its solution (extended by zero for  $x < 0$ )  $\hat{\phi}(k) = \widehat{\chi_{\mathbb{R}_+} \phi}(k)$  is given by

$$\hat{\phi}(k) = \frac{i\phi(0)}{2\pi(k+i)X_+(k)}, \quad k \in \mathbb{R}, \quad (11.5)$$

where

$$X_+(k) := G^{1/2}(k) \exp\left(\frac{i}{2} \mathcal{H}[\log G](k)\right), \quad G(k) := \frac{\lambda(k^2 - k_0^2)}{(\lambda - \hat{K}(k))(k^2 + 1)}, \quad k \in \mathbb{R} \quad (11.6)$$

with  $\mathcal{H}$  denoting Hilbert transform operator as defined in the formulation of the Theorem.

Recalling that, for  $x > 0$ ,  $\phi(x) = f(x+a)$ ,  $\lambda = \hat{K}(k_0)$ , go back to (11.3), and use Parseval's identity to yield, for  $x \in A$ ,

$$\begin{aligned} f(x) = & -\frac{2\pi i}{(\log \hat{K})'(k_0)} \hat{\phi}(-k_0) \left( e^{-2\pi i k_0(a-x)} \pm e^{-2\pi i k_0(a+x)} \right) \\ & + \int_{\mathbb{R}} \hat{\phi}(k) T(k) \left( e^{-2\pi i k(a-x)} \pm e^{-2\pi i k(a+x)} \right) dk \end{aligned} \quad (11.7)$$

with

$$T(k) := \frac{\hat{K}(k)}{\hat{K}(k) - \hat{K}(k_0)} - \frac{2k_0}{(k^2 - k_0^2) (\log \hat{K})'(k_0)}, \quad k \in \mathbb{R}.$$

Since the half-line solution  $\phi(x) = f(x+a)$  is a smooth continuation of the solution  $f(x)$  on  $A$ , the two solutions should match by continuity:  $\phi(0^+) = f(a+0^+) = f(a-0^+)$ . We thus plug (11.5) into (11.7) and, evaluating both sides at  $x = a$ , cancel out the non-vanishing factor  $\phi(0) = f(a)$  (the property  $f(\pm a) \neq 0$  is mentioned in the previous section). This results in a pair of transcendental characteristic equations for determining values of  $\lambda$  corresponding to even or odd set of eigenfunctions depending on the choice of the sign  $\pm$  in (11.7). Namely, characteristic equations for even and odd part of the spectrum, respectively, are

$$\begin{aligned} \frac{i}{2\pi} \int_{\mathbb{R}} \left[ \frac{\hat{K}(k)}{\hat{K}(k) - \hat{K}(k_0)} - \frac{2k_0}{(k^2 - k_0^2) (\log \hat{K})'(k_0)} \right] \frac{1 + e^{-4\pi i k a}}{(k+i)X_+(k)} dk = 1 \quad (11.8) \\ + \frac{(1 + e^{-4\pi i k_0 a})}{(k_0 - i)X_+(-k_0) (\log \hat{K})'(k_0)}, \end{aligned}$$

$$\frac{i}{2\pi} \int_{\mathbb{R}} \left[ \frac{\hat{K}(k)}{\hat{K}(k) - \hat{K}(k_0)} - \frac{2k_0}{(k^2 - k_0^2) (\log \hat{K})'(k_0)} \right] \frac{1 - e^{-4\pi i k a}}{(k+i) X_+(k)} dk = 1 \quad (11.9)$$

$$+ \frac{(1 - e^{-4\pi i k_0 a})}{(k_0 - i) X_+(-k_0) (\log \hat{K})'(k_0)}.$$

These equations are enormously more simple than those obtained by the author in [3] for a particular kernel of the considered class. However, we make another observation that provides even further complexity reduction. We notice that, in some small neighborhood of  $x = 0$ , the integral term is small, i.e. at least  $\mathcal{O}(1/a^2)$  as asymptotics at infinity of Fourier transform of a smooth function (and hence this smallness is eventually related to the smoothness of  $\hat{K}$ ), and hence, in the middle of the interval, the non-integral oscillatory term in (11.7) dominates. On the other hand, we know that all eigenfunctions are real-valued (up to a choice of normalization). This imposes a restriction on the complex phase of the constant in front of the oscillatory function which is either  $\cos(2\pi k_0 x)$  (in case of even eigenfunctions) or  $\sin(2\pi k_0 x)$  (in case of odd eigenfunctions). Employing (11.6), (11.5), we thus deduce the following versions of characteristic equations to be solved for  $k_0 > 0$  (or, equivalently, for  $\lambda = \hat{K}(k_0)$ )

$$2\pi k_0 a - \arctan \frac{1}{k_0} - \frac{1}{2} \mathcal{H}[\log G](k_0) = \pi m, \quad m \in \mathbb{Z}, \quad (\text{even eigenfunctions}) \quad (11.10)$$

$$2\pi k_0 a - \arctan \frac{1}{k_0} - \frac{1}{2} \mathcal{H}[\log G](k_0) = \pi \left( m + \frac{1}{2} \right), \quad m \in \mathbb{Z} \quad (\text{odd eigenfunctions}) \quad (11.11)$$

with the large-value  $\lambda$  corresponding to the solutions with small positive values of  $k_0$ .

For each solution  $k_0$  of transcendental equations (11.8)-(11.9) or (11.10)-(11.11), the corresponding eigenfunction (up to a normalization constant) would be given by (11.7) (with the choice of the appropriate sign  $\pm$ ). That is, we have explicitly, up to a multiplicative normalization constant, even eigenfunctions:

$$f(x) = - \frac{2e^{-2\pi i k_0 a}}{(k_0 - i) X_+(-k_0) (\log \hat{K})'(k_0)} \cos(2\pi k_0 x)$$

$$+ \frac{i}{\pi} \int_{\mathbb{R}} \frac{e^{-2\pi i k a}}{(k+i) X_+(k)} \left[ \frac{\hat{K}(k)}{\hat{K}(k) - \hat{K}(k_0)} - \frac{2k_0}{(k^2 - k_0^2) (\log \hat{K})'(k_0)} \right] \cos(2\pi k x) dk, \quad (11.12)$$

odd eigenfunctions:

$$f(x) = - \frac{2ie^{-2\pi i k_0 a}}{(k_0 - i) X_+(-k_0) (\log \hat{K})'(k_0)} \sin(2\pi k_0 x)$$

$$- \frac{1}{\pi} \int_{\mathbb{R}} \frac{e^{-2\pi i k a}}{(k+i) X_+(k)} \left[ \frac{\hat{K}(k)}{\hat{K}(k) - \hat{K}(k_0)} - \frac{2k_0}{(k^2 - k_0^2) (\log \hat{K})'(k_0)} \right] \sin(2\pi k x) dk, \quad (11.13)$$

where  $X_+$  and  $G$  are given in terms of  $\hat{K}$  and  $k_0$  by (11.6). Note that the pre-trigonometric factors in the first term of (11.12)-(11.13) simplify due to characteristic equations (11.10)-(11.11) leading to the form of eigenfunctions as in the statement of Theorem. □

### 11.3 Solution for small $A$

Theoretical works where the case of small interval is considered are rare but do exist (e.g. see [11]) for the Wiener-Hopf treatment corresponding to a class of inhomogeneous integral equations).

It is convenient to start by rescaling. We denote  $\varphi(x) := f(ax)$ ,  $\eta = \lambda/a$  and rewrite equation (11.2) as

$$\int_{-1}^1 K(a(x-t)) \varphi(t) dt = \eta \varphi(x), \quad x \in (-1, 1). \quad (11.14)$$

Since the interval  $A$  is small, a kernel function can be well approximated by a span of very few elementary basis functions such as monomials in case of Taylor expansion  $K(ax) = \sum_{m=0}^M \frac{K^{(m)}(0)}{m!} (ax)^m$ . This approximation, however, has natural limitations since the resulting integral operator is of finite rank and hence cannot have more than  $M+1$  eigenfunctions. Clearly, to reproduce rich enough structure of the original operator,  $M$  has to be taken very large.

The idea of our approach is still to take advantage of the fact that only a couple of degrees of freedom are needed for decent approximation of a kernel function in the neighborhood of the origin (i.e. on the small interval  $A$ ), and select a class of functions which is, on one hand, solvable and, on the other hand, corresponds to a non-degenerate compact operator, that is an operator with infinite dimensional range.

In particular, as such approximant class, we consider, for  $x \in (-1, 1)$ , a family of functions

$$K_{b,c}(x) := \frac{\sin cx}{\sinh bx}, \quad b, c \in \mathbb{R} \cup i\mathbb{R}. \quad (11.15)$$

All integral operators with kernels from the class (11.15) are very special as they remarkably commute with a differential operator  $-\frac{d}{dx} \left(1 - \frac{\sinh^2 bx}{\sinh^2 b}\right) \frac{d}{dx} + (b^2 + c^2) \frac{\sinh^2 bx}{\sinh^2 b}$  which is an extremely rare situation [10, 32]. Due to such commutation, the integral and differential operators possess a common set of eigenfunctions, and since the spectrum is simple, the original problem is equivalent to solving a boundary-value ODE problem. Namely, the eigenfunctions are regular solutions of

$$-\left(\left(1 - \frac{\sinh^2 bx}{\sinh^2 b}\right) \varphi'(x)\right)' + (b^2 + c^2) \frac{\sinh^2 bx}{\sinh^2 b} \varphi(x) = \mu \varphi(x), \quad x \in (-1, 1). \quad (11.16)$$

The condition of finiteness of solution at the endpoints  $x = \pm 1$  restricts the values of eigenparameter  $\mu \in \mathbb{R}$  to an infinite discrete set. Note that despite sharing the same set of eigenfunctions, eigenvalues  $(\mu_n)_{n=1}^\infty$  of differential operator are different from eigenvalues  $(\lambda_n)_n^\infty$  of the original problem (11.2). The latter can be recovered from (11.14) in a numerically stable way as

$$\lambda_n = \frac{a \int_{-1}^1 \varphi_n(x) \int_{-1}^1 K(a(x-t)) \varphi_n(t) dt dx}{\|\varphi_n\|_{L^2(-1,1)}^2}, \quad n \in \mathbb{N}_+.$$

Let us now consider a particular instance of the described approximation procedure.

In common practical applications a convolution kernel has a “hump” structure, that is a symmetric function concentrated near the origin. Such behavior can be approximated by hyperbolic secant function  $\operatorname{sech} x \equiv \frac{1}{\cosh x}$  belonging to the considered family (11.15) with  $b = 2$ ,  $c = i$ . In other words, instead of (11.14), we now consider its approximate version

$$\int_{-1}^1 \operatorname{sech}(a(x-t)) \varphi(t) dt = \eta \varphi(x), \quad x \in (-1, 1).$$

The corresponding ODE is then

$$-\left(\left(1 - \frac{\sinh^2 ax}{\sinh^2 a}\right) \varphi'(x)\right)' + 3a^2 \frac{\sinh^2 ax}{\sinh^2 a} \varphi(x) = \mu \varphi(x), \quad x \in (-1, 1).$$

Upon further approximation for  $a \ll 1$ , this ODE becomes

$$((1-x^2) \varphi'(x))' + (\mu - 3a^2 x^2) \varphi(x) = 0, \quad x \in (-1, 1)..$$

which is a well-studied equation [24] whose solutions are bounded on  $[-1, 1]$  only for special values  $\mu_n = \chi_{n-1}(\sqrt{3}a)$ ,  $n \in \mathbb{N}_+$  and are expressible as prolate spheroidal wave functions  $\varphi_n(x) = S_{0(n-1)}(\sqrt{3}a, x)$ ,  $n \in \mathbb{N}_+$  (see [27] for the notation).

The efficiency of such approximation was demonstrated on the Poisson kernel  $K(x) = \frac{1}{1+x^2}$  in [3]. This success might be related to the fact that Fourier transform of both kernels have, in some sense, similar structure (in Fourier domain), but this has to be investigated further.

## 11.4 Conclusion

We have described new methods for obtaining asymptotical solutions of convolution integral equations on a finite interval focussing on a notoriously difficult spectral version of such equation.

When the interval is large, under assumption of even parity of the kernel function, as well as mild assumptions on its decay and regularity (and with additional simplifying assumptions on its Fourier transform: positivity and strictly monotonic decay from of the origin), we have found a closed-form approximation to eigenfunctions of the integral operator and formulated characteristic equations for eigenvalues of odd and even part of the spectrum. We also pointed out an alternative form of such transcendental characteristic equations which provides tremendous simplification in spectrum calculation with respect to previously obtained results for particular instances of the kernel functions of the considered class. Structural simplicity of eigenfunctions is also remarkable: away from the interval endpoints they are essentially sine and cosine functions of special frequencies whereas a more complicated integral term dominates behavior near the endpoints. Such behavior is not unexpected as it has been observed for a more restrictive class of kernel functions, namely those rapidly decaying at infinity [12, 16].

While the situation for small intervals is theoretically and practically less interesting, we attempt to make some contribution by advocating the use of non-orthodox kernel approximation. Namely, instead of classical finite-rank operator approximation by polynomials or trigonometric function, we propose to approximate kernel function by a function from a 2-parameter function family that corresponds to a set of compact self-adjoint operators possessing an infinite set of eigenfunctions. The advantage of the selected function family is that it allows reducing the integral equation to an ODE problem, and in some cases solutions are readily available in terms of known special functions. In view of rather standard behavior of general smooth kernel function

near the origin, a suitable approximant from the considered family would suffice to reproduce the main features of the integral operator better than its low dimensional spectral approximation.

In this work, we have only outlined a solution procedure focussing on constructive aspects and providing intuitive justification whereas details, rigorous proofs and study of approximation properties are not given here. For example, from a structure of the neglected term in our large-interval approximation (which we did not even write), it is clear that the faster  $K$  decays at infinity, the better is the approximation, but it is necessary to quantify this precisely and propagate this error of approximation of auxiliary problem into the estimates of the final error terms  $\delta_{n,a}^{(e)}$ ,  $\delta_{n,a}^{(o)}$ ,  $\left\| \mathcal{E}_{n,a}^{(e)} \right\|_{L^\infty(A)}$ ,  $\left\| \mathcal{E}_{n,a}^{(o)} \right\|_{L^\infty(A)}$  appearing in the formulation of Theorem 1. The errors in the small interval case should be estimated as well.

We are confident that presented results can be extended (at the expense of more cumbersome expressions) to even more general class of kernels encompassing those whose Fourier transforms do not necessarily decay strictly monotonically. Additionally, we expect that some of the assumptions can be tightened (e.g. assuming  $\hat{K} \in L^1(\mathbb{R})$  instead of  $K \in C^1(\mathbb{R})$ ).

Detailed account of study of these aspects will be published separately elsewhere [25].

## Acknowledgement

I am very grateful to organizers of UKBIM12 conference and London Mathematical Society for providing me with a travel bursary to partially finance my participation in the conference and hence motivating me to perform this research. I am also indebted to Prof. Arnold's group at the Institute of Analysis and Scientific Computing (TU Wien) for reimbursing the conference fee and my UK visa expenses, and for general support under FWF project I3538-N32.

## References

- [1] Atkinson, C., Leppington, F. G.: The asymptotic solution of some integral equations. *IMA J. App. Math.* **31 (3)** (1983), 169-182.
- [2] Barakat, R.: Finite range integral equations with band-limited displacement kernels. *Int. J. Control* **15 (3)** (1972), 587-594.
- [3] Baratchart, L., Leblond, J., Ponomarev, D.: Solution of a Homogeneous Version of Love Type Integral Equation in Different Asymptotic Regimes. *Integral Methods in Science and Engineering*, Springer (to appear).
- [4] Bellman, R., Latter, R.: On the integral equation  $\lambda f(x) = \int_0^a K(x-y) f(y) dy$ . *Proc. Amer. Math. Soc.* **3** (1952), 884-891.
- [5] Davis, E. A., Lii, K.-S., Politis, D. N.: *Selected works of Murray Rosenblatt*. Springer (2011).
- [6] Gakhov, F. D., Cherskiy, Yu. I.: *The equations of convolution type*. Nauka (1978) (in Russian).
- [7] Gori, F., Palma, C.: On the eigenvalues of the sinc<sup>2</sup> kernel. *J. Phys. A: Math. Gen.* **8** (1975), 1709-1719.
- [8] Grenander, U., Szego, G.: *Toeplitz Forms and Their Applications*. Chelsea Publishing Company (1956).

- [9] Griffiths, R. B.: Magnetization curve at zero temperature for the antiferromagnetic Heisenberg linear chain. *Phys. Rev.* **133** (3A) (1964), A768-A775.
- [10] Grunbaum, F. A.: Differential operators commuting with convolution integral operators. *J. Math. Anal. Appl.* **91** (1983), 80-93.
- [11] Grudsky, S. M., Mikhakovich, S. S.: The convolution equation on small interval. *Izv. VUZov. Sev.-Kav. reg.* **4** (2001), 18-23 (in Russian).
- [12] Hutson, V.: Asymptotic solutions of integral equations with convolution kernels. *Proc. Edinburgh Math. Soc.* **14** (1964), 5-19.
- [13] Hutson, V.: The circular plate condenser at small separations. *Proc. Camb. Phil. Soc.* **59** (1963), 211-224.
- [14] Hutson, V.: The coaxial disc viscometer. *ZAMM* **44** (1964), 365-370.
- [15] Kirsch, A.: *An Introduction to the Mathematical Theory of Inverse Problems*. Springer (2011).
- [16] Knessl, C., Keller, J. B.: Asymptotic properties of eigenvalues of integral equations. *SIAM J. Appl. Math.* **51** (1) (1991), 214-232.
- [17] Latter, R.: Approximate solutions for a class of integral equations. *Quart. Appl. Math.* **16** (1958), 21-31.
- [18] Leblond, J., Ponomarev, D.: On some extremal problems for analytic functions with constraints on real or imaginary parts. *Advances in Complex Analysis and Operator Theory* (2017), 219-236.
- [19] Leonard, A., Mullikin, T. W.: Integral equations with difference kernels on finite intervals. *Trans. Amer. Math. Soc.* **116** (1965), 465-473.
- [20] Love, E. R.: The electrostatic field of two equal circular co-axial conducting disks. *Quat. Journ. Mech. & Appl. Math.* **2** (4) (1949), 428-451.
- [21] Masry, E., Liu, B., Steiglitz, K.: Series expansion of wide-sense stationary random processes. *IEEE Trans. Inf. Theory* **14** (6) (1968), 792-796.
- [22] Noble, B.: *Methods based on Wiener-Hopf technique for the solution of partial differential equations*. AMS/Chelsea Publication (1988).
- [23] Olmstead, E. W., Gautesen, A. K.: Asymptotic solution of some singularly perturbed Fredholm integral equations. *ZAMP* **40** (2) (1989), 230-244.
- [24] Osipov, A., Rokhlin, V., Xiao, H.: *Prolate spheroidal wave functions of order zero*. Springer (2013).
- [25] Ponomarev, D.: Asymptotic solutions of convolution integral equations with even kernels on small or large intervals (in preparation).
- [26] Sakhnovich, L.: *Integral Equations with Difference Kernels on Finite Intervals*. Springer (2015).
- [27] Slepian, D., Pollack, H. O.: Prolate spheroidal wave functions, Fourier analysis and uncertainty - 1. *B. S. T. J.* **40** (1961), 43-64.
- [28] Tracy, C. A., Widom, H.: On the ground state energy of the  $\delta$ -function Bose gas. *J. Phys. A.: Math. Theor.* **49** (2016), 19 pp.
- [29] Tracy, C. A., Widom, H.: On the ground state energy of the  $\delta$ -function Fermi gas. *J. Math. Phys.* **57** (2016), 14 pp.
- [30] van Trigt, C.: Analytically solvable problems in radiative transfer - 1. *Phys. Rev.* **181** (1) (1969), 97-114.
- [31] Widom, H.: Asymptotic behaviour of the eigenvalues of certain integral equations II. *Arch. Rat. Mech. Anal.* **17** (1964), 215-229.
- [32] Wright, P. E.: Finite symmetric convolution operators and singular symmetric differential operators. *J. Math. Anal. Appl.* **148** (1990), 538-547.

## Chapter 12

# On united boundary-domain integral equation for variable coefficient Neumann problem with general right hand side

S.E. Mikhailov<sup>1</sup>, T.G. Ayele<sup>2</sup>, Z.W. Woldemicheal<sup>3</sup>

<sup>1</sup> Department of Mathematics  
Brunel University London  
Kingston Lane  
UB8 3PH, Uxbridge, Middlesex, UK.

<sup>2</sup> Department of Mathematics  
Addis Ababa University  
Addis Ababa  
Ethiopia.

<sup>3</sup> Department of Mathematics  
Addis Ababa University  
Addis Ababa  
Ethiopia.

---

**Abstract.** *The Neumann boundary value problem (BVP) for the linear stationary diffusion second order elliptic Partial differential equation with variable coefficient is reduced to a direct boundary-domain integral equation (BDIE) using an appropriate parametrix (Levi function). The PDE right hand side belongs to the Sobolev space  $\tilde{H}^{-1}(\Omega)$ , when neither classical nor canonical co-normal derivatives are well defined. Solvability, solution uniqueness/non uniqueness, and equivalence of the BDIE to the original BVP, as well as invertibility of the associated operators are analysed in Sobolev (Bessel potential) spaces. It is shown that the BDIE operator for the Neumann BVP are not invertible, and appropriate finite-dimensional perturbations are constructed leading to invertibility.*

---

## 12.1 Introduction

Many applications in science and engineering can be modelled by boundary-value problems (BVPs) for partial differential equations with variable coefficients. Reduction of the BVPs with arbitrarily variable coefficients to explicit boundary integral equations is usually not possible, since the fundamental solution necessary for such reduction is generally not available in an analytical form (except for some special dependence of the coefficients on coordinates). Using a parametrix (Levi function) as a substitute of a fundamental solution, it is possible however to reduce such a BVP to a boundary-domain integral equation (see, e.g., [12, Sect. 18], [17, 18], where the Dirichlet, Neumann and Robin problems for some PDEs were reduced to *indirect* BDIEs). However, many questions about their equivalence to the original BVP, solvability, solution uniqueness and invertibility of corresponding integral operator remained open for rather long time.

Let  $\Omega$  be a bounded open three-dimensional region of  $\mathbb{R}^3$ . For simplicity, we assume that the boundary  $\partial\Omega$  is a simply connected, closed, infinitely smooth surface. Let  $a \in C^\infty(\bar{\Omega})$ ,  $a(x) > 0$  for  $x \in \bar{\Omega}$ .

We consider the scalar elliptic differential equation, which for sufficiently smooth  $u$  has the following strong form

$$Au(x) := A(x, \partial_x)u(x) := \sum_{i=1}^3 \frac{\partial}{\partial x_i} \left( a(x) \frac{\partial u(x)}{\partial x_i} \right) = f(x), \quad x \in \Omega \quad (12.1)$$

where  $u$  is an unknown function and  $f$  is a given function in  $\Omega$ .

In what follows  $\mathcal{D}(\Omega) := C_{comp}^\infty(\Omega)$  denotes the space of Schwartz test functions, and  $\mathcal{D}^*(\Omega)$  denotes the space of Schwartz distributions,  $H^s(\Omega) = H_2^s(\Omega)$ ,  $H^s(\partial\Omega) = H_2^s(\partial\Omega)$  are the Bessel potential spaces, where  $s \in \mathbb{R}$  (see, e.g., [4, 10]). We recall that  $H^s$  coincide with the Sobolev-Slobodetski spaces  $W_2^s$  for any non-negative  $s$ . We denote by  $\tilde{H}^s(\Omega)$  the subspace of  $H^s(\mathbb{R}^3)$ ,  $\tilde{H}^s(\Omega) := \{g : g \in H^s(\mathbb{R}^3), \text{supp } g \subset \bar{\Omega}\}$ . And the space  $H^s(\Omega)$  denotes the space of restriction on  $\Omega$  of distributions from  $H^s(\mathbb{R}^3)$ ,  $H^s(\Omega) = \{r_\Omega g : g \in H^s(\mathbb{R}^3)\}$  where  $r_\Omega$  denotes the restriction operator on  $\Omega$ . We denote the space  $H_{\partial\Omega}^s$  by  $H_{\partial\Omega}^s := \{g : g \in H^s(\mathbb{R}^3), \text{supp } g \subset \bar{\Omega}\}$ .

## 12.2 Co-normal Derivative and the Boundary Value Problem

For  $u \in H^1(\Omega)$ , the partial differential operator  $A$  is understood in the sense of distributions,

$$\langle Au, v \rangle_\Omega := -\mathcal{E}(u, v) \quad \forall v \in \mathcal{D}(\Omega) \quad (12.2)$$

where

$$\mathcal{E}(u, v) := \int_\Omega a(x) \nabla u(x) \cdot \nabla v(x) dx$$

and the duality brackets  $\langle g, \cdot \rangle_\Omega$  denote the value of a linear functional (distribution)  $g$ , extending the usual  $L_2$  dual product.

Since the set  $\mathcal{D}(\Omega)$  is dense in  $\tilde{H}^1(\Omega)$ , formula (12.2) defines (cf. e.g. [20, Section 3.1]), the continuous linear operator  $A : H^1(\Omega) \rightarrow H^{-1}(\Omega) = [\tilde{H}^1(\Omega)]^*$ , where

$$\langle Au, v \rangle_\Omega := -\mathcal{E}(u, v) \quad \forall v \in \tilde{H}^1(\Omega).$$

Let us also consider the different operator,  $\check{A} : H^1(\Omega) \rightarrow \tilde{H}^{-1}(\Omega) = [H^1(\Omega)]^*$

$$\langle \check{A}u, v \rangle_\Omega = -\mathcal{E}(u, v) \quad (12.3)$$

which is evidently continuous and can be written as

$$\check{A}u := \nabla \cdot \check{E}[a\nabla u]$$

Here  $\check{E}$  denotes the operator of extension of functions, defined in  $\Omega$ , by zero outside  $\Omega$  in  $\mathbb{R}^3$ . For any  $u \in H^1(\Omega)$ , the functional  $\check{A}u$  belongs to  $\tilde{H}^{-1}(\Omega)$  and is an extension of the functional  $Au \in H^{-1}(\Omega)$  which domain is thus extended from  $\tilde{H}^1(\Omega)$  to the domain  $H^1(\Omega)$  for  $\check{A}u$ .

From the trace theorem (see, e.g., [4, 5, 10]) for  $u \in H^1(\Omega)$ , it follows that  $\gamma^+u \in H^{\frac{1}{2}}(\partial\Omega)$ , where  $\gamma^+ := \gamma_{\partial\Omega}^+$  is the trace operator on  $\partial\Omega$  from  $\Omega$ . Let also  $\gamma^{-1} : H^{\frac{1}{2}}(\partial\Omega) \rightarrow H^1(\Omega)$  denote a (non-unique) continuous right inverse to the trace operator  $\gamma^+$ , i.e.,  $\gamma^+\gamma^{-1}w = w$  for any  $w \in H^{\frac{1}{2}}(\partial\Omega)$ , and  $(\gamma^{-1})^* : \tilde{H}^{-1}(\Omega) \rightarrow H^{-\frac{1}{2}}(\partial\Omega)$  is the continuous operator dual to  $\gamma^{-1} : H^{\frac{1}{2}}(\partial\Omega) \rightarrow H^1(\Omega)$ , i.e.,  $\langle (\gamma^{-1})^*\tilde{f}, w \rangle_{\partial\Omega} := \langle \tilde{f}, \gamma^{-1}w \rangle_{\Omega}$  for any  $\tilde{f} \in \tilde{H}^{-1}(\Omega)$  and  $w \in H^{\frac{1}{2}}(\partial\Omega)$ .

For  $u \in H^2(\Omega)$ , we can denote by  $T^{c+}$  the corresponding classical (strong) co-normal derivative operator on  $\partial\Omega$  in the sense of traces,

$$T^{c+}u(x) := \sum_{i=1}^3 a(x)n_i^+(x)\gamma^+\left(\frac{\partial u(x)}{\partial x_i}\right) = a(x)\gamma^+\left(\frac{\partial u(x)}{\partial n(x)}\right)$$

where  $n^+(x)$  is the outward (to  $\Omega$ ) unit normal vectors at the point  $x \in \partial\Omega$ . However the classical co-normal derivative operator is generally not well defined if  $u \in H^1(\Omega)$  (cf. an example in [15, Appendix A]).

Let  $u \in H^1(\Omega)$  and  $Au = r_{\Omega}\tilde{f}$  in  $\Omega$  for some  $\tilde{f} \in \tilde{H}^{-1}(\Omega)$ . Then one can correctly define the *generalised co-normal derivative*  $T^+(\tilde{f}, u) \in H^{-\frac{1}{2}}(\partial\Omega)$  with the help of Green's formula (cf., for example, [10, Lemma 4.3], [20, Definition 3.1]),

$$\langle T^+(\tilde{f}, u), w \rangle_{\partial\Omega} := \langle \tilde{f}, \gamma^{-1}w \rangle_{\Omega} + \mathcal{E}(u, \gamma^{-1}w) = \langle \tilde{f} - \check{A}u, \gamma^{-1}w \rangle_{\Omega} \quad \forall w \in H^{\frac{1}{2}}(\partial\Omega). \quad (12.4)$$

By ([10, Lemma 4.3]), ([20, Theorem 5.3]), we have the estimate

$$\left\| T^+(\tilde{f}, u) \right\|_{H^{-\frac{1}{2}}(\partial\Omega)} \leq C_1 \left\| u \right\|_{H^1(\Omega)} + C_2 \left\| \tilde{f} \right\|_{\tilde{H}^{-1}(\Omega)}$$

and the first Green identity holds in the following form for  $u \in H^1(\Omega)$  such that  $Au = r_{\Omega}\tilde{f}$  in  $\Omega$  for some  $\tilde{f} \in \tilde{H}^{-1}(\Omega)$ ,

$$\langle T^+(\tilde{f}, u), \gamma^+v \rangle_{\partial\Omega} = \langle \tilde{f}, v \rangle_{\Omega} + \mathcal{E}(u, v) = \langle \tilde{f} - \check{A}u, v \rangle_{\Omega} \quad \forall v \in H^1(\Omega). \quad (12.5)$$

As follows from Definition (12.4), the generalized co-normal derivative is non-linear with respect to  $u$  for a fixed  $\tilde{f}$ , but still linear with respect to the couple  $(\tilde{f}, u)$ .

Let us also define some subspaces of  $H^s(\Omega)$ , cf. [9, 19, 20, 13].

**Definition 1** Let  $s \in \mathbb{R}$  and  $A_* : H^s(\Omega) \rightarrow \mathcal{D}^*(\Omega)$  be a linear operator. For  $t \geq -\frac{1}{2}$ , we introduce the space  $H^{s,t}(\Omega; A_*) := \{g : g \in H^s(\Omega) : A_*g|_{\Omega} = \tilde{f}_g|_{\Omega}, \tilde{f}_g \in \tilde{H}^t(\Omega)\}$  endowed with the norm  $\|g\|_{H^{s,t}(\Omega; A_*)} := \left( \|g\|_{H^s(\Omega)}^2 + \|\tilde{f}_g\|_{\tilde{H}^t(\Omega)}^2 \right)^{\frac{1}{2}}$ .

The distribution  $\tilde{f}_g \in \tilde{H}^t(\Omega)$ ,  $t \geq -\frac{1}{2}$  in the above definition is an extension of the distribution  $A_*g|_{\Omega} \in H^t(\Omega)$ , and the extension is unique (if it does exist) since any distribution from the

space  $H^t(\mathbb{R}^3)$  with a support in  $\partial\Omega$  is identical zero if  $t \geq -\frac{1}{2}$  (see e.g. [[10], lemma 3.39], [[20], Theorem 2.10]). We denote this extension as the operator  $\tilde{A}_*$ , i.e.,  $\tilde{A}_*g = \tilde{f}_g$ . The uniqueness implies that the norm  $\|g\|_{H^{s,t}(\Omega; A_*)}$  is well defined.

We will mostly use the operators  $A$  or  $\Delta$  as  $A_*$  in the above definition. Note that since  $Au - a\Delta u = \nabla a \cdot \nabla u \in L_2(\Omega)$  for  $u \in H^1(\Omega)$ , we have  $H^{1,-\frac{1}{2}}(\Omega; A) = H^{1,-\frac{1}{2}}(\Omega; \Delta)$ .

For  $u \in H^{1,-\frac{1}{2}}(\Omega; A)$ , we define the *canonical co-normal derivative*  $T^+u \in H^{-\frac{1}{2}}(\partial\Omega)$  (cf. [13, Definition 6.5]),

$$\langle T^+u, w \rangle_{\partial\Omega} := \langle \tilde{A}u, \gamma^{-1}w \rangle_{\Omega} + \mathcal{E}(u, \gamma^{-1}w) = \langle \tilde{A}u - \check{A}u, \gamma^{-1}w \rangle_{\Omega} \quad \forall w \in H^{\frac{1}{2}}(\partial\Omega). \quad (12.6)$$

By Theorem 3.9 in [20] and Theorem 6.6 in [13] the canonical co-normal derivatives  $T^+u$  is independent of (non-unique) choice of the operator  $\gamma^{-1}$ , the operator  $T^+ : H^{1,-\frac{1}{2}}(\Omega; A) \rightarrow H^{-\frac{1}{2}}(\partial\Omega)$  is continuous, and the first Green identity holds in the following form,

$$\langle T^+u, \gamma^+v \rangle_{\partial\Omega} := \langle \tilde{A}u, v \rangle_{\Omega} + \mathcal{E}(u, v) \quad \forall v \in H^1(\Omega). \quad (12.7)$$

The operator  $T^+ : H^{1,t}(\Omega; A) \rightarrow H^{-\frac{1}{2}}(\partial\Omega)$  in Definition (12.6) is continuous for  $t \geq -\frac{1}{2}$ . The canonical co-normal derivative is defined by the function  $u$  and operator  $A$  only and does not depend separately on the right hand side  $\tilde{f}$  (i.e. its behaviour on the boundary), unlike the generalized co-normal derivative defined in (12.4) and the operator  $T^+$  is linear in  $u$ .

For  $u \in H^{1,-\frac{1}{2}}(\Omega; A)$ . Then Definitions (12.4) and (12.6) imply that the generalized co-normal derivative for arbitrary extension  $\tilde{f} \in \tilde{H}^{-1}(\Omega)$  of the distributions  $Au$  can be expressed as

$$\langle T^+(\tilde{f}, u), w \rangle_{\partial\Omega} := \langle T^+u, w \rangle_{\partial\Omega} + \langle \tilde{f} - \tilde{A}u, \gamma^{-1}w \rangle_{\Omega} \quad \forall w \in H^{\frac{1}{2}}(\Omega). \quad (12.8)$$

If  $u \in H^1(\Omega)$  and  $v \in H^{1,0}(\Omega; A)$ , then swapping over the roles of  $u$  and  $v$  in (12.7), we obtain the first Green identity for  $v$ ,

$$\mathcal{E}(u, v) + \int_{\Omega} u(x)Av(x)dx = \langle T^+v, \gamma^+u \rangle_{\partial\Omega}. \quad (12.9)$$

If, in addition,  $Au = \tilde{f}$  in  $\Omega$ , where  $\tilde{f} \in \tilde{H}^{-1}(\Omega)$ , then according to definition of  $T^+(\tilde{f}, u)$  in (12.5), the second Green identity can be written as

$$\langle \tilde{f}, v \rangle_{\Omega} - \int_{\Omega} u(x)Av(x)dx = \langle T^+(\tilde{f}, u), \gamma^+v \rangle_{\partial\Omega} - \langle T^+v, \gamma^+u \rangle_{\partial\Omega}. \quad (12.10)$$

If moreover,  $u, v \in H^{1,0}(\Omega; A)$ , then we arrive at the familiar form of the second Green identity for the canonical extension and canonical co-normal derivatives

$$\int_{\Omega} [v(x)Au(x) - u(x)Av(x)]dx = \langle T^+u, \gamma^+v \rangle_{\partial\Omega} - \langle T^+v, \gamma^+u \rangle_{\partial\Omega}. \quad (12.11)$$

### 12.3 Parametrix and Potential Type Operators

A function  $P(x, y)$  is a parametrix (the Levi function) for the operator  $A(x, \partial_x)$  if

$$A(x, \partial_x)P(x, y) = \delta(x - y) + R(x, y), \quad (12.12)$$

where  $\delta(\cdot)$  is the Dirac distribution and  $R(x, y)$  possesses a weak singularity at  $x = y$ .

It is easy to see that for the operator  $A(x, \partial_x)$  given by the left hand side in (12.1), the function

$$P(x, y) = \frac{-1}{4\pi a(y)|x - y|}, \quad x, y \in \mathbb{R}^3, \quad (12.13)$$

is a parametrix and the corresponding remainder function is

$$R(x, y) = \sum_{i=1}^3 \frac{x_i - y_i}{4\pi a(y)|x - y|^3} \frac{\partial a(x)}{\partial x_i}, \quad x, y \in \mathbb{R}^3 \quad (12.14)$$

Evidently, the parametrix  $P(x, y)$  given by (12.13) is related with the fundamental solution to the operator  $A(y, \partial_x) := a(y)\Delta(\partial_x)$  with the “frozen” coefficient  $a(x) = a(y)$  and  $A(y, \partial_x)P(x, y) = \delta(x - y)$ .

Let  $a \in C^\infty(\mathbb{R}^3)$  and  $a > 0$  a.e. in  $\mathbb{R}^3$ . For scalar functions  $g$ , for which the integrals have sense, the parametrix-based volume potential operator and the remainder potential operator, corresponding to parametrix (12.13) and remainder (12.14) are defined as

$$\begin{aligned} \mathbf{P}g(y) &:= \int_{\mathbb{R}^3} P(x, y)g(x)dx, \quad y \in \mathbb{R}^3 \\ \mathcal{P}g(y) &:= \int_{\Omega} P(x, y)g(x)dx, \quad y \in \Omega \\ \mathcal{R}g(y) &:= \int_{\Omega} R(x, y)g(x)dx, \quad y \in \Omega \end{aligned}$$

The single and double layer surface potential operators, are defined as

$$Vg(y) := - \int_{\partial\Omega} P(x, y)g(x)dS_x, \quad y \notin \partial\Omega \quad (12.15)$$

$$Wg(y) := - \int_{\partial\Omega} [T(x, n(x), \partial_x)P(x, y)]g(x)dS_x, \quad y \notin \partial\Omega \quad (12.16)$$

where the integrals are understood in the distributional sense if  $g$  is not integrable.

The corresponding boundary integral (pseudodifferential) operators of direct surface values of the single layer potential  $\mathcal{V}$  and of the double layer potential  $\mathcal{W}$ , and the co-normal derivatives of the single layer potential  $\mathcal{W}'$  and of the double layer potential  $\mathcal{L}^+$ , for  $y \in \partial\Omega$  are

$$\mathcal{V}g(y) := - \int_{\partial\Omega} P(x, y)g(x)dS_x, \quad (12.17)$$

$$\mathcal{W}g(y) := - \int_{\partial\Omega} [T_x^+ P(x, y)]g(x)dS_x \quad (12.18)$$

$$\mathcal{W}'g(y) := - \int_{\partial\Omega} [T_y^+ P(x, y)]g(x)dS_x, \quad (12.19)$$

$$\mathcal{L}^+g(y) := T^+Wg(y). \quad (12.20)$$

When integrals in (12.15)-(12.19) are not well defined, they can be understood, e.g., as pseudo-differential operators or dual forms.

From definitions (12.13), (12.15), (12.16) one can obtain representations of the parametrix-based potential operators in terms of their counterparts for  $a = 1$  (i.e. associated with the Laplace

operator  $\Delta$ ), which we equip with the subscript  $\Delta$ , cf. [2],

$$\mathbf{P}g = \frac{1}{a}\mathbf{P}_{\Delta}g, \quad \mathcal{P}g = \frac{1}{a}\mathcal{P}_{\Delta}g, \quad \mathcal{R}g = -\frac{1}{a}\sum_{i=1}^3\partial_i\mathcal{P}_{\Delta}[g(\partial_ia)], \quad (12.21)$$

$$Vg = \frac{1}{a}V_{\Delta}g, \quad Wg = \frac{1}{a}W_{\Delta}(ag), \quad (12.22)$$

$$\mathcal{V}g = \frac{1}{a}\mathcal{V}_{\Delta}g, \quad \mathcal{W}g = \frac{1}{a}\mathcal{W}_{\Delta}(ag), \quad (12.23)$$

$$\mathcal{W}'g = \mathcal{W}'_{\Delta}g + \left[ a\frac{\partial}{\partial n}\left(\frac{1}{a}\right) \right] \mathcal{V}_{\Delta}g, \quad (12.24)$$

$$\mathcal{L}^{\pm}g = \mathcal{L}_{\Delta}(ag) + \left[ a\frac{\partial}{\partial n}\left(\frac{1}{a}\right) \right] \mathcal{W}_{\Delta}^{\pm}(ag). \quad (12.25)$$

The jump relations as well as mapping properties of potentials and operators are well known for the case  $a = \text{const}$ . They were extended to the case of variable coefficient  $a(x)$  in [2].

## 12.4 The Third Green Identity and Integral Relations

For  $u \in H^1(\Omega)$  and  $v(x) = P(x, y)$ , where the parametrix  $P(x, y)$  is given by (12.13), the following *generalised third Green identity* can be obtained from (12.4), (12.3), (12.12), see [15, Theorem 4.1], [14, Theorem 4.1],

$$u + \mathcal{R}u + W\gamma^+u = \mathcal{P}\check{A}u \quad \text{in } \Omega,$$

where

$$\mathcal{P}\check{A}u(y) := \langle \check{A}u, P(\cdot, y) \rangle_{\Omega} = -\mathcal{E}(u, P(\cdot, y)) = -\int_{\Omega} a(x)\nabla u(x) \cdot \nabla_x P(x, y) dx.$$

If  $Au = \tilde{f}|_{\Omega}$  in  $\Omega$ , where  $\tilde{f} \in \tilde{H}^{-1}(\Omega)$ , then the generalised third Green identity takes the following form,

$$u + \mathcal{R}u - VT^+(\tilde{f}, u) + W\gamma^+u = \mathcal{P}\tilde{f} \quad \text{in } \Omega, \quad (12.26)$$

For some functions  $\tilde{f}, \Psi$  and  $\Phi$ , let us consider a more general ‘‘indirect’’ integral relation associated with equation (12.26).

$$u + \mathcal{R}u - V\Psi + W\Phi = \mathcal{P}\tilde{f} \quad \text{in } \Omega \quad (12.27)$$

The following statement proved in [15, Lemma 4.2] (see also [14, Lemma 4.2] for Lipschitz domains and more general spaces and coefficients) extends Lemma 4.1 from [2], where the corresponding assertion was proved for  $\tilde{f} \in L_2(\Omega)$ .

**Lemma 1** *Let  $u \in H^1(\Omega)$ ,  $\tilde{f} \in \tilde{H}^{-1}(\Omega)$ ,  $\Psi \in H^{-\frac{1}{2}}(\partial\Omega)$ ,  $\Phi \in H^{\frac{1}{2}}(\partial\Omega)$  satisfy equation (12.27). Then*

$$Au = r_{\Omega}\tilde{f} \quad \text{in } \Omega, \quad (12.28)$$

$$r_{\Omega}V(\Psi - T^+(\tilde{f}, u)) - r_{\Omega}W(\Phi - \gamma^+u) = 0 \quad \text{in } \Omega, \quad (12.29)$$

The following statement was proved in [2, Lemma 4.2].

**Lemma 2 .**

(i) If  $\Psi^* \in H^{-\frac{1}{2}}(\partial\Omega)$  and  $r_\Omega V\Psi^* = 0$  in  $\Omega$ , then  $\Psi^* = 0$ .

(ii) If  $\Phi^* \in H^{\frac{1}{2}}(\partial\Omega)$  and  $r_\Omega W\Phi^* = 0$  in  $\Omega$ , then  $\Phi^* = 0$ .

Let us now generalise Theorem 5.1 from [8] to the right hand side  $\tilde{f} \in \tilde{H}^{-1}(\Omega)$ .

**Theorem 1** Let  $\tilde{f} \in \tilde{H}^{-1}(\Omega)$ . A function  $u \in H^1(\Omega)$  is a solution of PDE  $Au = \tilde{f}|_\Omega$  in  $\Omega$  if and only if it is a solution of boundary-domain integro-differential equation (12.26).

**Proof:** If  $u \in H^1(\Omega)$  solves PDE  $Au = \tilde{f}|_\Omega$  in  $\Omega$ , then it satisfies (12.26). On the other hand, if  $u \in H^1(\Omega)$  solves boundary-domain integro-differential equation (12.26), then using Lemma 1 with  $\Psi = T^+(\tilde{f}, u)$ ,  $\Phi = \gamma^+u$  we obtain that  $u$  satisfies (12.28), which completes the proof.  $\square$

## 12.5 United boundary-domain integral equation for the Neumann problem

We will consider the following *Neumann boundary value problem*. Find a function  $u \in H^1(\Omega)$  satisfying the conditions

$$Au = r_\Omega \tilde{f} \quad \text{in } \Omega, \quad (12.30)$$

$$T^+(\tilde{f}, u) = \psi_0 \quad \text{on } \partial\Omega. \quad (12.31)$$

where  $\tilde{f} \in \tilde{H}^{-1}(\Omega)$ ,  $\psi_0 \in H^{-\frac{1}{2}}(\partial\Omega)$ .

Equation (12.30) is understood in the distributional sense and the Neumann boundary condition (12.31) is understood in the weak sense (12.5). The following assertion is well-known and can be proved e.g. using variational settings and the Lax-Milgram Lemma.

**Theorem 2** (i) The Neumann homogeneous problem, associated with (12.30)-(12.31), admits only one linearly independent solution  $u^0 = 1$  in  $H^1(\Omega)$ .

(ii) The non-homogeneous Neumann problem (12.30)-(12.31) is solvable if and only if the following solvability condition is satisfied

$$\langle \tilde{f}, u^0 \rangle_\Omega - \langle \psi_0, \gamma^+ u^0 \rangle_{\partial\Omega} = 0 \quad (12.32)$$

The united BDIE for the Neumann problem with respect to the unknown function  $u$  has the following form which is similar to the corresponding BDIE in [8] and for localised BDIE system in [7].

**BDIE(N):** Taking (12.26) in the domain, substituting boundary condition (12.31) we derive the following BDIE(N) for  $u \in H^1(\Omega)$  :

$$u + \mathcal{R}u + W\gamma^+u = \mathcal{F}^N \quad \text{in } \Omega \quad (12.33)$$

where

$$\mathcal{F}^N = \mathcal{P}\tilde{f} + V\psi_0 \quad (12.34)$$

Due to the mapping properties of operators involved in (12.33) we have  $\mathcal{F}^N \in H^1(\Omega)$ .

## 12.6 Equivalence and Invertibility Theorem

**Theorem 3** Let  $\tilde{f} \in \tilde{H}^{-1}(\Omega)$ ,  $\psi_0 \in H^{-\frac{1}{2}}(\partial\Omega)$ .

- (i) If a function  $u \in H^1(\Omega)$  the Neumann problem (12.30)-(12.31) in  $\Omega$ . The function  $u$  solves also BDIE (12.33).
- (ii) Vice versa, if a function  $u \in H^1(\Omega)$  solves the BDIE (12.33). The function  $u$  solves also Neumann boundary value problem (12.30)-(12.31) in  $\Omega$ .
- (iii) The homogeneous BDIE(N) has unique linear independent solution  $u^0 = 1$  in  $H^1(\Omega)$ . Condition (12.32) is necessary and sufficient for solvability of the non-homogeneous BDIE (N) in  $H^1(\Omega)$ .

**Proof:**

- i) Let  $u \in H^1(\Omega)$  be a solution of the Neumann problem (12.30)-(12.31). Then due to the third Green identity (12.26), we immediately obtain that  $u$  solves BDIE (12.33).
- ii) Conversely, let  $u \in H^1(\Omega)$  solve BDIE (12.33). Then Lemma 1 for equation (12.33) implies that  $u$  is a solution of equation (12.30) and  $V(\psi_0 - T^+(\tilde{f}, u)) = 0$  in  $\Omega$ . Lemma 2 (i) implies the Neumann boundary condition (12.31) satisfied for  $u$ .
- iii) Theorem 2 along with item (i) and (ii) imply the claims of item (iii) for BDIE (12.33).

□

Let us write BDIE (N) as

$$\mathcal{A}^N u := u + \mathcal{R}u + W\gamma^+ u = \mathcal{F}^N \quad \text{in } \Omega$$

where

$$\mathcal{F}^N = \mathcal{P}\tilde{f} + V\psi_0$$

**Theorem 4** The operator

$$\mathcal{A}^N : H^1(\Omega) \longrightarrow H^1(\Omega) \tag{12.35}$$

is continuous. Moreover, the kernel (null-space) of this operator is spanned by the element  $u^0 = 1$  and thus the kernel of the operator is one-dimensional.

**Proof:** The mapping properties of the potentials, imply continuity of operator (12.35). By Theorem 3 (iii),  $\ker \mathcal{A}^N$  is one-dimensional and is spanned over the element  $u = 1$ . i.e., the equivalence Theorem 3 and Theorem 2 imply that the homogeneous BDIE (12.33) have only one linear independent solution  $u^0 = 1$  in  $H^1(\Omega)$ . Indeed, consider for example, the homogeneous equation  $\mathcal{A}^N u = 0$ . Its zero right hand side  $\mathcal{F}^N = 0$  can be represented (12.34) as interms of  $\tilde{f} = 0$  and  $\psi_0 = 0$ . Then by Theorem 3 (ii),  $u$  is a solution of the Neumann problem (12.30)-(12.31) with the right hand sides  $f = 0$  and  $\psi_0 = 0$ , which has only the one linearly independent solution  $u = 1$ , due to Theorem 2. □

The following Theorem describes the range of the operator  $\mathcal{A}^N$ , i.e give more information about cokernel of this operator. The proof is similar to the proof in [15]. Let  $\gamma^* : H^{s-\frac{3}{2}}(\partial\Omega) \rightarrow H_{\partial\Omega}^{s-2}$  denote the operator adjoint to the trace operator  $\gamma : H^{2-s}(\mathbb{R}^3) \rightarrow H^{\frac{3}{2}-s}(\partial\Omega)$  for  $s < \frac{3}{2}$ .

**Theorem 5** *The cokernel of operator (12.35) is spanned over the functional  $g^{*N} \in \tilde{H}^{-1}(\Omega)$  defined as*

$$g^{*N} := -a\gamma^{+*}\mathcal{V}_{\Delta}^{-1}\gamma^+u^0 \quad (12.36)$$

where  $u^0 = 1$ .

## 12.7 Perturbation of the BDIE (N)

Theorem 3 implies, that even when the solvability condition (12.32) is satisfied, the solution of the BDIE (N) is not unique. By Theorem 5.3, in turn, the BDIE left hand side operator  $\mathcal{A}^N$  has non-zero kernels and thus are not invertible. To find a solution  $u$  from uniquely solvable BDIE with continuously invertible left hand side operator, let us consider, following [11], some BDIE obtained from BDIE (N) by finite-dimensional operator perturbations cf.[7, 16]. Therefore, let us introduce the perturbed counterparts of the BDIE (N):

$$\hat{\mathcal{A}}^N u = \mathcal{F}^N \quad (12.37)$$

where

$$\hat{\mathcal{A}}^N := \mathcal{A}^N + \mathring{\mathcal{A}}^N \text{ and } \mathring{\mathcal{A}}^N u(y) := g^0(u)\mathcal{G}^N(y) = \frac{1}{|\partial\Omega|} \int_{\partial\Omega} u(x)dS (a^{-1}(y)u^0(y))$$

that is,

$$g^0(u) := \frac{1}{|\partial\Omega|} \int_{\partial\Omega} u(x)dS, \mathcal{G}^N(y) := a^{-1}(y)u^0(y) \text{ with } u^0 = 1, \text{ and } |\partial\Omega| := \int_{\partial\Omega} dS.$$

**Theorem 6** (i) *The operator  $\hat{\mathcal{A}}^N : H^1(\Omega) \rightarrow H^1(\Omega)$  is continuous and continuously invertible.*

(ii) *If condition  $g^{*N}(\mathcal{F}^N) = 0$  (or condition (12.32) for  $\mathcal{F}^N$  in the form (12.34) is satisfied, then the unique solution of perturbed BDIE (12.37) gives a solution of original BDIE (N) such that*

$$g^0(u) = \frac{1}{|\partial\Omega|} \int_{\partial\Omega} u(x)dS = 0.$$

**Proof:** For the functional  $g^{*N}$  given by (12.36) in Theorem 5, since the operator  $\mathcal{V}_{\Delta}^{-1} : H^{\frac{1}{2}}(\partial\Omega) \rightarrow H^{-\frac{1}{2}}(\partial\Omega)$  is positive definite and  $u^0 = 1$ , there exists a positive constant  $C$  such that

$$\begin{aligned} g^{*N}(\mathcal{G}^N) &= \langle -a\gamma^{+*}\mathcal{V}_{\Delta}^{-1}\gamma^+u^0, a^{-1}u^0 \rangle_{\Omega} = -\langle \mathcal{V}_{\Delta}^{-1}\gamma^+u^0, \gamma^+u^0 \rangle_{\partial\Omega} \\ &\leq -C \|\gamma^+u^0\|_{H^{\frac{1}{2}}(\partial\Omega)}^2 \\ &\leq -C \|\gamma^+u^0\|_{L(\partial\Omega)}^2 = -C|\partial\Omega|^2 < 0 \end{aligned}$$

On the other hand for  $u^0 = 1$  in  $H^1(\Omega)$

$$g^0(u^0) = \frac{1}{|\partial\Omega|} \int_{\partial\Omega} u^0 dS = 1.$$

Hence Lemma 2 from [11] implies the Theorem claims.  $\square$

## 12.8 Conclusion

In this paper, we have considered the interior Neumann Boundary value problem for a variable coefficient PDE in a bounded domain, where the right hand side function is from  $\tilde{H}^{-1}(\Omega)$  and the Neumann data from the space  $H^{-\frac{1}{2}}(\partial\Omega)$ . The BVP was reduced to a BDIE and the equivalence to the original BVP was shown. The null space of the corresponding BDIE are not trivial. Moreover, the BDIE are neither uniquely nor unconditionally solvable. The kernel and cokernel of this operator was analysed, and appropriate finite dimensional perturbation is constructed to make the perturbed operator invertible and provide a solution of the original BDIE and of the Neumann BVP.

In a similar way one can consider also the BDIEs for other BVP problems in interior and exterior domains, united BDIEs as well as the localised BDIEs, which were analysed in [1, 2, 3, 6, 8].

### Acknowledgement

The third author acknowledges the support of London Mathematical Society Scheme 5 and 1 Grant. He would like also to thank the Department of Mathematics at Oxford Brookes University and Brunel University for hosting his research stay, the Department of Mathematics at Addis Ababa University and ISP (Sweden) for financial support.

## References

- [1] Ayele, T.G. and Mikhailov, S.E.: Analysis of two-operator boundary-domain integral equations for variable-coefficient mixed BVP. *Eurasian Math. J.*, **2(3)**: 20–41, (2011).
- [2] Chkadua, O. Mikhailov, S.E. and Natroshvili, D.: Analysis of direct boundary-domain integral equations for a mixed BVP with variable coefficient, I: Equivalence and Invertibility. *J. Integral Equat. and Appl.* **21(4)**: 499-543, (2009).
- [3] Chkadua, O. Mikhailov, S.E. and Natroshvili, D.: Analysis of direct boundary-domain integral equations for a mixed BVP with variable coefficient, Part II: Solution regularity and asymptotics. *J. Integral Equations Appl.*, **22(1)**: 19–37, (2010).
- [4] Lions, J.L., Magenes, E.: *Non-Homogeneous Boundary Value Problems and Applications*, Vol. 1. Springer, Berlin, Heidelberg, New York (1972).
- [5] Dautray, R. and Lions, J.: *Mathematical Analysis and Numerical Methods for Science and Technology. Integral Equations and Numerical Methods*, vol. 4. Springer: Berlin, Heidelberg-New York, (1990).
- [6] Mikhailov, S.E.: Localized boundary-domain integral formulation for problems with variable coefficients. *International Journal of Engineering Analysis with Boundary Elements.*, **26**: 681–690, (2002).
- [7] Mikhailov, S.E. and Nakhova, I.S.: Mesh-based numerical implementation of the Localized boundary-domain integral equation method to a variable coefficient Neumann problem. *Journal of Engineering Mathematics* ., **51**: 251–259, (2005).
- [8] Mikhailov, S.E.: Analysis of united boundary-domain integral and integro-differential equations for a mixed BVP with variable coefficients. *Math. Meth. Appl. Sci.* **29** 715-739, (2006).
- [9] Costabel, M.: Boundary integral operators on Lipschitz domains: Elementary results. *SIAM J. Math. Anal.*, **19**: 613–626, (1988).

- [10] McLean, W.: *Strongly Elliptic Systems and Boundary Integral Equations*. Cambridge University Press, UK, (2000).
- [11] Mikhailov, S.E.: Finite-dimensional perturbations of linear operators and some applications to boundary integral equations. *Engineering Analysis with Boundary Elements*, **23**: 805—813, (1999).
- [12] Miranda, C.: *Partial differential equations of elliptic type*, Second revised edition. Springer-Verlag, Berlin, (1970).
- [13] Mikhailov, S.E.: *Solution regularity and co-normal derivatives for elliptic systems with non-smooth coefficients on Lipschitz domains*. *J. Math. Anal. Appl.*, **400(1)**: 48—67, (2013).
- [14] Mikhailov, S.E.: Analysis of segregated boundary-domain integral equations for BVPs with non-smooth coefficients on Lipschitz domains. *Boundary Value Problems*, **2018**:87, 1–52, (2018).
- [15] Mikhailov, S.E.: Analysis of segregated Boundary-Domain Integral Equations for Variable-Coefficient Dirichlet and Neumann Problems with General Data. *ArXiv*, 1509.03501:1-32, (2015).
- [16] Mikhailov, S.E. and Mohammed, Nurul A.: Numerical solution and spectrum of boundary-domain integral equation for the Neumann boundary value problem with variable coefficient. *International Journal of Computer Mathematics*, **89(11)**: 1488—1503, (2012).
- [17] Pomp, A.: *The boundary-domain integral method for elliptic systems. with applications in shells*, volume 1683 of *Lecture notes in Mathematics*. Springer, Berlin-Heidelberg- New York, (1998).
- [18] Pomp, A.: *Levi functions for linear elliptic systems with variable coefficients including shell equations*. *Comput. Mech.*, 22:93–99, (1998).
- [19] Grisvard, P.: *Elliptic Problems in Nonsmooth Domains*. Pitman, Boston—London—Melbourne, (1985).
- [20] Mikhailov, S.E.: Traces, extensions and co-normal derivatives for elliptic systems on Lipschitz domains. *J. Math. Analysis and Appl.*, **378**: 324-342, (2011).

## Chapter 13

# BEM for stress concentration and fracture analysis (from jet turbine blades to dental implants)

**M.N. Perelmuter**

Ishlinsky Institute for Problems in Mechanics RAS  
Vernadsky avenue 101-1, Moscow, 119526, Russia.

---

**Abstract.** *The direct boundary integral equation method in the multi-domain formulation is used for solution stress concentration and fracture mechanics problems. Several 3D problems for load-bearing parts of aviation jet engine with stress concentrators of complex shape have been studied. 2D stress analysis of dental implants with screw connection between implant and bone was also performed.*

---

### 13.1 Introduction

Holes, notches, grooves and fillets of various shapes and orientations widely used in modern designs. Among them through - thickness holes with axes inclined to surface (oblique holes) are widely used in cylindrical and spherical shells, jet turbine blades and disks [6, 8]. The stress state is triaxial in nature at the neighborhood of such complex shape stress concentrators and these problems should be considered as the three-dimensional ones. General analytical solutions for stress distributions around stress concentrators exist only for a few two-dimensional problems. For essential three-dimensional stresses concentration problems (for example, oblique holes) analytical solutions do not exist and only experimental analysis, approximate evaluations and numerical modelling can be used [16]. Stress concentration near one oblique hole or arrays of such holes have been analyzed by photoelasticity method [17, 18, 9]. The problems with one oblique hole in flat plates and in thick-walled cylinders were considered with finite and boundary element methods [10, 7, 1].

In this paper the results of numerical analysis of 2D/3D problems for some technical structures with stress concentrators of complex shape and cracks are presented. 2D stress analysis of dental implants with screw connection between implants and bones was also performed. The direct boundary integral equations (DBIE) method in the multi-domain formulation [2] is used as the computation tool. The DBIE for elastostatic problems were written using the fundamental

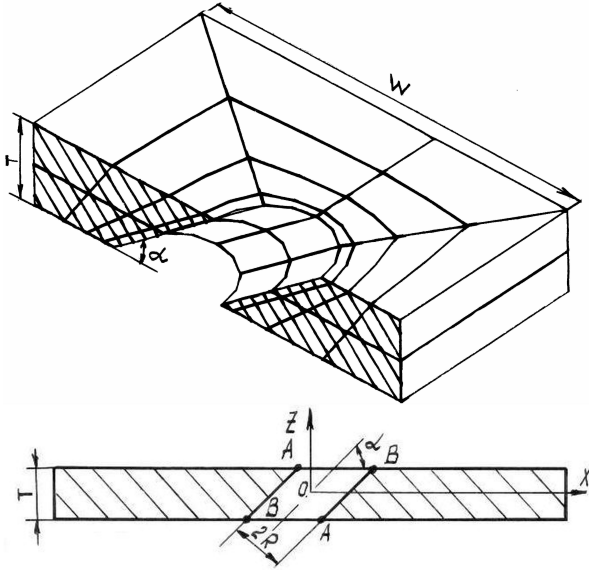


Figure 13.1: Plate with the oblique hole,  $\alpha = 30^\circ$ ,  $W/T = 10$ ,  $T/R = 2$ ,  $|Z| \leq T/2$ , boundary elements model of plate half, number of nodes - 194.

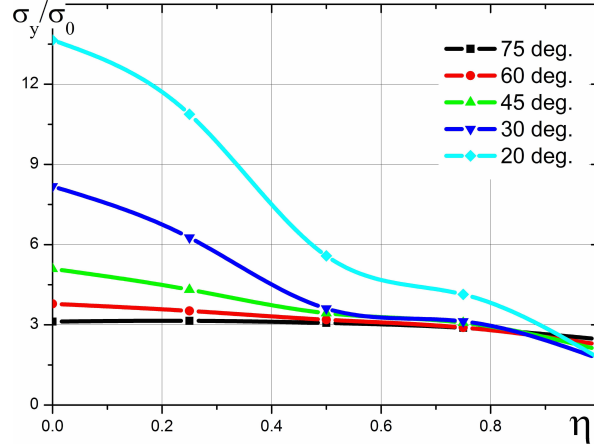


Figure 13.2: Normal stress distribution over thickness of the plate with the oblique hole (along line  $AB$ , Fig. 13.1),  $\eta = (Z/T) + 0.5$ , uniaxial tension.

solutions for isotropic and anisotropic materials [14]. The DBIE multi-domain formulation is applied for modelling of multi-material structures with interfacial cracks. Boundaries of the whole structure subregions are subdivided into isoparametric boundary elements for DBIE numerical solution. Special singular quarter-points boundary elements for modelling asymptotic of displacements and stresses are placed near the crack tips (or along the crack front).

The numerical procedure including the anisotropic fundamental solutions computation has been developed as the author's computer code for the analysis of 2D/3D and axially-symmetrical thermo-elastic multi-material problems. Details of the numerical algorithm and some results for different problems presented in [4, 12, 13]. This author's software have been also used to obtain all results presented in this paper.

## 13.2 Cooling holes in turbine blades walls

Jet turbine blades have very high operational temperature. Holes with axis inclined to a detail wall surfaces are widely used to supply cooling air for decreasing temperature of blades. We will consider plates with oblique and conical holes as a model of cooling holes in turbine blade walls.

Stress concentration analysis for some plates with oblique and conical holes has been performed for different angles of the hole axis obliquity. All computations were performed for Poisson's ratio  $\nu = 0.3$  under uniaxial tension loading  $\sigma_0$ .

At first, we consider the computation results for in-plane uniaxial tension of the plate with one oblique hole. Note, that the sections set of this plate, parallel to its surface, content ellipses with semi-axes  $a = R$  and  $b = R \sin \alpha$ , where  $R$  is the radius of cylindrical surface. The plane  $XOZ$  is the plane of symmetry for uniaxial plate tension in the directions  $OX$  and  $OY$ . The boundary element model with accounting of the problem symmetry is presented in Fig. 13.1, axis  $OY$  is the normal to the plane  $XOZ$ . The computational analysis has been shown that under

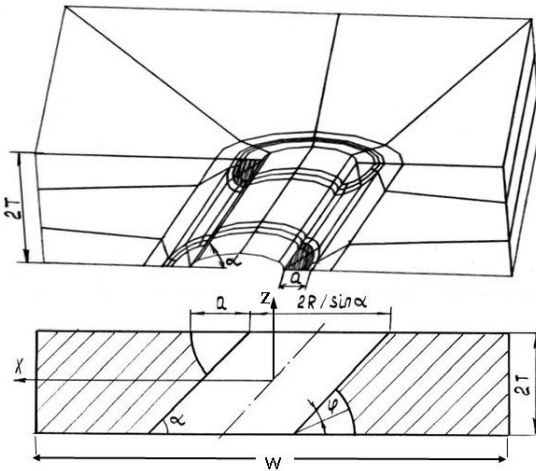


Figure 13.3: Plate with the oblique hole and cracks, number of nodes - 416,  $\alpha = 45^\circ$ ,  $W/T = 10$ ,  $T/R = 1$ ,  $a/2T = 0.25$ .

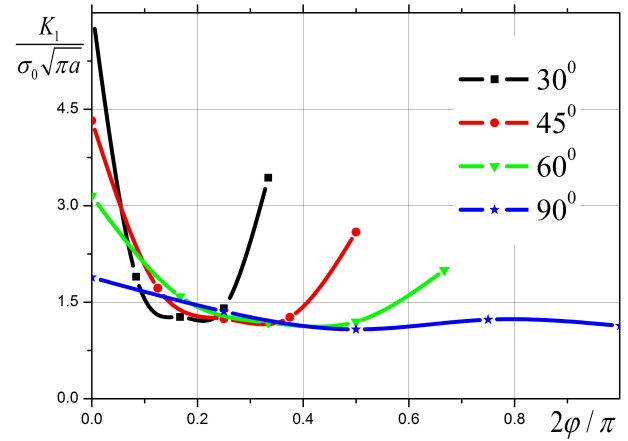


Figure 13.4: SIF distribution over the crack front, uniaxial tension normal to cracks faces.

uniaxial tension in the direction  $OY$  (orthogonal to the hole axis) for hole obliquity angles more than  $75^\circ$  the position of the normal stress maximum ( $\sigma_y$ ) occurs at the plate middle section (see Fig. 13.2). If the hole axis turns in the plane normal to the direction of tensile loading, then the position of the normal stress maximum is shifted to the hole acute-angled edge (for angles less than  $75^\circ$ ). For tension in the orthogonal direction  $OX$  the largest stress  $\sigma_y$  is compressive and occurs also at the hole acute-angled edge.

The distribution of normal stresses along the edge of an inclined hole is highly non-uniform (see Fig. 13.2). The most likely is formation of cracks emanating from the sharp edge of the hole. Taking this into account, plates with two angular cracks, emanating from sharp edges of the hole were analyzed. Plate sizes are:  $R/W = 0.1$ ,  $T/R = 1$  and  $a/2T = 0.25$ . The corresponding discrete model of the plate is shown in Fig. 13.3. The hole inclination angles are  $\alpha = 90^\circ, 60^\circ, 45^\circ, 30^\circ$ . Normal tensile loads were applied on the external plate face ( $y = W/2$ ) parallel to the crack plane. The SIF distributions along the crack front from the hole surface ( $\varphi = 0$ ) to the outer surface of plate are shown in Fig. 13.4. The SIF values are maximal at the hole surface, with  $K_1(0) = (1.5 - 1.8)K_1(\pi/2)$ . The most likely, formation and growth of cracks can be occurred along the oblique hole axis. It should be noted, that for problems with cracks emanating from oblique hole published results were not found. At  $\alpha = 90^\circ$ , the results are qualitatively agreed with the data for two symmetric corner cracks [5, 11].

The rounding of holes edges is used to decrease the stress concentration at the hole acute-angle. To assess this effect computations by BIEM were performed for plates with rounded edges of oblique holes (see Fig. 13.8), where  $\rho$  is the radius of rounding and values of  $\rho/T = 0.25; 0.125$  were used. The boundary conditions for this task are similar to the previous problems (see Fig. 13.1 and Fig. 13.3). The computation results are presented in Fig. 13.5. For rounded hole edges the normal stress at the plate surface becomes less than for an acute angle of the hole. The position of the stress maximum shifts along the hole axis away of the hole edge in the distance about rounded radius. For  $\alpha = 90^\circ$  and  $\alpha = 60^\circ$  the decreasing of the stress maximum is not very noticeable (see see Fig. 13.2). If  $\alpha = 45^\circ$  and  $\alpha = 30^\circ$  the decreasing of the stress maximum is more noticeable, it is up to 20% for  $\alpha = 30^\circ$ .

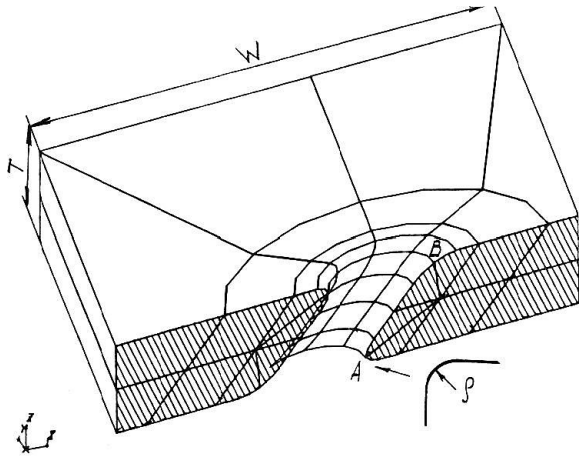


Figure 13.5: Plate with the hole rounded edge,  $W/T = 10$ ,  $T/R = 2$ ,  $\alpha = 45^\circ$ ,  $\rho/T = 0.25$ , number of nodes - 200, tension is transversally to the hole axis.

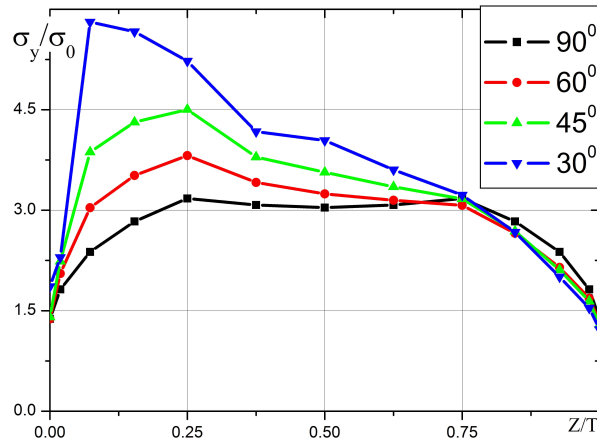


Figure 13.6: Normal stress distribution over thickness of the plate (along line  $AB$ , Fig. 13.5), rounded edge of hole,  $\rho/T = 0.25$ ,  $\eta = Z/T$ ,  $0 \leq Z \leq T$ .

Effects analogous to those observed at the oblique holes edges are also possible near the edges of conical holes. To check this effect numerical analysis of the stress state under uniaxial tension was performed for flat plates with holes in the form of a truncated cone. The radius of the small circle of the truncated cone was assigned equal to the size of small semi-axis of the oblique hole elliptical section. The boundary element model of the plate quarter (with accounting the problem symmetry) for one of the calculation variants is shown in Fig. 13.7. The tensile stresses distribution along the plate thickness as a function of the hole generatrix slope are shown in Fig. 13.8. In the acute edge zone of the conical hole, as in the case of oblique holes, a considerable stress concentration is observed. The maximum of stress is lower at the conical holes acute edge than on the acute edge of the "ordinary" oblique hole.

### 13.3 Cooling holes and locking-joints in jet engines disks

Oblique holes in turbine disks rim serve to supply of cooling air to blades. The angle between the axis of the cooling hole and the radial direction usually does not exceed  $\beta = 20^\circ$  (see Fig. 13.9), which corresponds to  $\alpha \sim 70^\circ$  (see Fig. 13.1). The effect of the hole axis inclination on the stress concentration for such angles is relatively small (see Fig. 13.2). The predominant effect in this case is intersection of the stress concentrators (hole and groove) in the hole transition zone at the groove for attaching of the blade tail. A simplified boundary element model of this problem with the oblique hole and the part of the groove for the blade attaching is shown in Fig. 13.10. On the rear invisible part of the model (Fig. 13.9) uniform tensile loading, simulating the action of circumferential stresses, was applied. On the lower invisible part of this model surface and in the plane passing through the axis of the hole, normal displacements and tangential tractions were assumed to be zero. The sides and top faces of the model, as well as the hole surface, were assumed to be as free of loads. The computation with DBIE gives the normal stress concentration coefficient on the hole edge in the zone intersection between the hole and groove as  $K = 8.02$ . This value is rather high and the hole and groove intersection zone should be

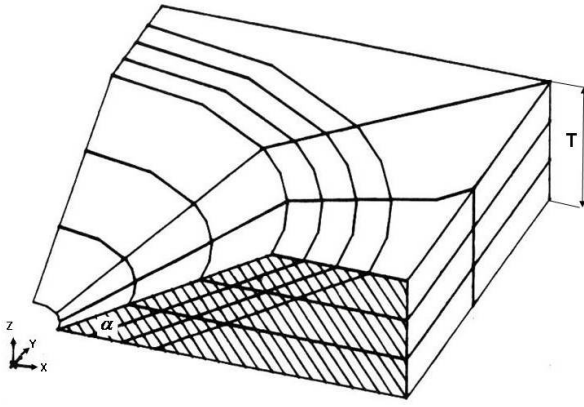


Figure 13.7: Plate with a conical hole, the cone generatrix slope is  $\alpha = 45^\circ$ , boundary element model, number of nodes - 200, uniaxial tension.

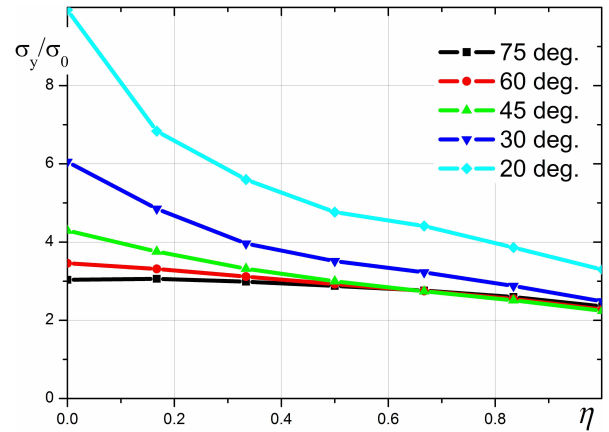


Figure 13.8: Distribution of normal stress over thickness of the plate at the hole edge, the cone generatrix slope variation,  $\eta = Z/T$ ,  $0 \leq Z \leq T$ .

modified to increase the structure durability.

Inclined dovetail-type locking joints (see Fig. 13.11a) are used to fasten compressor blades to disks. The stress concentration in such joints occurs at the base of the fillet (or inter-gap lug) under the action of operational loads. The fillet orientation (or inter-gap lug) relatively the disk rotation axis is determined by the angle between the axis of fillet and the disk rotation axis (installation angle). The stress concentration maximum in structures with inclined fillets occurs near sharp edges, similarly to sharp edges of inclined holes. The study of the stress concentration dependence on the fillet installation angle was performed on the model of the disk lug (2 subregions, see Fig. 13.11b). The blade contact forces distribution along the lug surfaces (in height and length) was assumed to be uniform. The contact stress value was determined by solving 2D contact problem. On the cut surfaces along the disk profile (the visible part of the surface is covered with shading, Fig. 13.11b), constant circumferential stresses were applied. The radial displacements obtained from solving the axisymmetric stress problem were applied on the cut surface across the disk profile. The remain surface part was free of load. The calculation is performed for the installation angles  $\alpha = 0, 10^\circ, 21^\circ, 30^\circ, 40^\circ, 50^\circ$ . With the increasing of the installation angle, the value of the contact stresses was decreased to maintain the same value of the stresses acting on the disk lug. The isolines of the direct stresses on the edge surfaces of the disk lug for  $\alpha = 0$  and  $\alpha = 21^\circ$  (the actual installation angle for the disk) are shown in Fig. 13.12. For direct lug ( $\alpha = 0$ ), the stress distribution is symmetric. At an installation angle of  $\alpha = 21^\circ$ , a significant stress concentration is observed on the sharp edge of the disk lug. Stress concentration factor relatively direct lug is about  $SCF = 1.5$ .

## 13.4 Dental implants with screw connection to bones

Currently, the target of stresses analysis is shifted to biomechanical problems. Among them the big part is occupied by problems of stress concentration analysis in dental implants [3, 15].

We consider the stress analysis of dental implants with screw connection between implants and bones. Screw implants provide good osseointegration at the implant-bone tissue interface. Stress analysis in dental implants is performed in two stages: 1) analysis of the structure as

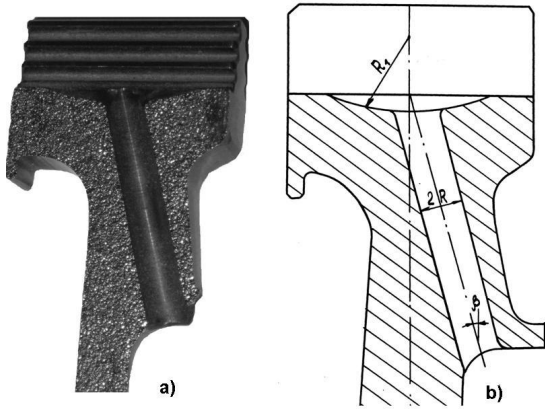


Figure 13.9: a) Photo of the section segment of the rim a turbine disk with a cooling hole; b) the simplified sketch of that segment,  $\beta = 20^\circ$ ,  $R = 3.1 \text{ mm}$ ,  $R_1 = 3R$ .

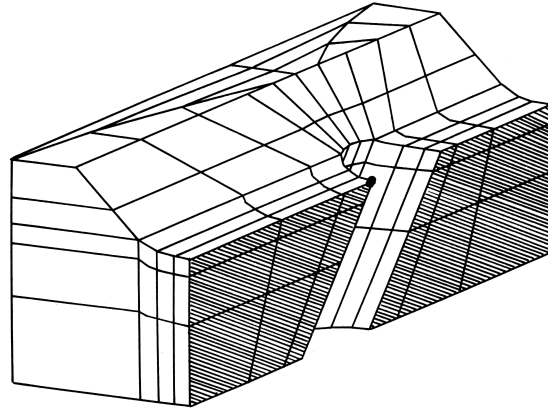


Figure 13.10: Boundary elements model of intersection zone the cooling hole and the fillet for the blade attaching, 2 subregions, number of nodes - 574.

a whole with smoothed screw at the junction of an implant with a bone; 2) analysis of stress concentration in the screwed junction at the interface between an implant and a bone. At the stage of stress concentration analysis it was assumed that hollows in the cancellous bone have formed in the bone after the implant is penetrated into it, are conformed to the screw thread on the implant.

The stress concentration analysis in the joint of an implant and a bone was analyzed under a vertical compressive load for two type of implants materials: ceramics ( $E_1 = 70 \text{ GPa}$ ) and titanium ( $E_1 = 113.8 \text{ GPa}$ ). Due to the problem symmetry, the calculations were performed on a model of half the implant structure (2D, plane strain state). The computational model contains 4 subregions (the implant, the cancellous bone ( $E_2 = 0.49 \text{ GPa}$ ), the cortical bone ( $E_3 = 18.1 \text{ GPa}$ ) and the internal canal ( $E_4 = 18.1 \text{ GPa}$ )) with the total number of nodes 1022 (see Fig. 13.13). On the structure symmetry axis (line  $MN$ ), the displacement along the axis  $OX$  and the tractions along the axis  $OY$  were assumed to be zero. On most part of the cortical bone outer surface (with the exception of the last segment adjacent to the cervical zone), the displacement in the directions of the coordinates axes was assumed to be zero (the narrow dashed strips in Fig. 13.13 are the boundary conditions indicators). A uniformly distributed compressive load was applied to the upper section of the implant. The distributions of the relative equivalent von Mises stresses (stresses were normalized by the external load applied to the implant) along the implant and the cancellous bone boundaries are shown in Fig. 13.14 (for ceramic implant). Stresses along the implant boundary are non-uniformly distributed. The highest stress concentration is observed in the area of the first thread of the implant. The stresses in the bone tissue also have nonuniform distribution, but the greatest stresses in the cancellous bone do not exceed the value of the external stresses applied to the implant. Replacing the implant material with titanium does not lead to significant changes in the distribution of stresses, due to a large difference in the elastic moduli of the implants materials (ceramics or titanium) and the bone tissue.

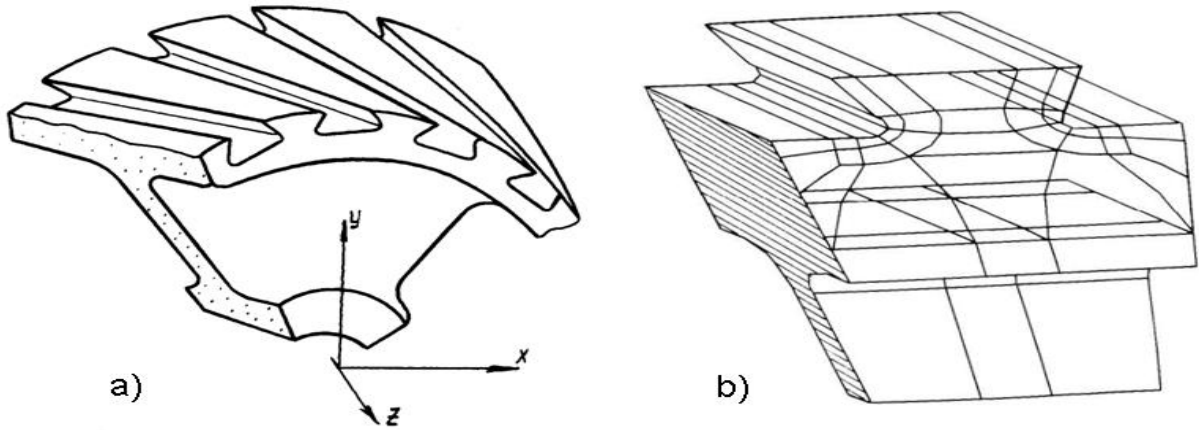


Figure 13.11: a) Sketch of compressor disk with fillet for blades attachment, b)- boundary element model of disk rim part with the oblique edge, installation angle -  $21^\circ$ , two subregions, number of nodes - 412.

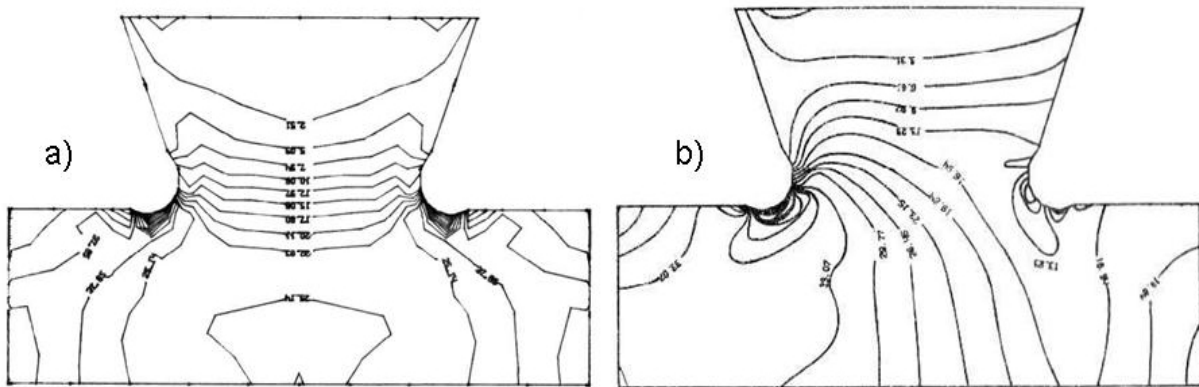


Figure 13.12: Isolines of direct stresses  $\sigma_1$  on the edge section of disk rim part with oblique fillets for blades attachment - a): installation angle  $\alpha = 0$ , b): - installation angle -  $\alpha = 21^\circ$

## 13.5 Conclusions

The presented results demonstrate the effectiveness of the boundary elements method for solution of the complex 2D/3D stress concentration and fracture mechanics problems for wide structures range. This approach may be equally applied for piecewise homogeneous isotropic and anisotropic materials. The regions with the highest stress concentration are very dangerous and these places could very often be as sources of cracks origination. Coatings with self-healing ability will be effective to prevent fatigue in these zones of structures.

## Acknowledgements

This work is supported by the Russian Science Foundation, Project No. 19-19-00616.

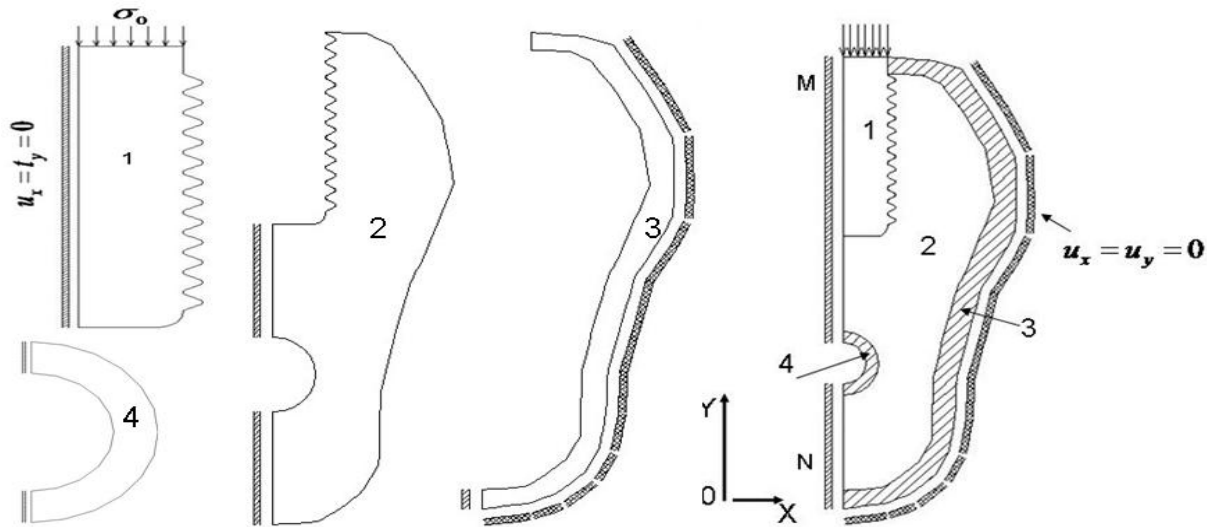


Figure 13.13: 2D model for the analysis of joint the implant and the bone tissue, 4 sub-domains, 1022 nodes (1 - implant, 2 - cancellous bone, 3, 4 - cortical bone), narrow dashed vertical strips in 1, 2, 3, 4 are corresponded to the slide boundary conditions ( $u_x = t_y = 0$ ), dashed strip in 3 is the indicator of the fixed boundary ( $u_x = u_y = 0$ ).

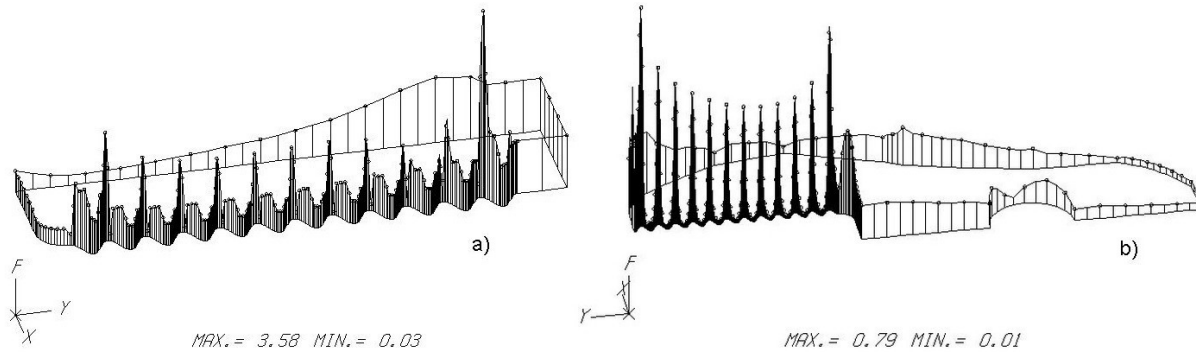


Figure 13.14: Distribution of relative equivalent von Mises stresses  $\sigma_i/\sigma_0$  along the boundary of the analyzed region: a)- ceramic implant; b)- cancellous bone.

## References

- [1] M. J. Abdul-Mihsein, R. T. Fenner, and C. L. Tan. Boundary integral equation analysis of elastic stresses around an oblique hole in a at plate. *The Journal of Strain Analysis for Engineering Design*,

- 14(4):179–185, (1979).
- [2] P.K. Banerjee and R. Butterfield, *Boundary Element Methods in Engineering Science*, McGraw-Hill, London New-York, (1981).
- [3] H.-S. Chang, Y.-C. Chen, Y.-D. Hsieh, and M.-L. Hsu. Stress distribution of two commercial dental implant systems: A three-dimensional finite element analysis. *Journal of Dental Sciences*, **8(3)**:261–271, (2013).
- [4] F. Genna and M. Perelmuter. Speeding-up Finite Element analyses by replacing the linear equation solver with a Boundary Element Part 1: 2D linear elasticity. *Computers & Structures*, **88(13- 14)**: 845–858, (2010).
- [5] A. F. Grandt Jr. and T. E. Kullgren. Stress intensity factors for corner cracked holes under general loading conditions. *Journal of Engineering Materials and Technology*, **103**: 171–176, (1981).
- [6] Trailing edge cooling of a gas turbine blade with perforated blockages with inclined holes. *International Journal of Heat and Mass Transfer*, **73**:9–20, (2014).
- [7] H.-P. Li and F. Ellyin. Determination of stress concentration around an oblique hole by a finite-element technique. *Journal of Vibration, Acoustics, Stress, and Reliability in Design*, **105(2)**:206–211, (1983).
- [8] X. Li, B. Sun, H. You, and L. Wang. Evolution of rolls-royce air-cooled turbine blades and feature analysis. *Procedia Engineering*, **99**:1482–1491, 2015. Asia-Pacific International Symposium on Aerospace Technology, APISAT2014 September 24–26, 2014 Shanghai, China.
- [9] H. W. McKenzie and D. J. White. Stress concentration caused by an oblique round hole in a at plate under uniaxial tension. *Journal of Strain Analysis*, **3(2)**:98–102, (1968).
- [10] G. C. Nihous, C. K. Kinoshita, and S. M. Masutani. Stress concentration factors for oblique holes in pressurized thick-walled cylinders. *Journal of Pressure Vessel Technology*, **130(2)**: 021202–1– 021202–6, (2008).
- [11] D. Peng, C. Wallbrink, and R. Jones. Stress intensity factor solutions for finite body with quarter-elliptical flaws emanating from a notch. *Engineering Fracture Mechanics*, **72(9)**:1329–1343, (2005).
- [12] M. Perelmuter. Boundary element analysis of structures with bridged interfacial cracks. *Computational Mechanics*, **51(4)**:523–534, (2013).
- [13] M. Perelmuter. Analysis of interaction of bridged cracks and weak interfaces. *International Journal of Mechanical Sciences*, **149**:349–360, (2018).
- [14] M. Perelmuter and S. Kuznetsov. BEM analysis of 3D stresses concentration problems of anisotropic composite structures. In V. Wunderlich, editor, *European Conference on Computational Mechanics (ECCM '99), CD-ROM Proceedings, pages 1–8*, Munich, Germany, August 31–September 3 (1999).
- [15] M. Perrella, P. Franciosa, and S. Gerbino. FEM and BEM stress analysis of mandibular bone surrounding a dental implant. *The Open Mechanical Engineering Journal*, **9**:282–292, (2016).
- [16] W. D. Pilkey and R. E. Peterson. *Peterson's stress concentration factors*. Wiley, NewYork, 3rd ed, (2008).
- [17] P. Stanley and B. V. Day. Photoelastic investigation of stresses at an oblique hole in a thick at plate under uniform uniaxial tension. *The Journal of Strain Analysis for Engineering Design*, **25(3)**:157–175, (1990).
- [18] P. Stanley and B. V. Day. On the stresses at arrays of oblique holes in thick plates under equi-biaxial in-plane loading. *Proceedings of the Institution of Mechanical Engineers, Part E: Journal of Process Mechanical Engineering*, **208(1)**: 75–83, (1994).

## Chapter 14

# A boundary element formulation for stress concentration problems in the context of couple-stress elasticity

P. A. Gourgiotis<sup>1</sup>, G. Hattori<sup>2</sup>, J. Trevelyan<sup>1</sup>

<sup>1</sup> Department of Engineering  
Durham University  
South Road  
DH1 3LE, Durham, County Durham, UK.

<sup>2</sup> Department of Engineering  
University of Cambridge  
Trumpington Street  
CB2 1PZ, Cambridge, Cambridgeshire, UK.

---

**Abstract.** *The macroscopic behaviour of materials with non-homogeneous microstructure like composites, bones and concrete is strongly influenced by their material characteristic lengths. Standard continuum mechanics theories are inherently size independent. Couple-stress is the simplest generalised continuum mechanics theory that can encompass the possibility of predicting size effects. Its origins date back to the early works of the Cosserat brothers, and has attracted renewed attention from researchers recently. In this work, we derive a new set of fundamental solutions in closed form to be used conjointly with the boundary element method (BEM). A new boundary integral equation arises to obtain the moments and rotations introduced by the couple-stress formulation. We validate our proposed approach with analytical results obtained by Mindlin.*

---

### 14.1 Introduction

The macroscopical behaviour of most microstructured materials with non-homogeneous microstructure, like ceramics, composites, bones and foams is strongly influenced by their material characteristic lengths, especially in the presence of large stress (or strain) gradients [6]. Relevant size effects have been found when the representative scale of the deformation field becomes comparable to the length scale of the microstructure [3]. However, the classical theory of elasticity does not take the length scale into account, hence size effects are not included in this framework.

To overcome this limitation, a generalised continuum approach is employed in the present study based on the theory of couple-stress elasticity (also known as constrained Cosserat theory) [9, 13]. This theory may be viewed as a first step generalisation of classical elasticity theory where the strain-energy density and the resulting constitutive relations depend, besides the usual infinitesimal strains, on rotation gradients. Characteristic material lengths are introduced through the constitutive formulation showing that the couple-stress theory encompasses the analytical possibility of size effects, absent from the classical theory.

The boundary element method (BEM) has been largely used in continuum mechanics applications, especially fracture mechanics [1, 5] and more recently using isogeometric approaches [10]. The BEM has several advantages, including the boundary-only discretisation and high accuracy, which are desirable characteristics when studying generalised continuum mechanics problems. In the present work, we present a BEM for plane-strain problems in isotropic Cosserat materials. The Green's functions for a concentrated force and moment are derived in closed form. Additionally, a new boundary integral equation is introduced since the rotation and the displacements are independent on the boundary of the body. Our numerical results are compared with known analytical solutions in the context of couple-stress theory, such as the hole in an infinite space and a half-space, where the effects of the pertinent Cosserat lengths upon the macroscopic response of the material are investigated.

## 14.2 Governing equations

In the couple-stress framework, the equations of equilibrium for a 2D body under plane-strain conditions are given by:

$$\sigma_{11,1} + \sigma_{21,2} + b_1 = 0 \quad (14.1)$$

$$\sigma_{12,1} + \sigma_{22,2} + b_2 = 0 \quad (14.2)$$

$$\sigma_{12} - \sigma_{21} + m_{13,1} + m_{23,2} + Y_3 = 0 \quad (14.3)$$

where  $\sigma_{ij}$  is the asymmetric stress tensor,  $m_{13}$  and  $m_{23}$  are the non-vanishing components of the couple-stress tensor,  $b_j$  represents the body force vector and  $Y_3$  is the out-of-plane component of the body couple. The indices  $i$  and  $j$  range from 1 to 3. Also,  $(,i)$  stands for the partial derivative with respect to  $x_i$ .

The kinematic relations are given by:

$$\varepsilon_{11} = u_{1,1}; \quad \varepsilon_{22} = u_{2,2}; \quad \varepsilon_{12} = \varepsilon_{21} = \frac{1}{2}(u_{1,2} + u_{2,1}) \quad (14.4)$$

$$\omega = \frac{1}{2}(u_{2,1} - u_{1,2}); \quad \kappa_{13} = \omega_{,1}; \quad \kappa_{23} = \omega_{,2} \quad (14.5)$$

where  $\varepsilon_{ij}$  is the strain tensor,  $u_i$  are the displacements,  $\omega$  represents the rotation with respect to the  $x_3$ -axis and  $\kappa_{13}$  and  $\kappa_{23}$  are the non-vanishing components of the curvature tensor.

Finally, the constitutive equations in the couple-stress theory have the following form [11]:

$$\sigma_{11} = (\lambda + 2\mu)\varepsilon_{11} + \lambda\varepsilon_{22} \quad (14.6)$$

$$\sigma_{22} = (\lambda + 2\mu)\varepsilon_{22} + \lambda\varepsilon_{11} \quad (14.7)$$

$$\sigma_{12} + \sigma_{21} = 4\mu\varepsilon_{12} \quad (14.8)$$

$$m_{13} = 4\mu\ell^2\kappa_{13} \quad (14.9)$$

$$m_{23} = 4\mu\ell^2\kappa_{23} \quad (14.10)$$

where  $\lambda$  and  $\mu$  are the Lamé moduli, and  $\ell$  is the characteristic material length.

Combining Eqs. (14.1-14.10), we obtain the following system of fourth order partial differential equations for the displacements

$$\mu \nabla^2 u_1 + (\lambda + \mu) d_{,1} + 2\mu \ell^2 (\nabla^2 \omega)_{,2} + b_1 + \frac{1}{2} Y_{3,2} = 0$$

$$\mu \nabla^2 u_2 + (\lambda + \mu) d_{,2} + 2\mu \ell^2 (\nabla^2 \omega)_{,1} + b_2 - \frac{1}{2} Y_{3,1} = 0$$

where  $d$  is the dilatation and is defined as

$$d = \frac{\partial u_1}{\partial x_1} + \frac{\partial u_2}{\partial x_2}$$

### 14.3 The boundary element method (BEM) for the couple-stress theory

The BEM formulation relies on boundary integral equations (BIE). In the couple-stress formulation, we require two BIEs, a vector equation for the displacements (DBIE) and a scalar equation for the out-of-plane rotation for the rotation, which we denote as rotation boundary integral equation (RBIE). The displacement boundary integral equation (DBIE) can be written as

$$c_{ij}(\xi) u_i(\xi) + \int_{\Gamma} T_{ij}^F(x, \xi) u_i(x) d\Gamma(x) + \int_{\Gamma} R_j^F(x, \xi) \omega(x) d\Gamma(x) = \int_{\Gamma} U_{ij}^F(x, \xi) t_i(x) d\Gamma + \int_{\Gamma} \Omega_j^F(x, \xi) m(x) d\Gamma(x)$$

where  $\Gamma$  stands for the boundaries of the domain  $\Omega$ ;  $f$  denotes the Cauchy Principal Value (CPV) integration;  $t_i$  are the tractions;  $m$  represents the moment traction;  $c_{ij}$  is the free term deriving from the CPV integration of the strongly singular kernels  $T_{ij}^F$ ;  $U_{ij}^F$  and  $T_{ij}^F$  are the displacement and traction fundamental solutions, respectively, while  $R_j^F$  and  $\Omega_j^F$  are the moment and rotation fundamental solutions. One should note that the superscript  $F$  relates to a concentrated unit force load acting in an infinite domain for the fundamental solutions present in the DBIE.

The RBIE is defined as

$$c(\xi) \omega(\xi) + \int_{\Gamma} T_i^C(x, \xi) u_i(x) d\Gamma(x) + \int_{\Gamma} R^C(x, \xi) \omega(x) d\Gamma(x) = \int_{\Gamma} U_i^C(x, \xi) t_i(x) d\Gamma + \int_{\Gamma} \Omega^C(x, \xi) m(x) d\Gamma(x)$$

where  $T_i^C$ ,  $U_i^C$ ,  $R^C$  and  $\Omega^C$  respectively denote the traction, displacement, moment and rotation fundamental solutions arising from an out-of-plane concentrated unit moment about the  $x_3$  axis in an infinite domain. The additional free term  $c(\xi)$  arises from the strongly singular kernel  $R^C$ .

The fundamental solutions were obtained using the plane-strain assumptions and an isotropic couple-stress material. As mentioned previously, the Green's functions are calculated for two different loading conditions: one for the in-plane concentrated unit force (as in classical elasticity)

and one for the out-of-plane concentrated unit moment. The fundamental solutions arising from the unit force are given as:

$$\begin{aligned}
U_{ik} &= \frac{1}{8\pi\mu(1-\nu)} [r, {}^i r, {}^k - (3-4\nu) \log r \delta_{ik}] \\
&\quad - \frac{1}{2\pi\mu} \left[ \left( r, {}^i r, {}^k - \frac{1}{2} \delta_{ik} \right) \left( \frac{2\ell^2}{r^2} - K_2 \left[ \frac{r}{\ell} \right] \right) + \frac{1}{2} K_0 \left[ \frac{r}{\ell} \right] \delta_{ik} \right] \\
\Omega_k &= -\frac{e_{qk} r, {}^q}{4\pi\mu\ell} \left[ \frac{\ell}{r} - K_1 \left[ \frac{r}{\ell} \right] \right] \\
\Sigma_{ijk} &= \frac{1}{4\pi(1-\nu)r} [(1-2\nu)(r, {}_j \delta_{ik} + r, {}_i \delta_{kj} - r, {}_k \delta_{ij}) + 2r, {}_i r, {}_j r, {}_k] - \frac{1}{\pi r} (r, {}_j \delta_{ik} + r, {}_j \delta_{kj} + r, {}_k \delta_{ij} \\
&\quad - 4r, {}_i r, {}_j r, {}_k) \left( \frac{2\ell^2}{r^2} - K_2 \left[ \frac{r}{\ell} \right] \right) - \frac{1}{\pi\ell} (r, {}_i r, {}_j r, {}_k - r, {}_j \delta_{ik}) K_1 \left[ \frac{r}{\ell} \right] \\
M_{i3k} &= \frac{e_{qk}}{\pi} r, {}^i r, {}^q \left( \frac{2\ell^2}{r^2} - K_2 \left[ \frac{r}{\ell} \right] \right) - \frac{e_{ik}\ell}{\pi r} \left( \frac{\ell}{r} - K_1 \left[ \frac{r}{\ell} \right] \right)
\end{aligned}$$

where  $K_n[x]$  is the modified Bessel function of  $n$ -th order,  $\delta_{ij}$  is the Kronecker delta,  $r_i = x_i - \xi_i$ ,  $r = |\mathbf{x} - \boldsymbol{\xi}|$  is the distance between collocation and observation points, and  $e_{ij}$  stands for the 2D permutation tensor ( $e_{11} = e_{22} = 0$ ,  $e_{12} = -e_{21} = 1$ ).

In the same way, the fundamental solutions for the unit moment applied in the  $x_3$ -axis are defined by:

$$\begin{aligned}
U_{i3} &= -\frac{e_{iq} r, {}^q}{4\pi\mu r} \left( 1 - \frac{r}{\ell} K_1 \left[ \frac{r}{\ell} \right] \right) \\
\Omega_3 &= \frac{1}{8\pi\mu\ell^2} K_0 \left[ \frac{r}{\ell} \right] \\
\Sigma_{ij3} &= \frac{1}{4\pi\ell^2} (e_{iq} r, {}_j r, {}^q + e_{jq} r, {}^q r, {}_i) \left( \frac{2\ell^2}{r^2} - K_2 \left[ \frac{r}{\ell} \right] \right) - \frac{e_{ij}}{4\pi\ell^2} K_0 \left[ \frac{r}{\ell} \right] \\
M_{i33} &= -\frac{r, {}^i}{2\pi\ell} K_1 \left[ \frac{r}{\ell} \right]
\end{aligned}$$

The force tractions  $T_{ij}^F$  and  $T^C$  and the moment tractions  $R_j^F$  and  $R^C$  are obtained by multiplying the stress tensor  $\Sigma_{ijk}$  and moment tensor  $M_{i3k}$  by the unit outward normal  $\mathbf{n}$ .

### 14.3.1 Regularisation

The DBIE and RBIE present strong and weak singularities that must be dealt with before a numerical integration scheme can be applied. In the case of weak singularities, the Telles transformation [12] provides a simple regularisation procedure to remove the  $\mathcal{O}(\ln r)$  singularity, making it possible to use a regular Gauss-Legendre quadrature.

For the strongly singular kernels, there is a singularity of  $\mathcal{O}(1/r)$ . An easy and simple way to evaluate the singular integrals is to employ the rigid body translation and rotation assumptions. These procedures avoid the calculation of the singular integral in an explicit form, such as that performed by Guiggiani [4] using the singularity subtraction technique. The rigid body approach is explained in detail in [2]. The rigid body rotation follows the same idea for a fixed rotation with respect to a given point in space. In this work we assume a rotation with respect to the origin of the coordinate system.

## 14.4 Numerical examples

### 14.4.1 Hole in an infinite domain subjected to bi-axial loading

We validate our BEM formulation for couple-stress using the analytical solution proposed by Mindlin [8], who investigated the couple-stress influence in the stress field for an infinite plate containing a hole of radius  $a$  for uniaxial and biaxial loading conditions. The problem is illustrated in Figure 14.1.

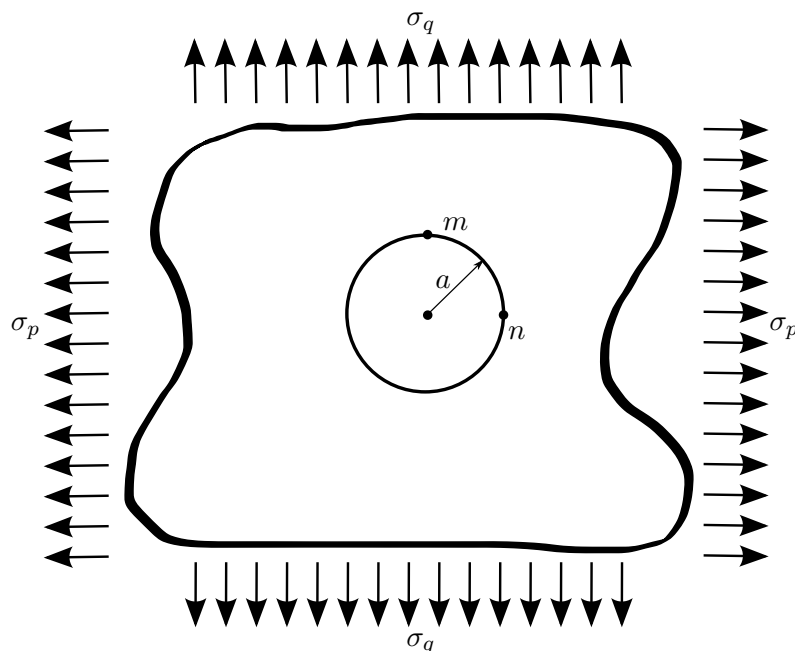


Figure 14.1: Infinite plate with a hole.

We model the infinite plate as a square plate of dimension  $w$  where  $w = 500a$  for an arbitrary material. The material properties are  $E = 10000$  (Young's modulus) and  $\nu = 0.33$  (Poisson's ratio) with  $a = 1$ . We assume  $\sigma_p = 1$  and  $\sigma_q = 2$ . The results are illustrated in Figures 14.2(a) and 14.2(b). An excellent agreement is obtained between the BEM couple-stress and the analytical solution.

### 14.4.2 Hole near surface in a half-space

Next, we study a hole near a traction-free surface in a half-space problem, subjected to a remote tensile loading. Mindlin [7] has obtained an analytical solution in the context of classical elasticity using a bipolar coordinates formulation for the so-called "tunnel" problem, illustrated in Figure 14.3. The stress concentration factors (SCF) obtained at different positions ( $m$ ,  $n$  and  $p$  in Figure 14.3) are evaluated using the following expressions:

(a) Maximum stress

(b) Minimum stress

Figure 14.2: Tangential stress on the hole due to a biaxial loading.

$$\begin{aligned}\sigma_p &= 2T \left[ 1 + (\cosh \alpha_1 - 1) \left( 0.5 \sinh^{-1} \alpha_1 + 2 e^{-2\alpha_1} + \sum_{n=2}^{\infty} N_n \right) \right] \\ \sigma_n &= 2T \left[ 1 + (\cosh \alpha_1 + 1) \left( 0.5 \sinh^{-1} \alpha_1 - 2 e^{-2\alpha_1} + \sum_{n=2}^{\infty} (-1)^n N_n \right) \right] \\ \sigma_m &= T \left[ 1 + 4 \left( e^{-\alpha_1} \sinh^{-1} \alpha_1 + 2 \sum_{n=2}^{\infty} (-1)^n n A_n \right) \right]\end{aligned}$$

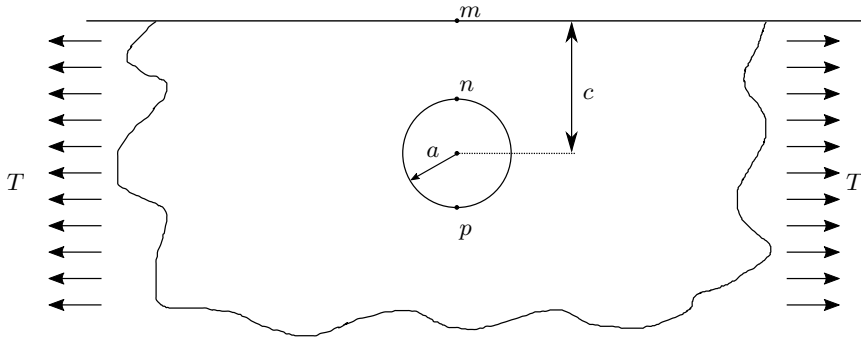


Figure 14.3: Hole near surface in a half-space.

where  $T$  is the tensile loading, and  $\alpha_1$  is a dimensionless parameter that depends upon the geometric ratio  $c/a$  and is given in [7], and

$$A_n = -\frac{n^2 \sinh \alpha_1^2 - n \sinh \alpha_1 \cosh \alpha_1 + e^{-n\alpha_1} \sinh n\alpha_1}{2(\sinh n\alpha_1^2 - n^2 \sinh \alpha_1^2)}$$

$$N_n = \frac{n^2 \sinh \alpha_1 \cosh n\alpha_1 - n \sinh n\alpha_1 \cosh \alpha_1}{\sinh n\alpha_1^2 - n^2 \sinh \alpha_1^2} - 2n(n \sinh \alpha_1 - \cosh \alpha_1)e^{-n\alpha_1}$$

Figure 14.4 depicts the analytical SCFs for different ratios of  $c/a$  for the classical continuum mechanics framework. While the SCF does not vary significantly at  $m$  and  $p$ , it depends on the distance  $c$  at point  $n$ . As expected, lower values of  $c$  lead to larger values of the SCF at that location. For larger values of  $c$ , the solution will become equivalent to the infinite plate with a hole problem.

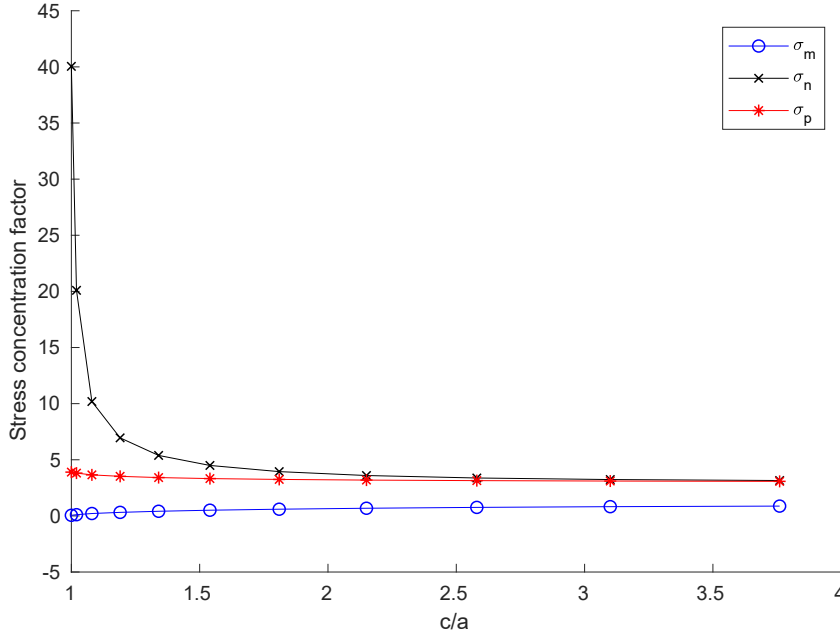


Figure 14.4: Analytical solution for the hole near surface in a half-space.

We model the half-space plate as a square plate of dimension  $w$  where  $w = 500a$ . The material properties are  $E = 10000$  (Young's modulus) and  $\nu = 0.33$  (Poisson's ratio). We

investigate the influence of the length scale for several values of  $c/a$  taken from [7]. Figure 14.5 shows the SCF variation for  $c/a = 3.76$  for values of  $1 \leq a/\ell \leq 1000$ . We can verify that for  $a/\ell \geq 50$ , the values of the SCFs match the analytical solutions for classical continuum mechanics (dashed lines). As  $a/\ell$  decreases, we can observe that the SCF at  $n$  and  $p$  decreases accordingly, which is in agreement with the fact that the length scale becomes predominant, leading to a stiffer zone around the hole. In this case, since the ratio  $c/a$  is large, the decrease of the SCF is similar for the point ( $n$ ) which is closer to the free surface and its antipodal point ( $p$ ) away from the free surface. The SCF at the surface increases as  $a/\ell$  becomes smaller.

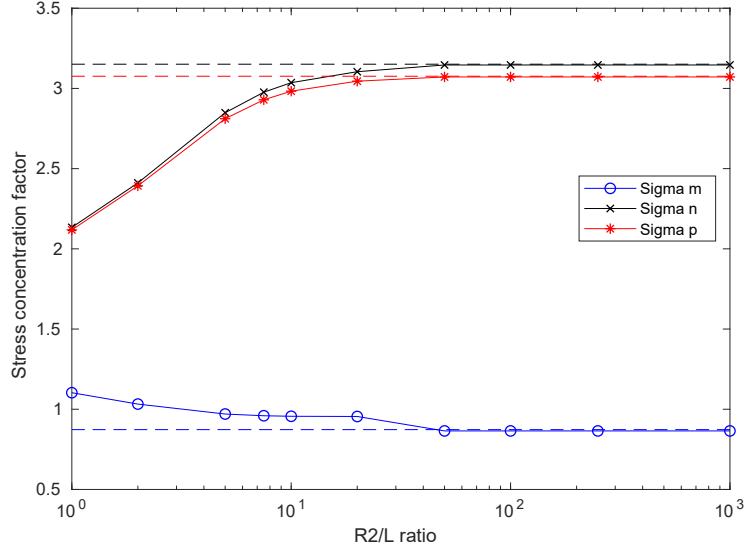


Figure 14.5: Stress concentration factors due to tensile loading -  $c/a = 3.76$ .

Next, we investigate  $c/a = 1.54$ , where the hole is very close to the surface. Figure 14.6 depicts the results. In this case, the results agree with the analytical solution for  $a/\ell \geq 100$ , and as the ratio  $c/a$  decreases, the SCF at  $n$  decreases at a faster rate than at  $p$ . The SCF only presents higher values at  $m$  for  $a/\ell < 20$ , where a fast increase of the SCF is observed as compared to its classical counterpart. The influence of the length scale  $\ell$  becomes more evident when the distance between the hole and the surface is reduced.

## 14.5 Conclusions

We presented a formulation for couple-stress elasticity in the BEM framework. New fundamental solutions have been obtained in closed form. The formulation has been validated against benchmark problems with known analytical solutions, illustrating the accuracy of the proposed approach. Future work will involve the development of an isogeometric formulation to obtain a smoother representation of the variables.

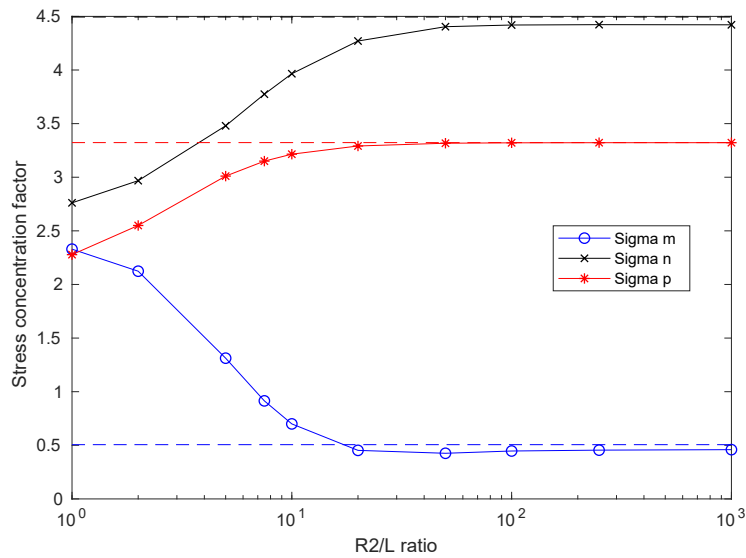


Figure 14.6: Stress concentration factors due to tensile loading -  $c/a = 1.54$ .

## References

- [1] Alatawi, I. A. and Trevelyan, J.: A direct evaluation of stress intensity factors using the extended dual boundary element method. *Engng. Anal. Bound. Elem.* **52** (2015) 56–63.
- [2] Brebbia, C. A. and Domínguez, J.: *Boundary Elements: An Introductory Course (second edition)*. Computational Mechanics Publications (1992).
- [3] Fleck, N. A. and Hutchinson, J. W.: Strain gradient plasticity. *Adv. Appl. Mech.* **33** (1997) 295–361.
- [4] Guiggiani, M.: Formulation and numerical treatment of boundary integral equations with hypersingular kernels. *Singular Int. Bound. Elem. Meth.* (1998) 85–124.
- [5] Hattori, G., Alatawi, I. A. and Trevelyan, J.: An extended boundary element method formulation for the direct calculation of the stress intensity factors in fully anisotropic materials. *Int. J. Numer. Meth. Engng.* **109(7)** (2017) 965–981.
- [6] Maranganti, R. and Sharma, P.: Length scales at which classical elasticity breaks down for various materials. *Phys. Rev. Lett.* **98** (2007) 195504.
- [7] Mindlin, R. D.: Stress distribution around a hole near the edge of a plate under tension. *Proc. Soc. Exp. Stress Anal.* **5(2)** (1948) 56–68.
- [8] Mindlin, R. D.: Influence of couple-stresses on stress concentrations. *Exp. Mech.* **3(1)** (1963) 1–7.
- [9] Mindlin, R. D. and Tiersten, H. F.: Effects of couple-stresses in linear elasticity. *Arch. Ration. Mech. Anal.* **11** (1962), 415–448.

- [10] Simpson, R.N., Bordas, S.P.A., Trevelyan, J. and Rabczuk, T.: A two-dimensional isogeometric boundary element method for elastostatic analysis. *Comput. Meth. Appl. Mech. Engng.* **209-212** (2012) 87–100.
- [11] Sokolowski, M.: *Theory of Couple-Stresses in Bodies with Constrained Rotations*. Springer, (1970).
- [12] Telles, J. C. F.: A self-adaptive co-ordinate transformation for efficient numerical evaluation of general boundary element integrals. *Int. J. Numer. Meth. Engng.*, **24(5)**, (1987) 959–973.
- [13] Toupin, R. A.: Elastic materials with couple-stresses. *Arch. Ration. Mech. Anal.* **11**, (1962) 385-414.

## Chapter 15

# A Single-Layer Approach for Biharmonic Data Completion

Roman Chapko<sup>1</sup>, B. Tomas Johansson<sup>2</sup>

<sup>1</sup> Faculty of Applied Mathematics and Informatics  
Ivan Franko National University of Lviv  
79000 Lviv, Ukraine

<sup>2</sup> Mathematics, EAS  
Aston University  
B4 7ET Birmingham, UK

---

**Abstract.** *An annular thin plate with a given load is considered having clamped boundary conditions on the outer boundary and the normal derivative being zero on the inner boundary. Data is completed on the inner boundary from the additional information of the normal bending moment on the outer boundary. It leads to an inverse ill-posed problem for the biharmonic equation. The solution is represented as a biharmonic single-layer potential, and matching against the given data renders a system of boundary integrals to be solved for densities over the boundary curves. This system is discretised using the Nyström method and then solved by incorporating Tikhonov regularization. Numerical results are presented for annular domains showing the efficiency of the data completion approach.*

---

### 15.1 Introduction

Let  $u$  be a solution to the biharmonic equation

$$\Delta^2 u = 0 \quad \text{in } D \tag{15.1}$$

and suppose additionally that  $u$  satisfies the following conditions on the boundary,

$$u = f \quad \text{on } \Gamma_2, \quad Nu = g \quad \text{on } \Gamma \quad \text{and} \quad Mu = h \quad \text{on } \Gamma_2. \tag{15.2}$$

Here,  $D$  is an annular domain in  $\mathbb{R}^2$  with boundary  $\Gamma$  consisting of two simple closed non-intersecting curves  $\Gamma_2$  and  $\Gamma_1$ , with  $\Gamma_1$  contained in the bounded interior of  $\Gamma_2$ . The boundary operators are defined as

$$\begin{aligned} Nu &= \frac{\partial u}{\partial n}, \\ Mu &= \nu \Delta u + (1 - \nu) (u_{x_1 x_1} n_1^2 + 2u_{x_1 x_2} n_1 n_2 + u_{x_2 x_2} n_2^2), \end{aligned} \tag{15.3}$$

with  $n = (n_1, n_2)$  the outward unit normal to  $\Gamma$  and  $0 < \nu < 1$ . In plate theory,  $M$  is the normal bending moment and  $\nu$  the Poisson ratio, and the solution  $u$  is the vertical deflection. We assume that there exists a classical or weak solution to (15.1)–(15.2). Uniqueness of a solution follows from [5, Lemma 3.2]. Stability with respect to the data cannot be guaranteed, that is the problem is ill-posed.

An application of (15.1)–(15.2) is the following. Given is the load of a thin plate together with clamped boundary conditions on  $\Gamma_2$  (zero deflection and normal derivative). The inner boundary is inaccessible for measurements but it is known that the boundary conditions there are either clamped or roller-supported (normal derivative and normal twisting moment being zero). Hence, only zero normal derivative is known on  $\Gamma_1$ . To complete the data on  $\Gamma_1$ , an additional measurement consisting of the normal bending moment on  $\Gamma_2$  is taken. Due to linearity, the problem can be transformed into one with zero load and non-homogeneous boundary conditions, and we obtain the model (15.1)–(15.2).

The similar problem but with  $u$  given on  $\Gamma_1$  instead of the normal derivative has recently been studied in [5, 6] proposing both an iterative method and an integral equation approach following [2, 4] for the Cauchy problem for the Laplace equation. We refer to the introduction in [5, 6] for further background as well as references to other biharmonic inverse problems, see also [1, 10].

The aim is to propose and investigate, following [6], a boundary integral approach for solving (15.1)–(15.2). Moreover, discretisation, implementation and numerical results shall be presented as well.

The outline of the work is the following. The solution to (15.1)–(15.2) is represented as a biharmonic single-layer potential, and by matching against the data a system of boundary integral equations is obtained. The representation and system are given in Section 15.2. Properties of this system in the form of existence of a solution for a dense set of data is collected in Theorem 1. The system is rewritten using a parametrization of the two boundary curves, see Section 15.2.1. In Section 15.3, discretisation of the boundary integral system is done using the Nyström method taking into account singularities in the integral kernels. Approximations to the missing data on  $\Gamma_1$  are stated at the end of Section 15.3. In Section 15.4, some numerical results are given showing the efficiency of the proposed approach for finding the missing data on the inner boundary curve.

## 15.2 A system of boundary integral equations for (15.1)–(15.2)

We search for the solution of (15.1)–(15.2) as a modified biharmonic single-layer potential,

$$u(x) = \sum_{k=1}^2 \int_{\Gamma_k} \left( G(x, y) \varphi_k(y) + N_y G(x, y) \psi_k(y) \right) ds(y) + w(x), \quad x \in D, \quad (15.4)$$

where  $w(x) = a_0 + a_1 x_1 + a_2 x_2$  and  $(a_0, a_1, a_2) \in \mathbb{R}^3$ ,  $\varphi_k, \psi_k \in C(\Gamma_k)$ ,  $k = 1, 2$ . For properties of the biharmonic single-layer potential with  $w = 0$ , see, for example, [8]. The need for the additional linear term  $w$  for direct problems for the biharmonic equation is explained in [7, Chap. 8.3].

Matching (15.4) against the data (15.2) using jump properties render the system of integral

equations consisting of

$$\begin{cases} \sum_{k=1}^2 \int_{\Gamma_k} \left( G(x, y) \varphi_k(y) + N_y G(x, y) \psi_k(y) \right) ds(y) + w(x) = f(x), & x \in \Gamma_2, \\ \sum_{k=1}^2 \int_{\Gamma_k} \left( N_x G(x, y) \varphi_k(y) + N_x N_y G(x, y) \psi_k(y) \right) ds(y) + Nw(x) = g(x), & x \in \Gamma, \\ \frac{1}{2} \psi_2(x) + \sum_{k=1}^2 \int_{\Gamma_k} \left( M_x G(x, y) \varphi_k(y) + M_x N_y G(x, y) \psi_k(y) \right) ds(y) = h(x), & x \in \Gamma_2, \end{cases} \quad (15.5)$$

and

$$\begin{cases} \sum_{k=1}^2 \int_{\Gamma_k} \varphi_k(y) ds(y) = A_0, \\ \sum_{k=1}^2 \int_{\Gamma_k} (y_1 \varphi_k(y) + n_1(y) \psi_k(y)) ds(y) = A_1, \\ \sum_{k=1}^2 \int_{\Gamma_k} (y_2 \varphi_k(y) + n_2(y) \psi_k(y)) ds(y) = A_2, \end{cases} \quad (15.6)$$

for a given triplet  $(A_0, A_1, A_2) \in \mathbb{R}^3$ .

We write the above system in a more compact form and state some properties of it. Let

$$K(x, y) = \begin{pmatrix} 0 & 0 & 0 & 1 & 0 \\ 0 & 0 & 0 & y_1 & n_1(y) \\ 0 & 0 & 0 & y_2 & n_2(y) \\ 1 & x_1 & x_2 & G(x, y) & N_y G(x, y) \\ 0 & n_1(x) & n_2(x) & N_x G(x, y) & N_x N_y G(x, y) \\ 0 & 0 & 0 & M_x G(x, y) & \frac{1}{2} \delta(x - y) + M_x N_y G(x, y) \end{pmatrix} \quad (15.7)$$

when  $x \in \Gamma_2$  and

$$K(x, y) = \begin{pmatrix} 0 & 0 & 0 & 0 & 0 \\ 0 & 0 & 0 & 0 & 0 \\ 0 & 0 & 0 & 0 & 0 \\ 0 & 0 & 0 & 0 & 0 \\ 0 & n_1(x) & n_2(x) & N_x G(x, y) & N_x N_y G(x, y) \\ 0 & 0 & 0 & 0 & 0 \end{pmatrix} \quad (15.8)$$

when  $x \in \Gamma_1$ . Furthermore, put

$$\bar{\zeta}(x) = \begin{pmatrix} a_0 \\ a_1 \\ a_2 \\ \varphi(x) \\ \psi(x) \end{pmatrix}, \quad x \in \Gamma, \quad \bar{f}(x) = \begin{pmatrix} A_0 \\ A_1 \\ A_2 \\ f(x) \\ g(x) \\ h(x) \end{pmatrix}, \quad x \in \Gamma_2 \quad \text{and} \quad \bar{f}(x) = \begin{pmatrix} 0 \\ 0 \\ 0 \\ 0 \\ g(x) \\ 0 \end{pmatrix}, \quad x \in \Gamma_1. \quad (15.9)$$

Define the operator

$$[A\bar{\zeta}](x) = \int_{\Gamma} K(x, y)\bar{\zeta}(y) ds(y), \quad x \in \Gamma, \quad (15.10)$$

with  $K$  and  $\bar{\zeta}$  from (15.7)–(15.8) and (15.9), respectively. It is assumed without loss of generality that  $\int_{\Gamma} ds(y) = 1$ , and we made the trivial extension of  $f$  and  $h$  to  $\Gamma$  by putting  $f = h = 0$  on  $\Gamma_1$ . The operator  $A$  is considered as a mapping

$$A : \mathbb{R}^3 \times L^2(\Gamma) \times L^2(\Gamma) \rightarrow \mathbb{R}^3 \times L^2(\Gamma_2) \times L^2(\Gamma) \times L^2(\Gamma_2).$$

The system (15.5)–(15.6) can be written

$$[A\bar{\zeta}](x) = \bar{f}(x), \quad x \in \Gamma.$$

Following [3, 6] one can show (the additional term  $w$  in (15.4) is needed in order to establish the result),

**Theorem 1** *The operator  $A$  corresponding to the system (15.5)–(15.6) and defined in (15.10) is injective and has dense range.*

This result implies that Tikhonov regularization is a well-defined strategy for solving (15.5)–(15.6), see [9, Chapt. 16.3].

### 15.2.1 Parametrization of (15.5)–(15.6)

The boundary curves  $\Gamma_{\ell}$ ,  $\ell = 1, 2$ , are assumed given by a parametric representation

$$\Gamma_{\ell} = \{x_{\ell}(s) = (x_{1\ell}(s), x_{2\ell}(s)) : s \in [0, 2\pi]\}.$$

The system (15.5)–(15.6) can then be written in parametric form ( $s \in [0, 2\pi]$ ),

$$\begin{cases} \frac{1}{2\pi} \sum_{k=1}^2 \int_0^{2\pi} \left( H_{2k}(s, \sigma)\varphi_k(\sigma) + \tilde{H}_{2k}(s, \sigma)\psi_k(\sigma) \right) d\sigma + w(x_2(s)) = f(x_2(s)), \\ \frac{1}{2\pi} \sum_{k=1}^2 \int_0^{2\pi} \left( L_{\ell k}(s, \sigma)\varphi_k(\sigma) + \tilde{L}_{\ell k}(s, \sigma)\psi_k(\sigma) \right) d\sigma + Nw(x_{\ell}(s)) = g(x_{\ell}(s)), \quad \ell = 1, 2, \\ -\frac{1}{2|x'_2(s)|} \psi_2(s) + \frac{1}{2\pi} \sum_{k=1}^2 \int_0^{2\pi} \left( Q_{2k}(s, \sigma)\varphi_k(\sigma) + \tilde{Q}_{2k}(s, \sigma)\psi_k(\sigma) \right) d\sigma = h(x_2(s)), \end{cases} \quad (15.11)$$

together with the parametric form of (15.6),

$$\begin{cases} \sum_{k=1}^2 \int_0^{2\pi} \varphi_k(\sigma) d\sigma = A_0, \\ \sum_{k=1}^2 \int_0^{2\pi} (x_{1k}(\sigma)\varphi_k(\sigma) + n_1(x_k(\sigma))\psi_k(\sigma)) d\sigma = A_1, \\ \sum_{k=1}^2 \int_0^{2\pi} (x_{2k}(\sigma)\varphi_k(\sigma) + n_2(x_k(\sigma))\psi_k(\sigma)) d\sigma = A_2. \end{cases} \quad (15.12)$$

We recall from [6] the notation

$$\varphi_\ell(s) := \varphi_k(x_\ell(s))|x'_\ell(s)| \quad \text{and} \quad \psi_\ell(s) := \psi_\ell(x_\ell(s))|x'_\ell(s)|$$

together with

$$\begin{aligned} H_{\ell k}(s, \sigma) &= G(x_\ell(s), x_k(\sigma)), & \tilde{H}_{\ell k}(s, \sigma) &= N_y G(x_\ell(s), x_k(\sigma)), \\ L_{\ell k}(s, \sigma) &= N_x G(x_\ell(s), x_k(\sigma)), & \tilde{L}_{\ell k}(s, \sigma) &= N_x N_y G(x_\ell(s), x_k(\sigma)), \\ Q_{\ell k}(s, \sigma) &= M_x G(x_\ell(s), x_k(\sigma)), & \tilde{Q}_{\ell k}(s, \sigma) &= M_x N_y G(x_\ell(s), x_k(\sigma)). \end{aligned} \quad (15.13)$$

Derivatives of the kernels in (15.13) can contain a logarithmic singularity. It is advantageous to make singularities explicit in order to apply quadratures for the numerical solution of the system (15.11). We rewrite kernels with such singularities as

$$\begin{aligned} H_{\ell\ell}(s, \sigma) &= H_{\ell\ell}^{(1)}(s, \sigma) \ln \left( \frac{4}{e} \sin \frac{s - \sigma}{2} \right) + H_{\ell\ell}^{(2)}(s, \sigma), \\ \tilde{H}_{\ell\ell}(s, \sigma) &= \tilde{H}_{\ell\ell}^{(1)}(s, \sigma) \ln \left( \frac{4}{e} \sin \frac{s - \sigma}{2} \right) + \tilde{H}_{\ell\ell}^{(2)}(s, \sigma), \\ L_{\ell\ell}(s, \sigma) &= L_{\ell\ell}^{(1)}(s, \sigma) \ln \left( \frac{4}{e} \sin \frac{s - \sigma}{2} \right) + L_{\ell\ell}^{(2)}(s, \sigma), \\ \tilde{L}_{\ell\ell}(s, \sigma) &= \tilde{L}_{\ell\ell}^{(1)}(s, \sigma) \ln \left( \frac{4}{e} \sin \frac{s - \sigma}{2} \right) + \tilde{L}_{\ell\ell}^{(2)}(s, \sigma), \\ Q_{\ell\ell}(s, \sigma) &= Q_{\ell\ell}^{(1)}(s, \sigma) \ln \left( \frac{4}{e} \sin \frac{s - \sigma}{2} \right) + Q_{\ell\ell}^{(2)}(s, \sigma), \end{aligned} \quad (15.14)$$

where

$$\begin{aligned} H_{\ell\ell}^{(1)}(s, \sigma) &= \frac{1}{8} |x_\ell(s) - x_\ell(\sigma)|^2, & \tilde{H}_{\ell\ell}^{(1)}(s, \sigma) &= -\frac{1}{4} n(x_\ell(\sigma)) \cdot (x_\ell(s) - x_\ell(\sigma)), \\ L_{\ell\ell}^{(1)}(s, \sigma) &= \frac{1}{4} n(x_\ell(s)) \cdot (x_\ell(s) - x_\ell(\sigma)), & \tilde{L}_{\ell\ell}^{(1)}(s, \sigma) &= -\frac{1}{4} n(x_\ell(s)) \cdot n(x_\ell(\sigma)) \end{aligned}$$

and

$$Q_{\ell\ell}^{(1)}(s, \sigma) = \frac{1 + \nu}{4}.$$

Furthermore, there is the representation

$$H_{\ell\ell}^{(2)}(s, \sigma) = H_{\ell\ell}(s, \sigma) - H_{\ell\ell}^{(1)}(s, \sigma) \ln \left( \frac{4}{e} \sin \frac{s - \sigma}{2} \right),$$

and similar for the other kernels. The diagonal terms are zero in general apart from

$$Q_{\ell\ell}^{(2)}(s, s) = \frac{1 + 3\nu}{4} + \frac{1 + \nu}{4} \ln(e|x'_\ell(s)|^2) \quad \text{and} \quad \tilde{Q}_{\ell\ell}(s, s) = \frac{1 - 3\nu}{4} \frac{n(x_\ell(s)) \cdot x''_\ell(s)}{|x'_\ell(s)|^2}.$$

Having done the above for the kernels, we can apply standard quadrature rules when discretising (15.11)–(15.12).

### 15.3 Discretisation of the system (15.11)–(15.12)

We can then, taking into account (15.14), apply the Nyström method to (15.11)–(15.12) based on the following trigonometric quadrature rules [9],

$$\begin{aligned} \frac{1}{2\pi} \int_0^{2\pi} f(\sigma) d\sigma &\approx \frac{1}{2m} \sum_{k=0}^{2m-1} f(s_k), \\ \frac{1}{2\pi} \int_0^{2\pi} f(\sigma) \ln \left( \frac{4}{e} \sin^2 \frac{s-\sigma}{2} \right) d\sigma &\approx \sum_{k=0}^{2m-1} R_k(s) f(s_k), \end{aligned} \quad (15.15)$$

with mesh points  $s_k = kh$ ,  $k = 0, \dots, 2m-1$ , with  $h = \pi/m$ , and weight functions

$$R_k(s) = -\frac{1}{2m} \left( 1 + 2 \sum_{j=1}^{m-1} \frac{1}{j} \cos j(s - s_k) - \frac{1}{m} \cos m(s - s_k) \right). \quad (15.16)$$

Applying (15.15)–(15.16) in (15.11)–(15.12), we obtain the linear system consisting of

$$\left\{ \begin{aligned} &\sum_{j=0}^{2m-1} \left( [H_{22}^{(1)}(s_i, s_j) R_{|i-j|} + \frac{1}{2m} H_{22}^{(2)}(s_i, s_j)] \varphi_{2j} + \frac{1}{2m} H_{2,1}(s_i, s_j) \varphi_{1,j} \right. \\ &[\tilde{H}_{22}^{(1)}(s_i, s_j) R_{|i-j|} + \frac{1}{2m} \tilde{H}_{22}^{(2)}(s_i, s_j)] \psi_{2j} + \frac{1}{2m} \tilde{H}_{2,1}(s_i, s_j) \psi_{1,j} \Big) \\ &+ w_{2i} = f(x_2(s_i)), \\ &\sum_{j=0}^{2m-1} \left( \frac{1}{2m} L_{\ell,3-\ell}(s_i, s_j) \varphi_{3-\ell,j} + [L_{\ell\ell}^{(1)}(s_i, s_j) R_{|i-j|} + \frac{1}{2m} L_{\ell\ell}^{(2)}(s_i, s_j)] \varphi_{\ell j} \right. \\ &+ \frac{1}{2m} \tilde{L}_{\ell,3-\ell}(s_i, s_j) \psi_{3-\ell,j} + [\tilde{L}_{\ell\ell}^{(1)}(s_i, s_j) R_{|i-j|} + \frac{1}{2m} \tilde{L}_{\ell\ell}^{(2)}(s_i, s_j)] \psi_{\ell j} \Big) \\ &+ Nw_{\ell i} = g(x_\ell(s_i)), \quad \ell = 1, 2, \\ &\sum_{j=0}^{2m-1} \left( \frac{1}{2m} Q_{21}(s_i, s_j) \varphi_{1j} + [Q_{22}^{(1)}(s_i, s_j) R_{|i-j|} + \frac{1}{2m} Q_{22}^{(2)}(s_i, s_j)] \varphi_{2j} \right. \\ &\left. + \frac{1}{2m} (\tilde{Q}_{21}(s_i, s_j) \psi_{1j} + \tilde{Q}_{22}(s_i, s_j) \psi_{2j}) \right) + \frac{\psi_{2i}}{2|x_2'(s_i)|} = h(x_2(s_i)), \end{aligned} \right. \quad (15.17)$$

and

$$\left\{ \begin{aligned} &h \sum_{k=1}^2 \sum_{j=0}^{2m-1} \varphi_{kj} = A_0, \\ &h \sum_{k=1}^2 \sum_{j=0}^{2m-1} (x_{1k}(s_j) \varphi_{kj} + n_1(x_k(s_j)) \psi_{kj}) = A_1, \\ &h \sum_{k=1}^2 \sum_{j=0}^{2m-1} (x_{2k}(s_j) \varphi_{kj} + n_2(x_k(s_j)) \psi_{kj}) = A_2, \end{aligned} \right. \quad (15.18)$$

for  $i = 0, \dots, 2m-1$ , to be solved for  $\varphi_{kj} \approx \varphi_k(s_j)$ ,  $\psi_{kj} \approx \psi_k(s_j)$ ,  $k = 1, 2$ ,  $j = 0, \dots, 2m-1$ . Here,  $w_{\ell i} = w(x_\ell(s_i))$ ,  $Nw_{2i} = Nw(x_2(s_i))$  and  $R_j = R_j(0)$ .

The system (15.17)–(15.18) has a high-condition number since (15.1)–(15.2) is ill-posed, and therefore Tikhonov regularization is incorporated. Denoting the matrix corresponding to this system by  $A$  and the right-hand side by  $F$ , the regularization means solving

$$(A^*A + \alpha I)\phi_\alpha = A^*F, \quad (15.19)$$

where  $A^*$  is the adjoint (transpose) of  $A$ , with  $\alpha > 0$  a regularization parameter to be chosen appropriately.

Using the representation (15.4) the solutions  $u$  is given on the inner boundary curve  $\Gamma_1$  as

$$u(x) = \sum_{k=1}^2 \int_{\Gamma_k} \left( G(x, y)\varphi_k(y) + N_y G(x, y)\psi_k(y) \right) ds(y) + w(x), \quad x \in \Gamma_1.$$

Applying the above discretisation,

$$\begin{aligned} \tilde{u}(x_1(s_i)) &= \sum_{j=0}^{2m-1} \left( [H_{11}^{(1)}(s_i, s_j)R_{|i-j|} + \frac{1}{2m}H_{11}^{(2)}(s_i, s_j)]\varphi_{1j} + \frac{1}{2m}H_{1,2}(s_i, s_j)\varphi_{2,j} \right. \\ &\quad \left. + [\tilde{H}_{11}^{(1)}(s_i, s_j)R_{|i-j|} + \frac{1}{2m}\tilde{H}_{11}^{(2)}(s_i, s_j)]\psi_{1j} + \frac{1}{2m}\tilde{H}_{1,2}(s_i, s_j)\psi_{2,j} \right) + w_{1i}. \end{aligned} \quad (15.20)$$

Similarly, for the normal bending moment

$$Mu(x_1(s_i)) = \frac{1}{2}\psi_1(x) + \sum_{k=1}^2 \int_{\Gamma_k} \left( M_x G(x, y)\varphi_k(y) + M_x N_y G(x, y)\psi_k(y) \right) ds(y), \quad x \in \Gamma_1,$$

with discretisation

$$\begin{aligned} M\tilde{u}(x_1(s_i)) &= \sum_{j=0}^{2m-1} \left( [Q_{11}^{(1)}(s_i, s_j)R_{|i-j|} + \frac{1}{2m}Q_{11}^{(2)}(s_i, s_j)]\varphi_{1j} + \frac{1}{2m}Q_{12}(s_i, s_j)\varphi_{2j} \right. \\ &\quad \left. + \frac{1}{2m} \sum_{k=1}^2 \tilde{Q}_{1k}(s_i, s_j)\psi_{kj} \right) + \frac{\psi_{1i}}{2|x_1'(s_i)|}. \end{aligned} \quad (15.21)$$

## 15.4 Numerical results

We present some numerical results of the data completion in (15.1)–(15.2) for the direct layer approach. In the examples, the Poisson ratio is taken as  $\nu = 0.5$ . The outer boundary curve  $\Gamma_2$  is chosen as a circle with centre at the origin and radius 2, and the inner boundary  $\Gamma_1$  is kite-shaped with parametrization

$$\Gamma_1 = \{x_1(s) = (\cos s + 0.4 \cos 2s, \sin s) : s \in [0, 2\pi]\}.$$

We consider an arbitrary source point  $z_1 \in \mathbb{R}^2 \setminus D$ , and construct the needed boundary data functions as

$$g(x) = NG(x, z_1), \quad x \in \Gamma, \quad f(x) = G(x, z_1), \quad h(x) = MG(x, z_1), \quad x \in \Gamma_2, \quad (15.22)$$

with the operators  $N$  and  $M$  given by (15.3). The exact solution to (15.1)–(15.2) with data (15.22) is  $u_{ex} = G(\cdot, z_1)$  and the computed one is denoted by  $\tilde{u}$ . We can then compare the exact and

$M$	$\delta = 0\%$			$\delta = 3\%$		
	$\alpha$	$e_{2M}$	$e_2$	$\alpha$	$e_{2M}$	$e_2$
8	1E-05	2.8049E-03	6.7686E-05	1E-03	0.22444	0.00718
16	1E-07	1.2493E-04	1.7738E-06	1E-03	0.14669	0.00526
32	1E-11	3.9962E-06	1.0615E-08	1E-04	0.08062	0.00397
64	1E-11	5.0133E-06	7.1706E-09	1E-03	0.07004	0.00194

Table 15.1: The errors on  $\Gamma_1$  for the “direct” single-layer approach with exact ( $\delta = 0\%$ ) and noisy data ( $\delta = 3\%$ ).

the numerically calculated data on the inner boundary  $\Gamma_1$ . The computed approximation of  $u$  and the normal bending moment on  $\Gamma_1$  is calculated using (15.20) and (15.21), respectively.

The discrete relative  $L_2$ -errors of the reconstructions for the data completion problem (15.1)–(15.2) on  $\Gamma_1$  with the proposed approach, that is the errors

$$e_2(\Gamma_1) = \frac{\left( \sum_{i=0}^{2m-1} (u_{ex}(x_1(s_i)) - \tilde{u}(x_1(s_i)))^2 \right)^{1/2}}{\left( \sum_{i=0}^{2m-1} (u_{ex}(x_1(s_i)))^2 \right)^{1/2}}$$

and

$$e_{2M}(\Gamma_1) = \frac{\left( \sum_{i=0}^{2m-1} (Mu_{ex}(x_1(s_i)) - M\tilde{u}(x_1(s_i)))^2 \right)^{1/2}}{\left( \sum_{i=0}^{2m-1} (Mu_{ex}(x_1(s_i)))^2 \right)^{1/2}}$$

are presented in Table 15.1. The sub-index  $2M$  means the (discrete)  $L_2$  norm of the normal bending moment ( $M$ ). In generating the collocation (grid) points  $m = 32$  was chosen and the source point is  $z_1 = (3, 0)$ .

For noisy data, random pointwise errors are added to the corresponding boundary function, with the percentage given in terms of the  $L_2$ -norm. Table 15.1 contains the corresponding errors obtained for the data completion (15.1)–(15.2) using the “direct” single-layer approach, with  $\alpha$  being the Tikhonov regularization parameter in (15.19) chosen by inspection. The choice of the constants in the right-hand side of (15.6) is  $A_0 = 1$ ,  $A_1 = 1$  and  $A_2 = 2$ . It is natural that the reconstruction of the normal bending moment  $Mu$  is less accurate than the function  $u$ , since  $Mu$  contains higher derivatives.

The reconstructions of  $u$  and  $Mu$  corresponding to Table 15.1 follow the respectively exact solution well as indicated by the reported error levels. Plots of the reconstructions versus exact solutions are of the form similar to what have been reported in for example [4], and figures of the approximations are therefore left out.

## 15.5 Conclusion

A boundary data completion problem has been investigated for the biharmonic equation in planar annular domains with clamped boundary conditions on the outer boundary and the normal derivative on the inner boundary. Using a supplementary measurement of the normal bending moment on the outer boundary, a boundary integral method is derived for finding the missing data on the inner boundary. The solution is represented as a biharmonic single-layer potential and the densities over the boundary is determined by imposing the given boundary conditions, rendering a system of boundary integral equations. Discretisation is done using the Nyström method giving a linear system solved by incorporating Tikhonov regularization. Numerical experiments show that stable approximations of the solution and normal bending moment can be obtained on the inner boundary with exact as well as noisy data.

## References

- [1] Atakhodzhaev, M. A.: *Ill-Posed Internal Boundary Value Problems for the Biharmonic Equation*. VSP, Utrecht (2002).
- [2] Borachok, I., Chapko, R. and Johansson, B. T.: Numerical solution of an elliptic 3-dimensional Cauchy problem by the alternating method and boundary integral equations. *J. Inverse Ill-Posed Probl.* **24** (2016), 711–725.
- [3] Cakoni, F. and Kress, R.: Integral equations for inverse problems in corrosion detection from partial Cauchy data. *Inverse Probl. Imaging* **1** (2007), 229–245.
- [4] Chapko, R. and Johansson, B. T.: Boundary-integral approach for the numerical solution of the Cauchy problem for the Laplace equation. Special Issue in Honour of Prof. V. L. Makarov, *Ukrain. Mat. Zh.* **68** (2016), 1665–1682.
- [5] Chapko, R. and Johansson, B. T.: An iterative regularizing method for an incomplete boundary data problem for the biharmonic equation. *ZAMM: Z. Angew. Math. Mech.* **98** (2018), 2010–2021.
- [6] Chapko, R. and Johansson, B. T.: Integral equations for biharmonic data completion. To be published in *Inverse Probl. Imaging*.
- [7] Chen, G. and Zhou, J.: *Boundary Element Methods with Applications to Nonlinear Problems*. Atlantis Press, Paris (2010).
- [8] Costabel, M. and Dauge, M.: Invertibility of the biharmonic single layer potential operator. *Integral Equations Operator Theory* **24** (1996), 46–67.
- [9] Kress, R.: *Linear Integral Equations*, ed. 3., Springer-Verlag, New York (2014).
- [10] Lesnic, D., Elliott, L. and Ingham, D. B.: An alternating boundary element method for solving Cauchy problems for the biharmonic equation. *Inverse Probl. Eng.* **5** (1997), 145–168.

## Chapter 16

# Gradient Recovery for the BEM-based FEM and VEM

D. Seibel, S. Weißer

Department of Mathematics,  
Saarland University  
P.O. Box 15 11 50  
66041 Saarbrücken, Germany

---

**Abstract.** *We propose new gradient recovery schemes for the BEM-based Finite Element Method (BEM-based FEM) and Virtual Element Method (VEM). Supporting general polytopal meshes, the BEM-based FEM and VEM are highly flexible and efficient tools for the numerical solution of boundary value problems in two and three dimensions. We construct the recovered gradient from the gradient of the finite element approximation via local averaging. For the BEM-based FEM, we show that, under certain requirements on the mesh, superconvergence of the recovered gradient is achieved, which means that it converges to the true gradient at a higher rate than the untreated gradient. Moreover, we derive a simple and very efficient a posteriori error estimator, which measures the difference between the unprocessed and recovered gradient as an error indicator. Since the BEM-based FEM and VEM are specifically suited for adaptive refinement, the resulting adaptive algorithms perform very well in numerical examples.*

---

### 16.1 Introduction

Gradient or stress recovery has a long tradition in the context of Finite Element Methods (FEM) [4, 15, 19, 2]. Considered as a post-processing procedure, its primary field of application is found in computational elasticity, where the stresses, fluxes and strains are the main interest rather than the displacements. In this context, the FEM with piece-wise linear elements yields discontinuous results for the gradient, which may be inconvenient for applications like visualisation. Therefore, it is common practice to use post-processing in order to obtain a continuous approximation. Remarkably, experiments indicate that the accuracy is improved thereby. Under certain conditions on the underlying mesh and regularity of the solution, it is even found that the recovered gradient converges at a higher rate than the untreated gradient [16]. This phenomenon is well known as gradient superconvergence or superconvergent recovery. In the past decades, it has been extensively studied and several different post-processing strategies

have been proposed, for example the  $L^2$ -recovery [13] or the popular patch recovery by Zienkiewicz and Zhu [18], which takes a least-squares approach to determine the recovered gradient.

Besides plain gradient reconstruction, the second main application is found in the field of a posteriori error estimation [2]. The approach is rather intuitive: based on the observation that the post-processed gradient is more accurate than the unprocessed gradient, one measures the distance between these two approximations. In other words, if  $\nabla u$  is the exact gradient,  $\nabla u_h$  the gradient of the finite element solution and  $\mathcal{G}u_h$  its reconstruction, the error is estimated by

$$\int_{\Omega} |\nabla u - \nabla u_h|^2 dx \approx \int_{\Omega} |\mathcal{G}u_h - \nabla u_h|^2 dx.$$

Such recovery-based error estimators are quite appealing because of several aspects. First of all, the post-processing, and hence the estimator, is typically designed to be cheap, fast and easy to implement. Secondly, there is a great variety of different recovery strategies available, which highlights the flexibility of the approach. Last but not least, the performance of the estimator is remarkably good, as the estimates are very accurate in most cases.

Yet, the application of gradient recovery is almost limited to standard FEM on triangular or quadrilateral discretisations. In [11], Guo and Zhao propose a Zienkiewicz-Zhu-type recovery scheme for Virtual Element Method (VEM), which is a new FEM-like method for the numerical solution of partial differential equations [5]. The VEM belongs to the family of Galerkin methods based on polytopal grids and, as such, features a great flexibility with handling complex geometries and allows for easy adaptive refinement and coarsening. Despite its newness, it has already been applied to a wide range of problems [6, 8]. Besides the VEM, the hybridised discontinuous Galerkin method [9], the mimetic finite difference method [12] and the BEM-based Finite Element Method (BEM-based FEM) [14] are prominent examples for numerical methods on polytopal grids.

In this work, we formulate gradient recovery schemes by averaging for the lowest order BEM-based FEM and VEM. In Section 16.3, we show that superconvergence is present in special cases. Thereafter, we derive an a posteriori error estimator based on this recovery scheme in Section 16.4. In the final Section 16.5, we see how the averaging technique needs to be modified to work with the VEM.

## 16.2 Preliminaries

Let  $\Omega \subset \mathbb{R}^2$  be a bounded polygonal domain that admits a finite decomposition  $\mathcal{T}_h$  into open non-overlapping polygonal elements  $E$  with maximal diameter  $h > 0$  such that

$$\bar{\Omega} = \bigcup_{E \in \mathcal{T}_h} \bar{E}.$$

The boundary  $\partial E$  of each element  $E$  is assumed to be not self-intersecting. We assume the mesh  $\mathcal{T}_h$  to be shape-regular, i.e., there exists some constant  $\rho > 0$  such that

- Every  $E \in \mathcal{T}_h$  is star-shaped with respect to a ball of radius  $\rho h_E$ , where  $h_E$  is the diameter of  $E$ .
- For every  $E \in \mathcal{T}_h$  and every edge  $e$  of  $E$  the length  $h_e$  of  $e$  is bounded from below  $h_e > \rho h_E$ .

Moreover, we denote by  $x_i$ ,  $i = 1, \dots, N$ , the set of interior nodes of  $\mathcal{T}_h$ .

We use the common notation for function spaces encountered in finite element analysis. We denote by  $L^2(\Omega)$  the space of square-integrable functions and by  $H^k(\Omega)$  the Sobolev space of order  $k \in \mathbb{N}$  with corresponding norms  $\|\cdot\|_{L^2(\Omega)}$  and  $\|\cdot\|_{H^k(\Omega)}$ . Furthermore, we define  $H_0^k(\Omega)$  to be the closure of  $C_0^\infty(\Omega)$  in  $H^k(\Omega)$ .

For simplicity, we consider the Poisson equation with zero Dirichlet conditions and right-hand side  $f \in L^2(\Omega)$ , i.e.,

$$\begin{aligned} -\Delta u &= f, & \text{in } \Omega, \\ u &= 0, & \text{on } \Gamma. \end{aligned} \tag{16.1}$$

It should be noted that the concepts presented here can be easily extended to more general partial differential equations in two and three dimensions. The Galerkin formulation reads: find  $u \in V = H_0^1(\Omega)$  such that

$$\int_{\Omega} \nabla u \cdot \nabla v \, dx = \int_{\Omega} f v \, dx, \quad \forall v \in V. \tag{16.2}$$

We abbreviate the left-hand side by  $a(\cdot, \cdot)$ . In the following, we introduce the shape functions of lowest order used by both methods. Let  $\mathcal{P}_p(E)$  and  $\mathcal{P}_p(e)$  be the spaces of polynomials of degree  $p$  on the element  $E$  and edge  $e$  respectively. We define the local space of shape functions by

$$V_h^E = \left\{ v_h \in H^1(E) \mid \left\{ \begin{array}{ll} -\Delta v_h = 0 & \text{on } E, \\ (v_h)|_e \in \mathcal{P}_1(e) & \text{for every edge } e \text{ of } E \end{array} \right\} \right\}.$$

Consequently, the global finite element space is given by

$$V_h = \{ v_h \in V \mid (v_h)|_E \in V_h^E \, \forall E \in \mathcal{T}_h \} \cap C^0(\bar{\Omega})$$

and we choose the degrees of freedom as nodal values

$$\mathcal{N}_i(v_h) = v_h(x_i), \quad i = 1, \dots, N.$$

The Galerkin approximation to (16.2) reads: find  $u_h \in V_h$  such that

$$\int_{\Omega} \nabla u_h \cdot \nabla v_h \, dx = \int_{\Omega} f v_h \, dx, \quad \forall v_h \in V_h. \tag{16.3}$$

Here is where the two methods depart. The BEM-based FEM uses the theory of boundary integral operators to reformulate (16.3), whereas the VEM reduces the problem to the polynomial component  $\mathcal{P}_1(E)$  of  $V_h^E$ . Regardless of the method in use, we end up with a discrete formulation of the form: find  $u_h \in V_h$  such that

$$a_h(u_h, v_h) = b_h(v_h), \quad \forall v_h \in V_h, \tag{16.4}$$

where

$$a_h(u_h, v_h) = \sum_{E \in \mathcal{T}_h} a_h^E(u_h, v_h), \quad b_h(v_h) = \sum_{E \in \mathcal{T}_h} b_h^E(v_h).$$

Firstly, we consider the discrete bilinear form of the BEM-based FEM. Since  $u_h$  is harmonic in each  $E$ , integration by parts yields

$$\int_E \nabla u_h \cdot \nabla v_h \, dx = - \int_E \Delta u_h v_h \, dx + \int_{\partial E} (\nabla u_h \cdot n) v_h \, dS = \int_{\partial E} (\nabla u_h \cdot n) v_h \, dS,$$

where  $n$  is the outer unit normal field to  $\partial E$ . The normal derivative  $(\nabla u_h \cdot n)|_{\partial E}$  is obtained by means of the Steklov–Poincaré operator  $\mathbf{S}^E$ , see [14] for details. Therefore, the discrete bilinear form is given by

$$a_h^E(u_h, v_h) = \int_{\partial E} \left( \mathbf{S}^E(u_h)|_{\partial E} \right) v_h dS$$

and the right-hand side

$$b_h^E(v_h) = \int_{\partial E} f v_h dS$$

is evaluated via numerical quadrature and the representation formula.

In comparison, the VEM introduces the  $H_0^1$ -orthogonal projection  $\Pi_q^\nabla : V_h^E \rightarrow \mathcal{P}_q(E)$  for  $q \in \mathbb{N}_0$  defined by the relation

$$\int_E \nabla m \cdot \nabla (\Pi_q^\nabla u_h) dx = \int_E \nabla m \cdot \nabla u_h dx, \quad \forall m \in \mathcal{P}_q(E),$$

and an additional constraint to fix the constant part [1]. After choosing a suitable stabilising term  $S^E(\cdot, \cdot)$ , we construct the discrete bilinear form and linear form as follows:

$$a_h^E(u_h, v_h) = \int_E \nabla (\Pi_1^\nabla u_h) \cdot \nabla (\Pi_1^\nabla v_h) dx + S^E(u_h, v_h), \quad b_h^E(v_h) = \int_E f \Pi_1^\nabla v_h dx.$$

It is important to note that the VEM is specifically designed in such a way that the projections are computable from just the degrees of freedoms [5].

Finally, we can rewrite the discrete formulation (16.4) as a system of linear equations by introducing the Lagrangian basis

$$\{\varphi_i\}_{i=1}^N \text{ with } \mathcal{N}_i(\varphi_j) = \begin{cases} 1, & i = j, \\ 0, & i \neq j, \end{cases} \quad \text{for } i, j = 1, \dots, N.$$

Then, the ansatz  $u_h = \sum_{i=1}^N c_i \varphi_i$  with  $c_i \in \mathbb{R}$  leads to

$$Ac = b, \text{ where } A_{ij} = a_h(\varphi_i, \varphi_j), b_i = b_h(\varphi_i), \quad i, j = 1, \dots, N.$$

### 16.3 Superconvergent Gradient Recovery

The primary use of superconvergence lies in the reconstruction of the finite element gradient  $\nabla u_h$  in order to obtain a more accurate approximation to the true gradient  $\nabla u$ .

To give an illustration, we consider the case of bilinear finite elements on a regular mesh made of identical quadrilaterals of size  $h$ . Then, the finite element solution  $u_h$  is bilinear on each element  $E$ , while its gradient  $\nabla u_h$  is piece-wise linear. The main idea now is to reuse the bilinear basis for the recovered gradient  $\mathcal{G}u_h$ . We sample  $\nabla u_h$  at the centroids of the elements and assign to each degree of freedom the average of these values on the corresponding patch, see Figure 16.1. One can prove that the recovered gradient is superconvergent, cf. [16, 2].

With this in mind, we return to the BEM-based FEM and try to replicate the averaging technique for regular hexagonal meshes. The recovery operator  $\mathcal{G} : V_h \rightarrow V_h^2$  produces a finite element function in each component, so we need to determine the degrees of freedom

$$\mathcal{N}_i(\mathcal{G}u_h) = (\mathcal{G}u_h)(x_i) \in \mathbb{R}^2, \quad i = 1, \dots, N.$$

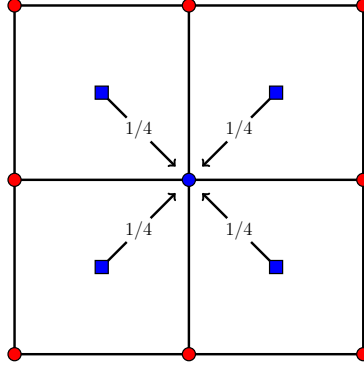


Figure 16.1: We assign to a node the average value of the gradient  $\nabla u_h$  at the adjacent centroids.

We denote by  $E(x_i) = \{E \in \mathcal{T}_h | x_i \in \overline{E}\}$  the patch of elements which share the node  $x_i$  and by  $x_c(E)$  the centroid of the element  $E$ . Then, we choose the degrees of freedoms of  $\mathcal{G}u_h$  as

$$\mathcal{N}_i(\mathcal{G}u_h) = \frac{1}{\#E(x_i)} \sum_{E \in E(x_i)} \nabla u_h(x_c(E)), \quad i = 1, \dots, N. \quad (16.5)$$

As before, the recovery process is fairly simple and localised and practically does not increase numerical costs. Moreover, we observe superconvergence of the recovered gradient in numerical experiments for the BEM-based FEM. To demonstrate this, we consider the Laplace problem on  $\Omega = (-1, 1)^2$  with Dirichlet condition

$$g(x, y) = \exp(2\pi(x - 0.3)) \cos(2\pi(y - 0.3)).$$

We compare the error in the  $L^2$ -norm between the exact gradient  $\nabla u$  and the approximate gradient  $\nabla u_h$  as well as the recovered gradient  $\mathcal{G}u_h$ . To this end, we use a series of meshes made of regular hexagons with decreasing size, solve with the BEM-based FEM and apply the averaging technique (16.5) on each level.

The error against the number of degrees of freedom for is depicted in Figure 16.2. We observe superconvergence, which is highlighted by an increase in the order of convergence, i.e., from  $\mathcal{O}(N^{-1/2})$  for  $\nabla u_h$  to approximately  $\mathcal{O}(N^{-3/4})$  for  $\mathcal{G}u_h$  with  $N$  being the number of degrees freedom in the mesh.

## 16.4 Recovery-based error estimator

Another significant application of gradient recovery lies in a posteriori error estimation with the aim of adaptive mesh refinement. We use the so called “recovery-based error estimator” [2]

$$\|\nabla u - \nabla u_h\|_{L^2(\Omega)}^2 \approx \|\mathcal{G}u_h - \nabla u_h\|_{L^2(\Omega)}^2.$$

It is important to note that the post-processed gradient does not need to be superconvergent to produce a reliable estimator [3]. Moreover, we modify our averaging scheme as follows

$$\mathcal{N}_i(\mathcal{G}u_h) = \frac{1}{|E(x_i)|} \sum_{E \in E(x_i)} |E| \nabla u_h(x_c(E)), \quad i = 1, \dots, N. \quad (16.6)$$

In this way, we take general meshes into account and are consistent with the special case (16.5).

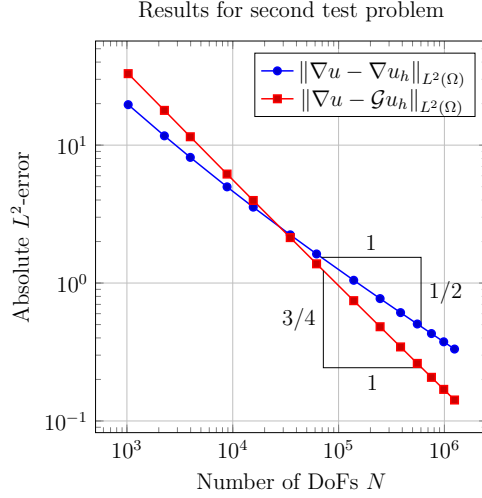


Figure 16.2: The error in the gradient between the exact solution and the approximate and recovered one respectively against the number of degrees of freedom in a log-log plot.

**Algorithm 1** We follow the basic concept of an adaptive FEM algorithm of the form

1. solve: We solve problem (16.1) on the current mesh level and compute the gradient  $\nabla u_h$ .
2. recover: Then, we apply the post-processing by averaging (16.6) and obtain the recovered gradient  $\mathcal{G}u_h$ .
3. estimate: Subsequently, we estimate the error on each element  $E$  by

$$\eta^2 = \sum_E \eta_E^2, \quad \eta_E^2 = \|\mathcal{G}u_h - \nabla u_h\|_{L^2(E)}^2.$$

4. mark: Afterwards, we mark the elements for refinement. Here, we apply the Dörfler marking strategy [10] with threshold  $\theta = 0.5$  for all experiments.
5. refine: Finally, we refine the marked elements and start again.

We stop the algorithm if the maximum mesh level is reached or  $\eta$  is sufficiently small.

In the following, we compare this recovery-based algorithm with a residual-based algorithm for the BEM-based FEM [17], which does not perform any post-processing but instead computes the residual

$$\eta_E^2 = \sum_{e \subset \partial E \setminus \Gamma} h_e \left\| \left[ \frac{\partial u_h}{\partial n} \right] \right\|_{L^2(e)}^2, \quad \left[ \frac{\partial u_h}{\partial n} \right] = \frac{\partial(u_h)|_E}{\partial n} + \frac{\partial(u_h)|_{(\Omega \setminus \bar{E})}}{\partial n}, \quad (16.7)$$

in step (3) of Algorithm 1. As our test problem, we consider the Laplace problem on the L-shaped domain  $\Omega = (-1, 1)^2 \setminus [0, 1]^2$  with Dirichlet conditions

$$g(r, \varphi) = r^{2/3} \sin(2(\varphi - \pi/2)/3) \text{ on } \Gamma,$$

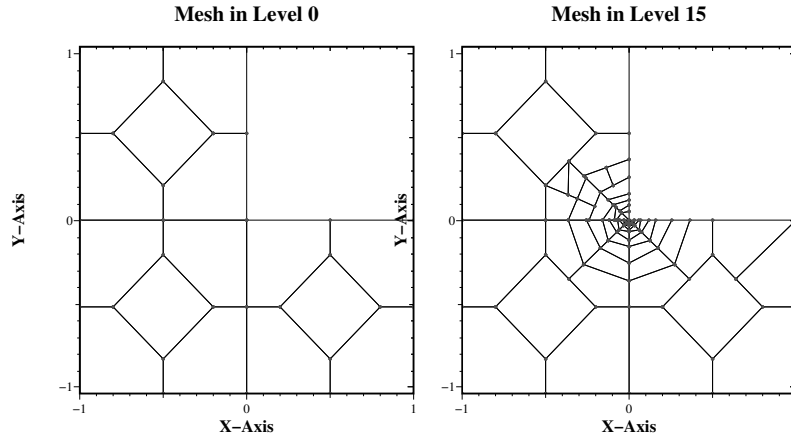


Figure 16.3: The initial Voronoi mesh (left) and after 15 refinement steps with the recovery-based estimator (right).

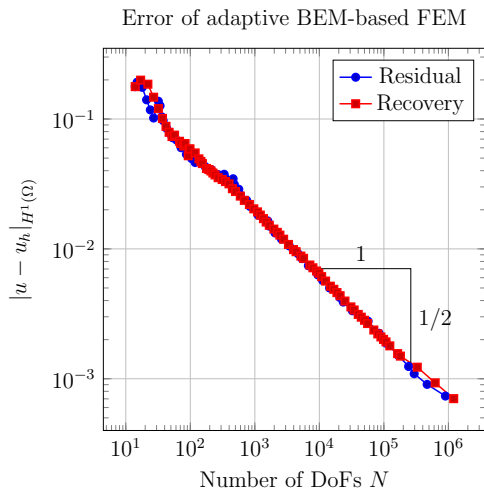


Figure 16.4: The error in the energy norm plotted against the number of degrees of freedom in the mesh for the recovery- and residual-based estimators in logarithmic scaling.

where  $(r, \varphi)$  are polar coordinates. Due to a singularity in the origin, the rate of convergence of the error is limited to  $\mathcal{O}(N^{-1/3})$  for uniform refinement. On the other hand, adaptive algorithms should recover the optimal convergence rate of  $\mathcal{O}(N^{-1/2})$  despite the singularity.

We use the same initial Voronoi mesh, which is depicted in Figure 16.3, and observe intensive refinement around the origin for the residual- and recovery-based estimator. Furthermore, we see in Figure 16.4 that both algorithms produce very similar results and succeed in achieving the convergence rate of  $\mathcal{O}(N^{-1/2})$ . In addition, we study the efficiency of the estimators given by

$$\Psi = \frac{\eta}{|u - u_h|_{H^1(\Omega)}},$$

which measures the quality of the estimated error. Overall, we see in Figure 16.5 that the recovery-based estimator operates nearly optimally and also outperforms the residual-based one. Taking the numerical work into consideration, we conclude that the recovery-based error estimator is our preferred choice for this particular example.

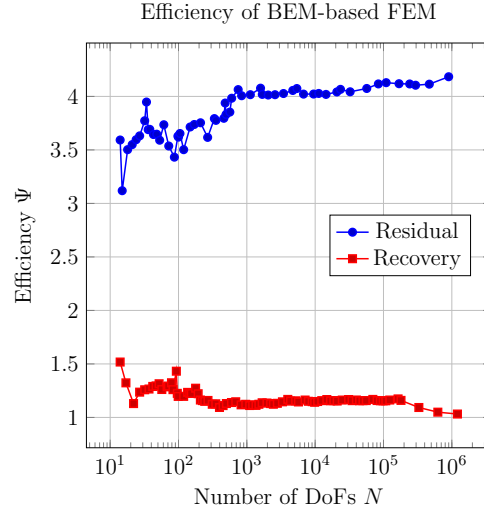


Figure 16.5: The efficiency of the two estimators against the number of degrees of freedom in a log-log plot.

## 16.5 Gradient Recovery for VEM

In this final section, we present an analogue of the recovery-based estimator (16.6) for the VEM. Once more, we consider the Poisson problem (16.1) with exact solution  $u \in V$  and virtual element solution  $u_h \in V_h$ . We rely on the projection operator  $\Pi_1^\nabla$  to guarantee computability and aim at estimating  $|u - \Pi_1^\nabla u_h|_{H^1(\Omega)}$  instead of  $|u - u_h|_{H^1(\Omega)}$ . The post-processed gradient  $\mathcal{G}u_h \in V_h^2$  is given by

$$\mathcal{N}_i(\mathcal{G}u_h) = \frac{1}{|E(x_i)|} \sum_{E \in E(x_i)} |E| (\nabla(\Pi_1^\nabla u_h))(x_c(E)), \quad i = 1, \dots, N. \quad (16.8)$$

Thus, the recovery-based error estimator for the VEM has the representation

$$\eta^2 = \sum_E \eta_E^2 \quad \text{with} \quad \eta_E^2 = \|\Pi_1^\nabla(\mathcal{G}u_h) - \nabla(\Pi_1^\nabla u_h)\|_{L^2(E)}^2.$$

We check the performance of this estimator as part of the adaptive Algorithm 1. To this end, we use the same setup from the previous section for the adaptive test problem with the re-entrant corner. Likewise, we compare this estimator with the residual-based one [7] of the form

$$\eta_E^2 = \sum_{e \in \partial E \setminus \Gamma} h_e \left\| [(\nabla(\Pi_1^\nabla u_h)) \cdot n] \right\|_{L^2(e)}^2 + S^E(u_h, u_h).$$

In Figure 16.6 we find that the error is of  $\mathcal{O}(N^{-1/2})$  for both strategies with the recovery-based one leading to marginally better results. In essence, the results for the VEM agree with the results for the BEM-based FEM. Judging by Figure 16.7, the efficiency of the recovery-based estimator is again nearly optimal and superior to that of the residual-based approach.

Overall, both estimators perform very well in this particular example. Due to the fact that the recovery-based scheme achieves slightly better results and estimates the error more accurately, we prefer it over the residual-based estimator.

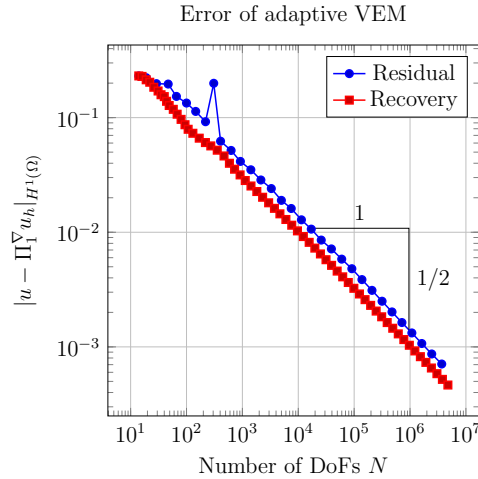


Figure 16.6: The error between the gradient of the exact solution and the projected gradient of the VEM solution plotted against the number of degrees of freedom in the mesh for the recovery- and residual-based estimators in logarithmic scaling.

## References

- [1] B. Ahmad, A. Alsaedi, F. Brezzi, L. D. Marini, and A. Russo. Equivalent projectors for virtual element methods. *Comput. Math. Appl.*, 66(3):376–391, 2013.
- [2] M. Ainsworth and J. T. Oden. *A posteriori error estimation in finite element analysis*. Pure and Applied Mathematics (New York). Wiley-Interscience [John Wiley & Sons], New York, 2000.
- [3] I. Babuška, T. Strouboulis, S. K. Gangaraj, and C. S. Upadhyay.  $\eta\%$ -superconvergence in the interior of locally refined meshes of quadrilaterals: superconvergence of the gradient in finite element solutions of Laplace’s and Poisson’s equations. *Appl. Numer. Math.*, 16(1-2):3–49, 1994.
- [4] J. Barlow. Optimal stress locations in finite element models. *Int. J. Numer. Meth. Eng.*, 10(2):243–251, 1976.
- [5] L. Beirão da Veiga, F. Brezzi, A. Cangiani, G. Manzini, L. D. Marini, and A. Russo. Basic principles of virtual element methods. *Math. Models Methods Appl. Sci.*, 23(1):199–214, 2013.
- [6] F. Brezzi and L. Donatella Marini. Virtual element methods for plate bending problems. *Comput. Methods Appl. Mech. Engrg.*, 253:455–462, 2013.
- [7] A. Cangiani, E. H. Georgoulis, T. Pryer, and O. J. Sutton. A posteriori error estimates for the virtual element method. *Numer. Math.*, 137(4):857–893, 2017.
- [8] A. Cangiani, V. Gyrya, and G. Manzini. The nonconforming virtual element method for the Stokes equations. *SIAM J. Numer. Anal.*, 54(6):3411–3435, 2016.

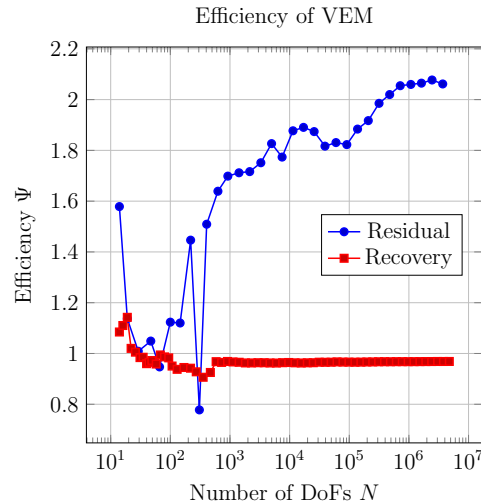


Figure 16.7: The efficiency of the two estimators against the number of degrees of freedom in a log-log plot.

- [9] B. Cockburn, J. Gopalakrishnan, and R. Lazarov. Unified hybridization of discontinuous Galerkin, mixed, and continuous Galerkin methods for second order elliptic problems. *SIAM J. Numer. Anal.*, 47(2):1319–1365, 2009.
- [10] W. Dörfler. A convergent adaptive algorithm for Poisson’s equation. *SIAM J. Numer. Anal.*, 33(3):1106–1124, 1996.
- [11] H. Guo, C. Xie, and R. Zhao. Superconvergent Gradient Recovery for Virtual Element Methods. *arXiv e-prints*, page arXiv:1804.10194, April 2018.
- [12] K. Lipnikov, G. Manzini, and M. Shashkov. Mimetic finite difference method. *J. Comput. Phys.*, 257(part B):1163–1227, 2014.
- [13] J. T. Oden and H. J. Brauchli. On the calculation of consistent stress distributions in finite element approximations. *Int. J. Numer. Meth. Eng.*, 3(3):317–325, 1971.
- [14] S. Rjasanow and S. Weißer. Higher order BEM-based FEM on polygonal meshes. *SIAM J. Numer. Anal.*, 50(5):2357–2378, 2012.
- [15] G. Strang and G. J. Fix. *An analysis of the finite element method*. Prentice-Hall, Inc., Englewood Cliffs, N. J., 1973. Prentice-Hall Series in Automatic Computation.
- [16] L. B. Wahlbin. *Superconvergence in Galerkin Finite Element Methods*, volume 1605 of *Lecture Notes in Mathematics*. Springer, Berlin, 1995.
- [17] S. Weißer. Residual based error estimate and quasi-interpolation on polygonal meshes for high order BEM-based FEM. *Comput. Math. Appl.*, 73(2):187–202, 2017.
- [18] O. C. Zienkiewicz and J. Z. Zhu. The superconvergent patch recovery and a posteriori error estimates. I. The recovery technique. *Internat. J. Numer. Methods Engrg.*, 33(7):1331–1364, 1992.
- [19] M. Zlámal. Superconvergence and reduced integration in the finite element method. *Math. Comp.*, 32(143):663–685, 1978.

## Chapter 17

# A Boundary Integral Method For Modeling Cell Motion Due To Chemotaxis

**P. J. Harris**

School of Computing, Engineering and Mathematics  
University of Brighton  
Lewes Road  
Brighton, BN2 4GJ, UK.

---

**Abstract.** *Chemotaxis is the biological process whereby a cell moves in the direction in which the concentration of a chemical in the fluid medium surrounding the cell is increasing. The chemical signal may be secreted by cells to signal other nearby cells (or clusters of cells) so that they can combine to form larger clusters. This paper presents a mathematical model for simulating the motion of the cells through a viscous fluid due to chemotaxis using a boundary integral representation of the resulting fluid flow. The boundary integral method is ideally suited to solving this problem as the clusters often form irregular geometrical shapes.*

---

### 17.1 Introduction

It is well known that biological cells can move in response to the concentration of particular chemical signals in the fluid in which they are immersed, a process known as chemotaxis. Usually the cells will try to move in the direction in which the concentration of the chemical signal is increasing. In some cases, the chemical may simply be present in the environment, but often it is secreted by one cell in order to signal and attract other nearby cells so that they can combine and form clusters. Such behavior has been observed experimentally and reported in the literature, and is summarised in Green and Mecsas [6].

A number of mathematical models have been proposed for simulating how cells can form clusters through chemotaxis. Many models which use diffusion-reaction type equations to determine the concentrations of cell have been proposed, and these form the basis of the widely reported Keller-Segel models (see [2, 4, 10, 11] for example). However, such models cannot be used to determine the motion of individual cells.

Harris [7] introduced a simple model that can be used to study how a large number of individual cells and small clusters can be combined to form larger clusters using chemotaxis. However, this simple model does not fully account for features such as the motion of the surrounding fluid. A more sophisticated model, presented in Harris [8] uses the boundary integral method to model the motion of cells due to a chemical signal that is present in the surrounding fluid where the chemical concentrations are given by a simple explicit formula. This paper modifies the methods presented in [8] to consider the case where one of the cells is secreting the chemical signal. A coupled finite element and boundary element method for modeling both the motion of cells and the spread of the chemical signal has been proposed in Harris [9] but this method is computationally very expensive and this paper presents a simpler method that is computationally much cheaper.

The methods presented in the paper will be for simulating the interactions between individual cells. However, the same methods can be used to model the interactions between clusters of cells as in this context a cluster can be considered as a single large irregular shaped cell.

## 17.2 Mathematical Model

The mathematical model presented here can be split into three stages. Firstly, there is the model of how the chemical signal from a cell spreads out into the surrounding fluid medium, then there is the model of how a cell moves in response to the chemical signal and finally there is the model of fluid motion due to the motion of the cells.

Here  $C_i$ ,  $i = 1, \dots, N$  is used to denote each of the  $N$  cells and  $(x_i, y_i)$ ,  $\mathbf{v}_i$  and  $\omega_i$  are used to denote the location of the centroid, translational velocity and angular velocity for the  $i^{\text{th}}$  cell. In addition,  $\Gamma^{[i]}$  denotes the boundary of the  $i^{\text{th}}$  cell and  $\Omega$  is used to denote the fluid-filled region exterior to cells.

### 17.2.1 Diffusion Of The Chemical Signal

The concentration  $c$  of the chemical signal being secreted from a cell immersed in a fluid moving with velocity field  $\mathbf{u}$  can be modelled using the convection-diffusion equation

$$\frac{\partial c}{\partial t} = \mu \nabla^2 c - \nabla \cdot (c\mathbf{u}) \quad (17.1)$$

where  $\mu$  is the diffusion constant. Harris [9] proposed a model of chemotaxis using the finite element method to solve (17.1) but the computation cost of such methods is prohibitive as the finite element stiffness matrix needs to be recalculated at each time-step. However, the results presented in Harris [9] suggest that the spread of the chemical signal around the emitting cell can be modeled using the simple linear diffusion equation

$$\frac{\partial c}{\partial t} = \mu \nabla^2 c \quad (17.2)$$

and that concentrations move with the emitting cell. That is, when using a Lagrangian frame of reference which follows the emitting cell, the chemical appears to spread out from the cell according to the linear diffusion equation. This simplifies the mathematical model as any appropriate solution to (17.2) can be used to model the concentrations, and allowing the concentrations to move with the emitting cell. Whilst this model is not as precise as the one

discussed in [9], since it is not a solution to the convection-diffusion equation (17.1), it does avoid the need for finding a numerical solution to (17.1).

For simplicity, assume the only cell emitting the chemical signal is cell  $C_1$  and that it is circular. Then, the solution to (17.2) can be expressed as

$$c(x, y, t) = \frac{A}{\mu(t + t_\epsilon)} \exp\left(-\frac{(x - x_1)^2 + (y - y_1)^2}{4(t + t_\epsilon)\mu}\right) \quad (17.3)$$

where  $A$  is a parameter that controls the magnitude of the concentration of the chemical signal and  $t_\epsilon$  is a small value used to avoid division by zero problems when  $t = 0$ . In this work (17.3) will be used to determine the concentrations of the chemical signal with  $(x_1, y_1)$  changing as  $C_1$  moves.

### 17.2.2 Motion Of The Cells

When chemotaxis occurs the cells respond to changes in the concentrations of the chemical signal through receptors located in the their outer membrane. Some highly sophisticated models of how cells move in response to such chemical signals have been developed, such as the one by Elliott [3]. However, there is also some experimental evidence the cells essentially move as rigid bodies (see the images in Nitta et. al [13] for example) and so the simple rigid body approach described below is adopted here.

Since the receptors that detect the concentrations of the chemical are in the cells outer membrane, the effect of the chemical on a given cell can be modeled as a force proportional to the gradient of the concentrations of the chemical acting on the cells boundary. Hence the total force  $\mathbf{F}_i$  acting on the  $i^{\text{th}}$  cell is

$$\mathbf{F}_i = \oint_{\Gamma_i} (k_i \nabla c + \mathbf{f}) \, d\Gamma$$

where  $\mathbf{f}$  is the hydrodynamic force due to the motion of the surrounding fluid (which will be discussed in Section 17.2.3 below) and  $k_i$  is a constant that can be used to control how strongly the cell reacts to the chemical signal. The value of  $k_i$  can be different for each cell, but here it is assumed to be the same for all cells.

The translational and angular accelerations of each cell are given by

$$\frac{d\mathbf{v}_i}{dt} = \mathbf{a}_i(t) = \frac{1}{m_i} \oint_{\Gamma_i} (k_i \nabla c + \mathbf{f}) \, d\Gamma$$

and

$$\begin{aligned} \frac{d\omega_i}{dt} = \alpha_i(t) = & \frac{1}{I_i} \left[ \int_{\Gamma_i} ((x - x_i)f_y(\mathbf{x}) - (y - y_i)f_x(\mathbf{x})) \, d\Gamma \right. \\ & \left. + \int_{\Gamma_i} \left( k_i(x - x_i)\frac{\partial c}{\partial y} - k_i(y - y_i)\frac{\partial c}{\partial x} \right) \, d\Gamma \right] \end{aligned}$$

respectively, where  $m_i$  and  $I_i$  denote the mass and moment of inertia of the cell respectively and  $\mathbf{f} = [f_x(\mathbf{x}), f_y(\mathbf{x})]^T$ .

For each cell, the velocity  $\mathbf{v}_i$ , angular velocity  $\omega_i$ , the location of its centre of mass  $\mathbf{x}_i$  and rotation  $\theta_i$  can be integrated through time using

$$\begin{aligned}\mathbf{v}_i(t+h) &= \mathbf{v}_i(t) + h\mathbf{a}_i(t) \\ \omega_i(t+h) &= \omega_i(t) + h\alpha_i(t) \\ \mathbf{x}_i(t+h) &= \mathbf{x}_i(t) + \frac{h}{2}(\mathbf{v}_i(t) + \mathbf{v}_i(t+h)) \\ \theta_i(t+h) &= \theta_i(t) + \frac{h}{2}(\omega_i(t) + \omega_i(t+h)).\end{aligned}$$

See Atkinson [1], for example, for further details of time integration schemes.

### 17.2.3 Boundary Integral Method For The Fluid Motion

Assuming that the fluid is incompressible and that there are no body forces acting on the fluid, the equations of motions for the fluid can be expressed as the continuity equation [12]

$$\nabla \cdot \mathbf{u} = 0 \tag{17.4}$$

for the conservation of mass, and the Navier-Stokes equation

$$\rho \left( \frac{\partial \mathbf{u}}{\partial t} + \mathbf{u} \cdot \nabla \mathbf{u} \right) = -\nabla p + \mu \nabla^2 \mathbf{u} \tag{17.5}$$

which can be considered as an expression of Newton's second law for a small particle of the fluid. Here  $\mathbf{u}$  denotes the fluid velocity,  $\rho$  and  $\mu$  are used to denote the density and dynamic viscosity of the fluid and  $p$  is the pressure. Since the length scale of a typical cluster of cells is very small (typically of the order of  $10^{-5}$ m) and the time scales over which the cells move very long (typically large fractions of a hour), the Reynolds number for the flow is very small. This mean that the inertial terms on the left-hand side of (17.5) can be neglected and (17.5) can be simplified to

$$-\nabla p + \mu \nabla^2 \mathbf{u} = \mathbf{0}. \tag{17.6}$$

At this point it is worth noting that (17.4) and (17.6) are usually referred to as the governing equations for a steady Stokes flow. However, in the application considered here the flow is not steady as the cell is moving and the fluid velocity field will move with the cell. However, for the reasons given above, the inertia terms in the Navier-Stokes equation can be neglected meaning that (17.4) and (17.6) can be used to determine the velocity field at any given instant but they have to be solved at every time that the velocity field is required.

The boundary condition are given in the form of a no-slip condition on the boundary of the each cluster, so

$$\mathbf{u}(\mathbf{x}) = \mathbf{v}_i + \begin{bmatrix} y - y_i \\ x - x_i \end{bmatrix} \omega_i \quad \mathbf{x} \in \Gamma^{[i]}. \tag{17.7}$$

An additional outer boundary  $\Gamma^{[0]}$  is needed to avoid the problems associated with the Stokes paradox, which states that there is no solution to (17.4) and (17.6) which satisfies the boundary conditions (17.7) and the condition that  $\mathbf{u} \rightarrow \mathbf{0}$  as  $|\mathbf{x}| \rightarrow \infty$  [12]. This outer boundary is chosen to be a long way from the cell (which in an experimental situation would correspond to a petri-dish containing the cells) and the boundary condition  $\mathbf{u} = \mathbf{0}$  is imposed on this outer boundary.

In two space dimensions it can be shown that if the fluid velocity  $\mathbf{u}$  satisfies (17.4) and (17.6) in a closed domain  $\Omega$  with a piecewise smooth boundary curve  $\Gamma$ , then the velocity also satisfies the boundary integral equation [14]

$$\oint_{\Gamma} T(\mathbf{x}, \mathbf{x}_0) \mathbf{u}(\mathbf{x}) \, d\Gamma(\mathbf{x}) - \oint_{\Gamma} G(\mathbf{x}, \mathbf{x}_0) \mathbf{f}(\mathbf{x}) \, d\Gamma(\mathbf{x}) = \frac{1}{2} \mathbf{u}(\mathbf{x}_0) \quad (17.8)$$

where  $\mathbf{f}$  denotes the surface forces,

$$T_{ij}(\mathbf{x}, \mathbf{x}_0) = -\frac{\mathbf{r} \cdot \mathbf{n}}{\pi r^4} r_i r_j$$

$$G_{ij}(\mathbf{x}, \mathbf{x}_0) = \frac{1}{4\pi\mu} \left( -\delta_{ij} \ln(r) + \frac{r_i r_j}{r^2} \right)$$

$\mathbf{r} = \mathbf{x} - \mathbf{x}_0$ ,  $r = |\mathbf{r}|$ ,  $\mathbf{n}$  is the unit normal to  $\Gamma$  directed onto the fluid domain  $\Omega$  and  $\delta_{ij}$  is the Kronecker delta function. Here  $\Gamma$  is used to denote the union of the boundaries of the cells and the outer fluid boundary. From the fluid velocity boundary conditions, the value of  $\mathbf{u}$  is known on the whole of  $\Gamma$ , and hence (17.8) is a first kind Fredholm integral equation for the unknown fluid-force  $\mathbf{f}$  on the boundary of the cells.

The approximate solution of the boundary integral equation (17.8) can be found using the boundary element method. Here a simple piece-wise constant approximation to the solution has been used with a piece-wise linear representation of the cell and outer boundaries. The full details of the boundary element method for solving (17.8) can be found in [14], for example, and are not repeated here.

### 17.3 Numerical Results

The results presented here are for some typical examples simulating the motion of cells due to chemotaxis. Here length of the sides of the outer boundary as 5,000 times the radii of the cells, simulating the motion of cells in the centre of a square petri-dish with sides of length 5cm. The diffusion parameter  $\mu$  and concentration parameter  $A$  are all scaled such that their values are all 1. The time parameter  $t_\epsilon$  for avoiding problems when  $t = 0$  was set to  $10^{-2}$ . The diffusion parameter  $\nu$  was set to 0.1 in Example 1 and 0.01 in Example 2. The boundary integral equation (17.8) was solved using 20 boundary elements on the boundary of each cell, and 20 boundary elements on each edge of the outer boundary as the results presented in [8] for solving a closely related problem show that this is sufficient for the level of accuracy required here.

The first example is slightly artificial, but does represent an example that can be used to check the consistency of the numerical method presented in this paper. This example considers five cells with one cell at the centre (which is the cell secreting the chemical signal) and the other cells arranged above, below to the left and to the right of the central cell, as shown in Figure 17.3. Figures 17.3 to 17.3 show the subsequent locations of the cells, and the concentrations of the chemical signal. The motion of the four outer cells towards the central cell is symmetric (as expected) and the difference in the distances of each of the outer cells from the central cell is less than  $10^{-10}$ . This symmetrical motion of the outer cells shows that the method is yielding consistent results.

The second example considers a problem with 10 irregularly placed cells, where one of the cells on the right secretes the chemical signal. The cells close to the emitting cell are strongly attracted towards it by the chemical signal. The motion of these cells sets up a flow in the fluid which pushes the emitting cell, and the concentrations of the chemical signal, towards the right.

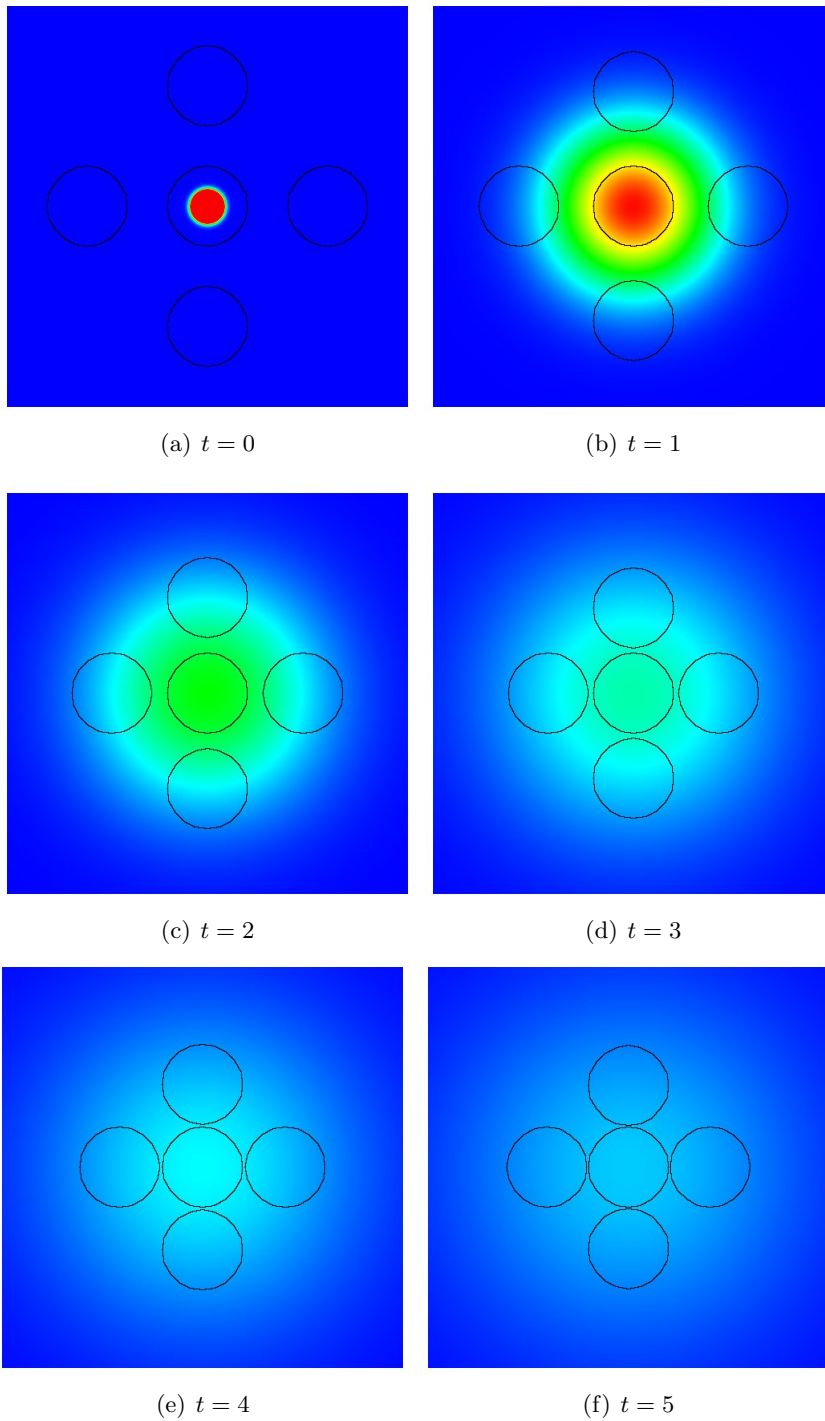


Figure 17.1: The locations cells and chemical concentrations for the 5 cell example.

## 17.4 Conclusions And Further Work

The method presented here is an efficient method for simulating the motion of a moderate number of cells through a viscous fluid due to chemotaxis. The computational cost of using

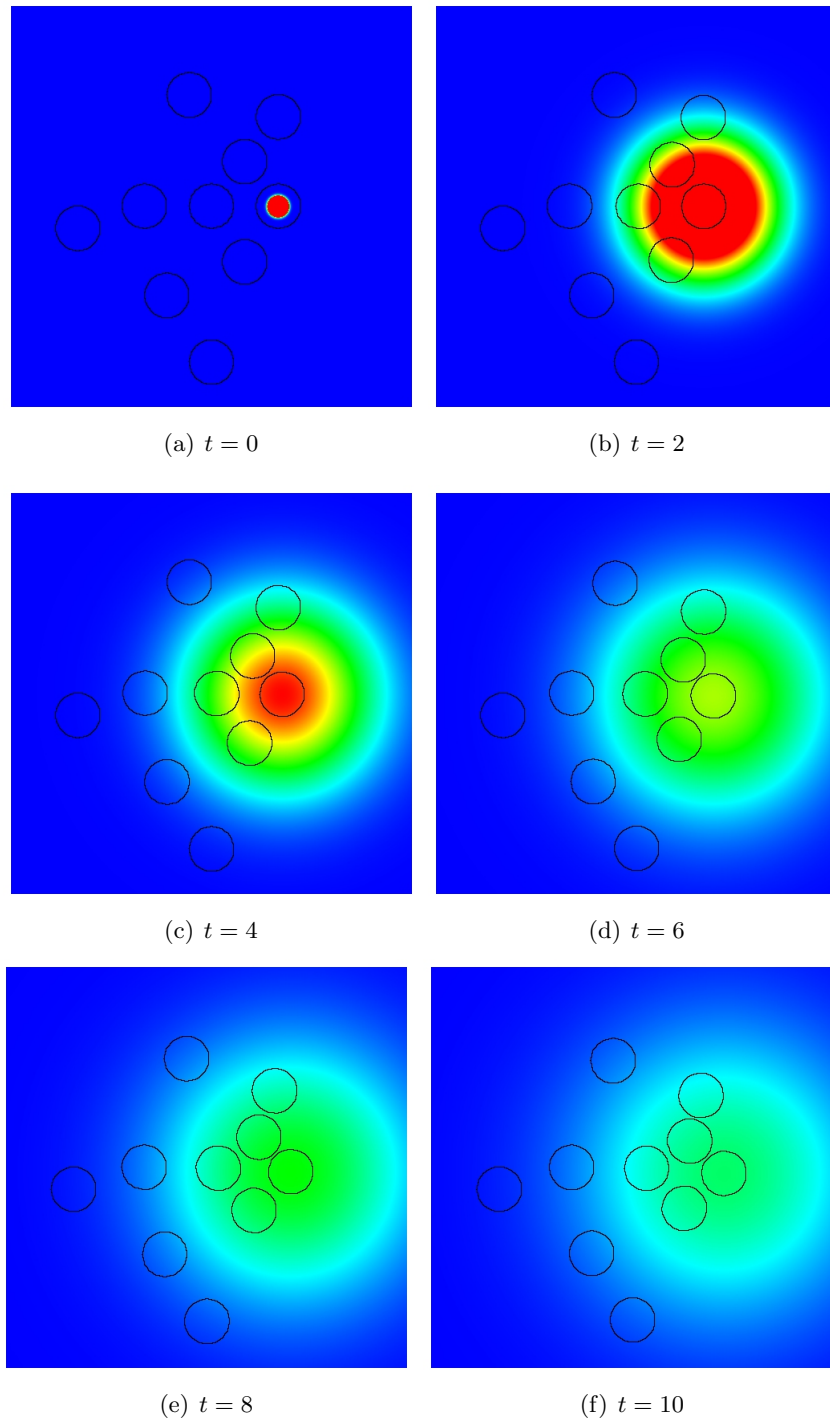


Figure 17.2: The locations cells and chemical concentrations for the 10 cell example.

this model is much less than if a full finite element method for modeling the concentrations of the chemical signal had been used, albeit with the possibility that the concentrations of the chemical signal are not being accurately determined. For example, the calculations for example 2 with 10 cells takes less than an hour on a typical desk-top PC, whereas the corresponding

calculations using the finite element method (with a reasonably fine mesh) for determining the chemical concentrations would take over 24 hours on the same PC.

The current model for the concentrations of the chemical is only applicable to when the emitting cell is circular, although there are no restrictions on the shapes of the other cells. A more sophisticated models for the way in which a cell secretes the chemical signal, and which can be applied to cells of other shapes, is currently being developed.

The model of what happens when two cells collide also needs to be developed as the current model has to stop if two (or more) cells collide. Models of cell adhesion, such as the model given in [15] could be utilized to simulate how two cells stick together once they have collided. Alternatively, a model which utilizes some coalescence scheme, such as those used to model how liquid droplet collide and coalesce (see [16] for example), could be developed although as noted in [8] there are significant differences in the physical processes that occur in the two type of collision.

## References

- [1] K. Atkinson, An introduction to numerical analysis, 2nd Edition, John Wiley and Sons, New York, 1989.
- [2] A. Chertock, A. Kurganov, X. Wang, Y. Wu, On a chemotaxis model with saturated chemotactic flux, *Kin. and Rel. Mod* 5 (1) (2012) 51 – 95.
- [3] C. Elliott, B. Stinner, C. Venkataraman, Modelling cell motility and chemotaxis with evolving surface finite elements, *J. R. Soc. Interface* 9 (2012) 3027 – 3044.
- [4] H. Gajewski, K. Zacharias, Global behaviour of a reaction - diffusion system modelling chemotaxis, *Math. Nachr* 195 (1998) 77 – 114.
- [5] A. Giere, T. Iliescu, V. John and D. Wells. SUPG reduced order models for convection-dominated convection-diffusion-reaction equations. *Comp. Meth. App. Mech. Eng.* 289, (2015), 454 – 474
- [6] E. R. Green and J. Meccas. Bacterial Secretion Systems: An Overview. *Microbiology Spectrum*, 4, 2016.
- [7] P. J. Harris. A simple mathematical model of cell clustering by chemotaxis, *Mathematical Biosciences*, 294, (2017), 62 – 70.
- [8] P. J. Harris. Modelling the motion of clusters of cells in a viscous fluid using the boundary integral method. *Mathematical Biosciences*, 306, (2018), 145 - 151.
- [9] P. J. Harris. A combined boundary element and finite element model of cell motion due to chemotaxis. In *Integral Methods in Science and Engineering*, eds C. Constanda and P. J. Harris, Birkhauser. (2019).
- [10] E. Keller, L. Segel, Model for chemotaxis, *J. Theor. Biol.* 30 (1971) 225 – 234.
- [11] I. Lapidus, R. Schiller, A mathematical model for bacterial chemotaxis, *Biophys. J.* 14 (1974) 825 – 834.
- [12] M. Lighthill, An informal introduction to theoretical fluid mechanics, Clarendon Press, Oxford, (1986).
- [13] N. Nitta, T. Tsuchiya, A. Yamauchi, T. Tamatani, S. Kanegasaki, Quantitative analysis of eosinophil chemotaxis tracked using a novel optical device — taxiscan, *Journal of Immunological Methods* 320 (1–2) (2007) 155 – 163

- [14] C. Pozrikidis, *Boundary Integral and Singularity Methods for Linearized Viscous Flow*, Cambridge Texts in Applied Mathematics, Cambridge University Press, 1992.
- [15] R. Thompson, C. Yates, R. Baker, Modelling cell migration and adhesion during development, *Bull. Math. Biol.* 74 (2012) 2793 – 2809.
- [16] Y R Zhang, X Z Jiang and K H Luo. Bounce regime of droplet collisions: A molecular dynamics study. *Journal of Computational Science*, 17, (2016), 457 – 462.

## PLENARY TALK I

### Highly accurate integral equation based methods for surfactant laden drops in two and three dimensions.

*Prof. A.K. Tornberg, KTH, Royal Institute of Technology, Stockholm, Sweden.*

#### **Abstract**

In micro-fluidics, at small scales where inertial effects become negligible, surface to volume ratios are large and the interfacial processes are extremely important for the overall dynamics. Integral equation based methods are attractive for the simulations of e.g. droplet-based microfluidics, with tiny water drops dispersed in oil, stabilized by surfactants.

We have developed highly accurate numerical methods for drops with insoluble surfactants, both in two and three dimensions. In this talk I will discuss some fundamental challenges that we have addressed, that are also highly relevant to other applications: accurate quadrature methods for singular and nearly singular integrals, adaptive time-stepping, and reparameterization of time-dependent surfaces for high quality discretization of the drops throughout the simulations. I will also discuss a recent extension to include electric fields, as well as quadrature error estimates in 2D and the extension of such estimates to 3D.

#### **Correspondance**

*akto@kth.se*

## PLENARY TALK II

### Does the Galerkin method converge for the standard second-kind integral equations for the Laplacian on Lipschitz domains?

*Dr Euan Spence* University of Bath, UK.

#### Abstract

It has not yet been proved that the Galerkin method converges when applied to the standard second-kind integral-equation formulations for Laplace's equation on general Lipschitz domains, or even general 3D Lipschitz polyhedra. This convergence result is equivalent to proving that the relevant integral operators are the sum of a coercive operator and a compact operator on  $L^2(\Gamma)$ , where  $\Gamma$  denotes the boundary of the Lipschitz domain. In this talk, I will describe recent results obtained with Simon Chandler-Wilde (University of Reading) that settle this question.

#### Correspondance

*eas25@bath.ac.uk*

# A direction preserving discretisation for transporting densities using a phase-space boundary integral operator

D.J.Chappell, M. Richter and G. Tanner

## Abstract

Boundary integral operator models for transporting phase-space densities through complex two [1] and three dimensional [2] domains have recently been proposed. In these papers, the dependence of the density on the momentum (or equivalently direction) variable is approximated using a basis expansion of orthogonal polynomials. This approach allows for the inclusion of directivity in the model, going beyond more conventional radiosity based methods. However, when the underlying transport only takes place in a finite number of deterministic directions, numerical diffusion leads to an accumulation of error each time the integral operator is applied. This issue is particularly problematic for transporting densities along rays through a mesh, transmitting from one cell to the next. In this talk, a direction preserving discretisation procedure will be outlined. Numerical results demonstrating the elimination of errors associated to numerical diffusion will be presented for some simple test cases.

## References

- 1 D.J. Chappell, G. Tanner, N. Søndergaard and D. Lochel, Discrete flow mapping: transport of phase-space densities on triangulated surfaces Proceedings of the Royal Society A, 469: 20130153.
- 2 J. Bajars, D.J. Chappell, N. Søndergaard and G. Tanner, Transport of phase-space densities through tetrahedral meshes using discrete flow mapping, Journal of Computational Physics, 328, (2017) 95–108.

## Correspondance

*david.chappell@ntu.ac.uk; Nottingham Trent University*

# A DRBEM Formulation for Two-Dimensional Coupled Viscous Non-Linear Burger's Equations

Salam Adel Ahmed, Luiz C. Wrobel, Jurij Iljaz

## Abstract

This work describes a numerical formulation of the dual reciprocity boundary element method (DRBEM) for a two dimensional non-linear parabolic system of Burger's equations with high Reynolds number. The problem is solved numerically by discretising only the external boundary of the channel under consideration using mixed linear and constant elements. Another objective is to discuss the treatment of the convective terms, which involve gradients of the problem variable, and their modeling using DRBEM. A

finite difference method is utilised to simulate the time evolution procedure for solving the resulting system of equations. The Newton-Raphson algorithm is used to solve the reduced non-linear matrix equations which is shown to be rapidly convergent. Numerical experiments are included for two different problems for which analytical solutions are available, to establish the validity of the proposed approach and to demonstrate the efficiency of the proposed technique. The numerical results are in reasonable agreement with the analytical solutions and do not show oscillations or damping of the wave front, as appear in other numerical techniques, even when using moderate and high Reynolds number.

## Correspondance

*salam\_ahmed@sc.nahrainuniv.edu.iq; Al-Nahrain University, Baghdad, Iraq*

# A Green's integral representation for the two-dimensional steady Navier-Stokes equation

E.A. Chadwick

## Abstract

Consider steady uniform flow past a fixed, closed body in an unbounded domain governed by the incompressible Navier-Stokes equations. A velocity representation is given as an integral distribution of Green's functions of the Navier-Stokes equations which we call NSlets, such that the strength of the NSlets is the same as the force distribution over the body boundary. We apply this theory to the benchmark problem of a two-dimensional circular cylinder over a range of Reynolds numbers up to 40 when the steady flow breaks down. A boundary element code is developed with collocation point weighting function and linear shape function, and with Dirichlet body boundary condition that the velocity is zero. Comparison against experiment and other numerical methods is given.

**Correspondance** *e.a.chadwick@salford.ac.uk; University of Salford, Gtr. Manchester UK*

# On Boundary-Domain Integral Equations for Stokes PDE System in $L_p$ -based spaces for Variable-Viscosity Compressible Fluid on Lipschitz Domain

S.E. Mikhailov

## Abstract

We consider Boundary-Domain Integral Equations (BDIEs) associated with the Robin boundary value problem for the stationary Stokes system in  $L_p$ -based Sobolev spaces in a bounded Lipschitz domain in  $\mathbb{R}^3$  with the variable viscosity coefficient. First, we introduce a parametrix and construct the corresponding parametrix-based variable-coefficient Stokes Newtonian and layer integral potential operators with densities and the viscosity coefficient in  $L_p$ -based Sobolev or Besov spaces. Then we generalize various properties of these potentials, known for the Stokes system with constant coefficients, to the case of the Stokes system with variable coefficients. Next, we show that the Robin boundary value problem for the Stokes system with variable coefficients is equivalent to a BDIE system. Then we analyse the Fredholm properties of the BDIE systems in  $L_p$ -based Sobolev and Besov spaces and finally prove their invertibility in corresponding spaces.

This is a joint work with Mirela Kohr and Massimo Lanza de Cristoforis, based on and further developing results of [1, 2, 3].

## References

- [1] O. Chkadua, S.E. Mikhailov and D. Natroshvili, Analysis of direct boundary-domain integral equations for variable-coefficient for a mixed BVP with variable coefficient, I: equivalence and invertibility *J. Integral Equations and Applications*, **21** (2009) 499-543.
- [2] S. E. Mikhailov, Analysis of segregated boundary-domain integral equations for BVPs with non-smooth coefficients on Lipschitz domains. *Boundary Value Problems*, **2018**:87 (2018), 1–52.
- [3] S.E. Mikhailov, C.F. Portillo, Analysis of Boundary-Domain Integral Equations to the Mixed BVP for a Compressible Stokes System with Variable Viscosity. ArXiv, **1805.00235** (2018), 1–29. (To appear in *Communic. Pure and Appl. Analysis*).

## Correspondance

*sergey.mikhailov@brunel.ac.uk; Brunel University London*

# Active control of nonstationary vibrations of plates under dynamic transverse loading

Dr Oleksandr Menshykov, School of Engineering, University of Aberdeen, UK

## Abstract

The current study is devoted to the development of active control methods for the nonstationary vibrations of the bottom-hinged rectangular isotropic elastic plate of medium thickness under dynamic transverse concentrated loading.

To solve the vibration control problem (to minimise or, if possible, fully eliminate the strain) the additional control loads are introduced into the mechanical system. The necessary control loads are determined from the solution of system of Volterra integral equations, which has been obtained from the initial boundary value problem. Furthermore, Tikhonov regularisation algorithm is used to numerically solve the ill-posed system of equations.

The resulting deflection of the median plane is presented for different combinations of the disturbing load and control functions. The advantages and disadvantages of particular control systems and possibility of their practical implementation are discussed.

*Joint study with Dr Alexey Voropay, National Technical University "Kharkiv Polytechnic Institute", Ukraine*

## Correspondance

*o.menshykov@abdn.ac.uk*

# Generalized Fourier Series Method for Elastic Plates

C. Constanda and D. Doty

## Abstract

A convenient way to approximate the solutions of boundary value problems for elliptic partial differential equations is to expand them in a complete set of functions that are intrinsically tied to the structure of the appropriate layer potentials. We show how such a method can be constructed and adapted to yield good numerical results, and illustrate the procedure in application to the interior Dirichlet, Neumann, and Robin problems for the mathematical model of bending of plates with transverse shear deformation.

## Correspondance

*christian-constanda@utulsa.edu, Department of Mathematics, The University of Tulsa, Tulsa, Oklahoma, USA*